N° Ordre...../ FT / UEHL / 2024

PEOPLE'S DEMOCRATIC REPUBLIC OF ALGERIA

MINISTRY OF HIGHER EDUCATION AND SCIENTIFIC RESEARCH

UNIVERSITY OF ECHAHID HAMMA LAKHDAR EL OUED

Faculty of **T**echnology

Department of **M**echanical **E**ngineering

Renewable **E**nergy **D**evelopment **U**nit in **A**rid **Z**ones **(UDERZA) L**aboratory

A THESIS

Submitted by

DEGHOUM Khalil

In Partial Fulfillment of the Requirements for the Degree of

Doctorate LMD in **Mechanical Engineering**

Option: Energy Installations and Turbomachines

Modeling the fatigue behavior of wind turbine under the extreme fluctuations aerodynamic load impact

Discussion on 15/01/2024

Board of Examiners:

MENECEUR Noureddine	MCA	Univ. of El Oued	Chairman
NOUR Abdelkader	Pr	Univ. of Boumerdes	Examiner
BOULIFA Mohamed Iliasse	MCA	Univ. of El Oued	Examiner
DJOUDI Tarek	MCA	Univ. of Biskra	Examiner
BOUKHARI Ali	MCA	Univ. of El Oued	Examiner
GHERBI Mohamed Tahar	MCA	Univ. of El Oued	Supervisor
NECIB Djilani	MCA	Univ. of El Oued	Co-Supervisor

Academic Year 2023/2024

ABSTRACT

In this thesis, we have undertaken a multifaceted approach to enhance the performance of wind turbine blades. Our investigation encompasses both the aerodynamic design of the blades, aimed at increasing power output, and a comprehensive examination of the blade's structural aspects to address issues about vibration, fatigue, and cracking. Through a thorough analysis of the blade's structural properties and material characteristics, we have developed strategies to bolster its durability, reliability, and overall efficiency. By optimizing the aerodynamic profile of the blade and tackling potential challenges like vibration, fatigue, and cracking, our thesis has contributed to the advancement of more efficient and sustainable wind turbine blades for renewable energy systems. in our thesis, we laid the foundation by offering a comprehensive literature review on horizontal-axis turbine blades. We introduced the methodology employed in designing small wind turbine blades, incorporating theories from Blade Element Momentum (BEM) and Computational Fluid Dynamics (CFD), illustrating how these methods can be harnessed to analyze wind turbine blades. An in-depth examination was also conducted of blade vibrations, encompassing the determination of natural frequencies and mode shapes to enhance blade performance. By delving into vibration-related concerns, this chapter sought to inform improvements in wind turbine blade design and operation. In our thesis, we also focused on the crucial topic of fatigue. We provided a comprehensive understanding of fatigue, particularly as it pertains to wind turbine blades. We presented advancements in blade design geared towards extending fatigue life and simplified fatigue equations for small wind turbine blades, introducing the Spectral Load Model (SLM) method and utilizing the FAST tool to infer fatigue. we conducted a detailed analysis of cracks in wind turbine blades resulting from prolonged operation under varying loads and weather conditions, we introduced the Extended Finite Element Method (XFEM), a specialized technique for studying cracks, to gain insights into the timing and extent of crack initiation and propagation within the blade structure. Finally, we synthesized the results obtained from the analyses discussed in our thesis. We aimed to consolidate these findings into a coherent and comprehensible framework, enhancing their overall clarity and significance. This integrated approach allowed us to contribute valuable insights into the improvement of wind turbine blade performance, thereby advancing the field of renewable energy.

Key words: Wind turbine, blade design, vibrations, fatigue, crack.

الملخص

في هذه الأطروحة، قمنا باتخاذ نهج متعدد الأوجه لتحسين أداء ريش توربينات الرياح. يشمل تحقيقنا كلا من التصميم الديناميكي الهوائي للشفرات، الذي يهدف إلى زيادة إنتاج الطاقة، وفحصًا شاملاً للجوانب الهيكلية للشفرة لمعالجة المشكلات المتعلقة بالاهتزاز والتعب والتشقق. ومن خلال التحليل الشامل للخصائص الهيكلية للشفرة وخصائص المواد، قمنا بتطوير استراتيجيات لتعزيز متانتها وموثوقيتها وكفاءتها الشاملة. من خلال تحسين المظهر الديناميكي الهوائي للشفرة ومعالجة التحديات المحتملة مثل الاهتزاز والتعب والتشقق، ساهمت أطروحتنا في تطوير شفرات توربينات الرياح الأكثر كفاءة واستدامة لأنظمة الطاقة المتجددة. في أطروحتنا، وضعنا الأساس من خلال تقديم مراجعة شاملة للأدبيات حول شفرات التوربينات ذات المحور الأفقي. قدمنا المنهجية المستخدمة في تصميم شفرات توربينات الرياح الصغيرة، ودمج النظريات من زخم عنصر الشفرة (BEM) وديناميكيات الموائع الحسابية (CFD)، مما يوضح كيف يمكن تسخير هذه الأساليب لتحليل شفرات توربينات الرياح. تم أيضًا إجراء فحص متعمق لاهتزازات الشفرة، بما في ذلك تحديد الترددات الطبيعية وأشكال الوضع لتعزيز أداء الشفرة. من خلال الخوض في المخاوف المتعلقة بالاهتزاز، سعى هذا الفصل إلى إعلام التحسينات في تصميم وتشغيل شفرات توربينات الرياح. في أطروحتنا، ركزنا أيضًا على موضوع التعب الحاسم. لقد قدمنا فهمًا شاملاً للتعب، خاصة فيما يتعلق بشفرات توربينات الرياح. لقد قدمنا تطورات في تصميم الشفرات موجهة نحو إطالة عمر الكلال ومعادلات الكلال المبسطة لشفرات توربينات الرياح الصغيرة، وإدخال طريقة نموذج الحمل الطيفي (SLM) واستخدام أداة FAST لاستنتاج الكلال. أجرينا تحليلًا تفصيليًا للشقوق في شفرات توربينات الرياح الناتجة عن التشغيل لفترة طويلة تحت أحمال وظروف جوية مختلفة، وقمنا بتقديم طريقة العناصر المحدودة الممتدة (XFEM)، وهي تقنية متخصصة لدراسة الشقوق، للحصول على نظرة ثاقبة حول توقيت ومدى الشقوق البدء والانتشار داخل هيكل النصل. وأخيرا، قمنا بتجميع النتائج التي تم الحصول عليها من التحليلات التي تمت مناقشتها في أطروحتنا. لقد هدفنا إلى دمج هذه النتائج في إطار متماسك ومفهوم، مما يعزز وضوحها وأهميتها بشكل عام. وقد أتاح لنا هذا النهج المتكامل المساهمة برؤى قيمة في تحسين أداء شفرات توربينات الرياح، وبالتالي النهوض بمجال الطاقة المتجددة.

الكلمات المفتاحية: عنفة رياح، تصميم الشفرة، اهتزازات، التعب، الصدع.

Résumé

Dans cette thèse, nous avons entrepris une approche multidimensionnelle pour améliorer les performances des pales d'éoliennes. Notre enquête englobe à la fois la conception aérodynamique des pales, visant à augmenter la puissance de sortie, et un examen complet des aspects structurels de la pale pour résoudre les problèmes de vibration, de fatigue et de fissuration. Grâce à une analyse approfondie des propriétés structurelles et des caractéristiques des matériaux de la pale, nous avons développé des stratégies pour renforcer sa durabilité, sa fiabilité et son efficacité globale. En optimisant le profil aérodynamique de la pale et en abordant les défis potentiels tels que les vibrations, la fatigue et la fissuration, notre thèse a contribué à l'avancement de pales d'éoliennes plus efficaces et durables pour les systèmes d'énergie renouvelable. Dans notre thèse, nous avons posé les bases en proposant une revue complète de la littérature sur les aubes de turbine à axe horizontal. Nous avons présenté la méthodologie utilisée dans la conception de petites pales d'éoliennes, incorporant les théories du moment des éléments de pale (BEM) et de la dynamique des fluides computationnelle (CFD), illustrant comment ces méthodes peuvent être exploitées pour analyser les pales d'éoliennes. Un examen approfondi a également été mené sur les vibrations des pales, englobant la détermination des fréquences naturelles et des formes de modes pour améliorer les performances des pales. En abordant les préoccupations liées aux vibrations, ce chapitre cherchait à éclairer les améliorations dans la conception et le fonctionnement des pales d'éoliennes. Dans notre thèse, nous nous sommes également concentrés sur le sujet crucial de la fatigue. Nous avons fourni une compréhension complète de la fatigue, en particulier en ce qui concerne les pales d'éoliennes. Nous avons présenté les avancées dans la conception des pales visant à prolonger la durée de vie en fatigue et des équations de fatigue simplifiées pour les petites pales d'éoliennes, en introduisant la méthode du modèle de charge spectrale (SLM) et en utilisant l'outil FAST pour déduire la fatigue. Nous avons effectué une analyse détaillée des fissures dans les pales d'éoliennes résultant d'un fonctionnement prolongé sous diverses charges et conditions météorologiques, nous avons introduit la méthode des éléments finis étendus (XFEM), une technique spécialisée pour étudier les fissures, pour mieux comprendre le moment et l'étendue des fissures. Initiation et propagation au sein de la structure de la pale. Enfin, nous avons synthétisé les résultats obtenus à partir des analyses discutées dans notre thèse. Notre objectif était de consolider ces résultats dans un cadre cohérent et compréhensible, en renforçant leur clarté et leur signification globales. Cette approche intégrée nous a permis d'apporter des informations précieuses sur l'amélioration des performances des pales d'éoliennes.

Mots clé : éolienne, dessin de pales, vibrations, fatigue, fissure.

ACKNOWLEDGEMENTS

I am truly honored to present the culmination of several years of dedicated research conducted within the Department of Mechanical Engineering at the University of Echahid Hamma Lakhdar in El Oued.

First and foremost, I would like to extend my heartfelt gratitude to my thesis supervisor, Dr. **Mohammed Tahar Gherbi**, and my co-supervisor, Dr. **Necib Djilani**. Their unwavering support, encouragement, and guidance have been invaluable in helping me achieve the objectives of this research.

I am also indebted to the esteemed professors who played a pivotal role in the completion of this work, with special mention to Pr. **Oday Ibrahim Abdullah** from the University of Baghdad, Iraq.

I would like to express my deep appreciation to each member of the thesis committee for their keen interest in this research and for bestowing upon me the honor of evaluating my thesis.

DEDICATION

My dear mother

In loving memory of my father, and my sister Khayriya

To my cherished family members, including my brothers, my wife, and my children

With gratitude to all my colleagues, and a special mention to our esteemed Smail HAMIDATOU.

TABLE OF CONTENTS

General Introduction

CHAPTER I:
Bibliographic Research and Aerodynamic Design

CHAPTER II
Wind Turbine Blade Vibration

CHAPTER III
Fatigue Of Wind Turbine Blade

CHAPTER IV
Crack of Wind Turbine Blade

CHAPTER V
Results And Discussion

General Conclusion

LIST OF FIGURES

Figures of Chapter I

Figures of Chapter II

Figures of Chapter III

Figures of Chapter IV

Figures of Chapter V

LIST OF TABLES

Tables of Chapter III

Tables of Chapter V

LIST OF APPENDICES

NOMENCLATURE

Symbols

c	chord length.
F_L	lift force.
F_D	drag force.
F_N	normal force.
F_T	tangential force.
F_G	gravitational force.
F_C	centrifugal force.
R	length of the blade (look stress ratio)
U_0	the wind velocity.
U_{rel}	relative wind velocity.
U_{ref}	reference wind velocity.
Cl	Lift coefficient.
Cd	Drag coefficient.
Cn	coefficients of normal force.
Ct	coefficients of tangential force.
$\{F\}$	Load vector
$\{u\}$	Displacement vectors
[K]	Stiffness matrix
[M]	Mass matrix
$\{\ddot{u}\}$	Acceleration
[A]	dynamic matrix
$[I]$	Identity matrix
X	eigenvector
V_f	fiber volume fraction
U_{e50}	extreme wind speed of the 50 years.
m_b	mass of blade.
P_{design}	design power.
B	blade number.
Q_{design}	the design torque.

A_B	root cross-section area.
$A_{p,B}$	projected area.
D_B	damage of blade (coefficient).
W_B	blade section modulus.
R_{en}	stress ratio.
n	number of fatigue cycles.
N_f	number of cycles to failure
R_{en}	stress ratio
M_{yB}	flapwise moment of the extreme wind speed
u_{STD}	FE displacement
u_{ENR}	Enrichment displacement
$N_i(x)$	Shape functions of standard FE
$E(x)$	Enrichment function
u_i	The standard degrees of freedom
e_i	Enriched degrees of freedom
$H(x)$	Heaviside enrichment function
$f_j(x)$	The branch enrichment functions
a_i	Degrees of freedom related to the Heaviside enrichment
b_{ij}	Degrees of freedom associated with the crack tip
n_h	The Heaviside enrichment nodes
ΔK_{eff}	The effective SIF range
ΔK	The applied SIF range
K_{max}	The maximum SIF
K_{op}	The SIF of the opening crack
K_{min}	The lowest value for the SIF
K_I	The first mode SIF
a	Crack length
D	Root diameter
n_c	The crack tip enrichment nodes
U	The range of the effective SIF

Greek symbols

θ	twist angle.
α	angle of attack.
Φ	inflow angle.
ρ	air density.

Ω	rotational speed of the blade. [rpm]
$\omega.$	angular velocity of blade rotation.
η	efficiency.
λ_{design}	tip speed ratio.
σ_{eqB}	equivalent stresses.
σ_{MB}	stress of bending.
σ_u	ultimate stress.
σ_{all}	allowable stress.
σ_B	associated stress level.
γ_f	safety factor for the loads.
γ_m	safety factor for the materials.
Ω	Main domain
Ω_d	Domain that contains discontinuities
σ_{yy}	The normal stress
$\{\emptyset\}$	vector of contractual amplitude
ω	angular natural frequency

Abbreviations

GWEC	Global Wind Energy Council
IEC	The International Electrotechnical Commission (IEC) standard 61400 Part 2
FAST	Fatigue Aerodynamics Structures and Turbulence
SLM	Simplified Load Model
FEM	Finite Element Model
BEM	Blade Element Momentum
S-N curve	Stress versus the Number of cycles to failure
SIF	Stress Intensity Factor
UD	Unidirectional
CFD	Computational Fluid Dynamics
HAWT	Horizontal Axis Wind Turbine
DOF	Degrees Of Freedom
AEP	Annual Energy Production
WWEA	World Wind Energy Association

GENERAL INTRODUCTION

I. General Introduction

Although wind energy is a sustainable and eco-friendly energy source that can help reduce carbon emissions and combat global warming in the power generation sector, its technology is often erroneously assumed to be fully developed. In reality, there is still room for advancement, particularly in extending the lifespan of the rotor.

The blade design of a wind turbine plays a crucial role in harnessing the power of the wind. The blades are carefully crafted to capture the maximum amount of energy from the wind while minimizing turbulence and noise. They are aerodynamically shaped, with a curved surface that allows them to efficiently convert the wind's kinetic energy into rotational energy. The length and shape of the blades are designed to optimize performance and maximize power output. Additionally, the materials used in the blade construction are lightweight yet durable, enabling them to withstand the forces exerted by strong winds. Overall, the blade design of a wind turbine is essential for maximizing energy production and ensuring the turbine operates efficiently and effectively.

Vibration is an important aspect to consider in wind turbine blade design and operation. As the blades rotate, they encounter varying wind speeds and turbulence, leading to aerodynamic forces that can induce vibrations. Excessive vibration can have detrimental effects on the turbine's performance, structural integrity, and overall lifespan. Engineers strive to minimize vibration through careful design and material selection, aiming for blades that are stiff enough to resist unwanted oscillations. Various techniques such as advanced blade geometry, damping materials, and active control systems are employed to mitigate vibration. By reducing blade vibration, wind turbines can operate more smoothly, improving energy production efficiency and ensuring long-term reliability.

Fatigue is a crucial factor affecting the lifespan and performance of wind turbine blades. Over time, cyclic loading and stress from wind gusts and turbulence can lead to material fatigue and crack formation, potentially compromising the structural integrity of the blades. Recent studies have explored various approaches to mitigate fatigue damage in wind turbine blades, including advanced materials such as composites with improved fracture toughness, and advanced monitoring systems that can detect early signs of damage. These studies aim to develop more durable and resilient blades that can withstand harsh operating conditions and minimize maintenance and repair costs. By better understanding and managing blade fatigue, wind energy can continue to be a reliable and sustainable source of power in the future.

Recent studies have been dedicated to understanding and mitigating the issue of cracking in wind turbine blades. Cracking occurs when the blades experience excessive stress or material fatigue, leading to the formation of fractures. These cracks can compromise the structural integrity of the blades and pose significant challenges in terms of maintenance and operation. Researchers have been investigating various factors contributing to blade cracking, including manufacturing defects, material properties, environmental conditions, and operational loads. Through advanced imaging techniques and modeling approaches, these studies aim to identify potential crack initiation sites, predict crack growth, and develop strategies for early detection and prevention. By addressing the issue of cracking, these studies contribute to improving the reliability, safety, and overall performance of wind turbine blades, ensuring sustainable and efficient renewable energy generation.

The objective of this thesis is to enhance wind turbine blade performance by investigating the aerodynamic design of the blades to increase power output and examining the structure of the blades to address issues related to vibration, fatigue, and cracking. Through a comprehensive analysis of the blade's structural properties and material characteristics, this thesis aims to develop strategies to improve the blade's durability, reliability, and overall efficiency. By optimizing the aerodynamic shape of the blade and addressing potential issues such as vibration, fatigue, and cracking, this thesis seeks to contribute to the development of more effective and sustainable wind turbine blades for renewable energy systems.

Chapter 1 offers a comprehensive introduction to horizontal-axis wind turbines, providing a thorough understanding of their functioning and significance. Moreover, it includes a detailed literature review focused on wind turbine blade design, with the goal of attaining an enhanced and optimized geometry. The review critically examines existing research, methodologies, and techniques employed in blade design, thereby facilitating the development of a final improved blade geometry. By delving into the intricacies of blade design, this chapter lays the foundation for subsequent chapters and sets the stage for the exploration of innovative approaches to achieve superior wind turbine performance.

Chapter 2 focuses on the vibration analysis of wind turbine blades, encompassing the determination of their frequencies and mode shapes. This investigation aims to identify potential issues related to blade vibration and to develop strategies for improving blade performance. The focus of this chapter is not limited to blade shape or material; rather, it addresses various aspects of blade vibration that may affect turbine efficiency, safety, and reliability. By investigating vibration-related issues, this chapter aims to contribute to the optimization of wind turbine blade design and operation.

Chapter 3 of this thesis primarily focuses on fatigue analysis, which is the central objective of the study. The concept of fatigue will be thoroughly examined, specifically in relation to wind turbine blades. The aim is to enhance the blade design in order to extend its fatigue life, while also striving to simplify the fatigue equations associated with wind turbine blades. By comprehensively studying and addressing fatigue issues, this chapter seeks to improve the longevity and reliability of wind turbine blades. It will delve into various factors contributing to fatigue and propose strategies for optimizing blade design to withstand cyclic loading and enhance fatigue resistance.

Extended operation of wind turbines under varying loads and atmospheric conditions can lead to the formation of cracks, ultimately resulting in failure. Consequently, Chapter 4 aims to comprehensively investigate the occurrence of cracks in wind turbine blades. The objective of this chapter is to enhance blade design and gain insights into the timing of crack initiation. By studying the nature and behavior of cracks, valuable knowledge will be gained, enabling improvements in blade performance and facilitating the prediction of cracking occurrences. This in-depth analysis will contribute to the development of more robust and durable wind turbine blades, ensuring long-term reliability and optimal energy generation

In the concluding chapter, Chapter 5, we will showcase and analyze the outcomes derived from the research conducted in the preceding chapters. Our primary objective is to consolidate these findings into a single, coherent chapter, enhancing their overall clarity and cohesiveness.

CHAPTER I

BIBLIOGRAPHIC RESEARCH AND AERODYNAMIC DESIGN

I. Introduction

The utilization of wind energy has emerged as a pivotal solution to combat the challenges posed by climate change and the depletion of fossil fuel resources. Wind turbines, the primary means of harnessing wind power, have witnessed significant advancements in their design and technology over the past few decades. This chapter aims to explore the intricate process of wind turbine design, with a focus on maximizing efficiency and performance.

Wind turbine design entails a complex interplay of various factors, including aerodynamics, structural engineering, materials science, and control systems. The objective is to create a turbine that can effectively convert the kinetic energy of wind into electrical energy while ensuring optimal performance, reliability, and cost-effectiveness. Achieving these goals requires a deep understanding of the underlying principles and the ability to strike a delicate balance between numerous design considerations.

The chapter begins by providing a comprehensive overview of the fundamentals of wind energy conversion and the key components of a modern wind turbine. This serves as the groundwork for delving into the design principles that govern the turbine's performance. Aerodynamic aspects, such as blade design, airfoil selection, and rotor configuration, are explored in detail, taking into account the intricate flow patterns and forces acting on the turbine.

Furthermore, structural design considerations are crucial to ensure the turbine's integrity, longevity, and safety. The chapter investigates the selection of suitable materials, load calculations, and the optimization of the turbine's structural components. Emphasis is placed on balancing the weight of the structure with the need for durability and resilience in the face of various environmental conditions.

In summary, this chapter aims to provide a comprehensive overview of wind turbine design, with a particular focus on maximizing efficiency and performance. By delving into the intricate interplay of aerodynamics, structural engineering, materials science, and control systems, it seeks to unravel the key considerations and challenges faced by wind turbine designers. Through this exploration, we can gain valuable insights into the future of wind energy and its potential to revolutionize our energy landscape.

II. Comprehensive Review of Horizontal Axis Wind Turbines (HAWTs)

II.1 Historical Development of Wind Energy

Since ancient times, mankind has harbored a deep passion for travel and exploration, driven by the thirst for knowledge and understanding of civilizations. This innate desire led humans to harness natural phenomena as a means of transportation over vast distances. Around 5000 BC[1], people began relying on the power of the wind to propel boats using sails. Furthermore, after the advent of the Babylonian Empire, this technique was employed to design wind-powered irrigation systems. In 600 BC, the Persians pioneered the development of water-pumping and grain-grinding systems. Archaeological findings reveal that the earliest windmills date back to 500 AD. Initially, these mills served as decorative structures in Asia rather than sources of renewable energy. However, by the 12th century, Europeans began constructing and advancing mills for grain production and water pumping. Among the earliest known factories in the United Kingdom is the Weedley mill in Yorkshire, which can be traced back to 1185[2].

During the 14th century, the Dutch employed Helios for significant endeavors like the drainage of the Rhine Delta[2]. Over time, windmills found wider applications, especially in agriculture and water extraction from wells. By the late 19th century, wind energy started gaining recognition as a potential electricity source, and in 1888, Charles F. Bush devised the first apparatus to power his own house[3]. This wind turbine featured vertical axis blades and multiple accumulators (batteries) for energy storage. Later, "Poul La-Cour", a Danish innovator, took over Bush's wind power system and designed several industrial wind turbines, one of which saw 72 units sold at the beginning of the 20th century[3]. By the turn of the century in Denmark, there were over 2,000 windmills generating more than 30 MW of power. This progress continued throughout the 20th century, even as others increasingly relied on fossil fuels for their energy requirements.

Today, there has been rapid advancement in various fields, including materials science, computer science, aerodynamics, analytical design and analysis methods, testing and monitoring, and electronics. Materials science has made significant progress by introducing new composites for blades and alloys for metal components. The monitoring and control, as well as aerodynamic design methods originally developed for the aerospace industry, have been adapted for use in wind turbines. As a result, this development has revitalized the manufacturing sector, leading to accelerated production of wind turbines and growth in the wind energy market. Several manufacturers have played a key role in this progress, with GoldWind, a Chinese manufacturer, contributing 12.5%, Vestas, a Danish manufacturer, contributing 11.8%, GE Wind, an American manufacturer, contributing 9.5%, and Siemens, a German manufacturer, contributing 8%[4].

In 2015, the global capacity for electricity generated from wind power reached 433 GW, with China leading the way at 148 GW, followed by the USA at 75 GW, Germany at 45 GW, and India and Spain both at 20 GW[4]. In the year 2021, the total installed capacity of wind turbines worldwide reached approximately 840 GW, reflecting a growth of 97.3 GW compared to the previous year of 2020 [5].

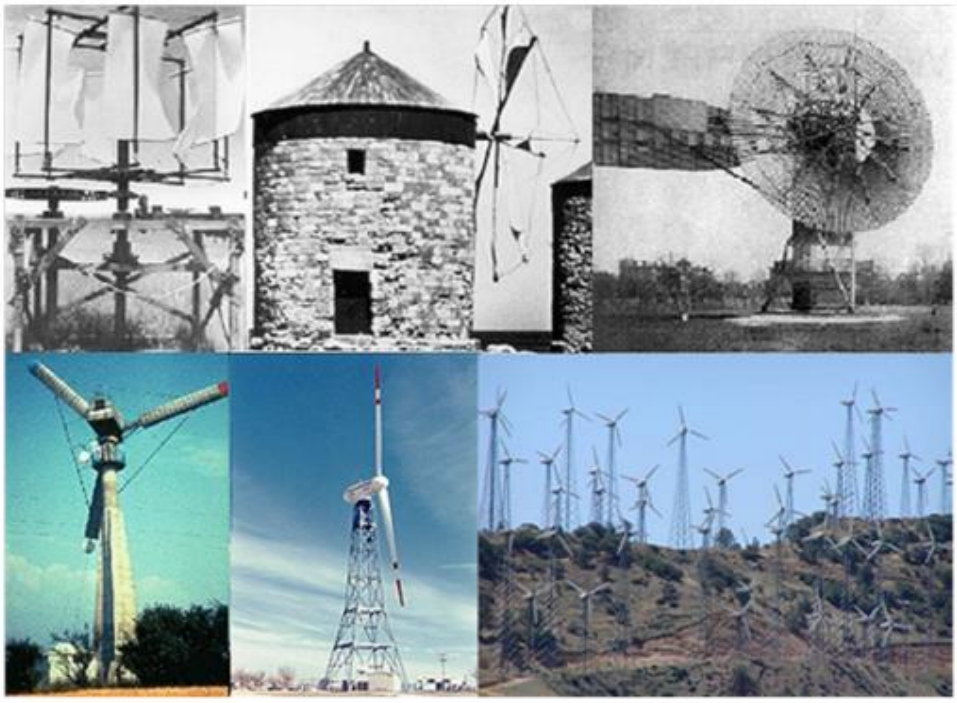

Figure I.1 phases of wind energy development [6]

II.2 Overview of Horizontal Axis Wind Turbine Development Work

The research on horizontal axis wind turbine development encompasses a wide range of complexities associated with modeling their operation. This involves various implicit parameters, site-specific factors like average wind speed and altitude, as well as parameters related to the design of the turbine blade. These parameters include the blade profile, angle of attack, coefficient of lift and drag, and induction factors, all of which directly influence the turbine's efficiency. The blade serves as the crucial component responsible for driving the wind turbine's movement mechanism.

The turbine blade plays a crucial role in transferring the wind's kinetic energy to the wind turbine's generator. Wind turbines are categorized into two types based on their usage in the electrical grid: fixed-speed turbines and variable-speed turbines. In this regard, the impact of blade shape holds greater significance in determining the performance of the wind turbine. This section provides a condensed overview of theories and studies that have examined this influence, as well as the essential parameters for defining the optimal shape of wind turbine blades. These findings will guide the enhancement of a blade configuration tailored to the wind conditions in Algeria.

The blade element theory is a versatile analysis method applicable to rotors, propellers, fans, and even lightly loaded compressors. It serves as the fundamental basis for analyzing propeller aerodynamics, as it delves into the intricacies of blade loading. This theory offers valuable insights into rotor performance and various other characteristics. Originally conceived by William Froude in 1878, the blade element theory was rigorously examined and applied by David W. Taylor and Stefan Drzewiecki between 1892 and 1920. The theory considers the blade as a composition of numerous thin elements, with the lift and drag estimated based on the 2D aerodynamic characteristics of each element section. These calculations can be performed for every blade element, where the flow is determined by the combined axial entry speed and blade rotation speed[7].

While blade element theory focuses on localized analysis, momentum theory takes a broader perspective and provides valuable insights, although it cannot be relied upon solely for rotor design. Originally developed to assess ship propellers by Rankine (1865) and Froude (1885)[8], momentum theory is also commonly referred to as the spinning disc theory. Betz (1920) further expanded upon the work of Rankine and Froude, albeit without accounting for wake rotation. Betz's extension assumes an inviscid and stable flow, treating the rotor as a disc with an infinite number of blades.

Several recent studies have focused on defining the operational parameters of wind rotors and establishing the relationship between these parameters in order to determine the optimal design parameters. In these studies, researchers have utilized the findings of momentum theory and blade element theory. Glauert's seminal work in 1926 introduced the rotational effect of air caused by the vortices generated by blade movement, particularly at high induction levels, which helped define the optimal operating parameters for wind power. Prandtl made a notable correction to Glauert's study in 1935, summarizing the losses occurring at the blade tips[8]. Eggleston and Stoddard provided a comprehensive overview in 1987 of aerodynamic theories relevant to wind turbine design[9]. Pandey et al. in 1989 presented various approaches to account for drag effects and the finite number of blades when calculating the axial and radial induction factors. Their findings aligned with Wilson's method from 1976[10]. Burton et al. conducted a study in 2001 on the yaw effect of wind power on the aerodynamic parameters of wind turbine blades[11]. Manwell et al. in 2002 proposed an enhanced algorithm to numerically design the shape of

wind turbine blades, building upon the classical Glauert model for optimal wind turbine design[3]. In 2005, Hoogedoorn et al. investigated the elastic behavior of flexible wind turbine blades using a 2D model. They explored various design parameters, wind speeds, and pitch angles for specific profiles, and found that increasing blade height enhanced lift, glide ratio, and wind rotor potential [12].

Marshall L. Buhl, Jr. in 2005 proposed a new empirical relation to correct the high operation of wind turbines, addressing the issue of discontinuity in Glauert's empirical relation for thrust force variation. Their findings demonstrated agreement with experimental results[13]. Kishinami et al. conducted experimental and theoretical investigations on the aerodynamic characteristics of horizontal-axis wind turbines. They developed a calculation code based on momentum theory and blade element theory and discovered that the induction and angle of attack significantly influence wind turbine performance[14].

Lampinen et al. in 2006 devised a method to evaluate the parameters of horizontal axis wind turbines using the axial fan theory. They utilized data from a similar airfoil axial fan and successfully matched their numerical solutions for blade pitch and chord angle with measurements from a commercial horizontal-axis wind turbine[15]. Nelson and Hau between 2006 and 2009 provided a historical account of the technological advancements in large industrial wind turbines that are currently in use[16]. Wilson et al. in 2009 further developed Glauert's method and performed a local optimization analysis to determine the contribution of each radial section in maximizing power output. They adjusted the axial induction factors until the power output reached a maximum stationary state[1, 17]. Lanzafame and Messina in 2010 examined the performance of a wind turbine operating continuously at maximum power coefficient. They developed a calculation code based on dynamic blade element theory and compared the results for different wind speeds and annual energy production with a variable speed model of a horizontal axis wind turbine operating at a constant rotational speed[18]. Vaz et al. in 2011 enhanced the classical Glauert model by developing an improved Blade Element Momentum (BEM) approach for predicting the performance of horizontal axis wind turbines.

Their mathematical model incorporated real phenomena such as blade tip losses and the rotational effect of the air in the wake caused by blade rotation and vortices [19]. Birajdar et al. in 2015 investigated the impact of design parameters, specifically pitch angle and blade rotation speed, on wind turbine performance. They utilized a modified blade element dynamic theory to analyze different types of wind turbines[20]. Sedaghat et al. in 2012 conducted a study to design a 300-kW horizontal axis wind turbine. They determined design parameters such as axial and radial induction factors, wind flow angle, and lift coefficient that would maximize power output for a selected average site wind speed and optimal blade tip speed ratio [21]. In 2013, Sharifi et al. proposed a novel algorithm to determine the radial distribution of pitch angles. They employed blade element momentum theory to calculate the maximum power coefficient at different wind speeds, taking into consideration the significant manufacturing cost associated with this blade configuration. Despite the increasing wind speed, the power generation potential of this blade configuration remains substantial [22]. In 2014, Sedaghat et al. examined the aerodynamic performance of horizontal axis wind turbines with variable rotation speeds, focusing on optimizing the blade shape. Building upon the study of fixed-speed wind turbines, their findings revealed a decrease in the power coefficient as the wind speed increased due to radial induction. They presented an approach to determine the optimal blade shape for this type of wind turbine [23]. In 2015, Z. Najafian Ashrafi et al. proposed a method to determine pitch angles that maximize the power coefficient while keeping the rotor

rotation speed constant. Their work introduced a controlled blade pitch system, and the results showcased improved performance compared to the basic model of a horizontal-axis wind turbine. They designed an iterative algorithm based on blade element dynamic theory specifically for a 200-kW production setup [24].

Wind turbines have a long history that spans several centuries, but the understanding and management of their vibrations have been refined and improved over time. The historical evolution of wind turbine vibrations demonstrates a growing understanding of the complex dynamics involved and the ongoing efforts to optimize wind turbine design, mitigate vibrations, and improve the overall efficiency and reliability of wind power generation.

Early windmills (200 BCE - 19th Century) were simple structures with wooden blades mounted on a vertical axis. Since these windmills had relatively slow rotation speeds, the issue of vibrations was not significant [25]. The Industrial Revolution (18th - 19th Century) marked a significant shift in windmill design and usage. Horizontal-axis windmills with a cloth or wooden blades emerged, and their speed of rotation increased. However, due to the relatively small size and low rotational speeds, vibrations were still not a major concern during this era [26].

Early wind turbines (Late 19th - Early 20th Century) had large blades and operated at higher rotational speeds. However, vibration-related issues were not yet a major focus [27]. As wind turbine technology advanced and larger turbines were developed, vibrations became a more significant concern. During the Mid-20th Century period, researchers and engineers started to investigate the impact of vibrations on wind turbine performance, structural integrity, and fatigue life[28]. In their 2015 study, Rahman et al.[29] conducted a comprehensive review of various vibration control dampers, including TMD (Tuned Mass Damper), TLD (Tuned Liquid Damper), Controllable Fluid Dampers, and other similar mechanisms. In their research, Aubrun et al.[30] conducted an insightful review that delved into active flow control strategies, with particular emphasis on techniques related to flow separation and circulation control. The study comprehensively examined the trailing edge flaps method, along with other methods such as Plasma actuators, synthetic jets, and Gurney Flaps. The authors provided abundant details and incorporated recent data, ensuring a thorough analysis of these approaches.

With the growth of the wind power industry and the emergence of utility-scale wind farms, the study and management of wind turbine vibrations became crucial. The main sources of vibrations in modern wind turbines include aerodynamic forces, rotor imbalances, and mechanical components such as gearboxes and generators [31].

The advancement of computer modeling and simulation techniques, coupled with the availability of comprehensive field data, allowed researchers and engineers to gain deeper insights into wind turbine vibrations. Efforts have been made to optimize turbine design, reduce vibrations, and enhance the overall performance and reliability of wind energy systems. Various strategies have been employed to mitigate vibrations in wind turbines. These include the use of advanced control algorithms, improved aerodynamic designs, optimized rotor balancing techniques, and enhanced structural dynamics analysis. Ongoing research and development continue to refine these methods and address new challenges. Additionally, monitoring and condition monitoring systems have been implemented to detect and diagnose potential

vibration issues in wind turbines. Regular inspection, maintenance, and repair protocols are now standard practices to ensure safe and efficient operation.

The history of wind turbine fatigue dates back to the early development of wind energy as a viable power source. As wind turbines began to gain prominence in the late 20th century, researchers and engineers recognized the importance of understanding and addressing the issue of fatigue in these structures. Research on structural reliability has been conducted for over six decades, whereas the examination of structural fatigue reliability has a comparatively shorter history. The initial investigations in this field were initiated by Wirsching in 1983 [32]. In 1997 the work of Byers[33], the current state and advancements in the theory and practical implementation of assessing structural fatigue reliability were documented. In 1966, Freudenthal [34] introduced a design method for fatigue reliability that involved utilizing a stress-strength interference model. In 1995, a study conducted by Murty et al. [35] focused on analyzing the distribution of fatigue strength and its implications in the calculation of reliability. The prediction of fatigue loads on wind turbines using 10-minute statistics of operational SCADA signals was proposed by Cosack and Kühn in 2009 [36]. This methodology employs neural networks and eliminates the need for additional sensors. In a review conducted by Kensche in 2006 [37], various aspects related to fatigue and the lifespan of composite rotor blades in wind turbines were examined. These aspects encompassed the necessary S-N curves, as well as the impact of environmental effects on fiber content and architecture. In 2014 Jang et al. [38] devised in their study a methodology to predict the fatigue life of a small-scale composite blade and investigated the influence of wind conditions on the blade's fatigue life. A comprehensive study conducted by Du et al. in 2020 [39] presented the latest six methods for detecting damage in wind turbine blades. In their study, Rezaeiha et al. 2017 [40] conducted a quantitative analysis to determine the respective contributions of fatigue loads. Their findings revealed that wind turbulence accounted for more than 65% of flapwise fatigue, highlighting its significant influence. Furthermore, gravity was identified as the primary contributor, responsible for over 80% of edgewise fatigue. Bazilevs et al. in 2016 [41] employed fluid-structure interaction (FSI) to predict fatigue damage in the full-size Sandia CX-100 wind turbine blade made of composite materials. Their results included the number of cycles until failure and the area with the most damage. in 2015 Lee et al.[42] conducted experimental work on a 3 MW, 56 m long wind turbine blade to investigate fatigue failure at the root. They also utilized a finite element (FE) model to validate their findings and provided further explanations. Rubiella et al. in 2018[43] published a state-of-the-art paper proposing a method for calculating fatigue loads in composite materials for wind turbines, revealing significant variations in the results. Shokrieh et al.[44] in 2006 employed an FE model to simulate and predict fatigue failure in the entire blade model, identifying the critical zone where cracks initiate. Dervilis et al.[45] in 2014 utilized Artificial Neural Networks (ANNs) and vibration modes to infer damage in a 9 m CX-100 wind turbine blade.

The history of wind turbine fatigue is characterized by a continuous pursuit of knowledge and innovation to ensure the long-term reliability and performance of these renewable energy systems. The ongoing research and advancements in this field continue to shape the design and operation of modern wind turbines, contributing to their increased efficiency, durability, and overall sustainability[46-49].

The history of wind turbine cracks is closely linked to the development and evolution of wind energy technology[50]. Cracks in wind turbines have been a concern since the early days of their deployment, and understanding and addressing this issue has been crucial for the industry's progress[51].

Cracks in wind turbine blades can result from a combination of factors, including material fatigue, manufacturing defects, and environmental conditions[52]. Early on, issues such as inadequate material selection, insufficient design considerations, and manufacturing inconsistencies contributed to a higher prevalence of cracks[53].

As the industry gained experience and knowledge, research efforts focused on understanding the root causes of cracks and developing strategies to mitigate their occurrence. This involved advancements in material science, including composite materials with enhanced fatigue resistance and improved manufacturing processes[54].

Over time, the industry learned valuable lessons from the occurrence of cracks and applied them to improve wind turbine design, manufacturing, and maintenance practices. The introduction of advanced computer simulations, such as finite element analysis, aided in optimizing the structural integrity of turbine components and predicting potential areas of vulnerability[55-58].

Today, the wind energy industry has made significant strides in mitigating the occurrence and impact of cracks in wind turbines. Improved design standards, stricter quality control measures, and comprehensive maintenance programs have contributed to increased reliability and durability of wind turbine systems[59].

III. The Composition of a Wind Turbine Rotor

The wind turbine is a machine to transform the kinetic energy of the wind into mechanical energy by the rotor, the rotation of the drive shaft which is linked to the wind turbine rotor will rotate the electromagnetic generator to give electrical energy, and the electricity can be injected directly into the network, or stored as a load isolated by accumulators. The wind turbine is made up of several parts:

III.1 Wind turbine foundation

The wind turbine foundation

Figure I**.2** and

Figure I**.3** serves as a critical component in supporting the structure and stability of the wind turbine. It is designed to withstand the dynamic loads and forces exerted by the turbine and ensure its safe and efficient operation. The foundation is typically constructed using reinforced concrete or steel, depending on the specific site conditions and turbine design. Its design considers factors such as soil properties, wind conditions, and the weight and dimensions of the turbine. Proper engineering and construction of the foundation are essential to ensure the longevity and reliability of the wind turbine, as it provides the necessary anchoring and structural support to withstand the forces imposed by the rotating blades and changing wind patterns. Additionally, the foundation may incorporate features such as vibration-damping systems and anchoring mechanisms to further enhance the stability and performance of the wind turbine[60].

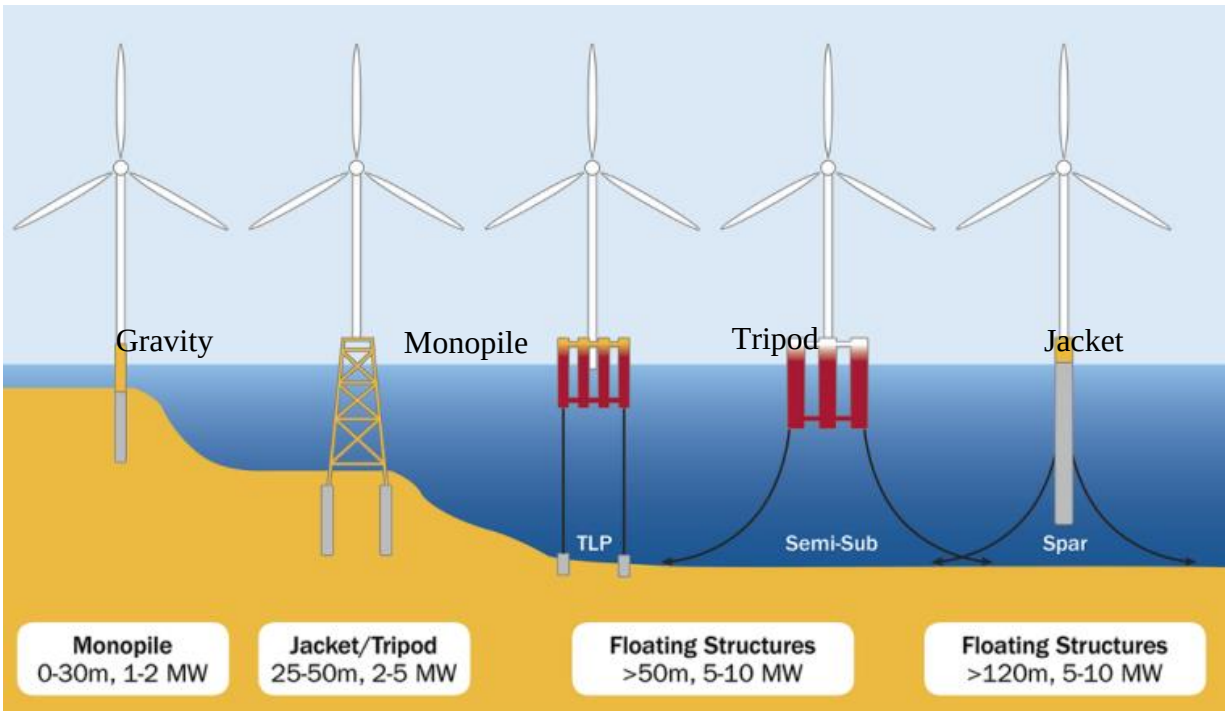

Figure I.2 Type offshore wind turbines foundations[61]

Figure I.3 classic onshore wind turbine foundations [62]

III.2 The nacelle of a wind turbine

The nacelle of a wind turbine is a crucial component located at the top of the tower. It houses the critical machinery and equipment for converting the wind's kinetic energy into electrical energy[63]. The nacelle typically contains the main drive shaft, gearbox, generator, and control systems. The main drive shaft connects the rotor blades to the gearbox, which increases the rotational speed to optimize power

generation. The generator, often a synchronous or asynchronous type, converts the mechanical energy from the rotor into electrical energy. The control systems within the nacelle monitor various parameters such as wind speed, direction, and turbine performance, enabling efficient operation and safeguarding against excessive loads or potential issues. The nacelle is designed to withstand harsh environmental conditions, including strong winds, temperature variations, and vibrations. It is also equipped with safety features such as braking systems to control turbine speed during maintenance or in case of emergencies. Regular maintenance and inspection of the nacelle are crucial to ensure optimal performance and longevity of the wind turbine[64].

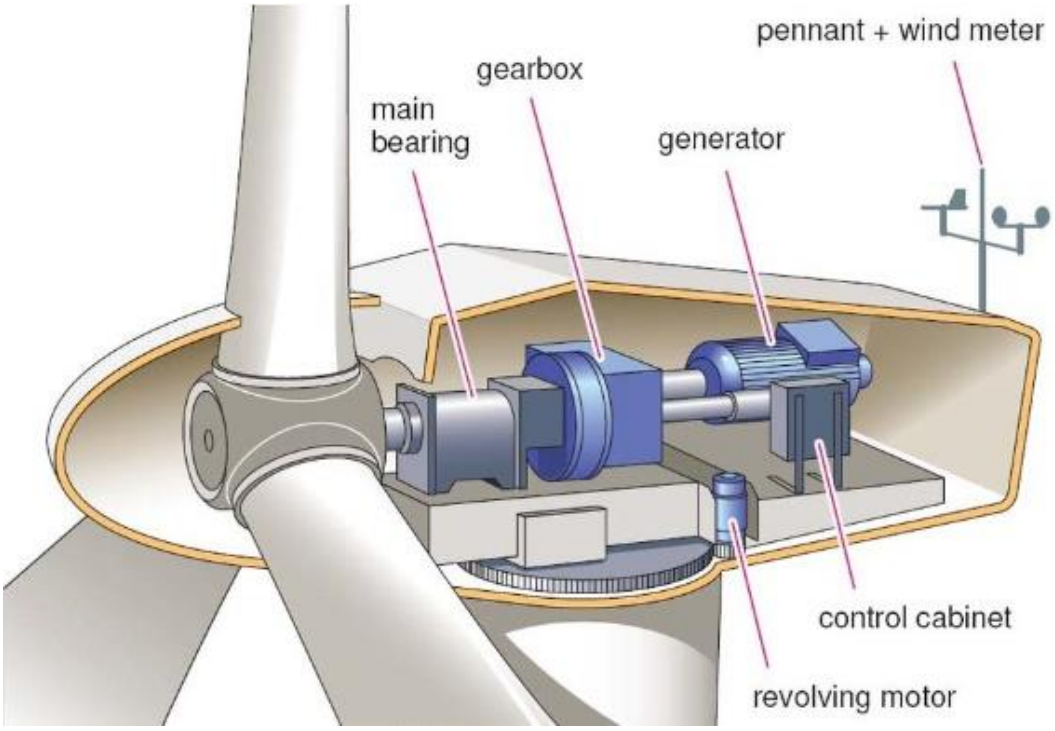

Figure I.4 nacelle cross-section of wind turbine [65]

III.3 Wind turbine rotors

Wind turbine rotors are the pivotal components that harness the power of the wind and convert it into clean, renewable energy. These massive rotating structures, often resembling giant propellers, consist of several aerodynamically designed blades attached to a central hub. The primary purpose of wind turbine rotors is to capture the kinetic energy of the wind and transfer it to the generator housed within the turbine. The blades are carefully crafted to maximize their efficiency in extracting energy from the wind while minimizing resistance and turbulence. Through their sleek and curved profiles, wind turbine rotors optimize the lift and drag forces acting on the blades, enabling them to spin at high speeds and generate electricity. The size and shape of the rotor blades, along with the number of blades, can vary depending on the specific wind turbine design and environmental conditions. With their remarkable ability to harness the power of nature, wind turbine rotors play a vital role in the global transition towards sustainable energy sources, contributing significantly to reducing carbon emissions and combating climate change.

Figure I. 5 Rotor of HAWT blade [66]

III.4 Tower of wind turbine

The wind turbine tower is a crucial structural component that supports the entire wind turbine system, providing stability and elevation to maximize the efficiency of energy generation. These towers are engineered to withstand the immense forces exerted by the wind and the weight of the rotor and nacelle. Typically made of steel or concrete, wind turbine towers are designed to be tall and robust, allowing the turbine to access stronger and more consistent wind resources found at greater heights. The height of a wind turbine tower is carefully chosen based on factors such as wind speed, wind direction, and local terrain conditions. By elevating the turbine, the tower helps to ensure that the rotor blades can capture the most kinetic energy from the wind. Additionally, the tower houses essential components like the generator, gearbox, and control systems, providing protection and easy access for maintenance and repairs. With their sturdy construction and strategic placement, wind turbine towers are essential in facilitating the efficient generation of renewable energy and contributing to a greener and more sustainable future.

Figure I. 6 Wind turbine tower types [67].

IV. Horizontal Axis Wind Turbine Design Criteria

IV.1 Wind turbine size criteria

Wind turbines, both horizontal-centered, come in various sizes. Small wind turbines, typically found in homes, generate less than 100 kW of power [68]. They are commonly used in conjunction with simple diesel generators and for water pumping purposes. Medium-scale wind turbines, on the other hand, provide power ranging from 100 kW to a few megawatts. The largest wind turbines are seen in wind farms and serve as the primary source of electricity for the electrical grid. These turbines are categorized according to local standards, as detailed in Table I. 1, Table I. 2 and, Table I. 3.

Table I. 1 The British classification (ITDG-UK) [69]

Scale	Nominal power	Diameter
Micro	50kW to 2kW	Lower than 3m
Small	2kW to 40kW	3m to 12m
medium	40kW to 999kW	12m to 45m
large	More than 1MW	46m or more

Table I. 2 The American classification (NREL-USA) [69]

Scale	Nominal power	Application
Small	Lower than 10 KW	Houses, farms.
middle	10kW to 250kW	Village supply, hybrid system or distribution
large	250kW to 2MW	Power plant or station, wind farms or distribution.

Table I. 3 The European classification (EWEA-Europe) [69]

Scale	Nominal power	Properties
Micro	Lower than 3 KW	Direct drive permanent magnet generators for battery charging
Small	3kW to 30kW	Low maintenance and high reliability Applied permanent magnet generators
Large	200kW to 1.5MW	Permanent magnet generators and wound rotor models applied: • Direct drive systems. • Variable speed operation
Megawatt	More than 1.5MW	Rotor Multi-systems

IV.2 Installation site criteria

IV.2.1 The availability of wind

The location of a wind turbine plays a crucial role in its efficiency. The amount of power generated is directly influenced by the wind speed, which is why sites are selected based on the wind speed and frequency of the area. A wind turbine performs optimally when there are consistent and frequent winds [70]. Various methods and algorithms have been developed to estimate the frequency of wind speeds at a site, such as the Weibull distribution Figure I. 7 [70, 71].

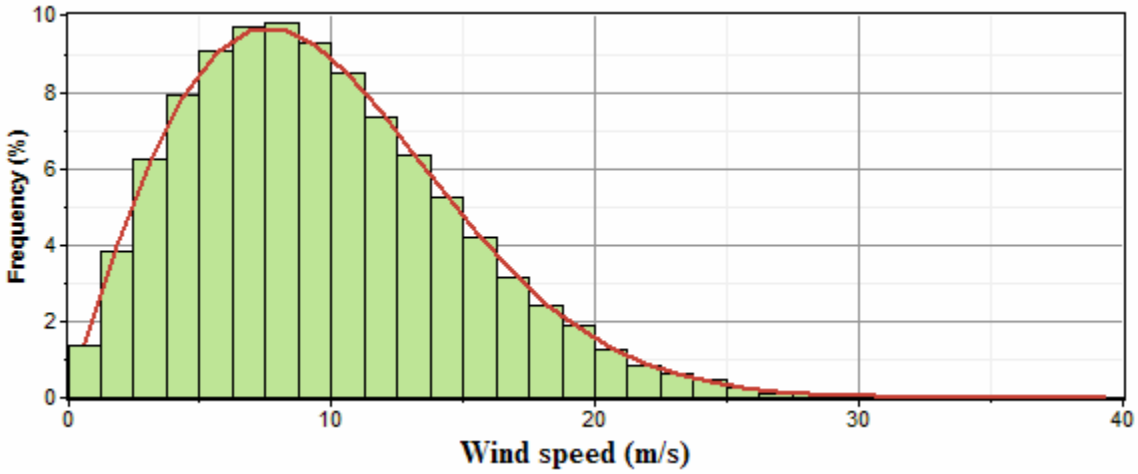

Figure I. 7 The Weibull distribution of wind frequency [71]

Meteorologists utilize wind roses as a visual aid to present a concise overview of wind speed and direction patterns at specific locations. Wind roses originated as predecessors to compass roses found on charts, as there was no distinction made between cardinal directions and the winds blowing from those directions. By employing a polar coordinate system, the frequency of winds during a given time period is graphed based on wind direction, with color-coded bands indicating different wind speed ranges. The longest spoken on the wind rose represents the wind direction that occurs most frequently[72]

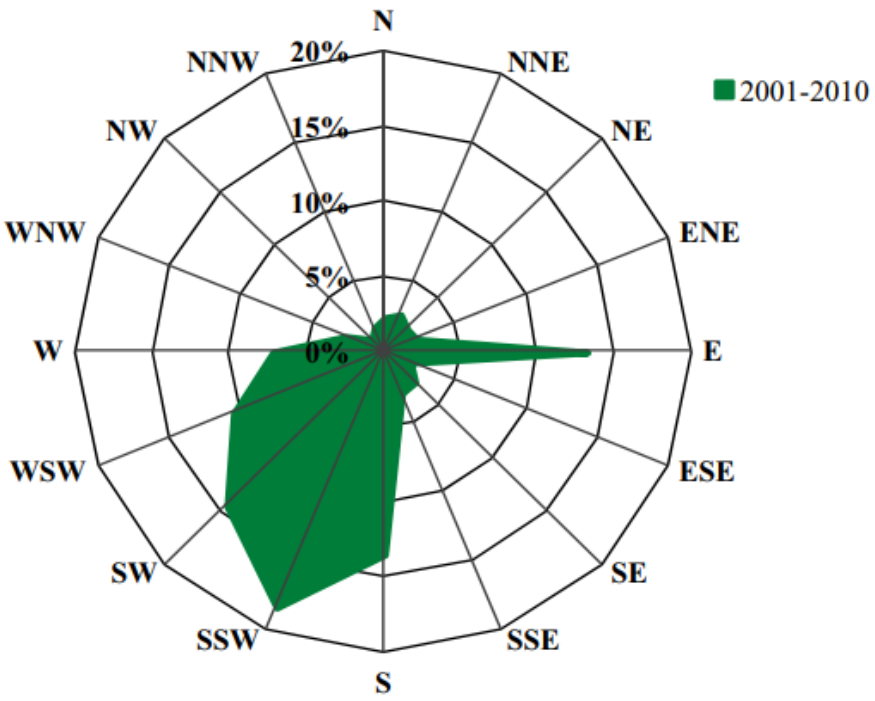

Figure I. 8 The rose of the wind [72]

IV.2.2 The Wind Classes

In the intricate process of planning a wind power plant installation, the wind class is a crucial consideration. Wind classes help determine the appropriate wind turbine for typical wind conditions at a specific location. These classes primarily depend on the average annual wind speed (measured at the wind turbine's hub height), the speed of extreme gusts that may occur over a 50-year period, and the turbulence intensity at the site. These factors collectively contribute to defining the wind class and inform the selection of suitable turbines for the desired location.

The International Electrotechnical Commission (IEC) has established a standard Table I.4 that defines the three wind classes for wind turbines. These classes are categorized as follows:[73]

Table I.4 Wind classification (IEC)

Wind turbine class	IEC I (High wind)	IEC II (Mean wind)	IEC III (Low wind)
Annual average wind speed	10 m/s	8.5 m/s	7.5 m/s
Extreme measured wind speeds every 50 years	70 m/s	59.5 m/s	52.5 m/s
Turbulence intensity	18%	18%	18%

IV.2.3 The nature of the soil

The foundation of a wind turbine plays a critical role in withstanding and supporting the ground conditions at the installation site. The presence of soft ground has a significant impact on the overall installation cost, particularly when dealing with loose soil that requires reinforcement through the use of piles[74].

IV.2.4 The nature of the site profile

The wind is generated by variances in temperature and pressure, and its behavior is affected by various factors at the installation site, including the soil profile, the presence of obstacles, and ground roughness. These factors can impede the flow of wind and alter its direction. Plains experience strong winds due to the absence of obstacles, while mountain passes channel high-altitude winds, resulting in strong wind conditions. Therefore, for optimal wind turbine installation, it is preferable to choose flat sites or higher locations to minimize disruptions in wind speed and direction [3].

IV.3 Blade aerodynamic criteria

IV.3.1 Blade section profile

Initially, the design of wind turbines drew inspiration from aeronautical aircraft design, utilizing section profiles derived from NACA (National Advisory Committee for Aeronautics) [75]. These NACA profiles (Figure I. 9) were commonly categorized into three types: four digits, five-digits, and six digits. Through experimental evaluations of these profile types, it was concluded that the six-digit NACA profiles demonstrated the highest efficiency and were most suitable for wind turbine blade design[76]. However, in addition to the NACA profiles, new profiles have been developed, expanding the options available for wind turbine blade design such as:

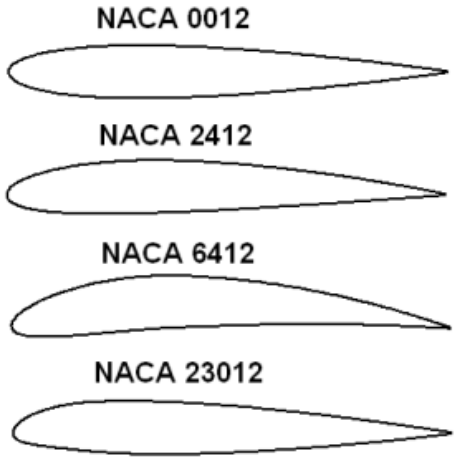

Figure I. 9 the NACA profiles for 4 and 5 digits

IV.3.1.1 NREL Profiles

The American Renewable Energy Institute (NREL) has spearheaded the development of specific blade profiles tailored for horizontal axis wind turbines Figure I. 10. These profiles, denoted as "S" profiles, have been designed to cater to various control categories. The corresponding designations for each category can be found in Table I. 5 [11, 74, 77].

Table I. 5 Types of NREL profiles [77]

Diameter	Type of control	Profile thickness	blade body	blade tip	Blade root
3-10 m	variable speed Variable pitch	thick	-	S822	S823
10-20 m	variable speed Variable pitch	thin	S802	S802/S803	S804
10-20 m	stall regulated	thin	S805/S805A	S806/S806A	S807/S808
10-20 m	stall regulated	thick	S819	S820	S821
20-30 m	stall regulated	thick	S809	S810	S811
20-30 m	stall regulated	thick	S812	S813	S814
20-40 m	variable speed Variable pitch	-	S825	S826	S814/S815
30-50 m	stall regulated	thick	S816	S817	S818
40-50 m	stall regulated	thick	S827	S828	S818
40-50 m	variable speed Variable pitch	thick	S830	S831/S832	S818

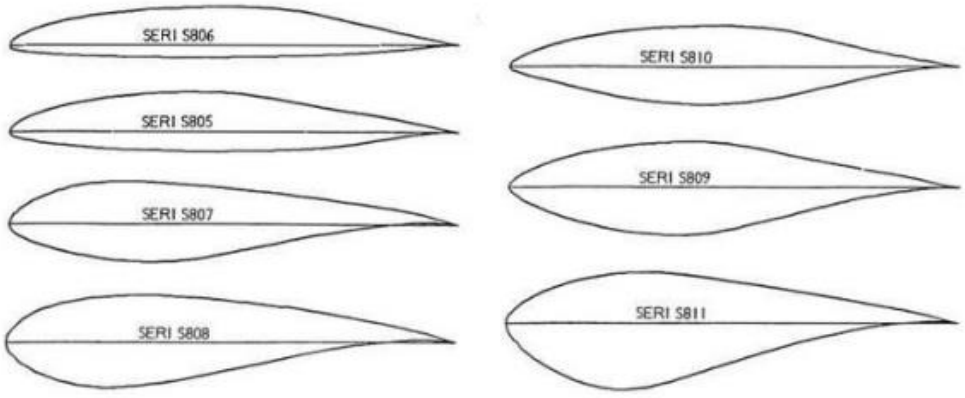

Figure I. 10 profiles of blade type NREL [78]

IV.3.1.2 Profiles of Risø

The development of these profiles is carried out at the Risø National Laboratory of Denmark, serving the same purpose as the NREL profiles. The development process is based on the utilization of the X-FOIL program code, developed by Derla, and the Ellipsys-2D CFD code, established by Sorensen. The Risø profiles are classified into three types: RisøA, Risø-P, and Risø-B.

The Risø-A profiles have been specifically developed for designing blades used in stall-regulated wind turbines (Figure I. 11). Building upon the Risø-A profiles, the Risø-P profiles have been upgraded to cater to wind turbines equipped with variable pitch and speed control mechanisms (Figure I. 12). On the other hand, the Risø-B profiles belong to a family of profiles characterized by a high coefficient of lift. These profiles are designed for high-power wind turbines featuring variable speed and stall-regulated mechanisms (Figure I. 13).

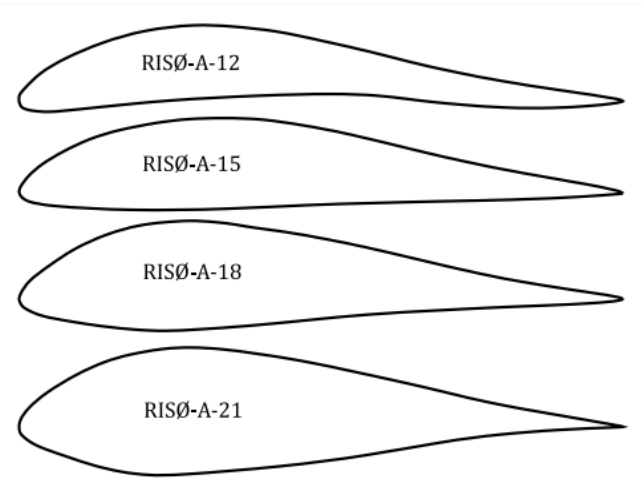

Figure I. 11 RISØ-A profiles of blade [79]

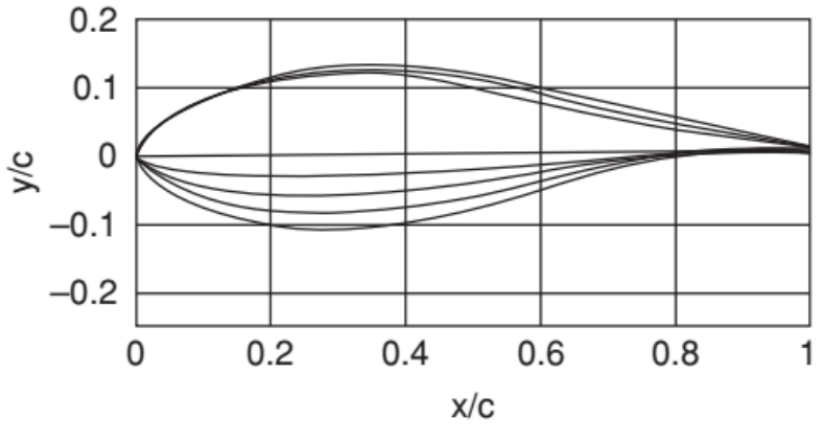

Figure I. 12 RISØ-P profiles of blade [11]

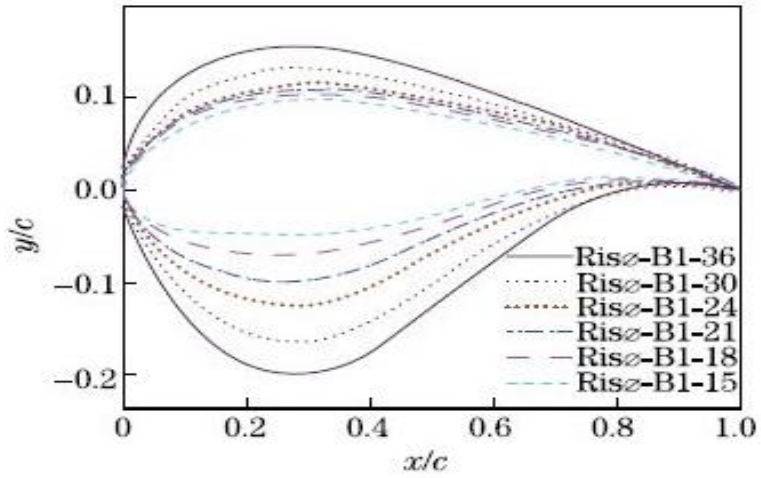

Figure I. 13 RISØ-B profiles of blade [80]

IV.3.1.3 Profiles of Delft

Delft profiles are a series of blade profiles used in the design of wind turbine blades. These profiles are developed at the Delft University of Technology in the Netherlands. They have been extensively researched and tested to optimize the aerodynamic performance and efficiency of wind turbine blades. Each profile within the Delft series is tailored for different wind turbine applications and operating conditions. The Delft profiles (Figure I. 14) play a significant role in maximizing energy capture and minimizing aerodynamic losses, ultimately enhancing the overall efficiency and power output of wind turbines.

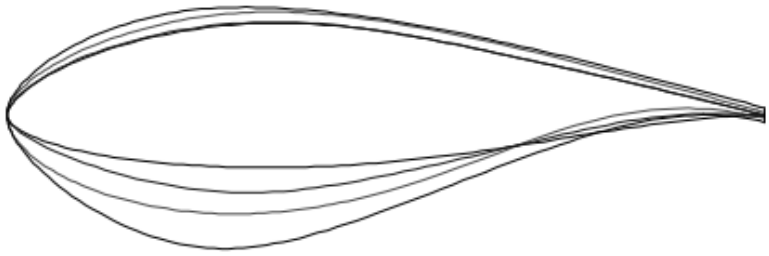

Figure I. 14 the DU airfoils for pitch-regulated wind turbines [81]

IV.4 The morphology of a wind turbine blade

The morphology of a wind turbine blade refers to its physical structure, shape, and dimensions. The design of the blade morphology plays a crucial role in determining the overall performance and efficiency of the wind turbine. The morphology of the blade includes various key aspects, such as its length, width, curvature, twist, and airfoil profile. These factors are carefully considered and optimized during the blade design process to maximize energy capture from the wind while minimizing aerodynamic losses and structural stresses.

The length of the blade is an important factor that determines the swept area, which directly influences the amount of wind captured and the power output of the turbine. The width of the blade, also known as the chord length, contributes to the overall lift and drag characteristics. The twist along the length of the

blade helps to optimize the angle of attack of the blade sections, allowing for efficient performance across a range of wind speeds.

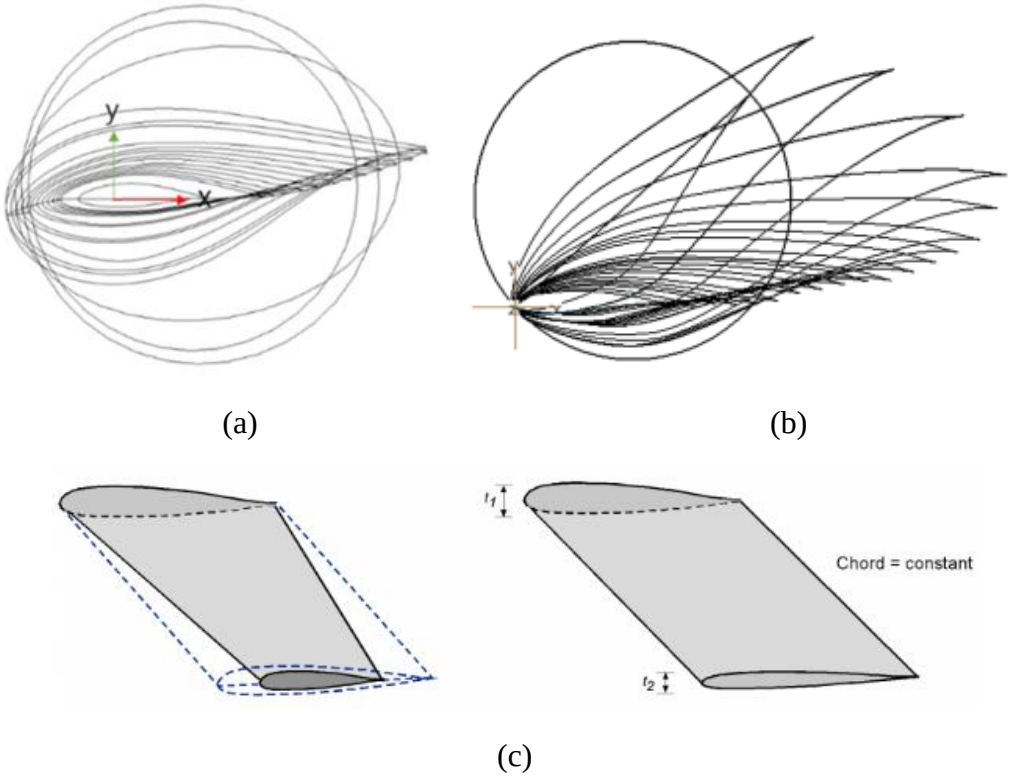

Figure I. 15 morphology of a wind turbine blade(a) constant airfoil twist (b) twisted airfoil and, (c) variable and constant chord [82, 83]

V. Aerodynamics of Wind Turbine blade

In this chapter, the functioning of a wind turbine and the aerodynamic forces acting on its blades are explained. Various modeling techniques are available to calculate these forces and estimate the power generated by wind turbines. Initial design phases often employ simplified numerical models based on the Blade Element Momentum theory (BEM) as mentioned in [84-86]. the BEM models are based on two-dimensional modeling, whereas the flow around wind turbines is inherently three-dimensional. Consequently, extensive modeling work is required to accurately represent the physics of the flow using such models. Another approach is Computational Fluid Dynamics (CFD), which relies on the Navier-Stokes equations and their approximations. Due to the breadth of this subject, a comprehensive literature review has been conducted to identify suitable numerical methods for simulating the flow around a rotating wind turbine.

The energy efficiency of wind turbines heavily relies on the aerodynamics of their blades. Figure I. 16 illustrates the aerodynamic forces acting on the blades. The wind speed is denoted as U_0, while U_{rot} represents the velocity generated by the rotational speed of the turbine. The combination of wind speed and rotational speed is referred to as the relative speed U_{rel}, which represents the velocity at which the blade is impacted by the wind. Near the blade root, where the rotational speed is low, the relative speed

closely matches the wind speed. Conversely, at the blade tip, the rotational speed is much higher than the wind speed.

The parameter β encompasses both the twist angle and the pitch angle of the blade, where the pitch angle represents the orientation angle of the blade around its axis and can change over time. β, referred to as the angle of incidence, is the angle formed between the chord line of the blade and the rotational plane of the rotor. On the other hand, α represents the angle of attack, which is the angle between the chord line and the relative speed U_{rel}. By adding α and β together, the flow angle, denoted as φ, can be calculated as:

$$\varphi = \alpha + \beta \tag{I. 1}$$

As a result of the airflow surrounding the airfoil, two forces act upon the blade: drag (F_D), which opposes the relative flow, and lift (F_L). Lift is the component perpendicular to the incoming flow direction and represents the upward force resulting from the acceleration of the fluid on the suction side of the airfoil. The combination of these two forces gives rise to the aerodynamic force (F), and when multiplied by the distance to the center point of the rotor, it provides the torque. The tangential component of this force F_T contributes to the rotation of the wind turbine, while the normal component (also known as the axial component or the rotor axis) of the aerodynamic force F_N corresponds to the thrust. The rotor experiences mechanical stresses as a result of these forces. Calculating these aerodynamic forces is essential for assessing the energy efficiency of the wind turbine.

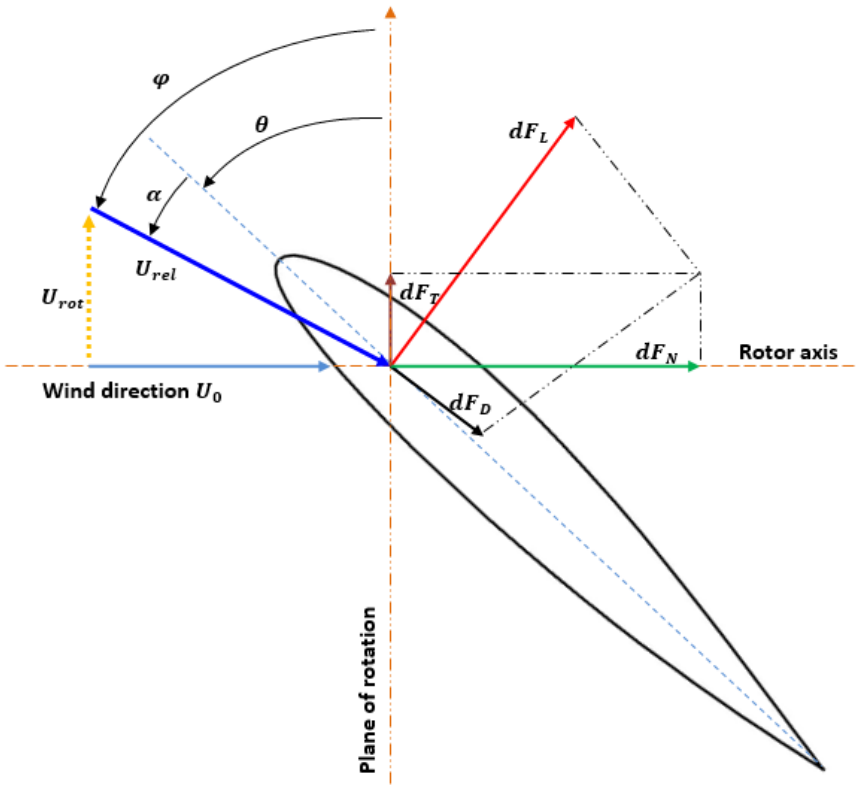

Figure I. 16 aerodynamic forces acting on the blade section

Analyzing the power extracted by a wind turbine is crucial, and a key metric for this analysis is the power coefficient. The power coefficient is defined as the ratio between the power extracted by the turbine and the available wind power.

$$C_P = \frac{P_{extract}}{P_{wind}} = \frac{P}{\frac{1}{2}\rho A U_0^3} \quad \text{(I. 2)}$$

Where $A = \frac{\pi D^2}{4}$ represents the swept area of the rotor. Similarly, the thrust coefficient can be introduced as follows:

$$C_T = \frac{F_N}{\frac{1}{2}\rho A U_0^2} \quad \text{(I. 3)}$$

The power coefficient C_P is dependent on the rotational speed of the rotor and can be represented as a function of the tip speed ratio λ. The tip speed ratio λ indicates the ratio between the rotational speed at the blade tip and the wind speed.

$$\lambda = \frac{\Omega R}{U_0} \quad \text{(I. 4)}$$

Where Ω represents the rotational speed of the rotor in radians per second (rad/s), and R denotes the blade radius. The torque of the wind turbine, denoted as Q, can be expressed as:

$$Q = \frac{P}{\Omega} = \vec{r} \wedge \vec{F} \quad \text{(I. 5)}$$

Where $\vec{r}$ represents the position vector, which is the vector from the origin of the defined coordinate system to the point where the force is applied, and $\vec{F}$ represents the aerodynamic force vector.

V.1 Blade Element Momentum Theory (BEM)

The BEM theory, a longstanding aerodynamic model in wind engineering, is extensively employed in the industrial realm for wind blade design[1, 11, 16]. Combining axial momentum and blade element theories, this model was originally developed by Betz in 1926 and has since been elucidated in numerous recent articles[19, 85]. Essentially, the axial momentum theory utilizes a one-dimensional model to represent wind energy extraction while assuming incompressible flow. On the other hand, the blade element theory incorporates the rotational aspect of the fluid induced by the blade's rotation. These theories are further expounded upon below.

V.1.1 The theory of axial momentum

Within this theory, a frictionless, axial, and incompressible flow is presumed, with the airflow traversing the rotor without any hindrance. The modeling approach involves conceptualizing the wind turbine rotor as a thin, permeable disc that is set into motion by the airflow passing through it. As depicted in Figure I.17, the air passing through the rotor experiences a velocity alteration. The axial induction factor, frequently referenced in literature, is introduced and represents the proportionate decrease in wind speed

between the upstream value $U_0$and the value of wind speed passing through the rotor's plane, denoted as U_1.

$$a = 1 - \frac{U_1}{U_0} \quad \text{(I. 6)}$$

The downstream wind speed, denoted as U_3, is represented by this variable. By applying the law of conservation of momentum, the theory posits that the force exerted on the actuator disc mitigates the change in axial momentum between the upstream and downstream portions of the stream tube.

$$F_N = \dot{m}(U_0 - U_3) \quad \text{(I. 7)}$$

In this context, the mass flow rate through the rotor can be expressed as $\dot{m} = \rho A U_1$, where A represents the area of the rotor. Similarly, by applying the principle of energy conservation, the energy extracted by the disc can be represented as follows:

$$E = \frac{1}{2}\dot{m}\left(U_0^2 - U_3^2\right) \quad \text{(I. 8)}$$

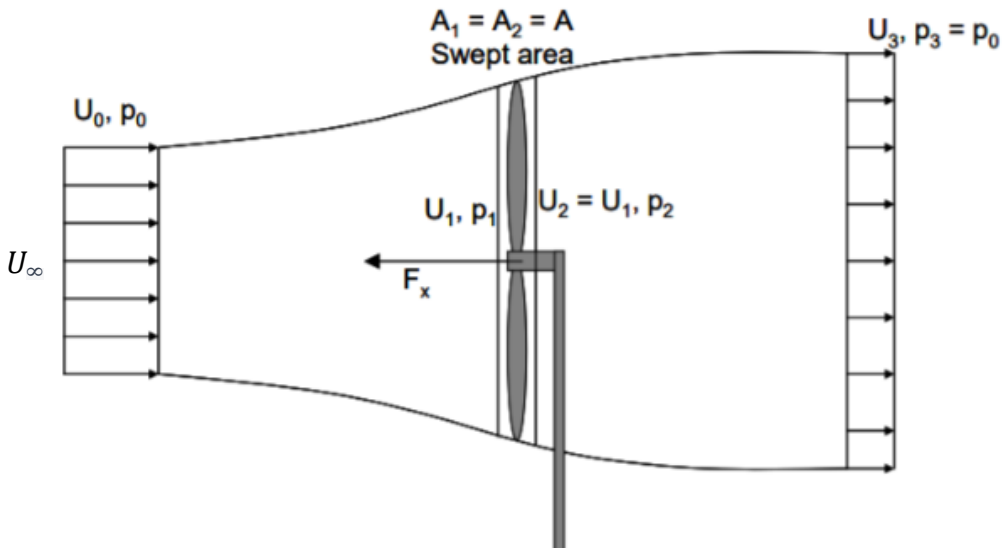

Figure I.17 stream tube and Actuator disc for a wind turbine [87]

The power harnessed from the flow field by the rotor can be expressed in two different ways. Firstly, power, defined as the energy transferred per unit of time, can be represented. By employing equation (I. 8), we arrive at the following expression:

$$P = \frac{1}{2}\dot{m}\left(U_0^2 - U_3^2\right) \quad \text{(I. 9)}$$

Alternatively, based on aerodynamics and under the condition of axial flow, we can derive the definition $P = F_N U_1$. Utilizing equation (I. 7), we obtain the following result:

$$P = \dot{m}(U_0 - U_3)U_1 \quad \text{(I. 10)}$$

By combining equations (I. 10) and (I. 9), we can infer the following:

$$U_1 = \frac{1}{2}(U_0 + U_3) \tag{I. 11}$$

Upon substituting U_3 into equation (I. 7), we obtain:

$$F_N = 2\rho A U_0^2 a(1-a) \tag{I. 12}$$

V.1.2 Power coefficient of Wind turbine

The power coefficient of a wind turbine is a dimensionless parameter that represents the efficiency of the turbine in converting the kinetic energy of the wind into electrical power. By utilizing equations (I. 2), (I. 6), (I. 10), and (I. 11), the non-dimensional power coefficient can be derived as follows:

$$C_P = \frac{\rho A U_1^2 (U_0 - U_3)}{\frac{1}{2}\rho A U_1^3} = 4a(1-a)^2 \tag{I. 13}$$

By solving the equation $\frac{dC_P}{da} = 0$ for equation (1.12), the maximum energy conversion efficiency can be determined at a value of $a = \frac{1}{3}$, resulting in $C_{Pmax} = 16/27 = 0.59$. This represents the highest achievable efficiency of an ideal wind turbine 59%, commonly known as the Betz limit. It is worth noting that the axial momentum theory, being a simplistic one-dimensional model, does not consider the rotational airflow within the air.

The $C_P - \lambda$ hold a crucial role in wind turbine design as they assist in determining the rotor power under various wind and rotor speed combinations. Figure I. 18 illustrates the power coefficient curve for different types of wind turbines.

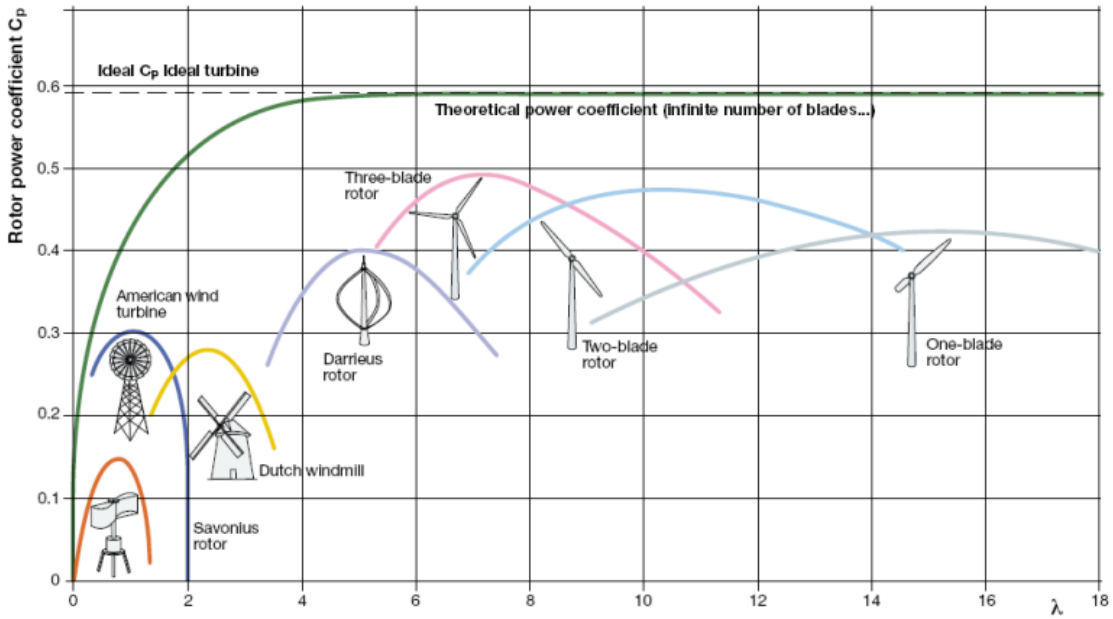

Figure I. 18 $C_P - \lambda$ curve for different types of wind turbines [88]

It is evident that the ideal power coefficient varies depending on the blade type, enabling the selection of a suitable turbine type based on the region's wind speed. By utilizing this curve in conjunction with pertinent wind turbine data, such as rated capacity and minimum/maximum wind speeds, it becomes possible to generate a power curve for the wind turbine. The power curve visually represents the electrical power output at different wind speeds. An example of a power curve is depicted in Figure I. 19.

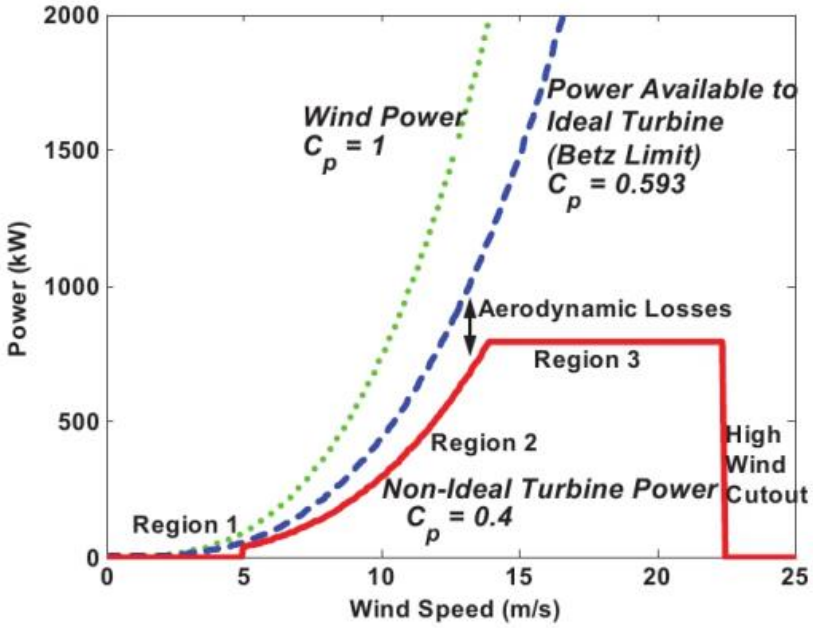

Figure I. 19 power output at different wind speeds [89]

V.1.3 Blade element theory

Blade element theory supposes a unidirectional axial flow in the upstream region away from the rotor, but incorporates the rotational speed of the flow at the rotor's plane. This model treats the blade as a collection of multiple elements. The theory assumes that there is no aerodynamic interaction among these elements, rendering each part independent from the others. In Figure I. 20, an element with a thickness of dr is shown, constituting a blade, along with a fictitious ring formed during the blade's rotation. Another assumption of the theory is that the flow around each element is solely bidirectional, simplifying the interaction forces on a blade element to lift and drag. By calculating the forces acting on each element and integrating the resulting stresses, the overall blade performance can be evaluated.

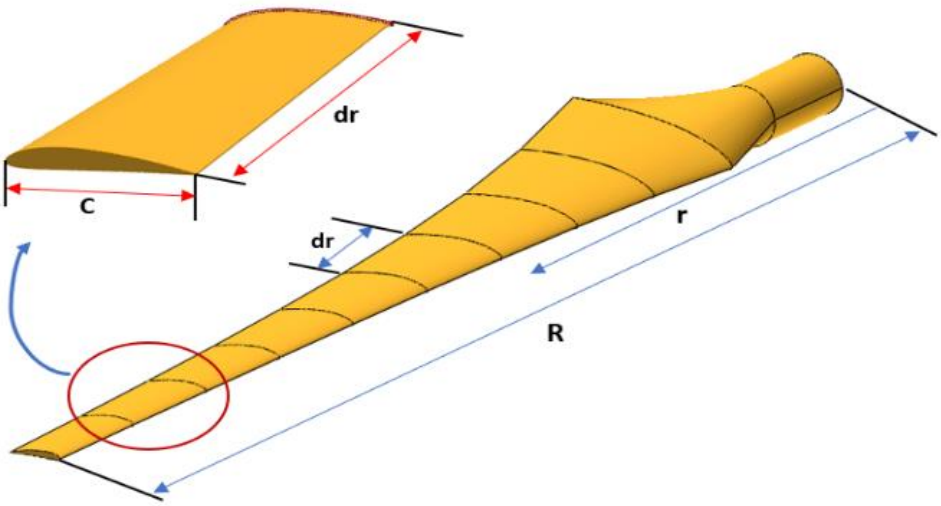

Figure I. 20 Blade sections Schematic

In blade element theory, the tangential flow induction factor, denoted as a', is introduced. It is defined as $a' = \omega/\Omega$, where ω represents the angular velocity of the flow at the rotor's plane, and Ω represents the rotational speed of the rotor. Referring to the notations in Figure I. 16 and Figure I. 20, these two relationships can be expressed in terms of the definitions of a and a':

$$U_1 = U_0(1-a) \tag{I. 14}$$

$$U_{rot} = \Omega + \omega r = \Omega r(1+a') \tag{I. 15}$$

Where U_0 denotes the wind speed far upstream, the following geometric relationships can be established:

$$\tan\varphi = \frac{U_0(1-a)}{\Omega r(1+a')} \tag{I. 16}$$

$$U_{rel} = \sqrt{U_0^2(1-a)^2 + \Omega^2 r^2(1+a')^2} \tag{I. 17}$$

The fundamental assumption of the theory is that the force applied to a blade element is equal to the change in momentum of the airflow passing through the blade. Consequently, the lift and drag forces can be expressed as:

$$dL = \frac{1}{2}\rho U_{rel}^2 B C_L dS \tag{I. 18}$$

$$dD = \frac{1}{2}\rho U_{rel}^2 B C_D dS \tag{I. 19}$$

By utilizing C_L and C_D as the lift and drag coefficients, respectively, and $dS = cdr$ as the surface area of the blade element under consideration, it should be noted that B represents the number of blades. the tangential force (which is related to torque) acting on the blade element can be determined through projection:

$$dF_T = \frac{1}{2}\rho c dr U_{rel}^2 B(C_L\sin(\varphi) - C_D\cos(\varphi)) \tag{I. 20}$$

And

$$C_T = C_L \sin(\varphi) - C_D \cos(\varphi) \quad \text{(I. 21)}$$

The torque exerted on a blade element dQ can be calculated by multiplying the tangential force by the local radius (r), resulting in the following expression:

$$dQ = \frac{1}{2}\rho c r dr U_{rel}^2 B(C_L \sin(\varphi) - C_D \cos(\varphi)) \quad \text{(I. 22)}$$

In order to determine the power generated by the wind turbine, it is necessary to compute this force. Similarly, the normal force (which is associated with thrust) can be expressed as follows:

$$dF_N = \frac{1}{2}\rho c dr U_{rel}^2 B(C_L \cos(\varphi) + C_D \sin(\varphi)) \quad \text{(I. 23)}$$

And

$$C_N = C_L \cos(\varphi) + C_D \sin(\varphi) \quad \text{(I. 24)}$$

By incorporating the definition of local solidity as:

$$\sigma = \frac{Bc}{2\pi r} \quad \text{(I. 25)}$$

the equations ((I. 23) and ((I. 22) can be reformulated as follows:

$$dQ = \sigma\pi\rho r^2 dr U_{rel}^2(C_L \sin(\varphi) - C_D \cos(\varphi)) \quad \text{(I. 26)}$$

$$dF_N = \sigma\pi\rho dr U_{rel}^2(C_L \cos(\varphi) + C_D \sin(\varphi)) \quad \text{(I. 27)}$$

V.1.4 Blade Element Momentum: Integration of Both Theories

By utilizing the notation from the blade element and considering an area of the blade element $A = 2\pi r dr$, equation (I. 12) can be reformulated to yield the following expression:

$$dF_N = 4\rho\pi r dr U_0^2 a(1-a) \quad \text{(I. 28)}$$

Similarly, by employing the notation depicted in Figure I.17 and extending the axial momentum theory, the change in momentum in the tangential direction provides us with the tangential force exerted on the blade:

$$dF_T = \rho A U_1 U_T \quad \text{(I. 29)}$$

where $U_T = \omega_3 r$, representing the tangential velocity of the flow immediately after the rotor, and ω_3 is defined as the angular velocity. To determine ω_3, the conservation law of angular momentum is applied between sections 1 and 2 of Figure I.17.

$$\omega_1 r_1^2 = \omega_2 r_2^2 \quad \text{(I. 30)}$$

Since the upstream flow far from the turbine is purely axial, ω_1 is equal to 0. Consequently, from equation (I. 30), it follows that ω_2 is also 0. It can be inferred that the angular velocity experiences a discontinuity at the rotor's plane, which is caused by the torque exerted on the rotor. The angular velocity of the flow at the rotor's plane is the average of the angular velocities just before and after the rotor.

$$\omega = \frac{\omega_2 + \omega_3}{2} = \frac{\omega_3}{2} \quad \text{(I. 31)}$$

Finally, by incorporating the definitions of a and a', equation (I. 29) can be rewritten as follows:

$$dF_T = \rho(2\pi r dr)U_0(1-a)2a'\Omega \quad \text{(I. 32)}$$

Subsequently, by noting that U_0 corresponds to U_∞ according to the notation in Figure I.17, we can obtain the torque.

$$dQ = 4\rho U_\infty(1-a)a'\Omega\pi r^3 dr \quad \text{(I. 33)}$$

V.1.5 Tip Losses

Tip losses refer to the reduction in efficiency and performance experienced by wind turbines due to the aerodynamic effects occurring at the tips of the rotor blades. As the blades rotate, the airflow near the tips becomes distorted, resulting in increased turbulence and reduced efficiency in energy extraction from the wind. Tip losses occur due to several factors, including the higher circumferential speed at the blade tips compared to the rest of the blade, the occurrence of vortices, and the interaction between the tip vortices and the downstream blades. These factors lead to increased drag and reduced lift, resulting in a decrease in overall power production. To account for tip losses in wind turbine analysis, correction models and empirical formulas are often applied. These models take into consideration the blade geometry, tip speed ratio, and other relevant parameters to estimate the magnitude of the tip losses. By incorporating these corrections, the predicted performance of the wind turbine can be adjusted to account for the impact of tip losses.

Prandtl's tip loss model, developed by Prandtl [11], is widely acknowledged and widely used in the field. This model proposes the inclusion of a correction factor, denoted as F, into the equations discussed earlier for the computation of net force and torque. This factor accounts for various factors such as the number of blades, the relative wind angle, the blade element position, and the blade radius. By incorporating Prandtl's correction factor, more accurate calculations of net force and torque can be achieved.

$$f(B, \varphi, r, R) \quad \text{(I. 34)}$$

The ultimate expression for the Prandtl tip loss factor is as follows:

$$F = \frac{2}{\pi}cos^{-1}\left(\exp\left(-\frac{B}{2}\frac{R-r}{r sin\varphi}\right)\right) \quad \text{(I. 35)}$$

By utilizing both theories, the torque and thrust have been represented in two distinct forms. Consequently, we can solve the problem and obtain the following results using equations (I. 27) and (I. 28):

$$a = \frac{1}{\frac{4F sin^2(\varphi)}{\sigma(C_L \cos(\varphi) + C_D \sin(\varphi))} + 1} \quad \text{(I. 36)}$$

By employing equations (1.22) and (1.29), we can derive:

$$a' = \frac{1}{\frac{4Fsin(\varphi)cos(\varphi)}{\sigma(C_L \sin(\varphi) - C_D \cos(\varphi))} - 1} \quad \text{(I. 37)}$$

Blade element momentum theory is therefore a simplified model that facilitates the calculation of forces exerted on a rotor and enables the determination of the power extracted from the rotor.

The tangential induction factor a' is computed directly using BEM theory (Equation (I. 37)). This calculation process involves an iterative procedure outlined in Figure I. 21 below. The loop continues until the desired accuracy is attained in the induction factors, and the procedure is applied to each blade element. Once the induction factors are determined, the thrust and torque of each blade element can be obtained using the equations (I. 32) and (I. 33).

During the iterative process, the program requires the input of lift and drag coefficients. For each blade element, airfoil information including chord and twist values is necessary. The lift and drag coefficients should be provided for various angle of attack values. The iteration and power calculation procedure described here is implemented using the MATLAB programming language. The BEM analysis tool allows for the prediction of wind turbine performance based on the specified geometric variables, as indicated in the inputs box of Figure I. 21. This tool is also utilized in the calculation of wind turbine power production during the optimization loop. To ensure its accuracy, the BEM analysis tool has been validated against experimental data obtained from the literature.

The flowchart loop of the Blade Element Momentum (BEM) method for optimizing wind turbine blades is depicted in Figure I. 21. This loop consists of the following steps:

1. Initialize the design parameters and set the convergence criteria.

2. Start the iteration loop.

3. Compute the local flow conditions (wind speed, angle of attack) for each blade element.

4. Calculate the lift and drag coefficients based on the local flow conditions and airfoil characteristics.

5. Update the induced velocity at each blade element using the BEM equations.

6. Calculate the net forces and torques on each blade element.

7. Compute the overall power and thrust of the wind turbine.

8. Check if the convergence criteria are met. If yes, exit the loop.

9. If not, update the blade twist angle or chord length based on the optimization algorithm.

10. Repeat steps 3 to 9 until convergence is achieved.

11. Output the optimized blade parameters and performance metrics.

This flowchart loop enables the iterative optimization of wind turbine blade design by adjusting the blade parameters and evaluating their impact on the overall performance of the turbine.

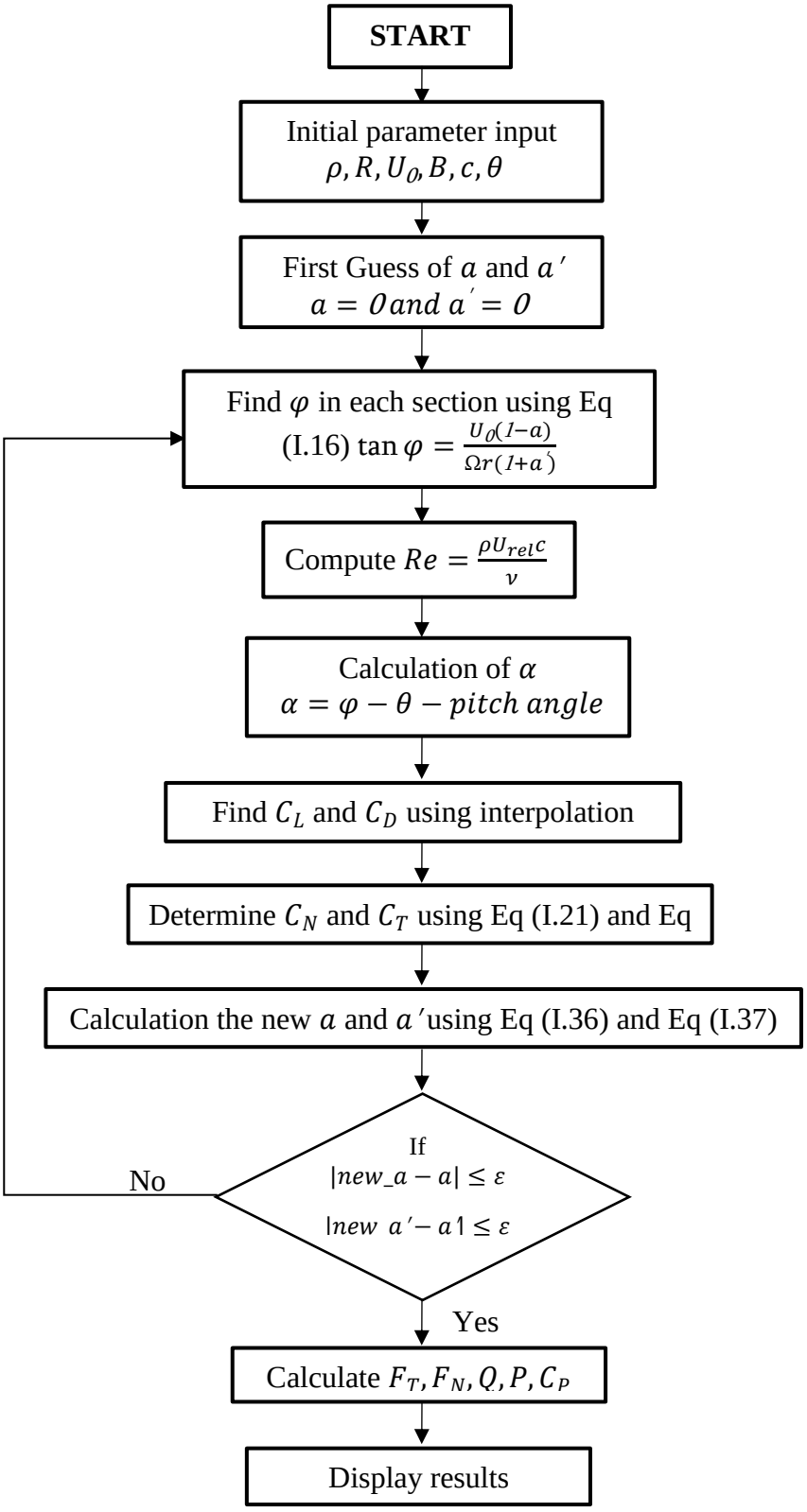

Figure I. 21 Flowchart loop of BEM to optimize wind turbine blade

V.2 Computational Fluid Dynamics (CFD) for Wind Turbines

In previous years, computational fluid dynamics (CFD) for wind turbines primarily centered around the solution of the incompressible Navier-Stokes equations [90]. The flow within wind turbines is typically incompressible, characterized by velocities ranging from 5 to 25 m/s. Although compressibility effects arise near the blade tips due to high rotational velocities, the Mach number at the tips remains relatively low ($M \leq 0.25$). Thus, it is reasonable to assume that the flow is incompressible, even when considering the detailed resolution of the blades.

V.2.1 Navier-Stokes equations

By formulating the principles of mass conservation, momentum conservation, and energy rate of change for a fluid particle, along with defining the equations of state, it becomes feasible to express the Navier-Stokes equations in a closed form. It is important to mention that the equations provided in equations (I. 38) to equation (I. 43) are formulated based on Reynold's decomposition, where the velocity quantity is separated into its mean and fluctuating components (e.g., $\Phi = \overline{\Phi} + \Phi'$), and Favre's density-weighted averaging is employed (e.g., for the mean velocity).

V.2.1.1 Continuity equation

The equation governing mass conservation at a specific point in a compressible fluid can be expressed as follows:

$$\frac{\partial \rho}{\partial t} + \nabla \rho \tilde{\boldsymbol{U}} = 0 \tag{I. 38}$$

With:

$$\nabla \tilde{U} = -\frac{1}{\rho}\frac{D\rho}{Dt} \tag{I. 39}$$

Where ρ represents the density, while $\tilde{\boldsymbol{U}} = ui + vj + wk$ denotes the velocity of the fluid in three-dimensional space.

Let's consider a fluid particle with constant mass m and variable volume $v = \frac{m}{\rho}$. By substituting the expression for volume v in equation (I. 39), we obtain:

$$-\frac{1}{\rho}\frac{D\rho}{Dt} = -\frac{1}{v}\frac{Dv}{Dt} \tag{I. 40}$$

The change rate of a fluid's volume element with mass m is equal to the divergence of the fluid's velocity u_j in three directions (u, v, and w). The volume density ρ of the fluid varies in both time and space. By rearranging the previous equations, we can express the rate of fluid expansion in tensorial form as follows:

$$-\frac{\partial \rho}{\partial t} + \mathrm{div}(\rho u_i) = 0 \tag{I. 41}$$

Theoretical considerations suggest that air can be treated as an incompressible fluid at speeds below 98 m/s [91]. In this condition, the air density ρ remains constant, and the Mach number M is low. The continuity equation for an incompressible fluid is derived from equation (I. 41) by neglecting the first term $\frac{\partial \rho}{\partial t}$, and it can be expressed as follows:

$$\frac{\partial u_i}{\partial x_i} = 0 \tag{I. 42}$$

V.2.1.2 Moment equations

The moment equations, which are also known as the Navier-Stokes equations, encompass the physical phenomena of temperature, particle diffusion, and dispersion that occur during the motion of a fluid. These equations provide a concise representation of these phenomena and can be expressed as follows:

$$\frac{\partial(\rho u_i)}{\partial t} + \frac{\partial}{\partial x_j}(\rho u_i u_j) = -\frac{\partial p}{\partial x_i} + \frac{\partial}{\partial x_j}\left[\mu\left(\frac{\partial u_i}{\partial x_j} + \frac{\partial u_j}{\partial x_i}\right)\right] + f_i \qquad \text{(I. 43)}$$

The equation (I. 43) consists of convective terms on the left-hand side, while the right-hand side includes pressure gradient, external forces, and viscous stress tensor terms. To evaluate these terms accurately, knowledge of the source and magnitude responsible for the moment variation is required. In this context, any alterations in fluid motion resulting from temperature changes are disregarded, focusing solely on the impact of external volumetric forces on the variation of air motion.

V.2.2 Turbulence modeling

Essentially, natural flows of fluids and industrial flows of fluids tend to become unstable once they surpass a specific Reynolds number (Re). The Reynolds number is determined by the average fluid velocity (U) at the inlet of the simulated domain, along with the fluid's density (ρ) and dynamic viscosity (μ).

The concept of the Reynolds number was initially introduced by Osborne Reynolds in 1883. It serves as a measure of the ratio between inertial forces and viscous forces in a fluid system. When the Reynolds number (Re) is below 2000, the fluid flow is classified as laminar, displaying an organized behavior. As the flow transitions into a transient state, the Reynolds number ranges from 2000 to 60000, showcasing a mix of laminar and turbulent characteristics. Finally, in the fully turbulent regime, which occurs at Reynolds numbers exceeding 60000, the flow becomes disorganized, exhibiting spatial and temporal fluctuations.

V.2.2.1 Averaged Reynolds Equations (RANS)

In the context of the averaged Reynolds equations, the solutions obtained from the instantaneous Navier-Stokes equations (I. 43) are separated into two parts: the mean component and the fluctuating component. The mean part can be determined through either an ensemble average or a time average. For instance, the total wind speed is the sum of the mean component (U_i) and the fluctuating component ($u_i^{'}$). Similarly, other quantities such as pressure, energy, and scalar solutions from the Navier-Stokes equations can be decomposed into mean and fluctuating components. The sum of these two components (Φ_i) is described by the following relationship:

$$\Phi_i = \overline{\Phi_\iota} + \Phi_i^{'} \qquad \text{(I. 44)}$$

By substituting φ_i in equations (I. 42) and (I. 43), we derive the resulting continuity and momentum equations:

$$\frac{\partial U_i}{\partial x_i} = 0 \qquad \text{(I. 45)}$$

With

$$u_i = U_i + u_i^{'} \qquad \text{(I. 46)}$$

Where the average speed U_i, is a temporal average, measured independently of the observation time.

The equation (I. 45) is common to the two fluid domains of the following Figure I. 22.

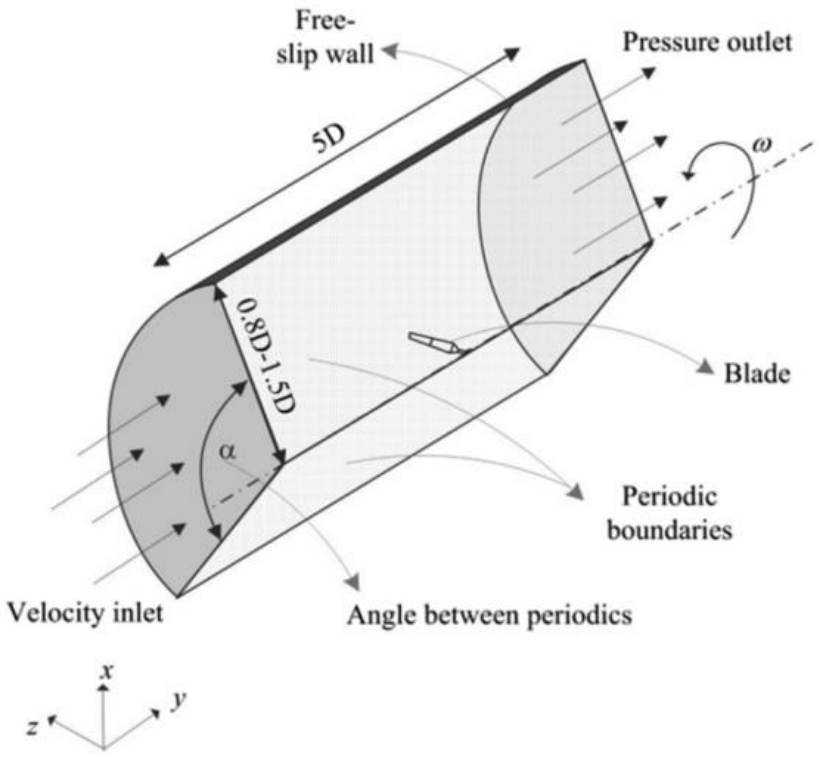

Figure I. 22 Computational Domain and Boundary Conditions [92]

$$\frac{\partial(\rho u_i)}{\partial t}+\frac{\partial(u_i u_j)}{\partial x_j}=-\frac{\partial p}{\partial x_i}+\frac{\partial}{\partial x_j}\left[\mu\left(\frac{\partial u_i}{\partial x_j}+\frac{\partial u_j}{\partial x_i}\right)-\rho\overline{u_i' u_j'}\right] \quad \text{(I. 47)}$$

The moment equation (I. 47) is applicable within the defined stationary region depicted in Figure I. 22. In the moving region, the averaged Reynolds equation undergoes modifications to account for the influence of the Coriolis force and the Centrifugal force. The expression of the averaged Reynolds equation within the rotating region is presented in the following relation:

$$\frac{\partial(\rho u_i)}{\partial t}+\frac{\partial(u_i u_j)}{\partial x_j}=-\frac{\partial p}{\partial x_i}+\frac{\partial}{\partial x_j}\left[\mu\left(\frac{\partial u_i}{\partial x_j}+\frac{\partial u_j}{\partial x_i}\right)-\rho\overline{u_i' u_j'}\right]+2\varepsilon_{ijk}\omega_i\omega_j x_j-\omega_i\omega_j x_i \quad \text{(I. 48)}$$

with $2\varepsilon_{ijk}\omega_i\omega_j x_j$ and $\omega_i\omega_j x_i$ are respectively the Coriolis forces and the centrifugal forces.

V.2.3 Closure of averaged Reynolds equations

Because of the averaging process taking place in the RANS formulation, extra terms appear: the Reynolds stresses and the transport equation time average terms. The use of turbulence modeling is necessary to have a closed problem. It exists many different types of models adding (or not) extra equations to ensure the closure: mixing length model, Spalart–Allmaras, $k-\epsilon$, $k-\omega$, SST $k-\omega$, and Reynolds stress model. The turbulence model developed by Menter (SST $k-\omega$) [93], is a combination of the best features of the $k-\epsilon$ and $k-\omega$ turbulence models. Near the wall, the $k-\omega$ model is used and far from the wall, where

the turbulence is fully developed, the k − ϵ is used. It relies on empirical constants which have been tuned since the first paper published in 1993. Only the SST k − ω model has been used as part of this thesis.

V.2.3.1 SST k − ω model

The SST k-ω model, which was devised by Menter and is a combination of the standard k-ε and k-ω models [93], aims to enhance the performance of flow with reverse pressure gradients. Additionally, it addresses the issue of parasite sensitivity for free flows [94, 95], Some researchers, like Christopher et al. in 2002, have criticized the k-ω model for its poor representation of flow with inverse pressure gradients[96]. However, due to its successful prediction of numerous flows in the aeronautical industries, we were motivated to utilize this turbulence model in our study. The governing equations of this turbulence model are as follows:

$$\frac{D\rho k}{Dt} = \mathrm{P}_k - \beta^*\rho\omega k + \frac{\partial}{\partial x_j}\left[(\mu + \frac{\mu_t}{\sigma_k})\frac{\partial k}{\partial x_j}\right] \quad \text{(I. 49)}$$

$$\frac{D\rho\omega}{Dt} = \frac{\gamma\rho}{\mu_t}\mathrm{P}_k - \beta\rho\omega^2 + \frac{\partial}{\partial x_j}\left[\left(\mu + \frac{\mu_t}{\sigma_\omega}\right)\frac{\partial\omega}{\partial x_j}\right] + 2(1-\mathrm{F}_1)\frac{\rho}{\sigma_{\omega 2}\omega}\frac{\partial k}{\partial x_j}\frac{\partial\omega}{\partial x_j} \quad \text{(I. 50)}$$

in which:

$$\mu_t = \frac{\rho a_1 k}{\max(a_1\omega, \Omega\mathrm{F}_2)} \quad \text{(I. 51)}$$

$$\mathrm{P}_k = \tau_{ij}\frac{\partial u_i}{\partial x_j} \quad \text{(I. 52)}$$

$\mathrm{P}_k \approx \mu t\Omega^2$ for boundary layer flow

$$\mathrm{F}_1 = \tanh(\Gamma^4) \quad \text{(I. 53)}$$

$$\Gamma = min\left[\max\left(\frac{\sqrt{k}}{\beta^*\omega d}, \frac{500\mu}{\rho\omega d^2}\right), \frac{4\rho k}{\sigma_{\omega 2} CD_{k\omega} d^2}\right] \quad \text{(I. 54)}$$

$$CD_{k\omega} = max\left(\frac{2\rho}{\sigma_{\omega 2}\omega}\frac{\partial k}{\partial x_j}\frac{\partial\omega}{\partial x_j}, 10^{-20}\right) \quad \text{(I. 55)}$$

$$\mathrm{F}_2 = tanh(\Pi^2) \quad \text{(I. 56)}$$

$$\Pi = max\left(\frac{2\sqrt{k}}{\beta^*\omega d}, \frac{500\mu}{\rho\omega d^2}\right) \quad \text{(I. 57)}$$

The parameters $\gamma, \sigma_k, \sigma_\omega$ and β are calculated by:

$$\gamma = \mathrm{F}_1\gamma_1 + (1-\mathrm{F}_1)\gamma_2 \quad \text{(I. 58)}$$

$$\sigma_k = \mathrm{F}_1\sigma_{k1} + (1-\mathrm{F}_1)\sigma_{k2} \quad \text{(I. 59)}$$

$$\sigma_\omega = \mathrm{F}_1\sigma_{\omega 1} + (1-\mathrm{F}_1)\sigma_{\omega 2} \quad \text{(I. 60)}$$

$$\beta = \mathrm{F}_1\beta_1 + (1-\mathrm{F}_1)\beta_2 \quad \text{(I. 61)}$$

where $\gamma_1 = 0.55317$, $\gamma_2 = 0.44035$, $\sigma_{k1} = 1.17647$, $\sigma_{k2} = 1$, $\sigma_{\omega 1} = 2$, $\sigma_{\omega 2} = 1.16822$, $\beta_1 = 0.075$, $\beta_2 = 0.0828$, $k = 0.41$, $a_1 = 0.31$, $\beta^* = 0.09$, ω is the magnitude of the vortices d is the distance close to the walls.

VI. CONCLUSION

In this chapter, we conducted a comprehensive review of wind turbines through extensive literature research. Our exploration began by delving into the historical background of the turbine blade and tracing its evolution over time. Subsequently, we elucidated the various components comprising a wind turbine, with special emphasis on the blade, which serves as the foundation of our study. We addressed essential considerations such as selecting an appropriate blade profile, analyzing wind distribution patterns, and identifying optimal placement locations. Furthermore, we provided theoretical equations for the two most renowned methods used to simulate the blade (BEM, and CFD), enabling the determination of applied loads, torque, power, and power factor. As demonstrated in this chapter, our objective was to foster familiarity with the wind turbine and its constituents, alongside the methodologies employed in its design and simulation, all geared towards enhancing its performance and maximizing productivity.

CHAPTER II

WIND TURBINE BLADE VIBRATION

I. Introduction

Wind turbine vibration refers to the oscillation or movement of wind turbines caused by various factors during their operation. Wind turbines are designed to convert wind energy into electricity, but the forces generated by wind can also induce vibrations in the structure. These vibrations can have both positive and negative effects, depending on their magnitude and frequency. Vibration in wind turbines can arise from multiple sources. The primary source is the interaction between the rotating blades and the wind. As the wind flows past the blades, it exerts dynamic forces that can lead to blade vibrations. Additionally, unbalanced rotor components, such as blades or hubs, can cause irregular vibrations. Other sources of vibration include turbulence in the wind flow, tower dynamics, generator operation, and mechanical imperfections in the turbine components.

Vibration can have several impacts on wind turbines. Excessive vibrations can lead to mechanical stress, fatigue, and premature wear of the turbine components, affecting their structural integrity and overall lifespan. This can result in increased maintenance costs, reduced energy production, and potential downtime for repairs. Furthermore, vibrations can generate noise and affect the comfort of nearby residents, leading to concerns about the environmental impact of wind farms.

Ongoing research and technological advancements are continuously enhancing wind turbine design and materials, aiming to mitigate vibration phenomena. These advancements contribute to the development of more robust and efficient wind turbine systems that operate reliably and have a reduced environmental impact. As a result, the second chapter will focus on studying wind turbine blade vibrations and accessing simplified mathematical models to support scientific research in a domain that still lacks extensive studies.

II. Vibration of wind turbine blade

The term 'vibration' refers to the back-and-forth motion of a particle or object within an elastic system, oscillating on either side of an equilibrium position. In wind turbines, vibrations are significant due to their partially elastic nature and operation in an unsteady environment, leading to a vibrating response. These vibrations can cause deflections that need to be considered during turbine design and may also lead to material fatigue, resulting in premature failure of the turbine.

Understanding vibrations is crucial for wind turbine applications as much of their operation can be explained in the context of vibratory motion. The following section presents an overview of the essential aspects of vibrations that hold significant importance for wind turbine systems.

II.1 Systems with a single degree of freedom

II.1.1 Vibrations without damping

The most basic vibrating system comprises a mass, denoted as "m," connected to a spring with negligible mass and a spring constant "k," as depicted in Figure II. 2. When displaced by a distance "x" and released to move freely, the mass undergoes oscillation in both directions.

By implementing Newton's Second Law, the equation that governs this scenario is:

$$m\ddot{x} + kx = 0 \quad \text{(II. 1)}$$

At the initial condition where time (t) equals 0 and displacement (x) equals x_0, the solution is:

$$x = x_0 \cos(\omega_n t) \quad \text{(II. 2)}$$

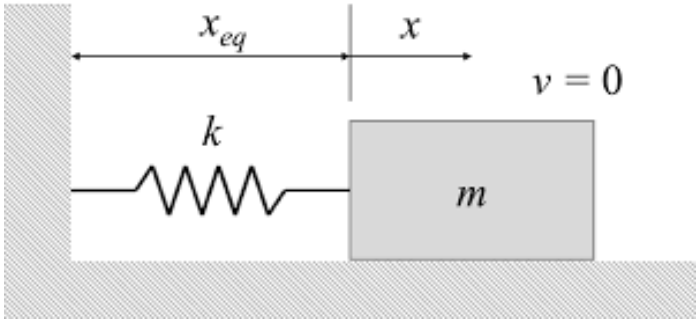

Figure II. 1 illustrates an undamped vibrating system[97]

Here, "ω_n" represents the natural frequency of the motion, and it is defined as "$\sqrt{k/m}$" In the broader context, when the mass isn't initially at rest at t=0, the solution comprises two sinusoidal components:

$$x = x_0 \cos(\omega_n t) + \frac{\dot{x}_0}{\omega_n} \sin(\omega_n t) \quad \text{(II. 3)}$$

Here, $\dot{x}_0$ signifies the velocity at time t=0.

The solution can alternatively be expressed using a single sinusoidal term, characterized by an amplitude C and a phase angle ϕ. This can be written as:

$$x = C \sin(\omega_n t + \phi) \quad \text{(II. 4)}$$

The amplitude and phase angle can be represented in relation to the other parameters as follows:

$$C = \sqrt{x_0^2 + \left(\frac{\dot{x}_0}{\omega_n}\right)^2} \quad \text{(II. 5)}$$

$$\phi = \tan^{-1}\left[\frac{x_0 \omega_n}{\dot{x}_0}\right] \quad \text{(II. 6)}$$

II.1.2 Damped Vibrations

The described vibrations, as mentioned earlier, would persist infinitely. However, real-world vibrations always exhibit a gradual decay over time. This behavior can be simulated by incorporating a term for viscous damping. Damping introduces a force, generally assumed to be proportionate to velocity, that counteracts the motion Figure II. 2. Consequently, the equation of motion is transformed into:

$$m\ddot{x} = -c\dot{x} - kx \quad \text{(II. 7)}$$

In the equation, c stands for the damping constant and k signifies the spring constant. Depending on the relationship between the damping and spring constants, the solution can exhibit oscillatory behavior (termed 'underdamped') or non-oscillatory behavior ('overdamped'). The transition between these two states is known as 'critically damped,' wherein:

$$c = c_c = 2\sqrt{km} = 2m\omega_n \quad \text{(II. 8)}$$

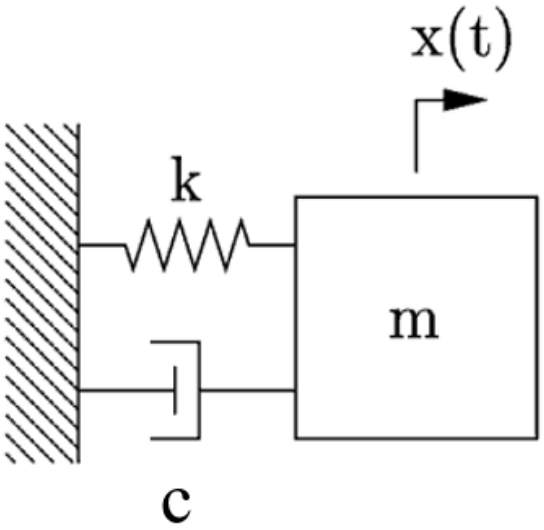

Figure II. 2 Damped free mechanical vibration system.

To simplify, a non-dimensional damping ratio $\xi = c/c_c$ is employed to describe the motion conveniently[98]. When $\xi < 1$, the motion is categorized as underdamped; and when $\xi > 1$, it is considered overdamped. The solution for underdamped oscillation is as follows:

$$x = Ce^{-\xi\omega_n t}\sin(\omega_d t + \phi) \quad \text{(II. 9)}$$

Here, $\omega_d = \omega_n\sqrt{1-\xi^2}$ denotes the natural frequency for damped oscillation. It's important to note that the frequency of damped oscillation slightly varies from that of undamped vibration. The amplitude C and the phase angle ϕ are determined based on the initial conditions.

II.1.3 Analysis of Forced Harmonic Vibrations

Let's contemplate the mass, spring, and damper systems mentioned earlier. Let's assume it's subjected to a sinusoidal force with an amplitude F_0 and a frequency ω (which might not be equivalent to $\omega_n$or ω_d) Figure II. 3. In this scenario, the equation of motion is given by[97]:

$$m\ddot{x} + c\dot{x} + kx = F_0\sin(\omega t) \quad \text{(II. 10)}$$

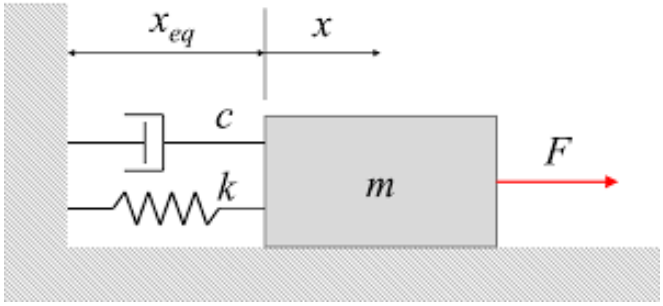

Figure II. 3 A system comprising a mass, spring, and damper, influenced by an external harmonic excitation force F.[97]

It can be demonstrated that the solution in a steady state to this equation is:

$$x(t) = \frac{F_0}{k} \frac{\sin(\omega t - \phi)}{\sqrt{[1-(\omega/\omega_n)^2]^2 + [2\xi(\omega/\omega_n)^2]}} \quad \text{(II. 11)}$$

In this instance, the phase angle is given by:

$$\phi = \tan^{-1}\left[\frac{2\xi(\omega/\omega_n)}{1-(\omega/\omega_n)^2}\right] \quad \text{(II. 12)}$$

Of special significance is examining the non-dimensional response amplitude (as depicted in Figure II. 4), denoted as xk/F_0, and it's computed as[98]:

$$\frac{xk}{F_0} = \frac{1}{\sqrt{[1-(\omega/\omega_n)^2]^2 + [2\xi(\omega/\omega_n)^2]}} \quad \text{(II. 13)}$$

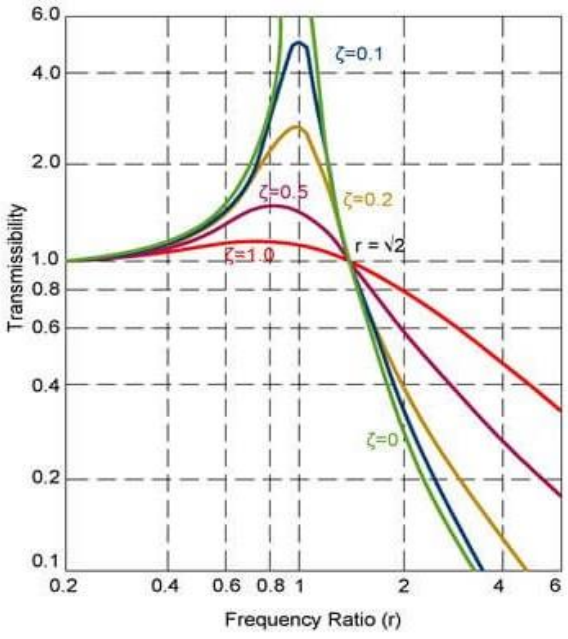

Figure II. 4 Graph depicting the ratio of vibration transmissibility [99].

As the frequency of the excitation force approaches the natural frequency, the amplitude of the response increases. Higher damping diminishes the peak value and introduces a slight shift. Moreover, even though the highest peak occurs when the excitation frequency matches the natural frequency (disregarding damping), there can still be a substantial amplitude rise when the excitation closely aligns with the natural frequency. This behavior is illustrated in Figure II. 4.

Upon applying a harmonic excitation force, such as a sinusoidal force $F(t)$, to a mass, the magnitude and phase of the resulting displacement x are notably contingent on the excitation frequency ω. This phenomenon delineates three discernible response regions:

- Quasi-static (or stiff) regime,
- Resonance, and
- Inertia-dominated (or soft) domain.

When the excitation frequencies are significantly lower than the natural frequency of the system, the response enters the quasi-static realm, as depicted in Figure II. 5. In this scenario, the mass displacement closely tracks the time-varying force, exhibiting only a minor phase lag. It's akin to the system being influenced by a static force.

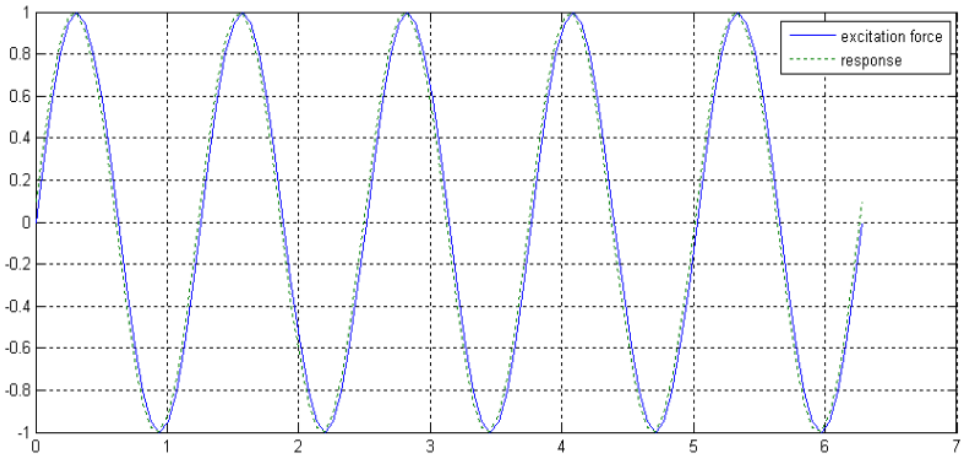

Figure II. 5 The quasi-static response of the vibrational system.[100]

Figure II. 6 depicts a standard response pattern for excitation frequencies situated within a narrow vicinity of the system's natural frequency. Within this range, the forces exerted by the spring and inertia nearly offset each other, generating a response that is several times greater than if it were purely static (the resultant amplitude is regulated by the system's damping characteristics).

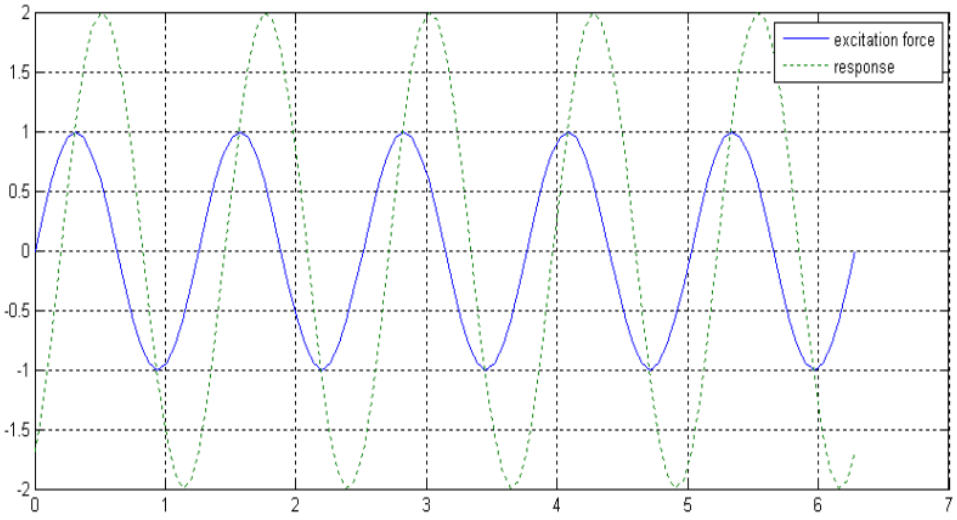

Figure II. 6 Resonant response of the forced damping system.[100]

When the excitation frequencies significantly exceed the natural frequency, the mass can no longer closely "track" the motion. As a result, the response amplitude is minimal and nearly in counter-phase, as portrayed in Figure II. 7. In this scenario, the system's response is predominantly governed by inertia, leading to a classification as "soft."

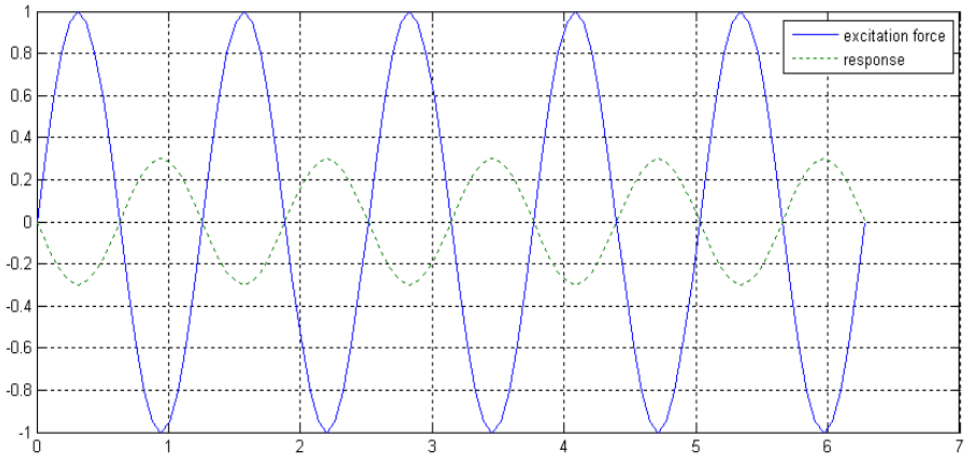

Figure II. 7 Inertia-Dominated Response in a Forced Vibration System.[100]

Across the three depicted figures, the excitation force F(t) maintains a consistent magnitude, albeit being applied at varying excitation frequencies. The normalized amplitude ratios illustrated in Figure II. 5 to Figure II. 7 highlight the following aspects:

- For steady-state conditions, sinusoidal inputs directed into linear systems yield sinusoidal outputs at the same frequency.
- However, there exist differences in the magnitude and phas1e (the shift between the sinusoidal input and output).

The altering effects of magnitude and phase in linear systems can be effectively summarized through the presentation of a frequency response function (FRF). This graphical representation delineates the ratio of output to input amplitudes, along with the accompanying phase shift, with respect to the excitation frequency. Figure II. 8 illustrates the Frequency Response Function (FRF) of the single degree of freedom system represented in Figure II. 3.

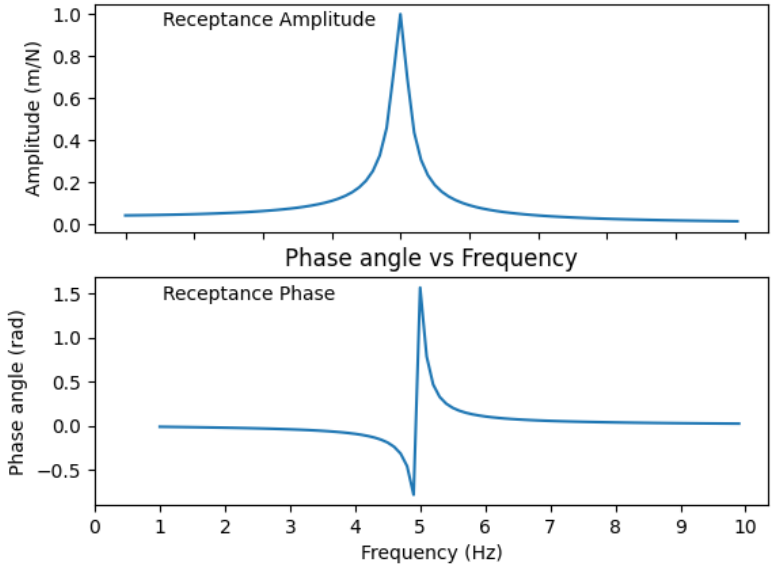

Figure II. 8 Frequency Response Function (FRF) of the single degree of freedom system

The pinnacle observed in Figure II. 8 corresponds to the natural frequency of the system. The peak's elevation is influenced by the damping characteristics. In the domain of structural dynamics, the frequency of the applied excitation force holds equal importance as its magnitude. Resonant behavior can lead to severe loading conditions, potentially resulting in failures, with particular concern for fatigue-related issues[1]. Material fatigue is instigated by time-varying external loads, leading to the emergence of cracks and internal damage. Wind turbines encounter fluctuating loads, which can induce such material breakdown. The operational lifespan of a wind turbine blade is contingent, in part, on the intensity and frequency of these loads. For structures exposed to dynamic loads, an intricate understanding of the anticipated frequencies of the excitation forces and the inherent natural frequencies of both the structure and its subcomponents becomes indispensable.

In precise terms, analyzing the vibrational dynamics of a multi-degree-of-freedom system necessitates considering the entire system as a cohesive unit. This is especially applicable when the dynamic interaction among the excited degrees of freedom is considerably potent, generating intricate modes of vibrational coupling that give rise to natural frequencies substantially different from those of the individual components involved. This scenario characterizes the fundamental nature of wind turbines [1]. Moreover, the computation must also encompass factors such as aerodynamic forces, gravitational forces, structural and aerodynamic damping, and control attributes.

Prior to initiating a mathematical simulation of such a comprehensive system, it proves advantageous to comprehensively understand the foundational vibrational attributes of the turbine. This ensures the identification of pivotal vibration modes. In many instances, it's plausible to individually analyze the

mathematical aspects of the constituents within a specific subsystem of the turbine. This entails calculating the initial natural frequencies of the variables, encompassing both the primary and certain higher modes.

II.1.3.1 Vibration of Rotating Blade

When a body with a polar mass moment of inertia J is connected to a rigid support through a rotational spring with rotational stiffness k_θ, as depicted in Figure II. 9, its equation of motion can be expressed as:

$$J\ddot{\theta} + k_\theta \theta = 0 \qquad \text{(II. 14)}$$

The solutions for rotational vibration resemble those for linear vibrations discussed earlier. Rotational vibration holds notable significance in wind turbine design, especially concerning shaft systems and the dynamics of the drive train.

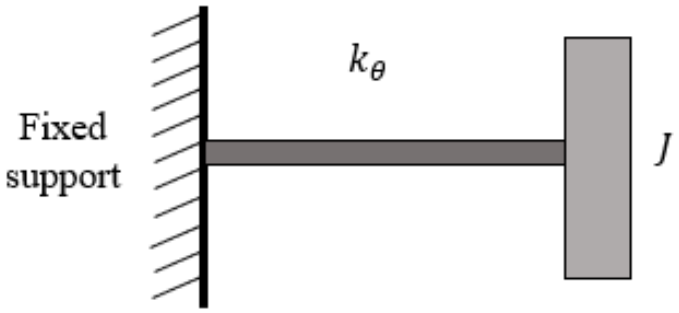

Figure II. 9 Rotating vibrational system of wind turbine

II.1.4 Cantilever Beam Vibrations

Examining the vibration of a cantilevered beam holds significance due to the resemblances between various aspects of wind turbines and cantilevered beams (see Figure II. 10). This similarity is particularly evident in components like the turbine-supporting tower and the blades.

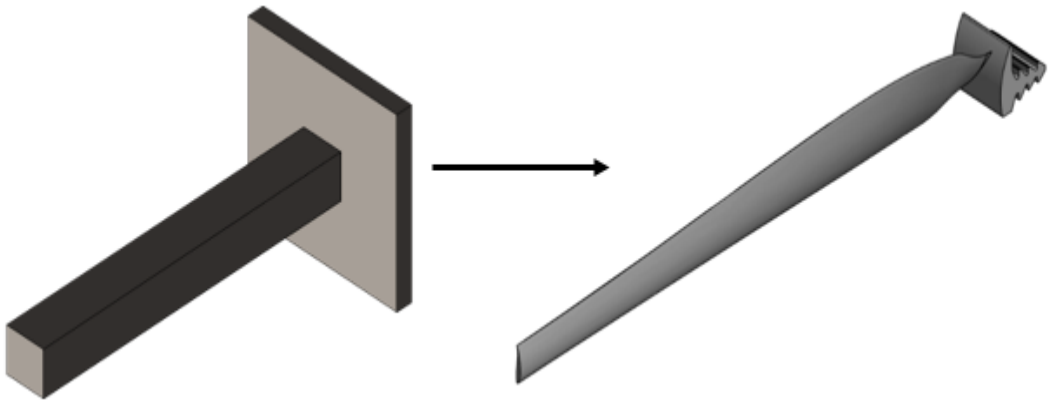

Figure II. 10 wind turbines and cantilevered beams

II.1.4.1 Vibration Modes and Modal Shapes

Remember that a solitary oscillating mass connected to a massless spring exhibits a lone distinctive natural frequency. In this case, the trajectory that the mass follows during its motion is singular. Yet, in

scenarios involving multiple masses, the count of natural frequencies and feasible pathways multiplies. In the context of continuous entities, a profusion of natural frequencies emerges – a multitude that's essentially boundless. Each natural frequency corresponds to a unique mode shape of vibration. However, in practical applications, the significance usually rests on only the lowermost natural frequencies of a beam.

II.1.4.2 Free vibration analysis of a uniform cantilever beam

The vibration exhibited by an ideal, uniform beam with uniform cross-section and consistent material properties can be mathematically represented by the Euler equation for beams. This equation offers a practical means of conveniently estimating first-order approximations of natural frequencies for numerous beams. For an in-depth insight into the formulation of the Euler beam equation, readers are advised to consult alternative sources [101]. However, this section is limited to providing the equation for a cantilevered beam, furnishing adequate details to facilitate its practical application.

The expression of the Euler equation for the deflection $y_i$of a uniform cantilevered beam with a length L and mode shape i can be represented as:

$$y_i = A\left\{\cosh\left(\frac{(\beta L)_i}{L}x\right) - \cos(\beta x) - \frac{\sinh(\beta L)_i - \sin(\beta L)_i}{\cosh(\beta L)_i + \cos(\beta L)_i}B\right\} \quad \text{(II. 15)}$$

Where:

$$B = \left[\sinh\left(\frac{(\beta L)_i}{L}x\right) - \sin\left(\frac{(\beta L)_i}{L}x\right)\right]$$

The parameter $(\beta L)_i$, devoid of dimensions, is interconnected with the beam's natural frequenciesω_i, linear density per unit length $\tilde{\rho}$, area moment of inertia I, and modulus of elasticity E, through the subsequent equation:

$$(\beta L)_i^4 = \tilde{\rho}\omega_i^2/(EIL^4) \quad \text{(II. 16)}$$

Derived from Equation (II. 16), the natural frequencies (expressed in radians per second) are as follows:

$$\omega_i = \frac{(\beta L)_i^2}{L^2}\sqrt{\frac{EI}{\tilde{\rho}}} \quad \text{(II. 17)}$$

For values of $(\beta L)_i$that satisfy:

$$\cosh(\beta L)_i \cos(\beta L)_i + 1 = 0 \quad \text{(II. 18)}$$

Equation (II. 15) empowers us to ascertain the mode shapes of the vibration. Notably, as A is undetermined, it can be ascertained by presuming a deflection of y_i at the unfettered end of the beam.

The quantities $(\beta L)_i^2$ represent dimensionless constants, and in the context of a uniform cantilevered beam, the numerical values for the initial three modes are 3.52, 22.4, and 61.7. Figure II. 11 visually presents the configuration of the initial three vibration modes of a uniform cantilevered beam, derived from Equations (II. 15) and (II. 18).

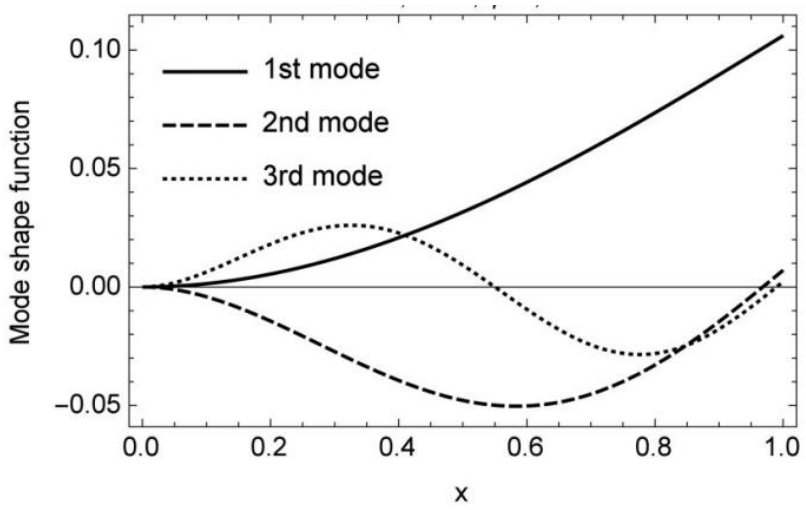

Figure II. 11 initial three vibration modes of a uniform cantilevered beam[102]

II.1.4.3 Vibrational Characteristics of General Beams (Myklestad method)

The preceding discourse centered on a uniform beam. This section, however, revolves around a broader scenario. It outlines the utilization of the Myklestad method, which entails depicting the beam as a collection of lumped masses connected by weightless beam components[103]. The Myklestad approach is incredibly adaptable and applicable to an extensive array of beams. Nevertheless, as previously, the discussion will be limited to the cantilevered beam. For further intricacies, readers can refer to [101]

The procedure is visually depicted in Figure II. 12. The beam is partitioned into $n-1$ segments, each containing the same number of massesm_i. There's an added station at the point of fixation. The distances λbetween the masses are uniform (in this case, equivalent to λ). In the illustration, it's assumed that the masses are positioned at the midpoint of equally sized segments, thus making the distance from the nearest mass to the attachment point half that of the others. The connectors possess moments of inertia I_i and a modulus of elasticityE_i. In this specific scenario, the beam could be rotating around an axis perpendicular to it and passing through station 'n', at a velocity of Ω.

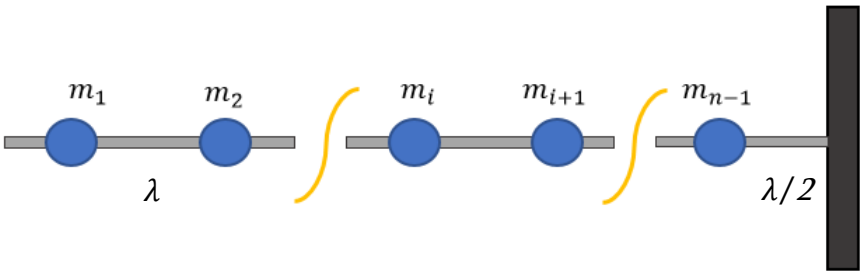

Figure II. 12 The Myklestad method to General Beams segments

The Myklestad technique revolves around resolving a series of sequential equations. These equations are derived by assessing the forces and moments exerted on each of the masses as well as the attachment point. Figure II. 13 portrays the free-body diagram of an individual segment of a rotating beam. Within this diagram, shear forces S_i, inertial (centrifugal) forces F_i, bending moments M_i, deflections y_i, and angular deflections θ_i are depicted.

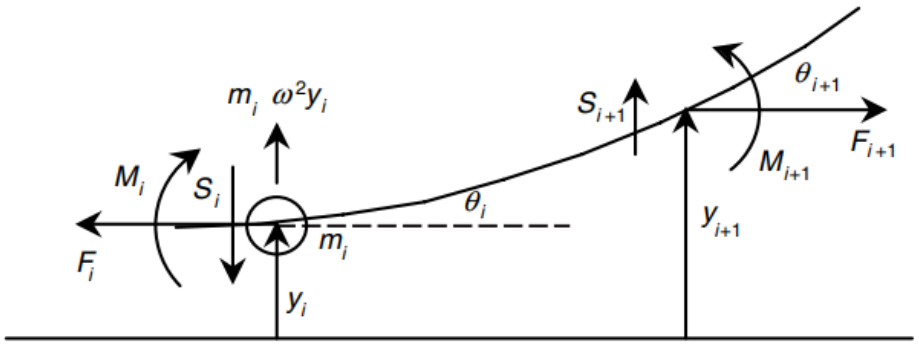

Figure II. 13 free-body diagram of an individual segment of a rotating beam

The comprehensive equations for a rotating beam ensue below. The centrifugal forces exerted at a distance x_j from the attachment point are as follows:

$$F_i = \Omega^2 \sum_{j=1}^{i-1} m_j x_j \tag{II. 19}$$

Consequently, it can be deduced that:

$$F_{i+1} = F_i + \Omega^2 m_i x_i \tag{II. 20}$$

Employing approximations for small angles, the shear forces can be expressed as:

$$S_{i+1} = S_i - m_i \omega^2 y_i - F_{i+1}\theta_i \tag{II. 21}$$

The moments can be defined as:

$$M_{i+1} = \left[M_i - S_{i+1}\left(\lambda_i - F_{i+1}\frac{\lambda_i^3}{3E_i I_i}\right) + \lambda_i \theta_i F_{i+1}\right] \Big/ \left(1 - F_{i+1}\frac{\lambda_i^2}{2E_i I_i}\right) \tag{II. 22}$$

The angles formed by the beam sections with respect to the horizontal are:

$$\theta_{i+1} = \theta_i + M_{i+1}\left(\frac{\lambda_i}{E_i I_i}\right) + S_{i+1}\left(\frac{\lambda_i^2}{2E_i I_i}\right) \tag{II. 23}$$

In conclusion, the deflections with reference to a horizontal line passing through the fixed end are as follows:

$$y_{i+1} = y_i + \lambda_i \theta_i + M_{i+1}\left(\frac{\lambda_i^2}{2E_i I_i}\right) + S_{i+1}\left(\frac{\lambda_i^3}{3E_i I_i}\right) \tag{II. 24}$$

The sequence of equations is tackled through iterative means, involving the identification of natural frequencies that lead to a computed deflection of zero at the attachment point. Typically conducted with computational assistance, this procedure commences by assuming a natural frequency ω and initiating a sequence of computations. The calculations are then reiterated with new presumptions for the natural

frequency until an approximation of zero deflection is achieved. This process entails two distinct sets of computations. The initial set commences at the beam's free end, with $y_{1,1} = 1$ and $\theta_{1,1} = 0$. The subsequent set begins with $y_{1,2} = 0$ and $\theta_{1,2} = 1$, where the secondary subscript pertains to the specific computation set. The calculations proceed successively for each segment until the final section, n, is reached. The outcomes furnish values for $y_{n,1}$, $y_{n,2}$, $\theta_{n,1}$, and $\theta_{n,2}$. The target deflection, which should tend towards zero, is expressed as:

$$y_n = y_{n,1} - y_{n,2}\left(\theta_{n,1}/\theta_{n,2}\right) \quad \text{(II. 25)}$$

The entire procedure can be replicated to identify supplementary natural frequencies. The count of natural frequencies should correspond to the count of masses. Owing to the impact of inertial forces on the rotating beam, the beam's stiffness is effectively heightened. As a result, the natural frequencies of a rotating beam will exceed those of an analogous non-rotating beam.

II.1.5 Torsional Vibrational Systems

Numerous components within wind turbines, notably those in the drive train, can be represented through a series of interconnected disks linked by shafts. In these models, the disks are presumed to possess inertia but exhibit full rigidity, whereas the shafts possess stiffness but lack inertia. Holzer's method can be employed to ascertain the natural frequencies of such systems[104]. Analogous to the Myklestad method, sequence equations can be applied to calculate the angles and torques along the shaft. The intricacies of this approach extend beyond the scope of this thesis. For a more comprehensive understanding, readers are advised to consult reference [105] or related literature.

III. Complex receptance of a vibrational system

The equation governing the displacement x of a single-degree-of-freedom mass-spring-damper system under the influence of a force $f(t)$ is as follows:

$$m\ddot{x} + c\dot{x} + kx = f(t) \quad \text{(II. 26)}$$

Consider x_{Re}as the system's response to a force $f_{Re}(t) = Fcos(\omega t)$, and x_{Im} as the response to a force $f_{Im}(t) = Fsin(\omega t)$. Expressing this relationship, we have [106]:

$$m\ddot{x}_{Re} + c\dot{x}_{Re} + kx_{Re} = f_{Re}(t) = Fcos(\omega t) \quad \text{(II. 27)}$$

$$m\ddot{x}_{Im} + c\dot{x}_{Im} + kx_{Im} = f_{Im}(t) = Fsin(\omega t) \quad \text{(II. 28)}$$

By multiplying Equation (II. 28) with $i = \sqrt{-1}$ and subsequently adding it to Equation (II. 27), the utilization of Euler's formula facilitates us in expressing [106-108]:

$$m\ddot{\bar{x}} + c\dot{\bar{x}} + k\bar{x} = \bar{f}(t) = Fexp(i\omega t) = Fcos(\omega t) + iFsin(\omega t) \quad \text{(II. 29)}$$

In this context, the complex displacement is presented as $\bar{x} = x_{Re} + ix_{Im}$. Throughout this chapter, the symbol $\overline{(\,)}$ will be employed to denote a complex number.

One potential solution for Equation (II. 29) is $\bar{x}(t) = \bar{D}\exp(\omega t)$. Substituting this into the equation of motion yields:

$$\left(k - \omega^2 m + i\omega c\right)\bar{D}\exp(\omega t) = Fexp(i\omega t) \quad \text{(II. 30)}$$

The proportionality between the complex displacement $\bar{x}$ and the complex force $\bar{f}$ is referred to as the complex receptance. For a system featuring single-degree-of-freedom and viscous damping, it's expressed as:

$$\bar{\alpha}(\omega) = \frac{\bar{x}(\omega,t)}{\bar{f}(\omega,t)} = \frac{\bar{D}}{F} = \frac{1}{(k - \omega^2 m) + i(\omega c)} = \frac{1/k}{\left(1 - \mathscr{R}^2\right) + i\left(\frac{\omega c}{k}\right)} \quad \text{(II. 31)}$$

where $\mathscr{R} = \omega/\omega_n$ the ratio between the forced frequency and the natural frequency of vibration.

The solution to the complex equation of motion is:

$$\bar{x}(\omega,t) = \bar{\alpha}(\omega)\bar{f}(\omega,t) \quad \text{(II. 32)}$$

$$\bar{x}(\omega,t) = |\bar{\alpha}(\omega)|exp(i\Gamma)Fexp(i\omega t) \quad \text{(II. 33)}$$

$$\bar{x}(\omega,t) = |\bar{\alpha}(\omega)|Fcos(\omega t + \Gamma) + i|\bar{\alpha}(\omega)|Fsin(\omega t + \Gamma) \quad \text{(II. 34)}$$

The modulus $|\bar{\alpha}(\omega)|$ and the phase angle Γ can be evaluated according to [107, 108]:

$$|\bar{\alpha}(\omega)| = \frac{1}{[(k - m\omega^2)^2 + (c\omega)^2]^{1/2}} \quad \text{(II. 35)}$$

$$\Gamma = -\arctan_2\left(\frac{c\omega}{k - m\omega^2}\right) \quad \text{(II. 36)}$$

In a forced vibration system, the negative sign of Γ is attributed to the consistent phase lag between the response x and the force f.

As outlined by Craig and Kurdila[106], the selection between the actual or imaginary component of $\bar{x}$ hinges on the nature of the harmonic function adopted to depict the force influencing the mass. When $f(t) = Fcos(\omega t)$, the response x corresponds to the real segment of $\bar{x}$. Conversely, if $f(t) = Fsin(\omega t)$ is tantamount to the imaginary portion of x.

The receptance represented by Equation (II. 31) will prove beneficial for progressing towards deriving the components of the complex receptance matrix for a multi-degree-of-freedom system featuring proportional damping.

IV. Natural frequencies and modes of vibration

The finite element method allows for the determination of a structure's natural frequencies and vibration modes through the utilization of mass m and stiffness k matrices. A comprehensive elucidation of this approach can be found in Craig's work [109].

The equation of motion of a system without damping with N degrees of freedom is given by:

$$m\ddot{x} + kx = 0 \tag{II. 37}$$

A possible solution for Equation (II. 37) is:

$$x = \phi cos(\omega t + \Gamma) \tag{II. 38}$$

In Equation (II. 38), we put a positive sign in front of Γ in order to maintain compatibility with Equation (II. 36).

$$\left(k - m\omega^2\right)\phi = 0 \tag{II. 39}$$

To render Equation (II. 39) more recognizable, resembling expressions encountered in resources addressing linear algebra, such as the work by Anton & Rorres [110], it is advantageous to reformulate it as follows:

$$(m^{-1}k)\phi = \omega^2\phi \tag{II. 40}$$

To achieve solutions that are not trivial, it is imperative that:

$$det\left(m^{-1}k - \omega^2 I\right) = 0 \tag{II. 41}$$

where I is the identity matrix. The determinant in Equation (II. 41) is equivalent to a polynomial of degree N on the variable $\lambda = \omega^2$. The roots $\lambda_r = \omega_r^2$of this polynomial are the eigenvalues of the matrix $m^{-1}k$.

By substituting the eigenvalues $\lambda_r = \omega_r^2$ into Equation (II. 40), it becomes possible to derive the corresponding eigenvectors ϕ_r. It's important to note that an eigenvector signifies a parameterized solution, implying that any scalar multiple of an eigenvector also constitutes a solution [111]. Consequently, a suitable normalization is applied, such as ensuring the largest entry is equal to 1.

The r-th natural frequency of vibration is given by $\omega_r = \sqrt{\lambda_r}$ (in radians per second if the international system is adopted). This natural frequency is associated with the mode of vibration translated by the eigenvector ϕ_r. It is convenient to order natural frequencies in ascending order [106]:

$$0 \leq \omega_1 \leq \omega_2 \leq \cdots \leq \omega_r \leq \cdots \leq \omega_N \tag{II. 42}$$

The modal matrix gathers the modal vectors in the columns in increasing order of natural frequency:

$$\Phi = [\phi_1 \quad \phi_2 \quad \ldots \quad \phi_r \quad \ldots \quad \phi_N] \tag{II. 43}$$

V. Modal Superposition

The equation of motion for a multi-degree-of-freedom system with viscous damping under the influence of a loading $f(t)$ is:

$$m\ddot{x} + c\dot{x} + kx = f(t) \tag{II. 44}$$

The concept of modal superposition posits that the solution $x(t)$ can be expressed as a linear combination of vibration modes [106]:

$$x(t) = \sum_{r=1}^{N} \phi_r q_r(t) = \Phi q(t) \tag{II. 45}$$

$$x_j(t) = \sum_{r=1}^{N} \phi_{jr} q_r(t) \tag{II. 46}$$

The vector q encompasses the generalized coordinates q_r, which are alternatively referred to as principal coordinates. These coordinates are determined by Equation (II. 47):

$$M\ddot{q} + C\dot{q} + Kq = \Phi^T f(t) = p(t) \tag{II. 47}$$

where $p(t)$ represents the vector of generalized forces. The modal mass matrix M, the generalized damping matrix C, and the modal stiffness matrix K are defined by [106]:

$$M = \Phi^T m \Phi = \text{diag}(M_r) \tag{II. 48}$$

$$C = \Phi^T \text{c} \Phi \tag{II. 49}$$

$$K = \Phi^T \text{k} \Phi = \text{diag}(K_r) = \text{diag}(\omega_r^2 M_r) \tag{II. 50}$$

As shown by Craig [109], to prove that $K_r = \omega_r^2 M_r$, it suffices to multiply Equation (II. 39) by ϕ_r^T in order to obtain $\phi_r^T k \phi_r = \omega_r^2 (\phi_r^T m \phi_r)$.

The modal vectors are orthogonal compared to the matrices of mass and rigidity. That is, for two different natural frequencies ω_r and ω_s , Equations (II. 51) and (II. 52) hold [106]:

$$\phi_s^T m \phi_r = 0 \qquad (\text{If } \omega_r \neq \omega_s) \tag{II. 51}$$

$$\phi_s^T k \phi_r = 0 \qquad (\text{If } \omega_r \neq \omega_s) \tag{II. 52}$$

This implies that the modal mass M and modal stiffness K matrices defined by Equations (II. 48) and (II. 50) are diagonal.

In the particular scenario where C is diagonal, the differential equations established by Equation (II. 47) are uncoupled (i.e., $q_r$is independent of q_s if $r \neq s$) and can be represented as follows:

$$M_r\ddot{q}_r + C_r\dot{q}_r + K_r q_r = \Phi_r^T f(t) = p_r(t) \qquad (r = 1,2,\dots,N) \tag{II. 53}$$

The generalized damping ratio ξ_r makes it possible to quantify the damping corresponding to the vibration mode r. This ratio, which can vary between 0 and 1, is given by [109]:

$$\xi_r = \frac{C_r}{(C_{cr})_r} \tag{II. 54}$$

where C_r is the generalized damping coefficient. The generalized critical damping coefficient $(C_{cr})_r$ is given by:

$$(C_{cr})_r = 2M_r\omega_r = \frac{2K_r}{\omega_r} = 2\sqrt{M_r K_r} \tag{II. 55}$$

The natural frequency of vibration ω_r can be expressed in terms of the modal mass M_r and the modal stiffness K_r according to:

$$\omega_r = \sqrt{\frac{K_r}{M_r}} \tag{II. 56}$$

Considering Equations (II. 54), (II. 55) and (II. 56), Equation (II. 53) can be written in terms of the modal damping factor ξ_r, the modal mass M_r and the natural frequency of vibration ω_r [106]:

$$M_r\ddot{q}_r + 2\xi_r\omega_r M_r\dot{q}_r + {\omega_r}^2 M_r q_r = \Phi_r^T f(t) = p_r(t) \qquad (r = 1,2,\dots,N) \tag{II. 57}$$

As outlined in Adhikari [112, 113], if any of the conditions specified in Equation (II. 58) to (II. 60) are met, the generalized damping matrix C becomes diagonal. Consequently, the vibration modes of the damped system remain consistent with the vibration modes of the corresponding undamped system.

$$km^{-1}c = cm^{-1}k \tag{II. 58}$$

$$mk^{-1}c = ck^{-1}m \tag{II. 59}$$

$$mc^{-1}k = kc^{-1}m \tag{II. 60}$$

The first of the three conditions was proven by Caughey and O'Kelly[114]. It is the best known and can also be found in the work of Inman [115].

VI. Normalization of a vibration mode

Let $\breve{\phi}_r$ be the normalized mode vector and ϕ_r the unnormalized mode vector. It is convenient to normalize each mode vector such that Equation (II. 61) is satisfied [106, 111]:

$$\breve{\phi}_r^T m\breve{\phi}_r = \breve{M}_r \tag{II. 61}$$

where $\check{M}_r$ is a scalar quantity (having unit mass) suitably chosen to normalize the modal vector ϕ_r. By forcing the value $M_r = 1$ for $r = 1,2,\ldots,N$ (which is often the case), the modal vectors ϕ_r become a set of orthonormal vectors [106]. In this case, Equations (II. 62) and (II. 63) hold:

$$\check{\Phi}^T m \check{\Phi} = \mathrm{I} \qquad (\text{If } M_r = 1 \text{ for all } r) \tag{II. 62}$$

$$\check{\Phi}^T k \check{\Phi} = \Lambda \qquad (\text{If } M_r = 1 \text{ for all } r) \tag{II. 63}$$

where Λ is a diagonal matrix which includes the squares of the natural frequencies:

$$\Lambda = \mathrm{diag}\left(\omega_r^2\right) = \begin{bmatrix} \omega_1^2 & & & \\ & \omega_2^2 & & \\ & & \ddots & \\ & & & \omega_N^2 \end{bmatrix} \tag{II. 64}$$

We want to find the scalar coefficient $\check{c}$ defined by:

$$\check{\phi}_r = \check{c}\phi_r \tag{II. 65}$$

$$\check{\phi}_r{}^T = \check{c}\phi_r{}^T \tag{II. 66}$$

Replacing Equations (II. 65) and (II. 66) in Equation (II. 61) implies [107]:

$$\check{\phi}_r = \phi_r \left[\frac{\check{M}_r}{\phi_r{}^T m \phi_r}\right]^{1/2} = \phi_r \left[\frac{\check{M}_r}{M_r}\right]^{1/2} \tag{II. 67}$$

VII. Dynamics of Wind Turbine Rotors

Applied loads and dynamic interactions give rise to forces and movements within wind turbines, necessitating a comprehensive understanding during the design phase. It's crucial to assess the impact of diverse load types, including static, constant, periodic, transient, sudden, and stochastic forces. In this section, we explore two methods for analyzing wind turbine forces and motions. Firstly, we employ a simplistic ideal rigid rotor model to elucidate fundamental principles related to steady turbine loads. Subsequently, we develop a highly linearized dynamic model for a horizontal-axis wind turbine, which offers insights into how turbines respond to continuous and periodic loads.

VII.1 Loads on an Ideal Wind Turbine Blade

The primary rotor loads in a wind turbine involve blade thrust and rotor torque. To grasp a fundamental understanding of the constant loads affecting a wind turbine, it's valuable to model the rotor as a basic, aerodynamically ideal rigid rotor. As we discussed in Chapter 1, we can relatively easily calculate the primary aerodynamic loads acting on an ideal rotor that adheres to the Betz limit.

VII.1.1 Thrust loads

As depicted, the thrust, denoted as F_T, can be determined using the following equation:

$$F_T = \frac{1}{2} C_T \rho R^2 U^2 \quad \text{(II. 68)}$$

Where C_T represents the thrust coefficient, with ρ denoting air density, R representing rotor radius, and U signifying the free stream velocity.

In the ideal scenario, C_T equals 8/9. In accordance with this straightforward model, the total thrust generated by a specific rotor is directly proportional to the square of the wind speed.

VII.1.2 Stresses and Bending Moments analysis

Blade bending moments are typically categorized as either flapwise or edgewise. Flapwise bending moments result in the bending of blades either upwind or downwind. Edgewise moments align parallel to the rotor axis and are responsible for generating torque for power production. These moments are occasionally referred to as 'lead-lag.'

VII.1.2.1 Moments and Axial Forces

The flapwise bending moment occurring at the base of an ideal blade within a multi-blade turbine is determined by multiplying the thrust force per blade by two-thirds of the radius. This relationship can be illustrated as follows.

Imagine the rotor being divided into a sequence of concentric annular sections, each with a width represented as dr. The flapwise bending moment at the root of an individual blade, denoted as M_β, in a turbine equipped with B blades, can be expressed as follows:

$$M_\beta = \frac{1}{B} \int_0^R r \left(\frac{1}{2} \rho \pi \frac{8}{9} U^2 2r dr \right) \quad \text{(II. 69)}$$

After performing the integration and combining the relevant terms, the outcome is as follows:

$$M_\beta = \left(\frac{2}{3} R \right) \left(\frac{T}{B} \right) \quad \text{(II. 70)}$$

Equation (II. 71) provides the formula for calculating the maximum flapwise stress, denoted as $\sigma_{\beta,max}$, arising from bending at the root.

$$\sigma_{\beta,max} = M_\beta c / I_b \quad \text{(II. 71)}$$

Here, 'c' represents the distance measured from the neutral axis in the flapwise direction, and 'I_b' stands for the area moment of inertia of the blade's cross-section at the root.

The shear force, denoted as S_β, at the blade's root is essentially the result of dividing the thrust by the number of blades:

$$S_\beta = T/B \quad \text{(II. 72)}$$

VII.1.2.2 Moments and Edgewise Forces

In a broader context, torque can be expressed using a torque coefficient, $C_Q = C_p/\lambda$, (dividing the power coefficient by the tip speed ratio). Where:

$$Q = \frac{1}{2} C_Q \rho \pi R^2 U^2 \quad \text{(II. 73)}$$

In an ideal rotor system, the rotational speed adjusts in accordance with the wind speed, resulting in torque fluctuating in proportion to the square of the wind speed. Additionally, rotors engineered for operation at higher tip speed ratios exhibit lower torque coefficients, leading to reduced torque levels (although this doesn't necessarily imply lower stress levels). In line with this uncomplicated model, there is no torque variation based on blade azimuth.

VII.1.2.3 Edgewise Moment (Lead–Lag)

At the blade's root, the edgewise bending moment denoted as M_ζ is essentially the result of dividing the torque by the quantity of blades:

$$M_\zeta = Q/B \quad \text{(II. 74)}$$

There isn't an equivalently straightforward relationship for the edgewise shear force, S_ζ. However, it can be determined by integrating the tangential force, which is given by:

$$S_\zeta = \int_0^R dF_T \quad \text{(II. 75)}$$

VII.1.2.4 Loads on the blade and their sources

In this section, the term "load" pertains to forces or moments that can affect the turbine. Wind turbines are typically situated in regions with consistently strong winds. Consequently, wind loads are a primary consideration when assessing the structural performance and longevity of wind turbine blades. The loads experienced by a wind turbine during operation are intricate, characterized by a multitude of forces with varying frequencies and amplitudes, which can lead to potentially hazardous dynamic structural reactions.

In the process of designing and operating a wind turbine, it is essential to:

- Gain a comprehensive understanding of the loads acting on the turbine.
- Comprehend how the turbine responds to these loads.

Wind turbine loads can be categorized into five distinct groups, as outlined by Manwell et al[3]:

- ❖ Steady loads encompass forces originating from factors such as the average wind speed, centrifugal forces within the rotating blades, and the weight of the machine on the tower.
- ❖ Cyclic loads arise due to the rotor's rotation. The fundamental periodic load occurs at the blade roots (in the case of Horizontal Axis Wind Turbines, HAWTs), primarily due to gravity. Additional periodic loads stem from factors like wind shear, crosswind effects (yaw error), vertical wind, yaw velocity, and tower shadow. Mass or pitch imbalances can also introduce periodic loads.

- Stochastic loads emerge from turbulence or short-term fluctuations in wind speed, both temporally and spatially across the rotor. These fluctuations lead to rapidly changing aerodynamic forces on the blades, exhibiting seemingly random variations that can be described statistically.
- Transient loads occur occasionally and briefly, typically linked to events such as turbine start-up and shutdown. Other transient loads can result from sudden gusts of wind, shifts in wind direction, blade pitch movements, or teetering. It's worth noting that wind turbines are rarely installed in areas with frequent gusts.
- Resonance-induced loads arise when a portion of the structure is stimulated at one of its natural frequencies. Designers strive to avoid such occurrences, but turbulence-induced responses often inadvertently trigger resonant effects.

These load categories and their sources are summarized and depicted in Figure II. 14 and Figure II. 15 for further clarification.

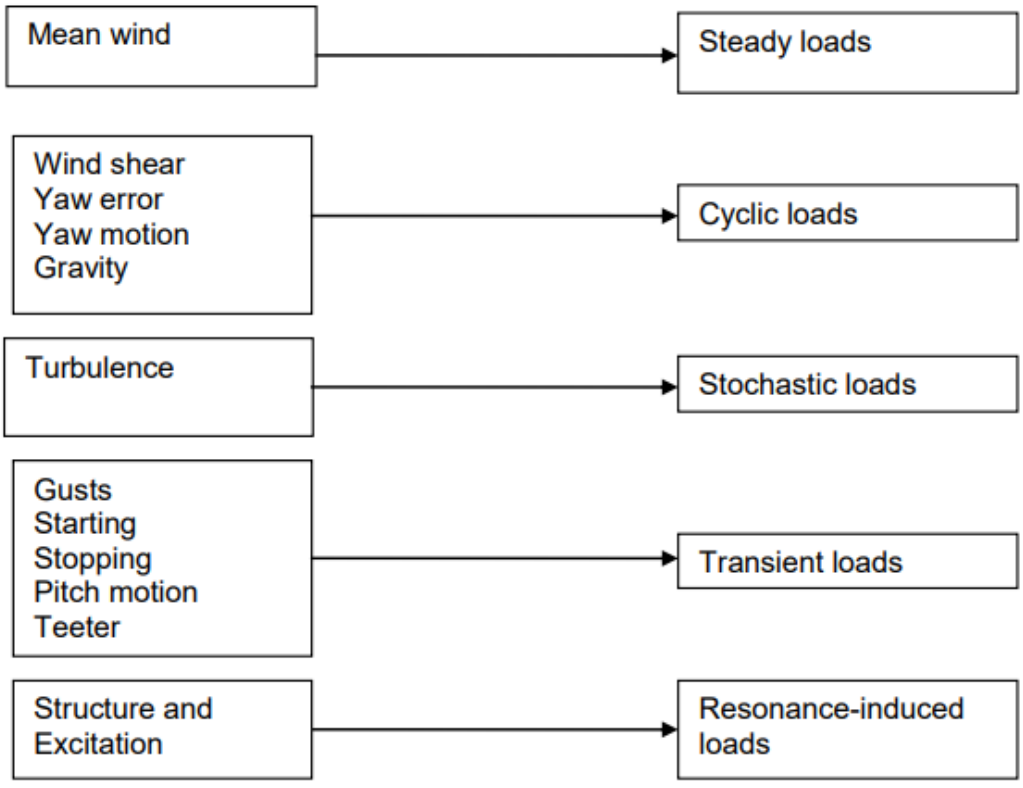

Figure II. 14 Origins of Wind Turbine Loads

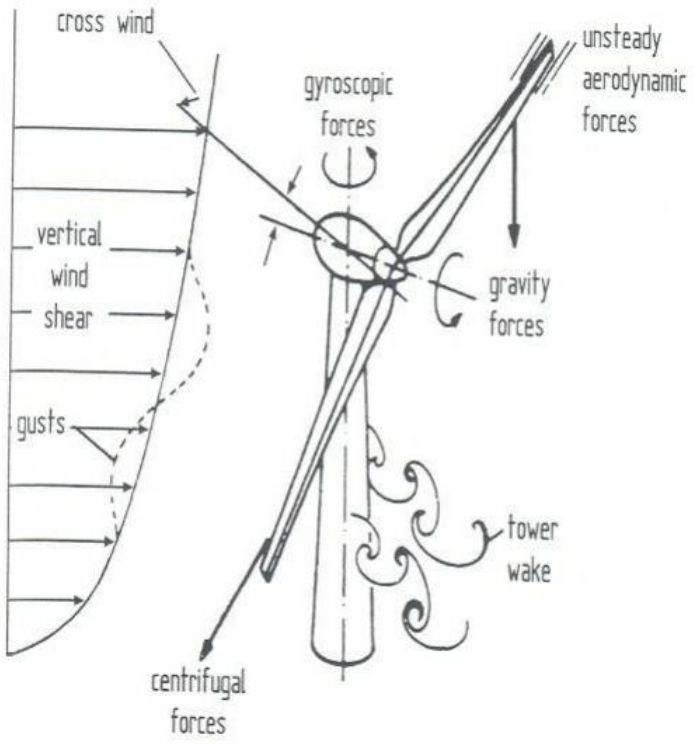

Figure II. 15 applied forces and the DOF of the vibrational a wind turbine

VIII. Conclusion

The study of wind turbine blade behavior places significant emphasis on vibration due to the blade's exposure to varying loads over time. In this chapter, we aim to elucidate and simplify concepts related to wind turbine blade vibration, beginning with single-degree-of-freedom vibration, progressing to multiple degrees of freedom, natural frequency and culminating in complex vibrations. We also delve into vibrations influenced by external forces and those mitigated by dampers, as these closely resemble the natural behavior and responses of the blade. Furthermore, the chapter includes an extensive exploration of the vibrations exhibited by cantilever beams, often referred to as Euler-Bernoulli beams, which bear a strong resemblance to the blade in terms of study characteristics. Lastly, we provide an overview of the various loads that impact blade dynamics and their effects on vibrational patterns.

CHAPTER III

FATIGUE OF WIND TURBINE BLADE

I. INTRODUCTIN

In the design of mechanical and structural components, two types of loads hold significant importance: extreme loads and fatigue loads. Extreme loads refer to loads that can result in structural failure by surpassing the material's yield strength. Thus, the objective of design is to minimize the probability of material exposure to such excessive loads. On the other hand, fatigue loads pertain to the weakening of a material's strength when subjected to cyclic stress patterns. This process often initiates at the surface of the material, where minor imperfections like scratches create stress concentrations. As cracks grow in size, stress concentrations also increase, causing further crack propagation. Eventually, this process leads to material rupture.

It's crucial to note that fatigue damage can occur even when applied loads are significantly below the material's elastic limit. This implies that not only are extreme load values important, but also the small-amplitude load history over time significantly impacts component reliability in terms of fatigue-induced damage. Hence, in this third chapter, our primary focus will be directed towards examining the fatigue of wind turbine blades. We aim to present these concepts in a simplified manner, ensuring that readers can readily grasp the intricacies surrounding the fatigue of materials in wind turbine blades.

Over time, the significance of fatigue in wind turbines has grown, owing to an improved comprehension of the underlying physics. The volume of publications in this domain has consistently risen over the years, as evident from data available on ScienceDirect[116]. Figure III. 1 visually depicts the growing interest in fatigue as it pertains to wind turbine challenges. Notably, the year 2009 marked a pivotal juncture, witnessing a substantial surge in the number of publications addressing fatigue in wind turbines.

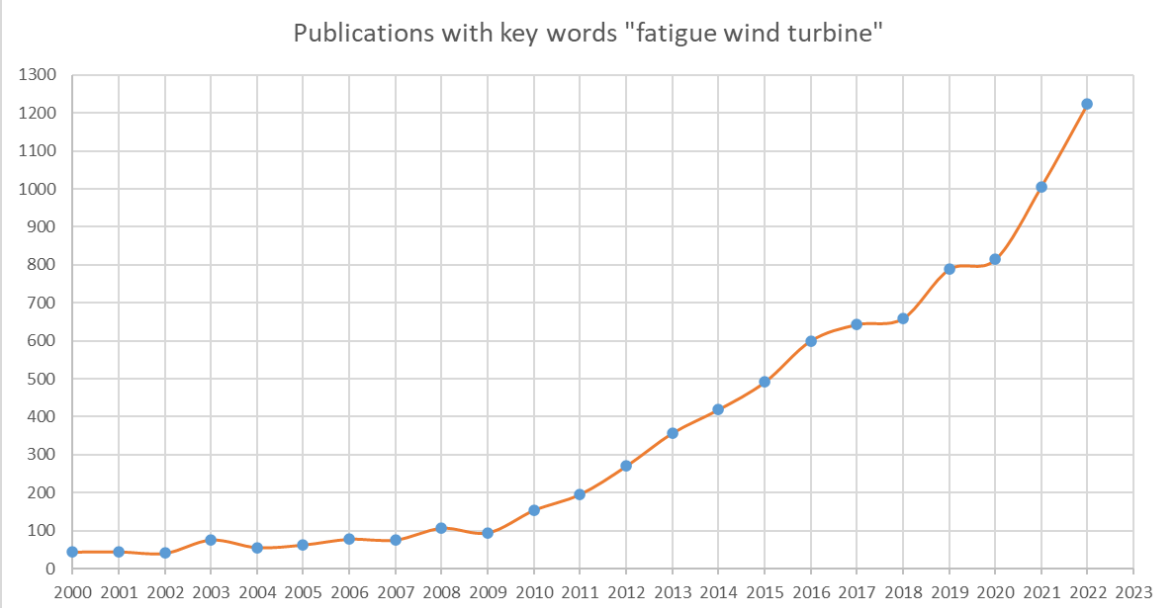

Figure III. 1 publications of the growing interest in the fatigue of wind turbines.

II. Description of a Loading Cycle

While the main goal of this chapter is to address variable amplitude fatigue analysis, certain concepts are better elucidated through the use of constant amplitude loading as an illustrative example (Figure III. 2). Take, for instance, a uniaxial loading pattern described by the equation:

$$\sigma(t) = \sigma_a \sin(\omega t) + \sigma_m \tag{III. 1}$$

The alternating component, σ_a, and the average component, σ_m, within a loading cycle can be represented in relation to the maximum stress, σ_{max}, and the minimum stress, σ_{min}, as follows:

$$\sigma_a = \frac{\Delta\sigma}{2} = \frac{\sigma_{max} - \sigma_{min}}{2} \tag{III. 2}$$

$$\sigma_m = \frac{\sigma_{max} + \sigma_{min}}{2} \tag{III. 3}$$

where $\Delta\sigma$ is the extent of the loading cycle. The load ratio R is defined by:

$$R = \frac{\sigma_{min}}{\sigma_{max}} \tag{III. 4}$$

Within a loading signal, each point corresponding to either σ_{min} or σ_{max} represents an inversion point where the derivative $d\sigma/dt$ equals zero. In cases where the loading exhibits variable and stochastic amplitudes, each loading cycle possesses a unique combination of σ_{min} and σ_{max} values, which are then employed to assess fatigue damage.

Imagine a specimen undergoing a uniaxial cyclic loading pattern (similar to Equation (III. 1)) where $\sigma_{min} < 0$ and $\sigma_{max} > 0$. In such a scenario, fatigue damage doesn't take place when the specimen experiences compressive loading[117]. Fatigue only ensues during moments when $d\sigma/dt > 0$ and $\sigma > 0$. In a theoretical examination of uniaxial fatigue, the negative portion of the stress signal needs to be excluded. Hence, if $\sigma_{min} < 0$, we should consider $\Delta\sigma = \sigma_{max}$, and $R = 0$.

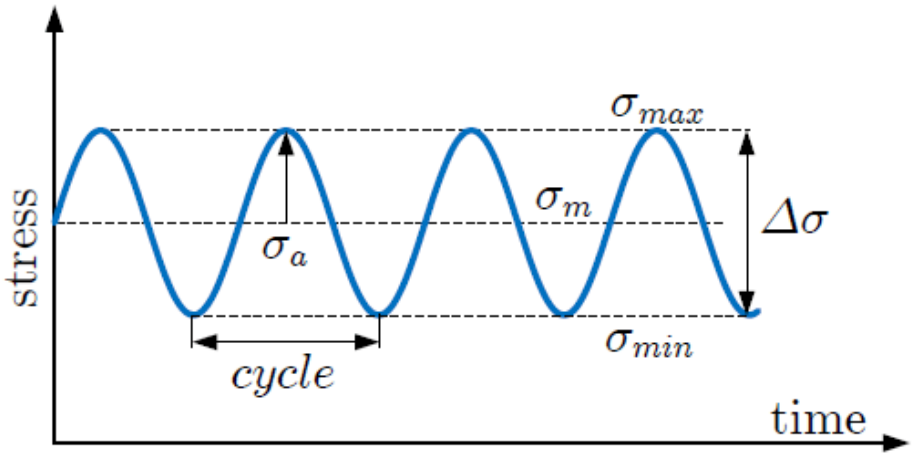

Figure III. 2 Stresses alternating with non-zero mean

III. Wöhler curves

The fatigue process of a material can be classified into two parts: crack initiation and crack propagation. This being so, we can write [118, 119]:

$$N_f = N_{in} + N_{pr} \quad \text{(III. 5)}$$

In this context, N_f represents the total count of loading cycles until the component experiences complete failure (with "f" denoting "failure"). N_{in} signifies the number of cycles needed for the initiation of a fatigue crack, while N_{pr} stands for the number of cycles necessary for the propagation of the crack until the component's ultimate failure.

The stress denoted as σ_f, often referred to as fatigue resistance, represents the magnitude of the alternating component σ_a in Equations (III. 1) and (III. 3) that corresponds to the number of cycles N_f required to induce the part's fatigue-induced failure.

As per Lee et al. [120], the initial investigations into material fatigue were conducted by August Wöhler between 1852 and 1870. In tribute to this German engineer, the graphs illustrating σ_f as a function of N_f are referred to as "Wöhler curves" in French-speaking regions. Conversely, in English-speaking nations, these curves are commonly known as "S-N curves".

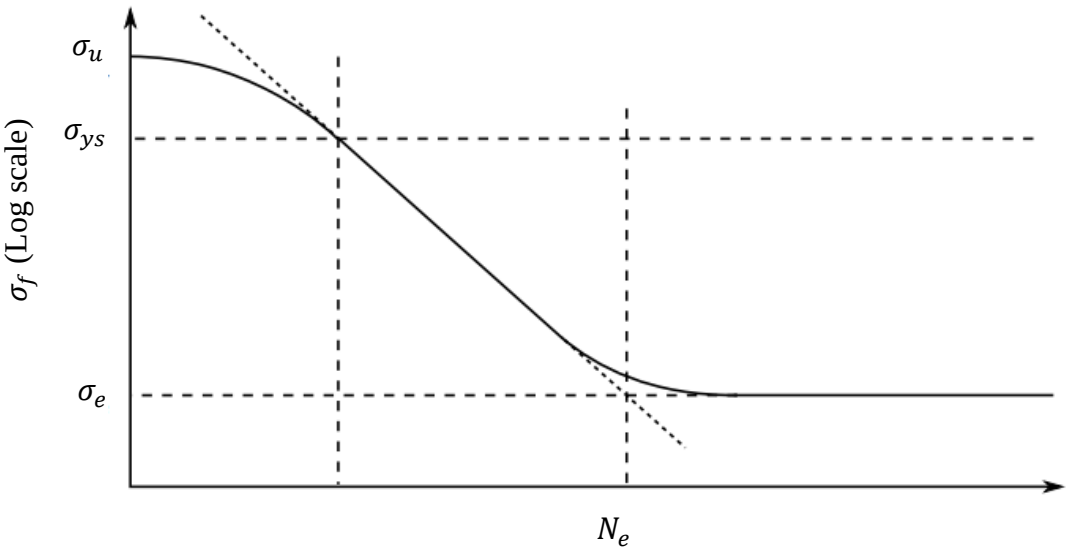

Figure III. 3 Typical behavior of the Wöhler curve of a steel, in log-log scale[121, 122]

The characteristic pattern of a steel's Wöhler curve is depicted in Figure III. 3. It's worth noting that this graph employs a bi-logarithmic scale.

When the alternating stress falls below the value of σ_e, it can be reasonably concluded that fatigue does not occur. In actuality, the rate of fatigue-induced damage significantly diminishes when σ_f becomes lower than σ_e. This threshold, defined as σ_e, is commonly referred to as the endurance limit.

According to Budynas and Nisbett [123] the endurance limit of a steel can be estimated as follows:

$$\sigma_e = \begin{cases} 0.5\sigma_u & \text{For } \sigma_u \leq 1400\,MPa \\ 700\,MPa & \text{For } \sigma_u \geq 1400\,MPa \end{cases} \quad \text{(III. 6)}$$

An endurance limit is not universally applicable to all materials. For instance, Wöhler curves for aluminum alloys don't exhibit a plateau. In such cases, it's common to designate σ_e as the stress σ_f corresponding to a specific number of cycles, such as 10^6 or 10^7. However, even with this definition of σ_e, material fatigue failure could still occur after subjecting it to 10^{10} loading cycles [124, 125]. This extremely high-cycle fatigue is commonly referred to as gigacycle fatigue.

Generally, fatigue tests are conducted until the specimen experiences complete failure rather than solely until the emergence of a visible crack[126]. In essence, this means that Wöhler curves typically feature N_f rather than N_{in} on the x-axis.

As outlined by Polák [127] and Grandt [128], a significant portion of the Wöhler curve can be accurately depicted using Basquin's law [129]:

$$\sigma_f = \sigma_f^{'}(2N_f)^b \quad \text{(III. 7)}$$

where: $\sigma_f^{'}$ represents the fatigue strength coefficient of the material. b signifies the fatigue strength exponent of the material, and $2N_f$ corresponds to the count of loading inversions required to result in material fatigue-induced fracture, where each inversion is characterized by $dS/dt = 0$.

Basquin's law can be expressed as follows [130]:

$$\log(N_f) = A - B\log(\sigma_f) \quad \text{(III. 8)}$$

where the fitting parameters A and B can be expressed in terms of $\sigma_f^{'}$ and b:

$$A = \frac{\log(\sigma_f^{'} 2^b)}{b} \quad \text{(III. 9)}$$

$$B = -1/b \quad \text{(III. 10)}$$

It is evident that Basquin's law was formulated to depict the linear segment of the Wöhler curve when presented on a bi-logarithmic scale. Various alternative models have been put forth to account for the curvatures observed in the curve illustrated in Figure III. 3. Notably, Stromeyer's law [131] is capable of describing the concave region, particularly when σ_f is proximate to σ_e:

$$\log(N_f) = A - B\log(\sigma_f - \sigma_e) \quad \text{(III. 11)}$$

In situations where there is insufficient experimental data to establish the horizontal asymptote of the curve in Figure III. 3, σ_e can be considered as a fitting parameter in Equation (III. 11), similar to coefficients A and B. When the endurance limit σ_e is evaluated in this manner, it can be described as the outcome of extrapolating experimental data.

The laws formulated by Palmgren [132], Weibull [133], and Stüssi [134] account for the curvature of the curve not only when σ_f is close to σ_e but also when σ_f approaches σ_u:

Palmgren law:

$$\log(N_f + C) = A - B\log(\sigma_f - \sigma_e) \quad \text{(III. 12)}$$

Weibull law:

$$\log(N_f + C) = A - B\log\left(\frac{\sigma_f - \sigma_e}{\sigma_u - \sigma_e}\right) \quad \text{(III. 13)}$$

Stüssi law:

$$\log(N_f) = A - B\log\left(\frac{\sigma_f - \sigma_e}{\sigma_u - \sigma_e}\right) \quad \text{(III. 14)}$$

The equations numbered (III. 8) to (III. 14) can be found in the work of Castillo[135].

In Equations (III. 13) and (III. 14), σ_u represents the tensile strength of the material, which is the maximum force applied during a tensile test divided by the nominal cross-sectional area of the specimen.

IV. Cycle counting rainflow method

Numerous methods exist for tallying fatigue cycles, including [136, 137]:

- Peak count method.
- Range-restricted peak count method.
- Level-restricted peak count method.
- Mean-crossing peak count method.
- Range method.
- Range-pair count method.
- Level crossing count method.
- PVP (peak valley pair) method.
- Hysteresis loop counting, introduced by Okamura and Sakai [138].
- Rainflow method.

IV.1 Rainflow counting method

The rainflow method for counting fatigue cycles was devised by Matsuishi and Endo [139]. According to Kondo [140], the rainflow method, being the one that best describes the physical mechanism of fatigue, represents the state of the art of cycle counting techniques.

Downing and Socie [141] introduced an algorithm for the rainflow method that employs three data points $(\sigma_i, \sigma_{i+1}, \sigma_{i+2})$ to establish two stress ranges$(\Delta\sigma_1, \Delta\sigma_2)$, which are compared at each iteration. This algorithm exclusively counts complete cycles. In contrast, certain algorithms, such as the one outlined in ASTM[142], permit the counting of half cycles. According to McInnes and Meehan [143], the three-point rainflow method is not suitable for real-time cycle counting as it necessitates access to the entire signal for rearrangement before counting. This rearrangement is carried out to ensure that the stress history commences either with the global maximum or minimum point [144].

IV.1.1 Original Definition

The rainflow method derives its name from an analogy to raindrops falling onto the edges of a pagoda roof, as depicted in
Figure III. **4** for a generic time, history. Initially, the stress or strain spectrum is reconfigured so that it begins and ends at the highest peak stress or strain value. This adjustment is made to avoid the inclusion of half-cycle counts. Subsequently, the time axis is rotated by 90 degrees, transforming the load history into a sequence of peaks and valleys resembling the structure of a pagoda roof. The roof's peaks are now aligned either on the right axis or the left. The falling process continues until it ceases due to one of the following reasons:

1. It encounters an opposing peak of greater magnitude than the one it originated from.
2. It intersects with a prior rainflow event. The drop might land on another roof and continue following the established rules. When the descent initiates from a valley, it persists until it halts for one of these two reasons:
3. The drop encounters a deeper valley compared to the one it began from.
4. Its descent intersects with the path of a drop descending from a preceding valley.

The drop has the option to descend onto another roof and follow the established rules, as illustrated in Figure III. 4. The rules outlined previously are depicted graphically in this figure. Initially, the original time history Figure III. 4-a has been reorganized to commence from the highest peak Figure III. 4-b. All peaks occurring prior to peak A have been relocated to the tail end of the fatigue spectrum. Subsequently, the time history has been rotated by 90 degrees, resulting in a load history represented as a sequence of roof-like structures, with peaks situated on the left side and valleys on the right Figure III. 4-c. The descent of the drop can initiate from either peaks or valleys, with the outcome being identical.

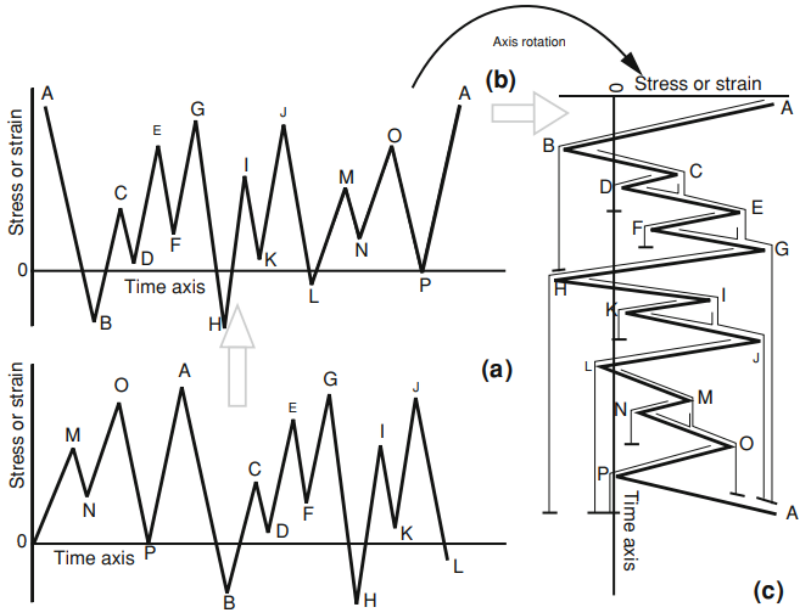

Figure III. 4 Illustration of the rainflow counting method[145]

IV.1.2 Practical Definition

A practical explanation of rainflow cycle counting is provided in ASTM E1049 - 85 "Standard Practices for Cycle Counting in Fatigue Analysis" [146]. According to this standard, rainflow cycle counting can be defined as follows:

- Consider X as the range in question, Y as the range immediately preceding X, and S as the initial point in the historical record.

1. Read the following peak or valley. If there's no more data, proceed to Step 6.
2. If there are fewer than three data points, return to Step 1. Create ranges X and Y using the three most recent peaks and valleys that haven't been discarded.
3. Compare the absolute values of ranges X and Y.
   a. If X is less than Y, return to Step 1.
   b. If X is greater than or equal to Y, go to Step 4.
4. Check if range Y contains the starting point S. If it does, proceed to Step 5. Otherwise, count range Y as one cycle, remove the peak and valley of Y, and go back to Step 2.
5. Count range Y as one-half cycle, remove the first data point (peak or valley) in range Y, move the starting point to the second data point in range Y, and return to Step 2.
6. Count each range that hasn't been counted previously as one-half cycle.

Figure III. 5 illustrates an example of the cycle described earlier. Table III. 1 provides a summary of the counted cycles, while Table III. 2 presents the outcomes of a range-mean matrix.

Table III. 1 summary of the counted cycles[146]

Range (units)	Cycle Counts	Events
10	0	-
9	0.5	D-G
8	1	C-D, D-H
7	0	-
6	0.5	H-I
5	0	-
4	1.5	B-C, E-F
3	0.5	A-B
2	0	-
1	0	-

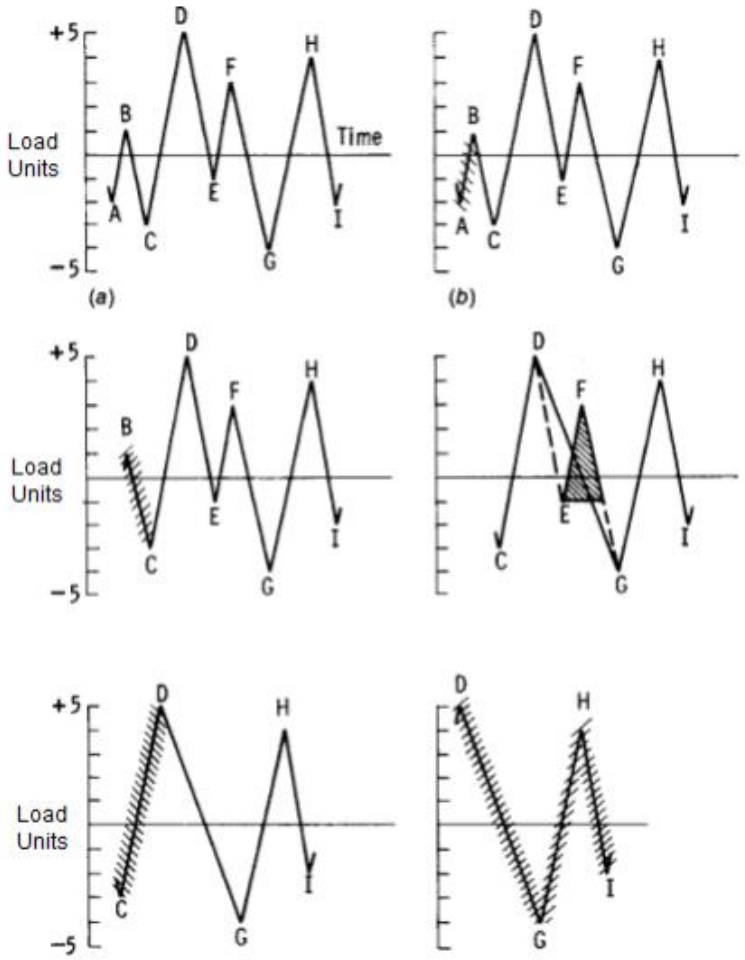

Figure III. 5 illustrates an example of the cycle described earlier[146]

Table III. 2 the results of a range-mean matrix [146]

Range (units)	Mean (units)								
	-2	-1.5	-1	-0.5	0	+0.5	+1	+1.5	+2
10	-	-	-	-	-	-	-	-	-
9	-	-	-	-	-	0.5	-	-	-
8	-	-	-	-	0.5	-	0.5	-	-
7	-	-	-	-	-	-	-	-	-
6	-	-	-	-	-	-	0 - 5	-	-
5	-	-	-	-	-	-	-	-	-
4	-	-	0.5	-	-	-	1	-	-
3	-	-	-	0.5	-	-	-	-	-
2	-	-	-	-	-	-	-	-	-
1	-	-	-	-	-	-	-	-	-

V. Constant Life Diagrams (Influence of Mean Stress)

The reliance on S-N curves on mean stress suggests that it would be imperative to experimentally establish the corresponding S-N curve for each mean stress value, as illustrated in Figure III. 6. However, this approach is highly labor-intensive, costly, and impractical, making it an unfeasible option. Therefore, in the nineteenth century, several methodologies were devised to account for the influence of mean stress.

As demonstrated in references [147-149], numerous constant life diagrams were introduced throughout the 20th century. These diagrams enable the utilization of the Wöhler curve while considering the impact of mean loading stress.

The Goodman diagram [150] can be characterized by the following equation:

$$\frac{\sigma_a}{\sigma_f} + \frac{\sigma_m}{\sigma_u} = 1 \tag{III. 15}$$

Where σ_f represents the fatigue strength provided by the Wöhler curve.

The Gerber equation [151] is given by:

$$\frac{\sigma_a}{\sigma_f} + \left(\frac{\sigma_m}{\sigma_u}\right)^2 = 1 \tag{III. 16}$$

The Soderberg equation [152] is founded on the material's yield strength σ_{ys}:

$$\frac{\sigma_a}{\sigma_f} + \frac{\sigma_m}{\sigma_{ys}} = 1 \tag{III. 17}$$

The ASME-elliptical diagram is derived according to [123]:

$$\left(\frac{\sigma_a}{\sigma_f}\right)^2 + \left(\frac{\sigma_m}{\sigma_{ys}}\right)^2 = 1 \tag{III. 18}$$

The Morrow equation [153] relies on σ_v, the actual material's ultimate tensile strength:

$$\frac{\sigma_a}{\sigma_f} + \frac{\sigma_m}{\sigma_v} = 1 \tag{III. 19}$$

σ_v takes into consideration the necking (reduction in cross-sectional area) of the test specimen undergoing a tensile test. It is the value of the tensile force at the point of rupture divided by the cross-sectional area in the necking region. Given that $\sigma_v > \sigma_u$, the Morrow diagram predicts a longer fatigue life compared to the Goodman diagram.

The Walker diagram [154] is characterized by:

$$\sigma_f = {\sigma_{max}}^{1-m} {\sigma_a}^m \tag{III. 20}$$

$$\sigma_f = \sigma_{max}\left(\frac{1-R}{2}\right)^m \quad \text{(III. 21)}$$

$$\sigma_f = \sigma_a\left(\frac{2}{1-R}\right)^{1-m} \quad \text{(III. 22)}$$

Where m is an empirical parameter dependent on material and is referred to as the Walker exponent. This parameter is also present in chapter 4, describing the fatigue crack growth rate. Equation (III. 22) can be located in Dowling's work [155], which provides a method for assessing m from fatigue tests.

Ultimately, the simplified analytical expression that defines the fatigue limit, σ_f, in the presence of a mean stress, σ_m, is provided as follows:

$$\sigma_f = \sigma_e\left[1-\left(\frac{\sigma_m}{\sigma_u}\right)^n\right] \quad \text{(III. 23)}$$

where $n = 2$ for the Gerber parabola, $n = 1$ for the Goodman line, and σ_u represents the material's ultimate tensile strength. Figure III. 7 illustrates the Goodman, Gerber, and Soderberg curves, from which the following general observations can be drawn:

- The Soderberg approach is notably conservative and less commonly employed.
- Empirical test data typically fall within the range delimited by the Goodman and Gerber curves.
- According to Gerber's model, the correlation between σ_f and σ_m ranges from zero to the ultimate strength σ_u.
- The Goodman model posits a linear association between σ_m and σ_f.

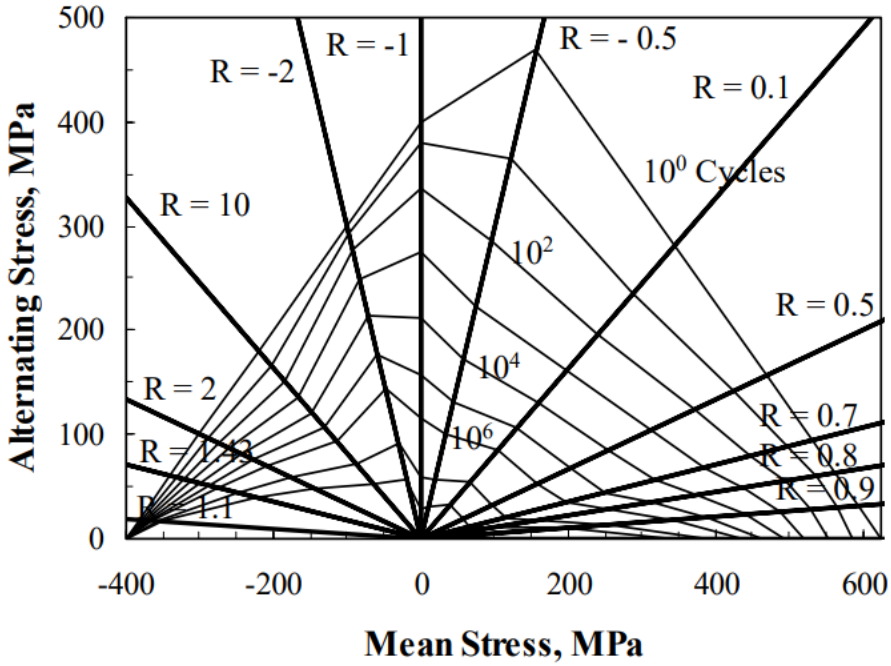

Figure III. 6 Mean Goodman Diagram for DD16 Material.[156]

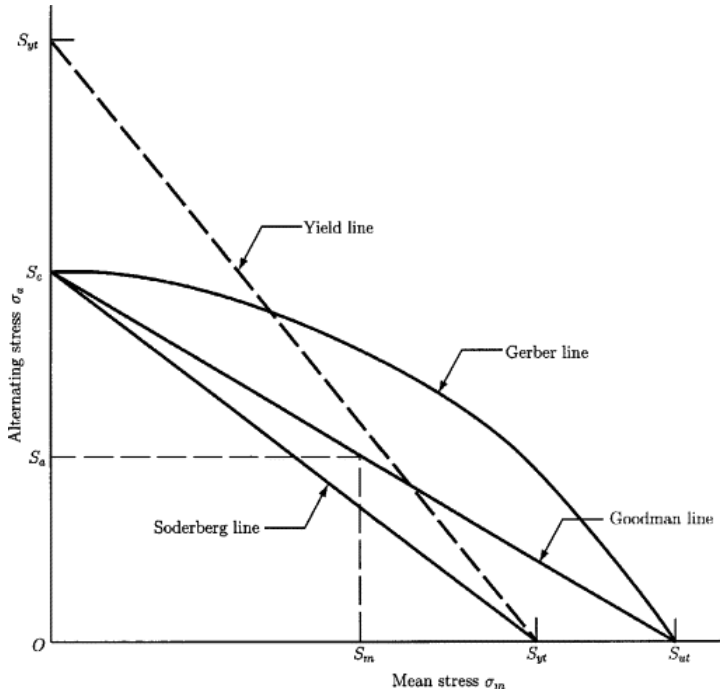

Figure III. 7 Comparison of constant life diagrams.[157]

VI. Damage Accumulation Rules

As a result of cyclic loading, fatigue damage accumulates progressively. This phenomenon has been a subject of study over the years. The earliest and most basic theory was proposed by Palmgren in 1924 [158], during his investigation into the lifespan of ball bearings, where he assumed linear damage accumulation [159]. Since then, research into cumulative damage rules has expanded significantly, leading to the publication of numerous theories and research papers on the topic.

Prior to the 1970s, damage models were predominantly phenomenological in nature. However, post-1970s, damage rules started to transition towards semi-analytical or analytical approaches. The phenomenological damage theories aimed to enhance the linear damage rule and were grounded in three key concepts: linear summation, alterations in endurance, and two-stage crack growth [160].

VI.1 Miner's Rule

As previously mentioned, Palmgren was the pioneer in 1924 to introduce the concept of linear summation of fatigue damage. Langer, in 1937, working in the electricity generation field, put forth a similar linear rule applicable to pressure vessels and steel piping components. Just a few years later, in 1945, Miner, while employed at Douglas Aircraft, applied a linear rule and demonstrated a remarkable consistency between predictions derived from this linear rule and actual experimental results. This is why it is often referred to as Miner's rule or Palmgren-Miner's rule of linear damage and accumulation. According to this rule, a component subjected to a stress level σ_1 has a lifespan of N_1 cycles. The damage accrued after n_1 cycles correspond to n_i/N_i, as depicted in Figure III. 8. This fraction n_1 represents a portion of the total damage D_{cr}. The same principle applies to stress σ_2. In this case, the lifespan is denoted as N_2, and the damage incurred after n_2 cycles is given by n_2/N_2. Figure III. 9 illustrates the damage fraction attributed to each cycle n_1 and n_2.

Fatigue failure ensues when the cumulative damage generated by multiple cycles of fatigue loading reaches a critical damage threshold.

$$D_{total} = \sum D_i = \sum \frac{n_i}{N_i} \leq D_{cr} \quad \text{(III. 24)}$$

In the context of multi-level fatigue loading,

$$\frac{n_1}{N_1} + \frac{n_2}{N_2} + \frac{n_3}{N_3} + \frac{n_4}{N_4} + \cdots = \sum \frac{n_i}{N_i} = 1 \quad \text{(III. 25)}$$

Mathematically, Miner's rule is expressed as:

$$\sum \frac{n_i}{N_i} = 1 \quad \text{(III. 26)}$$

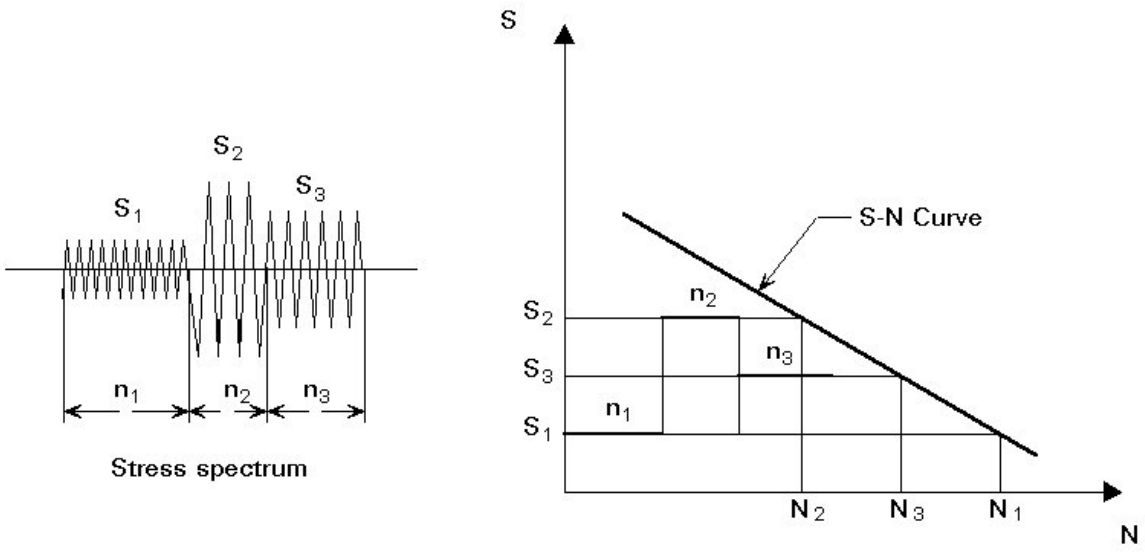

Figure III. 8 Schematic represents the S-N curve and the cumulative damage. [145]

This law presents significant drawbacks, including the following:

- It assumes that equal cycle ratios (n_i/N_i) result in equivalent damage, without accounting for stress amplitude variations.
- It implies load-sequence independence, meaning that regardless of the order in which two or more loads are applied, the damage will always be the same. This assumption doesn't hold true in reality. For instance, if cycles with low-stress amplitude loads are occasionally applied, they may not be sufficient to initiate damage. However, if a pre-existing crack is present, these cycles with low-stress amplitude loads could be adequate to propagate the damage within the component.

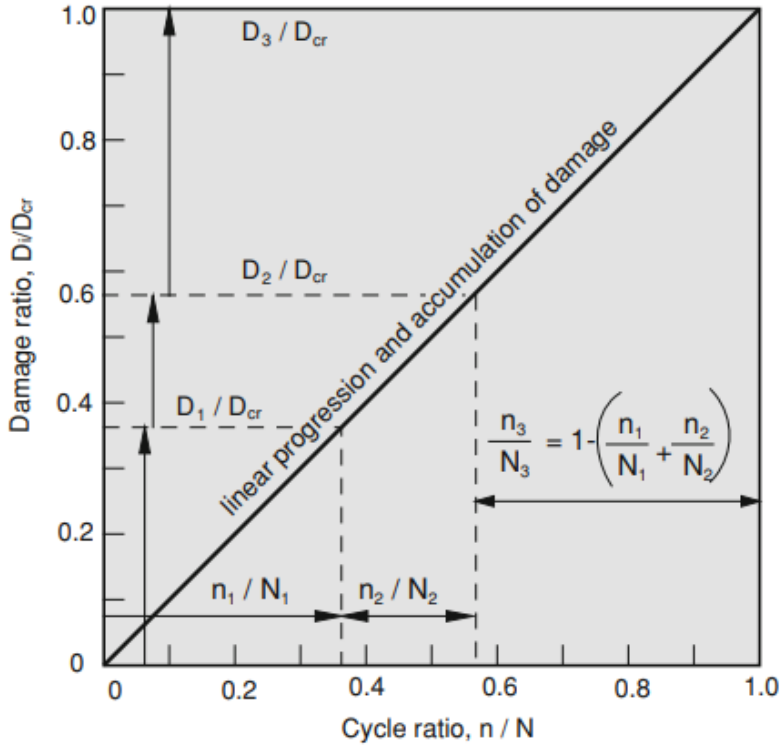

Figure III. 9 Linear progression and accumulation of damage in accordance with the Miner rule. [145]

VI.2 Nonlinear Damage and Accumulation

Because of the limitations of Miner's rule as discussed in the preceding section, there is a necessity to enhance damage rules by incorporating a dependency of the form,

$$\frac{D}{D_{cr}} \propto \left(\frac{n_i}{N_i}\right)^{m_i} \qquad \text{(III. 27)}$$

In this equation, the exponent "m" varies based on the stress amplitude σ_i. High cycle fatigue is characterized by elevated "m" values, which progressively decrease towards unity as stress levels increase. It's important to note that Miner's rule represents a specific instance of equation (III. 27) when m equals 1. This relationship takes into account the stress level, as illustrated in Figure III. 10, where loads with higher amplitudes induce greater damage at equal cycle ratios (n_i/N_i). Numerous studies have been conducted to achieve a reduced dependence of the form expressed in equation (III. 27).

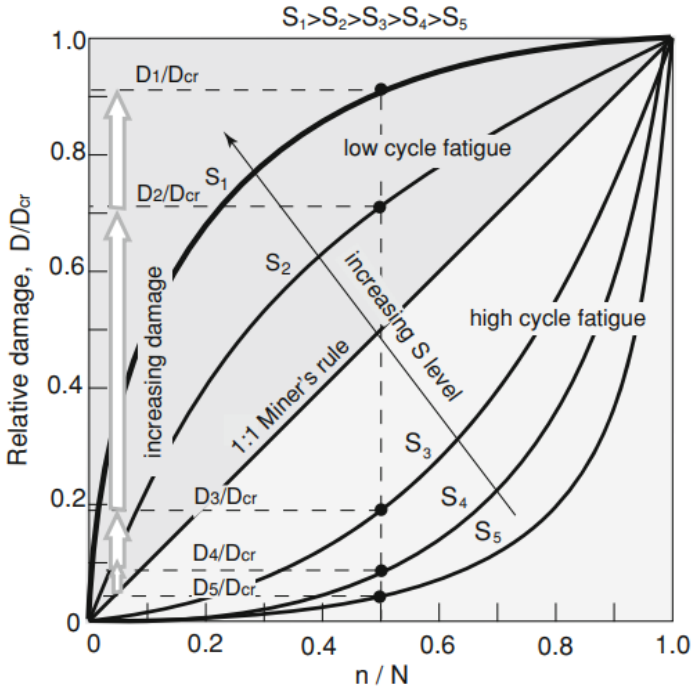

Figure III. 10 Power-law dependence of damage progression and accumulation for various load amplitudes. [145]

VII. Materials for Wind Turbines

Various materials find application in wind turbines, as outlined in Table III. 3. Among these, two stand out prominently: steel and composites. Composite materials commonly consist of fiberglass, carbon fibers, or wood combined with a matrix of either polyester or epoxy. Additionally, materials like copper and concrete are frequently utilized. Below, we present a summary of key material aspects that hold particular significance in wind turbine applications.

Table III. 3 Materials employed in wind turbines

Subsystem or Component Parts	Category of Materials	Subcategory of Materials
Blades	Composites	glass fibers, carbon fibers, laminated wood, polyester resins, and epoxies
Hub	Steel	
Gearbox	Steel	Various alloys, lubricants
Nacelle cover	Composites	Fiberglass
Tower	Steel	
Foundation	Steel, concrete	

VII.1 Fundamental Mechanical Characteristics of Materials

In this text, it is assumed that the reader has a familiarity with the fundamental concepts of material properties, as well as with the most common materials themselves. The following is a list of some of the essential concepts [161]:

- Hooke's Law;
- modulus of elasticity;
- yield strength, breaking strength;
- ductility and brittleness;
- hardness and machinability;
- failure by yielding or fracture.

Fatigue was discussed in the previous section. It should be noted, however, that fatigue properties differ significantly from one material to another.

VII.1.1 Steel material

Steel is a versatile and widely used material in various industries, including wind turbine construction (for example: the tower, hub, main frame, shafts, gears and gear cases). It possesses several favorable properties that make it suitable for wind turbine components. Steel's high strength-to-weight ratio, durability, and excellent fatigue resistance are particularly advantageous in the demanding conditions that wind turbines operate under. Different grades and types of steel are chosen based on specific requirements, ensuring optimal performance and longevity of wind turbine structures. For detailed information regarding steel properties, you can refer to [161, 162].

VII.1.2 Composites material

This text delves into composites in greater depth than many other materials because it assumes that composites may be less familiar to some readers compared to more conventional materials. Furthermore, composites serve as the primary material in blade construction. Composites refer to materials composed of at least two dissimilar components, most commonly fibers held in place by a binding matrix. Thoughtful selection of these fibers and binders enables customization of the composite's properties to suit the intended application. Wind turbine applications commonly employ composites based on materials like fiberglass, carbon fiber, and wood, with binders such as polyester, epoxy, and vinyl ester. The most prevalent composite used is fiberglass reinforced plastic, often referred to as GFRP[163]. In wind turbines, composites play a prominent role in blade manufacturing, but they also find utility in other components like the nacelle cover. The primary advantages of composites include their ability to (1) be easily fashioned into desired aerodynamic shapes, (2) offer high strength, and (3) possess a high stiffness-to-weight ratio. Additionally, composites exhibit resistance to corrosion, serve as electrical insulators, withstand environmental degradation, and are adaptable to various fabrication methods.

VII.1.2.1 Glass Fiber in Wind Turbine Blade Manufacturing

Glass fibers are produced through the process of spinning glass into lengthy threads. One of the most prevalent types of glass fiber is E-glass, which is composed of calcium aluminosilicate glass. E-glass is known for being an economical material while still possessing respectable tensile strength. Another

frequently used glass fiber is S-glass, which is calcium-free aluminosilicate glass. It boasts approximately 25-30% higher tensile strength compared to E-glass, but it comes with a significantly higher price tag (more than double). Additionally, Owens-Corning offers a glass fiber called HiPER-tex, which claims to offer the strength of S-glass at a cost closer to that of E-glass.

Fibers are occasionally utilized in their natural state, but more frequently, they are initially incorporated into alternative configurations, commonly referred to as 'preforms.' These fibers can be woven or knitted into cloth, shaped into continuous strands, or transformed into chopped strand mats. They can also be prepared as chopped fibers. In cases demanding exceptional strength, unidirectional bundles of fibers, referred to as 'tows,' are employed. Figure III. 11 provides visual representations of various fiberglass configurations[164, 165].

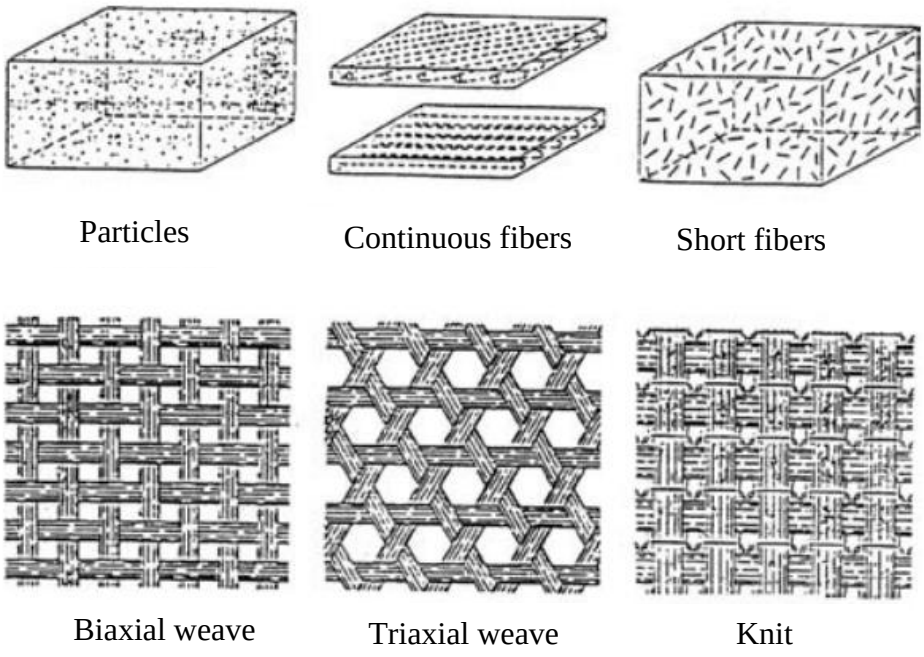

Figure III. 11 preforms of composite material Fiberglass[166]

VII.1.2.2 Binder material (Matrix)

There are three primary types of resins commonly employed as matrices in composites: (1) unsaturated polyesters, (2) epoxies, and (3) vinyl esters. These resins share the common characteristic of being in a liquid state during the composite's fabrication but solidify upon curing. When solidified, all these resins tend to possess a degree of brittleness, and the choice of resin significantly influences the composite's overall properties.

Polyesters have been the preferred choice in the wind industry due to their rapid curing time and cost-effectiveness. The curing process typically takes a few hours to overnight at room temperature, but the addition of an initiator enables curing within a few minutes at elevated temperatures. However, polyesters exhibit relatively high shrinkage upon curing. As of 2023, their cost ranged around $1.45/kg (approximately **198,54 DA/kg**).

Epoxies offer superior strength, excellent chemical resistance, strong adhesion, and minimal shrinkage during curing. However, they are more expensive (approximately 50% more expensive than polyesters) and have a longer curing time compared to polyesters.

Vinyl esters are epoxy-based resins that have gained popularity in recent years. They share similar properties with epoxies but come at a somewhat lower cost and have a shorter curing time. They also demonstrate good environmental stability and are widely utilized in marine applications.

VII.1.2.3 Carbon fiber reinforcement (CFR)

Carbon fibers are costlier than glass fibers, roughly eight times more expensive, yet they offer superior strength and stiffness. An economical approach to leverage the benefits of carbon fibers is to incorporate a blend of carbon and glass fibers within the composite structure.

VII.1.2.4 Wood–Epoxy materials Laminates

Wood is sometimes used in place of synthetic fibers in certain composites. Instead of using fibers, wood is preformed into sheets, known as laminates, for these composites. Douglas Fir is a commonly used type of wood for laminates in wind turbine applications. Wood properties can vary considerably depending on the direction of its grain. However, in general, wood offers a good balance between strength and weight and is resilient against fatigue.

Wood's tensile strength significantly depends on the direction of its grain, meaning that laminates must be constructed with grain oriented in different directions to ensure the composite's overall strength in all directions. For more detailed information about wood properties, you can refer to Hoadley's work[167].

The utilization of wood alongside an epoxy binder was adapted for wind turbine applications, drawing from prior expertise in high-performance boat construction. A method called the wood-epoxy saturation technique (WEST) is employed in this process. Wood-epoxy laminates exhibit favorable fatigue characteristics, and as per the National Research Council (NRC), there have been no instances of wood-epoxy blades failing in service due to fatigue[166].

VII.2 Fatigue Damage in composite materials

In contemporary times, composites have become the prevailing choice for constructing wind turbine blades. These composites exhibit heterogeneity, leading to distinct behavior when compared to homogeneous materials. Composite materials are essentially amalgamations of different substances. Typically, they feature a primary material, such as fibers, providing strength, while another material primarily serves as a filler. Given this intricate composition, the fatigue strength of a composite material is contingent upon:

- The composition of the fiber material.
- The proportion of fiber material to polymer resin.
- The alignment of the fibers.
- The choice of resin.
- The existence of wrinkles, misalignments, and porosities.
- The material's susceptibility to moisture.
- The thermal processing applied to the material

Composite materials can experience failure not only under tension but also under compression, making fatigue strength largely independent of mean stress levels. Unidirectional composites exhibit excellent fatigue resistance in multiple directions, primarily due to the robust endurance of their fibers. These composites are susceptible to two distinct damage mechanisms. In cases of high-stress loads, the damage initiates with the individual tearing of some fibers, creating a stress concentration zone that promotes the rupture of neighboring fibers, ultimately leading to component failure. Conversely, when subjected to low-stress loads, the stress on the fibers remains below their resistance threshold. However, the deformation of the matrix can surpass its fatigue limit, initiating damage with the rupture of the matrix itself, which can occur after approximately 10^6 fatigue cycles. For intermediate loads, the damage mechanism is a combination of the two previously described scenarios[168].

Multidirectional composites exhibit reduced fatigue resistance when subjected to loads along the fiber direction. In such cases, the damage behavior can be delineated into three distinct phases:

1. During this initial phase, a substantial decline in stiffness is observed. Damage commences within the layers that exhibit the highest degree of disorientation relative to the applied load. Typically, this phase involves the decohesion of the fiber/matrix interface due to the formation of microcracks, which, through coalescence, ultimately results in matrix rupture.
2. Following the initiation of the crack, it propagates parallel to the fibers and extends throughout the entire thickness of the layer.
3. As the cracks reach interfaces between layers oriented differently, delamination occurs. Rapid propagation leads to the separation of the laminate into isolated layers, which in turn promotes the rupture of the fibers within the layers aligned with the applied load, ultimately resulting in the component's final failure.

VIII. Computational Tool for Wind Turbine Aeroelastic Analysis: FAST

In the realm of wind energy technology development, the utilization of dependable and precise computational tools is imperative. Throughout this thesis, we employ software known as FAST to construct an aeroservoelastic wind turbine model. FAST, an acronym for Fatigue, Aerodynamics, Structures, and Turbulence [169], is the software of choice for simulating horizontal axis wind turbines. It was crafted by the United States National Renewable Energy Laboratory (NREL) and is adaptable for modeling both onshore and offshore wind turbines. This open-source software is coded in Fortran v90 and holds certification from Germanischer Lloyd WindEnergie for calculating wind turbine loads essential for design and certification [170].

FAST seamlessly integrates modal and multi-body dynamics methodologies. It conducts fully coupled simulations that encompass structural dynamics, aerodynamics, hydrodynamics, and control system dynamics, all executed within the time domain. To perform these simulations, diverse callable submodules of FAST are employed and integrated within the primary FAST code. The input and source files for these submodules are generated separately.

Figure III. 12 provides a schematic representation of the global coordinate axes, which are applicable not only to FAST but also to the majority of software employed in wind turbine technology [171]. The primary wind flow occurs in the positive X direction. In the literature, the pitch and surge motion of the wind

turbine system is commonly denoted as fore-aft motion, whereas roll and sway motion are referred to as side-side motion. Additionally, the torsional movement of the tower is termed yaw motion.

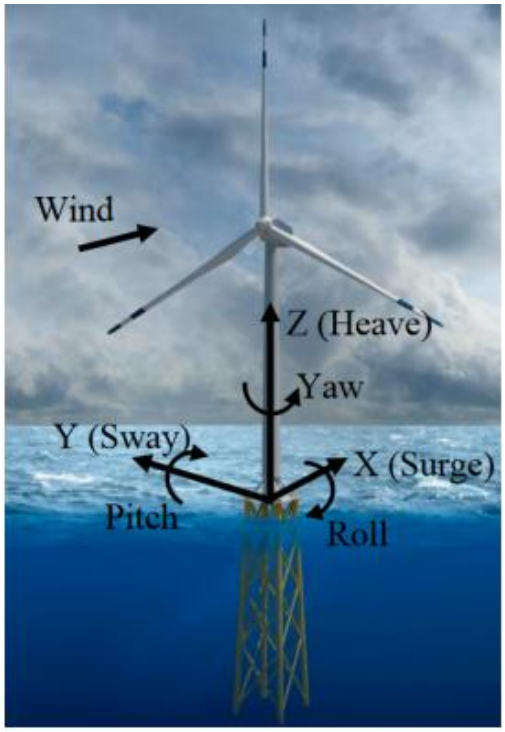

Figure III. 12 Coordinate axes on a global scale in FAST.[172]

To make use of wind turbine dynamics in FAST, a total of 24 degrees of freedom (DOFs) are needed, as depicted in Figure III. 13.

- 6 DOF: Representing 3 translational and 3 rotational movements of the platforms relative to the inertia frame, encompassing surge, sway, heave, roll, pitch, and yaw.
- 4 DOF: Signifying the tower's motion, including 2 longitudinal modes (fore-aft) and 2 lateral modes (side-side).
- 1 DOF: Corresponding to the yawing motion of the nacelle.
- 1 DOF: Pertaining to the generator's azimuth angle.
- 1 DOF: Reflecting compliance in the drivetrain, specifically between the generator and the hub/rotor.
- 3 DOF: Describing flapwise tip motion for the first mode.
- 3 DOF: Detailing tip displacement for each blade in the second mode.
- 3 DOF: Indicating edgewise tip displacement for the first mode.
- 2 DOF: Encompassing rotor and tail furl motions.

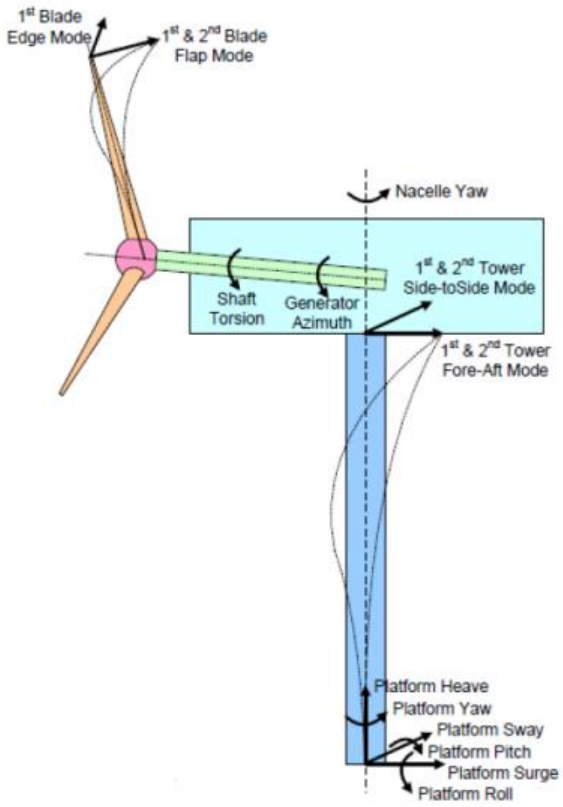

Figure III. 13 The wind turbine DOFs in the FAST tools model [173]

The connections between the tower and the ground, as well as between the blades and the hub, remain fixed and unyielding. Conversely, the tower, blades, and drive shaft possess flexibility.

VIII.1 Modularization Framework of FAST

FAST comprises a repository of diverse submodules essential for conducting comprehensive wind turbine analyses. The primary modules within FAST encompass:

- ElastoDyn: Responsible for modeling the elastic properties of the tower and blades, along with handling structural dynamics.
- SubDyn: Focused on modeling the structural dynamics of fixed-bottom substructures with multiple members.
- ServoDyn: Manages power generation and control system aspects.
- InflowWind: Deals with modeling wind conditions.
- HydroDyn: Addresses wave-induced loads.
- AeroDyn: Handles aerodynamic loads.

Furthermore, external modules are utilized to facilitate inputs for these submodules. For instance, Turbsim functions as a stochastic turbulence generator that supplies data to Inflow Wind. A visual representation of the input-output relationships between these submodules and their respective purposes is depicted in Figure III. 14.

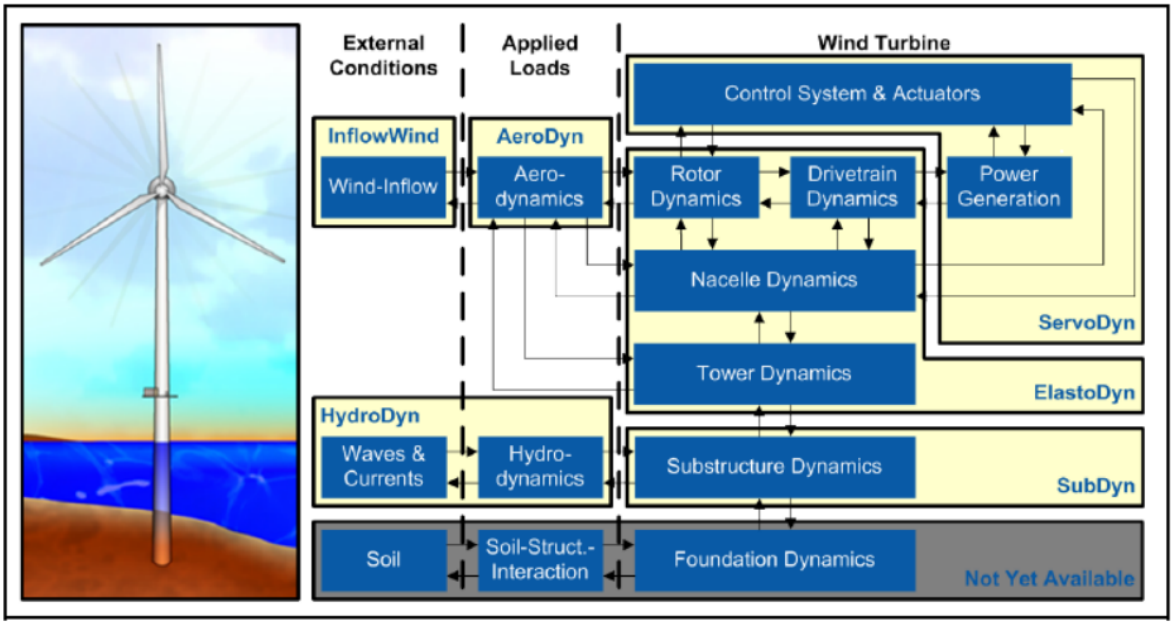

Figure III. 14 The input-output relationships between the submodules of FAST [174].

VIII.1.1 Module for Structural Dynamics: ElastoDyn

ElastoDyn serves as the core component of FAST, functioning as a structural dynamic's module designed for the modeling of various wind turbine components, including the tower, platform, rotor, drivetrain, and nacelle. It offers the flexibility to simulate a wide range of wind turbine configurations, whether they are horizontal axis, two or three-bladed, upwind or downwind, and situated on land or offshore.

Users have the capability to customize numerous parameters within ElastoDyn, such as enabling or disabling specific degrees of freedom, defining initial conditions, and configuring the wind turbine as needed. It is essential to provide the structural properties of the tower and blades in a section-wise manner through ElastoDyn input files.

Notably, ElastoDyn relies on an assumed modes approach. This involves defining the first and second fore-aft and side-side mode shapes of the tower, along with the first and second flapwise mode shapes and the first edgewise mode shape for the blades as coefficients within a 6th order polynomial. It is possible to calculate these mode shapes externally to FAST, and the results can be incorporated using the BModes feature[175].

In ElastoDyn, the tower and blade modeling adhere to the Euler-Bernoulli beam methodology. This approach excludes axial and torsional degrees of freedom and does not account for shear deformation. Moreover, it assumes small strains and employs small-angle approximations, while incorporating nonlinear corrections to maintain coordinate system orthogonality.

VIII.1.2 Modules for Turbulence: InflowWind and Turbsim

Turbsim [176] is a turbulence software that constructs a statistical model to digitally replicate stochastic 3D turbulence over time within a two-dimensional rectangular grid. To achieve this, it necessitates specific input details, including spectral models like the Kaimal and von Karman spectrum, turbulence intensity, mean wind speed, and wind profile parameters. Additionally, users are required to choose a seed number,

which is used to create random phases for the wind velocity time series. Turbulence intensity can be specified in accordance with the IE61400-1 standard categories A, B, C, or as a percentage value. The InflowWind submodule in FAST is responsible for processing the time series wind data generated by Turbsim.

VIII.1.3 Module for Unsteady Aerodynamics: AeroDyn

AeroDyn [177] serves as the unsteady aerodynamics module within FAST. It acquires undisturbed wind data from InflowWind and, in the time domain, computes aerodynamic forces, specifically drag, lift, and pitching moments, acting on both the blades and the tower. This module can be utilized in two ways: integrated with FAST, considering aero-structural coupling effects, or as a standalone code by disregarding such coupling effects.

The aerodynamic computations in AeroDyn are rooted in approximating the three-dimensional flow around the wind turbine as a two-dimensional flow, segmented into discrete elements for the blades and tower. The resultant two-dimensional lift, drag, and pitching moments are consolidated at the nodes of these elements.

For assessing the impact of wake on the turbine, AeroDyn employs a quasi-steady Blade Element Momentum (BEM) theory. This theory combines blade element theory with momentum theory and necessitates the use of an iterative nonlinear solver [2]. AeroDyn also accounts for dynamic stall using the Beddoes-Leishman formulation, considers hub and tip losses, and incorporates axial and tangential induction effects.

VIII.1.4 Module for Control System: ServoDyn

ServoDyn stands as a pivotal submodule within FAST, employed for the emulation of electrical drive and control systems associated with various wind turbine components, including blade pitch, nacelle yaw, generator torque, blade-tip brakes, and high-speed shaft brakes. Within ServoDyn, the pitch control system of the NREL 5 MW reference wind turbine is integrated as a dynamic link library (DLL). The coordination of yaw and pitch control enhances the efficiency of power generation. When the wind speed exceeds the turbine's cutout threshold, the pitch control system adjusts the blade angles, effectively "feathering" them, and positions the wind turbine in a parked state. Meanwhile, the nacelle yaw control ensures that the rotor plane aligns perpendicularly with the prevailing wind direction.

VIII.1.5 Module for Hydrodynamics: HydroDyn

HydroDyn [178] functions as a hydrodynamics submodule within FAST, facilitating comprehensive aero-hydro-aeroelastic simulations for offshore wind turbines. It accommodates both fixed-bottom and floating offshore platforms, enabling the computation of hydrodynamic forces. These forces encompass linear hydrostatic restoring components derived from buoyancy and waterplane area, viscous drag computed using Morison's equation, added mass and damping contributions originating from linear wave radiation, the free surface memory effect, and the incident wave excitation arising from diffraction.

In HydroDyn, waves can be generated in various modes, including regular (periodic), irregular (stochastic, with JONSWAP and white noise spectrum options), long-crested (unidirectional), or short-crested models (with a range of different wave directions) [179].

VIII.1.6 Fatigue Analysis Tool: MLife

MLife [180] is a MATLAB code software based on the rainflow cycle counting (shown in Section IV.1) to calculate the fatigue life, designed for the post-processing of time-series data derived from wind turbine simulations. It facilitates the analysis of statistics and fatigue load estimations based on the simulation outcomes. The statistical results encompass key parameters such as minimum and maximum values, mean, standard deviation, skewness, kurtosis, and maximum range. Additionally, MLife conducts fatigue computations, including short-term Damage Equivalent Loads (DELs) and damage rates calculated from a single time series. It also evaluates lifetime DELs using a set of time series, determining the total damage sustained and estimating the time until component failure.

MLife calculates Damage Equivalent Loads (DELs), which serve as assessments of fatigue loads for wind turbines and were initially pioneered by NREL [181]. DELs can be classified into short-term and lifetime categories. Short-term DEL quantifies fatigue loads from a singular time series, while lifetime DEL extends this calculation using a probability distribution extrapolation. DEL, acting as a constant amplitude load at a specific frequency, induces equivalent damage to the original time-series load.

IX. The Standard IEC 61400-2 for small wind turbines

The IEC safety standard, IEC 61400-2 [182], which governs small wind turbines, along with the guidelines set by Germanischer Lloyd (GL) [183], present both a significant challenge and an opportunity for designers of small wind turbines. As indicated in the Preface's initial sentence, IEC 61400-2 defines a small turbine as one with a rotor-swept area of less than 200 m2, approximately equating to a rated power of under 50 kW. Furthermore, the standard offers provisions for micro-turbines with a rotor area of 2 m2 or smaller; these can undergo certification independently of their tower. However, for all other turbines, an evaluation of the tower must be conducted in conjunction with the turbine assessment.

IEC 61400-2 offers three approaches for assessing turbine safety:

1. The "Simple Load Model" (SLM) employs uncomplicated equations for primary loads, often accompanied by generous safety factors.
2. "Aero-elastic Modeling" employs advanced computer modeling, such as the FAST tool, for a more precise analysis of wind turbine loads under stochastic conditions, accounting for factors like wind direction changes and gusts.
3. Load measurements with extrapolations for extreme conditions necessitate field testing and are primarily used for real-world validation, unlike the first two methods, which can be applied during the design phase.

The SLM is an exclusive feature within the IEC 61400-2 standard for small wind turbines. It was conceived as an economical substitute for the intricate and costly aero-elastic modeling typically employed in the assessment of large turbines. The "cost" associated with the SLM lies in the utilization of a substantial safety factor.

The initial step in implementing the Simplified Load Model (SLM) involves determining the turbine class, as outlined in Table III. 4. Table III. 5, sourced from IEC 61400-2[182], outlines the ten load cases that constitute the SLM, with it being noteworthy that only Case A pertains to fatigue loads.

Table III. 4 The turbine categorizations defined by the IEC

Category	I	II	III	IV	Special case (S)
U_{ref}	50	42.5	37.5	30	Parameters to be designated
U_{ave}	10	8.5	7.5	6	

Table III. 5 The load cases for design purposes in the Simplified Load Model

Design scenario	Load case	Explanation	Type of analysis
Power generation	A	Normal operation	Fatigue
	B	Yawing	Ultimate
	C	Yaw error	Ultimate
	D	Maximum thrust	Ultimate
Power generation in combination with the presence of a fault	E	Maximum rotational speed	Ultimate
	F	Short at the load connection	Ultimate
Shutdown	G	Shutdown (braking)	Ultimate
Stationary or Idle	H	Wind loading during the parked state	Ultimate
Stationary under fault conditions	I	Maximum wind loading during the parked state	Ultimate
Transportation, assembly, maintenance, and repair	J	To be provided by the manufacturer	Ultimate

IX.1 The Simple Load Model (SLM) for small wind turbine

The Simplified Load Model (SLM) is specifically applicable to horizontal-axis turbines with two or more cantilevered blades and a rigid (non-teetering) hub. Vertical-axis turbines are excluded from all IEC standards. The initial stage entails gathering or assigning the following parameters:

- Rotational speed for design, denoted as Ω_{design}
- Wind speed for design, $U_{design} = 1.4U_{ave}$ ($U_{ave}$the average wind speed)
- Shaft torque for design, referred to as Q_{design}
- Maximum achievable rotational speed, Ω_{max}

The design rotational speed is established based on aerodynamic factors, while the maximum speed is determined by the overspeed protection mechanism, particularly in the context of furling. The design power, denoted as P_{design}, is calculated at the design wind speed with the nominal electrical load connected. Additionally, the design torque, referred to as Q_{design}, is determined by:

$$Q_{design} = \frac{30P_{design}}{\eta\pi\Omega_{design}} \quad \text{(III. 28)}$$

for P_{design} in kW. The efficiency, represented as η, should be considered as:

$$\eta = \begin{cases} 0.6 + 0.005P_{design} & \text{for } P_{design} \leq 20 \text{ kW} \\ 0.7 & \text{for } P_{design} \geq 20 \text{ kW} \end{cases} \quad \text{(III. 29)}$$

IX.1.1 loads of case A: Normal Operation

While all cases are part of the SLM approach, it's important to note that "Normal Operation" (Case A) is the only one addressing fatigue. The primary objective of SLM "Case A" is to assess the loads and forecast the fatigue life and damage of the wind turbine blade. In "Case A," the loads, as per the SLM, are applied to the blade's root. The flapwise moment within "Case A" ranges from a minimum value (50%) to a maximum value (150%). When SLM equations are applied, the stresses generated at the root result from a combination of three forces: the centrifugal force (ΔF_{zB}) directed toward the blade tip, the flapwise moment (ΔM_{yB}) parallel to the blade's length, and the lead-lag moment (ΔM_{xB}) in the direction of rotation. Notably, "Case A" equations do not incorporate any unstable effects, such as yaw error or the influence of gyroscopic loads. The subsequent equations will be employed to compute fatigue loads.

$$\Delta F_{zB} = 2m_b r_g \Omega_{design}^2 \quad \text{(III. 30)}$$

$$\Delta M_{xB} = \frac{Q_{design}}{B} + 2m_b g r_g \quad \text{(III. 31)}$$

$$\Delta M_{yB} = \frac{\lambda_{design} Q_{design}}{B} \quad \text{(III. 32)}$$

Where: m_b represents the mass of the blade, r_g signifies the radial distance from the hub's center to the blade's center of gravity, B stands for the number of blades.

These moments should be exerted on the segment of the blade root possessing the least ultimate strength. It's worth mentioning that in the context of turbine blades, the term "bending" associated with "moment" generally pertains to flexural forces specifically in the flapwise direction. This is due to the inherent stiffness of turbine blades in the lead-lag direction.

IX.1.2 Loads of case H

Small wind turbines frequently operate under wind conditions that exceed their design wind speed. For this reason, the blade structure must be engineered to withstand extreme wind forces. Within the Simplified Load Model (SLM) framework, Case H is dedicated to investigating these extreme wind loads as applied to the blade. The goal of Case H is to assess the blade structure's robustness and its ability to endure extreme wind forces, ensuring blade safety.

In Case H equations, the calculation of extreme wind loads doesn't rely on the design wind speed; instead, it employs the extreme wind speed for a 50-year period to compute flapwise moments and stresses. According to the IEC 61400-2 standard, wind turbines are categorized based on their average wind speed into Sections I to IV and Special Status S (see Table III. 4). In this specific study, the design wind speed

is 10.5 m/s, corresponding to an average wind speed of 7.5 m/s, placing the studied wind turbine in Class III per IEC 61400-2. Therefore, the reference wind speed is U_{ref}= 37.5 m/s, and the extreme wind speed for 50 years can be determined as $U_{e50} = 1.4\,U_{ref} = 52.5$ m/s.

To calculate the equivalent stress σ_{MB} for Case H, the following equations are employed[182]:

$$M_{\mathrm{yB}} = \frac{1}{4} C_d \rho U_{e50}^2 A_{p,B} R \quad \text{(III. 33)}$$

$$\sigma_{MB} = \frac{M_{\mathrm{yB}}}{W_B} \quad \text{(III. 34)}$$

Where M_{yB} represents the flapwise moment at the extreme wind speed, and $A_{p,B}$ denotes the blade's projected area.

IX.2 Calculations of Stress and blade Safety Factors

The loads computed in Section IX.1 need to be transformed into equivalent stress levels for comparison with the permissible material stress threshold. The procedure for calculating stress levels remains consistent, whether the analysis involved the SLM or an aero-elastic approach.

IX.2.1 Equivalent Stresses Component

Following the SLM calculations, the individual forces and moments are amalgamated to derive the ultimate equivalent stress level acting on the critical load-bearing components, specifically the main shaft and the blade root. This amalgamation is carried out utilizing the equations outlined in Table III. 6. The computation of these equivalent stress levels necessitates considering several crucial factors:

- Variations in stress within the component
- Stress concentrations
- The magnitude and direction of the resultant load or stress
- Variations in component dimensions and thickness
- Surface treatment of the component
- The nature of the load applied to the component
- Any manufacturing impacts on the components, such as welding, machining, and so forth.

Table III. 6 SLM Equivalent stress equations from IEC 61400-2 [184]

	blade Circular root	blade rectangular root
Axial load	$\sigma_{zB} = \frac{F_{zB}}{A_B}$	$\sigma_{zB} = \frac{F_{zB}}{A_B}$
Bending	$\sigma_{MB} = \frac{\sqrt{M_{xB}^2 - M_{yB}^2}}{W_B}$	$\sigma_{MB} = \frac{M_{xB}}{W_{xB}} + \frac{M_{yB}}{W_{yB}}$
Combination of Axial load and bending	$\sigma_{eqB} = \sigma_{zB} + \sigma_{MB}$	

IX.2.2 IEC 61400-2 Partial Safety Factors

The SLM approach incorporates a substantial safety margin, rendering it a dependable method for computing various stresses aimed at validating the wind turbine blade's safety. Within the IEC standard

61400-2, partial safety factors are established, accounting for both the type of load and material properties. These factors include (γ_f) for loads and (γ_m)for materials, with their specific values detailed in Table III. 7 of IEC 61400-2. For materials that are presumed to be well-characterized, the partial safety factor for minimum characterization is notably high. Consequently, it's understandable why many researchers opt for full characterization, which employs lower safety factors. Various conditions, encompassing blade characteristics derived from materials and configurations, represent the ultimate structure of the blade.

Table III. 7 Partial safety factors of IEC standard 61400-2 for loads and materials[184]

method	Partial safety factors for loads(γ_f)		Partial safety factor for the materials(γ_m)			
			Fatigue loads		Ultimate loads	
	Fatigue loads	Ultimate loads	Minimal characterization	Full characterization	Minimal characterization	Full characterization
SLM	1.0	3.0	10	1.25	3.0	1.1
aeroelastic	1.0	1.35	10	1.25	3.0	1.1

The fatigue tests were performed within an appropriate range of loads and at a suitable rate of effect. Additionally, material properties were determined with a 95% high probability and a 95% confidence level.

IX.2.3 Analysis of Ultimate Stress

The safety factors and the ultimate stress within the Simplified Load Model (SLM) are employed to calculate the allowable stress (σ_{all}) using the following equation:

$$\sigma_{all} = \frac{\sigma_u}{\gamma_f \gamma_m} \quad \text{(III. 35)}$$

Where: σ_u represents the ultimate material strength. In essence, the ultimate safety factor is achieved by multiplying the load safety factor (γ_f) and the material safety factor (γ_m). To meet safety criteria, the equivalent Von Mises stress must be lower than the allowable stress:

$$\sigma_{eq} < \sigma_{all} \quad \text{(III. 36)}$$

IX.2.4 Blade fatigue damage analysis

To evaluate the fatigue-induced damage to the wind turbine blade, Miner's law, as recommended by the IEC 61400-2 standard, is employed. Miner's law leverages cumulative statistics to compute the damage, and according to this principle, the blade will fail if the cumulative damage surpasses a specific threshold. The subsequent equation is utilized for determining the blade's damage[185]:

$$D_B = \sum_i \frac{n_i}{N_f(\gamma_f \gamma_m \sigma_B)} \leq 1 \quad \text{(III. 37)}$$

In this equation, n_i represents the count of cycles conducted within the ith bin of the load characteristic spectrum, and N_f signifies the number of cycles leading to failure. Notably, N_f varies as a function of the stress level experienced during fatigue cycles (σ_B). The number of cycles leading to failure is closely

related to the stress level. In the context of SLM, Case A comprises a single 'bin,' and you can calculate the number of fatigue cycles as follows:

$$n = \frac{B\Omega_{design}T_d}{60} \quad \text{(III. 38)}$$

Where Ω_{design} represents the design rotational speed, and T_d denotes the design life of the composite material used in a wind turbine blade, with the lifetime typically estimated at approximately 20 years (equivalent to 6.31×10^8 s).

X. Conclusion

Wind turbine fatigue is indeed a pressing concern in our modern era. The growing utilization of wind energy as a clean and sustainable source of electricity marks a positive stride towards environmental preservation and the mitigation of greenhouse gas emissions.

In this chapter, we've introduced the concept of fatigue and highlighted the most significant challenges it poses. We've identified the loads responsible for causing fatigue and distilled them into equations that illustrate the cyclic stresses experienced by the blades during operation. Additionally, we've presented and simplified the key equations essential for predicting blade lifespan by defining the curve of the constant fatigue life. The FAST tool has been discussed as a pivotal resource for investigating wind turbine loads and fatigue. Furthermore, we've delved into the International Electrotechnical Commission's (IEC) simplified load model, which offers an efficient approach to calculating fatigue loads and estimating the lifespan of wind turbine blades.

Ultimately, mitigating wind turbine fatigue requires substantial investments in research and development to enhance the design of wind farm components and technologies. Additionally, diversifying our portfolio of renewable energy sources can alleviate pressure on wind farms and distribute our reliance on multiple sources. This strategy ensures the continued utilization of clean energy sources and contributes to the preservation of our planet for future generations.

CHAPTER IV

CRACK OF WIND TURBINE BLADE

I. INTRODUTION

The wind turbine stands as a pivotal player in the realm of alternative energy sources, significantly contributing to the pursuit of sustainable development and the reduction of greenhouse gas emissions worldwide. Nonetheless, the wind turbine industry grapples with a formidable obstacle: the issue of turbine breakage.

Fracture, in this context, refers to the structural damage or failure of wind turbines resulting from environmental stresses and corrosion, exerting a substantial influence on their operational efficiency and overall performance. Within the confines of this chapter, we will shed light on the predicament of wind turbine breakage, delving into its origins and repercussions. Additionally, we will delve into the concerted endeavors undertaken by industry experts and researchers to tackle this formidable challenge.

Our journey commences by examining the various categories of fractures that may afflict wind turbine blades, with a comprehensive exploration of their underlying causes, encompassing phenomena like transverse fractures and fatigue-induced fractures. Subsequently, we will dissect the ramifications of fracture on wind turbine functionality and ponder how this predicament can impinge on the economic viability of alternative energy ventures.

This chapter aspires to furnish us with an in-depth comprehension of the predicament of wind turbine breakage and underscore its significance in bolstering the sustainability of the alternative energy sector while elevating its performance standards.

II. Stress Concentration Factor

In Figure IV. 1, we observe a sample with a width denoted as W and thickness referred to as t, featuring a notch with a radius labeled as R_{en}. This specimen is exposed to two remote external forces of equal magnitude, f_y, uniformly distributed across its upper and lower surfaces. The stress distribution along the x-axis, as indicated by the σ_{yy} profile, reveals the presence of a stress concentration in the near of the notch.

The maximum stress and strain on a notch can be evaluated from the stress concentration factor $\mathcal{K}_\sigma$and the strain concentration factor $\mathcal{K}_\varepsilon$:

$$\mathcal{K}_\sigma = \frac{\sigma_{en}^{max}}{\sigma_{nom}} \tag{IV. 1}$$

$$\mathcal{K}_\sigma = \frac{\varepsilon_{en}^{max}}{\varepsilon_{nom}} \tag{IV. 2}$$

The nominal stress σ_{nom} is defined by:

$$\sigma_{nom} = \frac{f_y}{A_{y0}} = \frac{f_y}{t(W - R_{en})} \tag{IV. 3}$$

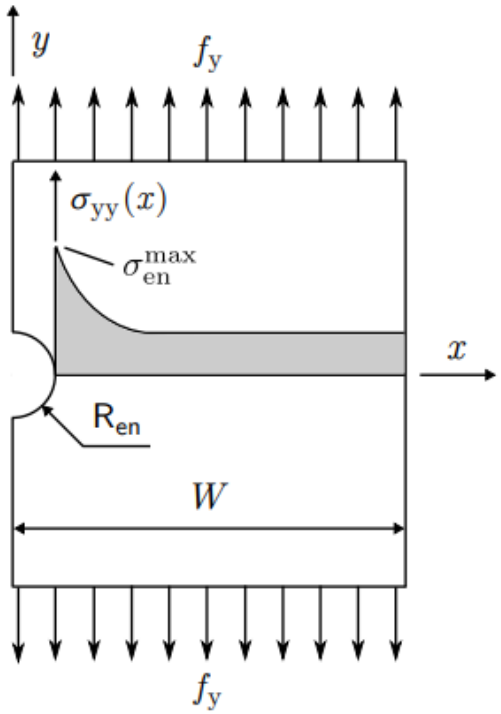

Figure IV. 1 Specimen with a notch of radius R_{en} subjected to a tensile force f_y.

where A_{y0} is the cross-sectional area of the specimen on the plane $y = 0$ (the plane of the notch). If the notch is small compared to the dimensions of the part, we can define σ_{nom} as the stress evaluated in the absence of the notch:

$$\sigma_{nom} \approx \frac{f_y}{tW} \qquad (\text{If } R_{en} \ll W) \qquad \text{(IV. 4)}$$

According to [186], in the elastic-linear deformation regime, the stress concentration factor and the strain concentration factor have the same value $\mathcal{K}_t$, which depends exclusively on the geometry of the notch concerned in the part. If the material is plastically deformed, $\mathcal{K}_\sigma \neq \mathcal{K}_\varepsilon$.

According to [187], even if the material is plastically deformed, the geometric mean between the stress concentration factor and the strain concentration factor provides the elastic stress concentration factor $\mathcal{K}_t$:

$$\mathcal{K}_t = \sqrt{\mathcal{K}_\sigma \mathcal{K}_\varepsilon} \qquad \text{(IV. 5)}$$

Equation (IV. 5) is called Neuber's rule.

While the material undergoes plastic deformation, $\mathcal{K}_\varepsilon$ experiences an increment while $\mathcal{K}_\sigma$ undergoes a decrease; nevertheless, the product of these two factors remains invariant [188].

The connection between the elastic stress concentration factor $\mathcal{K}_t$ and the stress concentration factor during fatigue, denoted as $\mathcal{K}_f$, is defined by the notch sensitivity factor q, as expressed in equation [123, 148, 189]:

$$\mathcal{K}_f = 1 + q(\mathcal{K}_t - 1) \qquad \text{(IV. 6)}$$

The notch sensitivity factor q is contingent not solely upon the part's geometry but also on its material, and it can assume values within the range of 0 to 1.0. Equation (IV. 7), introduced by [190], offers a means to compute this factor.

$$q = \frac{1}{1 + \sqrt{\frac{C_N}{R_{en}}}} \qquad \text{(IV. 7)}$$

The mechanical strength characteristics of a metallic material exhibit variation among individual crystallographic grains, and these properties also differ depending on the orientation of each grain. However, given that metal specimens significantly exceed the size of individual grains, the mechanical properties tend to be nearly uniform across all material samples. The Neuber constant, denoted as C_N and introduced by[190], represents the smallest material size capable of accurately representing its mechanical properties without distortion.

In general, fatigue cracks tend to initiate in regions where stress concentrations occur, although they can develop anywhere within a structure subjected to cyclic loading. Fracture mechanics is a field that investigates the propagation of these critical cracks resulting from structural fatigue.

III. State of stress near a crack

According to [191, 192] the stress state near the tip of a crack can be described by the infinite series shown in Equation (IV. 8):

$$\sigma_{ij}(r,\theta) = \frac{A_1}{\sqrt{2\pi r}} f_{ij}(\theta) + A_2 f_{ij}^2(\theta) + A_3 f_{ij}^3(\theta) + \cdots \qquad \text{(IV. 8)}$$

where r and θ are the polar coordinates shown in Figure IV. 2. The origin of the coordinate system is the tip of the crack.

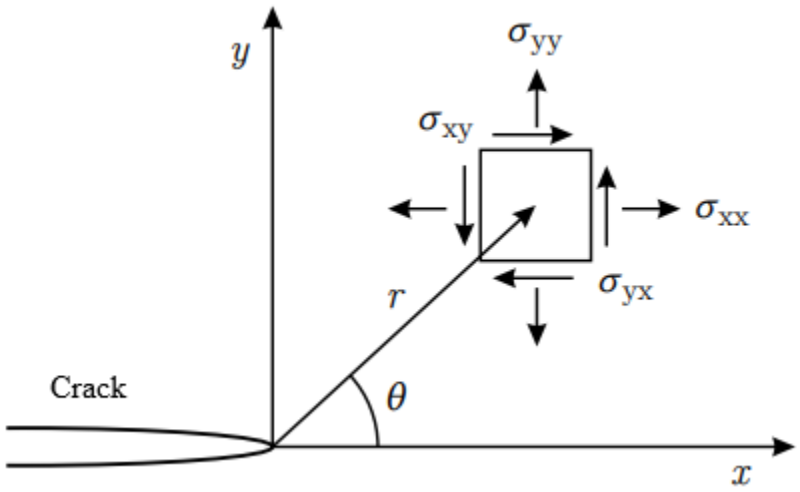

Figure IV. 2 Stress diagram on a point at a distance r and angle θ from the crack tip[193, 194].

Within Equation (IV. 8), A_1 corresponds to the stress intensity factor and will be denoted by the symbol K. A_2, on the other hand, represents a uniform and non-singular stress referred to as T-stress. It's worth noting that the initial two terms in Equation (IV. 8) are adequate for elucidating the crack propagation process. In simpler terms, terms of order greater than 2 can be disregarded as their contribution is insignificant.

IV. Definition of stress intensity factor (SIF)

When the T-stress becomes insignificant, the stress intensity factor (SIF) K alone provides an ample description of the stress distribution in the near of the crack tip. In cases where the crack is exclusively open in mode I, the stress pattern can be elucidated using Equations (IV. 9) to (IV. 11) [195]:

$$\sigma_{xx}(r,\theta) = \frac{K_I}{\sqrt{2\pi r}}\cos\left(\frac{\theta}{2}\right)\left[1-\sin\left(\frac{\theta}{2}\right)\sin\left(\frac{3\theta}{2}\right)\right] \quad \text{(IV. 9)}$$

$$\sigma_{yy}(r,\theta) = \frac{K_I}{\sqrt{2\pi r}}\cos\left(\frac{\theta}{2}\right)\left[1+\sin\left(\frac{\theta}{2}\right)\sin\left(\frac{3\theta}{2}\right)\right] \quad \text{(IV. 10)}$$

$$\sigma_{xy}(r,\theta) = \frac{K_I}{\sqrt{2\pi r}}\cos\left(\frac{\theta}{2}\right)\sin\left(\frac{\theta}{2}\right)\cos\left(\frac{3\theta}{2}\right) \quad \text{(IV. 11)}$$

Figure IV. **2** illustrates the coordinates r and θ. In a plane stress state, the component σ_{zz} assumes a value of zero, while in a plane strain state, it equals $\nu(\sigma_{xx}+\sigma_{yy})$. Both σ_{xz} and σ_{yz} components are zero.

As stated by [196], the stress intensity factor serves as a measure of a singular stress term that emerges near the crack tip. Equations (IV. 9) to (IV. 11) depicts how the stress intensity factor relates to the singularity of the stress field as r approaches zero. K is expressed in $Pa\sqrt{m}$, while $\mathcal{K}_t$, as defined in Section II, is a dimensionless quantity.

To ascertain the plastic zone's shape, it is valuable to derive expressions for the principal stress components σ_1, σ_2, and σ_3. The first two can be determined using Mohr's circle and are provided by Equation (IV. 12) and Equation (IV. 13) [197, 198]:

$$\sigma_1 = \frac{\sigma_{xx}+\sigma_{yy}}{2} + \sqrt{\left(\frac{\sigma_{xx}-\sigma_{yy}}{2}\right)^2 + {\sigma_{xy}}^2} \quad \text{(IV. 12)}$$

$$\sigma_2 = \frac{\sigma_{xx}+\sigma_{yy}}{2} - \sqrt{\left(\frac{\sigma_{xx}-\sigma_{yy}}{2}\right)^2 + {\sigma_{xy}}^2} \quad \text{(IV. 13)}$$

According to[197], the principal component σ_3 is always perpendicular to the plane. It is given by:

$$\sigma_3 \equiv \sigma_{zz} = \begin{cases} 0 & (Plane\ stress) \\ \nu(\sigma_{xx}+\sigma_{yy}) & (Plane\ strain) \end{cases} \quad \text{(IV. 14)}$$

By combining equations (IV. 9) to (IV. 14) we obtain:

$$\sigma_1(r,\theta) = \frac{K_I}{\sqrt{2\pi r}}\cos\left(\frac{\theta}{2}\right)\left[1+\sin\left(\frac{\theta}{2}\right)\right] \quad \text{(IV. 15)}$$

$$\sigma_2(r,\theta) = \frac{K_I}{\sqrt{2\pi r}}\cos\left(\frac{\theta}{2}\right)\left[1-\sin\left(\frac{\theta}{2}\right)\right] \quad \text{(IV. 16)}$$

$$\sigma_3(r,\theta) = \begin{cases} 0 & (Plane\ stress) \\ \frac{2\nu K_I}{\sqrt{2\pi r}}\cos\left(\frac{\theta}{2}\right) & (Plane\ strain) \end{cases} \quad \text{(IV. 17)}$$

IV.1 Stress Intensity Factor Due to Remote External Loading

Determining the stress intensity factor relies not just on the magnitude of the applied load and the crack length, but also on the geometry of the specific component under consideration. In the case of an infinitely wide and tall sheet (as illustrated in Figure IV. 3a), there exists a precise solution for calculating the stress intensity factor resulting from external loading from a distance. This solution is provided by Equation (IV. 18):

$$K_I = \sigma\sqrt{\pi a} \quad \text{(IV. 18)}$$

Let's examine the scenario of a sheet that is semi-infinite in the x direction and infinite in the y direction, featuring a lateral crack (as depicted in Figure IV. 3b). The stress intensity factor arising from remote external loading can be calculated using Equation (IV. 18) [199]:

$$K_I = 1.1215\sigma\sqrt{\pi a} \quad \text{(IV. 19)}$$

In the event that the sheet possesses a finite width W and the crack extends in this particular dimension, the stress intensity factor K_I, resulting from remote external loading, can be determined through an equation structured in the following manner:

$$K_I = F(a/W)\sigma\sqrt{\pi a} \quad \text{(IV. 20)}$$

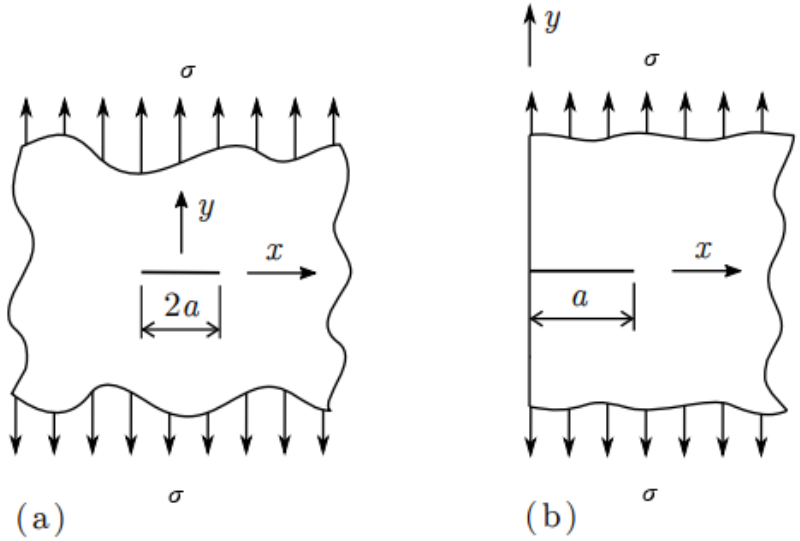

Figure IV. 3 (a) Metal sheet extending infinitely in both the x and y directions, experiencing remote external loading, while featuring a central crack (b) Metal sheet semi-infinite in the x direction and infinite in the y direction, under the influence of distant external loading, and exhibiting a lateral crack.[200]

where F is a function which depends on the ratio a/W.

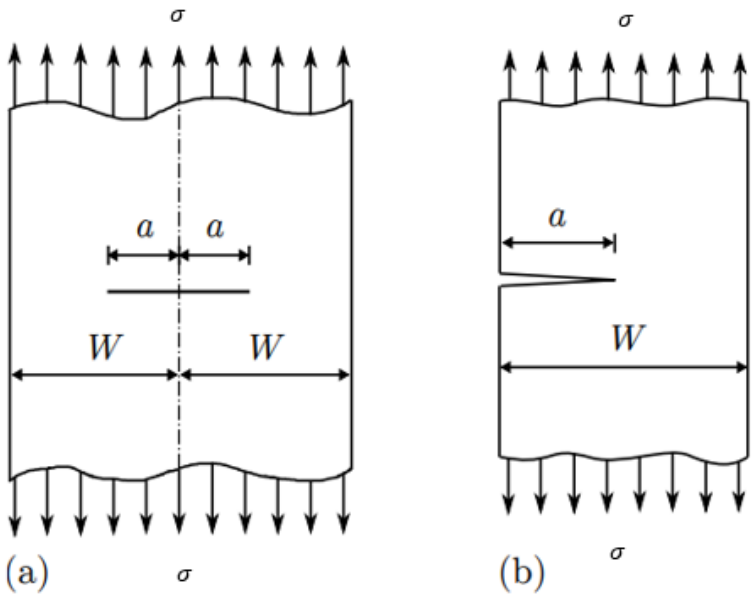

Figure IV. 4 (a) Sheet with a width of $2W$ exposed to a distant external load σ, accompanied by a central crack measuring $2a$ in length. (b) Metal sheet, possessing a width of W, under the influence of distant external load σ, and featuring a lateral crack of length a.

Tada et al. [201] present Equation (IV. 21) as a means to compute the function $F(a/W)$ associated with a central crack situated within a sheet that possesses a width of $2W$ and extends infinitely in height (as depicted in Figure IV. 4a):

$$F(a/W) = \left[1 - 0.025\left(\frac{a}{W}\right)^2 + 0.06\left(\frac{a}{W}\right)^4\right]\sqrt{\sec\left(\frac{a\pi}{2W}\right)} \qquad \text{(IV. 21)}$$

As indicated by the same authors, Equation (IV. 22) provides a method for assessing the function $F(a/W)$ that pertains to a lateral crack positioned within a sheet with a width of W and infinite height, as illustrated in Figure IV. 4b:

$$F(a/W) = \sqrt{\frac{2W}{a\pi}\tan\left(\frac{a\pi}{2W}\right)}\,\frac{0.752 + 2.02\left(\frac{a}{W}\right) + 0.37\left[1 - \sin\left(\frac{a\pi}{2W}\right)\right]^3}{\cos\left(\frac{a\pi}{2W}\right)} \qquad \text{(IV. 22)}$$

IV.2 SIF resulting from applied loads acting on fracture surfaces

As stated in reference [199], the stress intensity factor K_I associated with the loading $\sigma_{yy}(x)$ applied to the fracture surfaces of a sheet resembling the one depicted in Figure IV. 5 can be determined through the integration of Equation (IV. 23):

$$K_I = \int_0^a \sigma_{yy}(x)\mathrm{h}(x,a)dx \qquad \text{(IV. 23)}$$

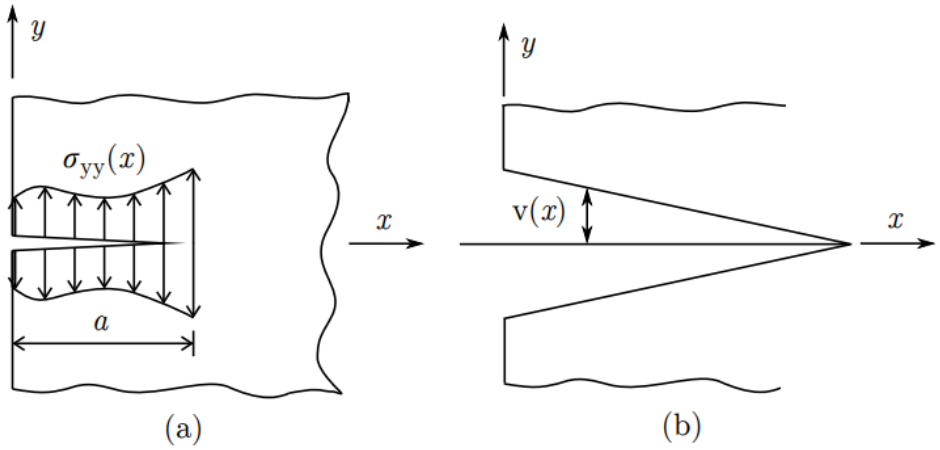

Figure IV. 5 (a) non-uniform loading $\sigma_{yy}(x)$ distributed on the fracture surfaces of a lateral crack in a semi-infinite sheet. (b) Definition of distance v(x)[202]

IV.2.1 Weighting functions

The weighting function h(x, a) exhibits low values when x is in proximity to zero, progressively rising as x nears a. In simpler terms, this implies that the stress intensity factor is most responsive to the applied load near the crack tip. Loads applied beyond the crack tip ($x > a$) hold no sway over the stress intensity factor.

Knowing that $\sigma_{yy}(x) = df_y(x)/(dxdz)$, Equation (IV. 24) can be rewritten as:

$$K_I = \sum_i P_i(x_i)h(x_i, a) \qquad \text{(IV. 24)}$$

where P_i is the value of each of the two opposing forces applied to each fracture surface at a distance x_i from the origin, per unit thickness of the sheet.

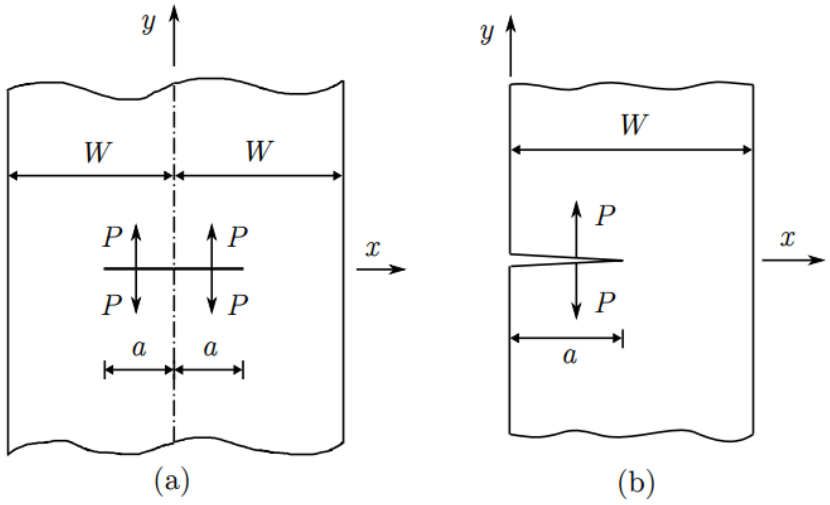

Figure IV. 6 (a) Sheet of width $2W$ and infinite height with a concentrated force P applied to the surfaces of the central crack. (b) Sheet of width W and infinite height with a force P applied to the surfaces of the lateral crack.[203]

When considering a central crack within a sheet measuring $2W$ in width and extending infinitely in height, as portrayed in Figure IV. 6a, and subject to symmetrical loading P applied to the fracture surfaces, Tada et al.[201] introduced the function $\mathrm{h}(x,a)$ as outlined in Equation (IV. 25):

$$\mathrm{h}(x,a)=\frac{2}{\sqrt{2W}}\left\{1+0.297\sqrt{1-\left(\frac{x}{a}\right)^2}\left[1-\cos\left(\frac{a\pi}{2W}\right)\right]\right\}\sqrt{\tan\left(\frac{a\pi}{2W}\right)}\left\{1-\left[\frac{\cos\left(\frac{a\pi}{2W}\right)}{\cos\left(\frac{\pi x}{2W}\right)}\right]^2\right\}^{-1/2} \quad \text{(IV. 25)}$$

When employing Equation (IV. 25) within the context of Equation (IV. 23), it necessitates conducting the integration over the range from $x=0$ to $x=a$. This is essentially stating that if we employ Equation (IV. 25) in Equation (IV. 24), we will perform the summation while considering $P_i(x_i)$ only for values of x_i within the range of $0<x_i<a$. Consequently, the stress intensity factor will be identical for both crack tips.

In the case depicted in Figure IV. 6b, specifically, a lateral crack within a sheet of width W and infinite height, Bueckner [204] introduced Equation (IV. 26a) to calculate h:

$$\mathrm{h}(x,a)=\frac{2}{\sqrt{2\pi(a-x)}}\left[1+m_1\left(\frac{a-x}{a}\right)+m_2\left(\frac{a-x}{a}\right)^2\right] \quad \text{(IV. 26a)}$$

With:

$$m_1=0.6147+17.1844\left(\frac{a}{W}\right)^2+8.7822\left(\frac{a}{W}\right)^6 \quad \text{(IV.26b)}$$

$$m_1=0.8502+3.2889\left(\frac{a}{W}\right)^2+70.0444\left(\frac{a}{W}\right)^6 \quad \text{(IV.26c)}$$

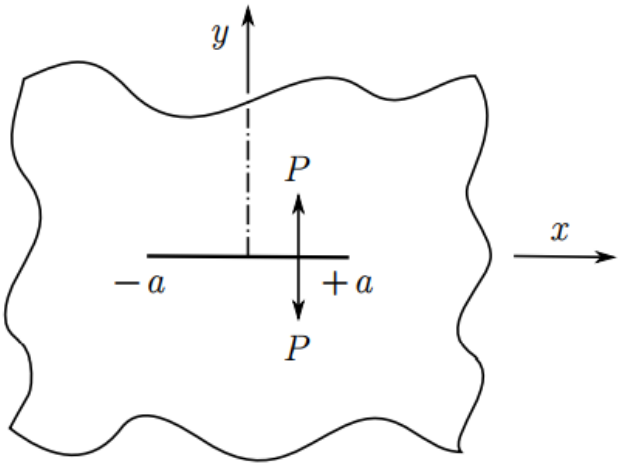

Figure IV. 7 a sheet of metal extending infinitely in both the x and y directions, experiencing an applied force P on its fracture surfaces.

In the instance of a central crack with a width of $2a$ located within a sheet of infinite extent along both the x and y directions, as illustrated in Figure IV. 7, it is feasible to obtain a precise solution for the weighting function $\mathrm{h}(x,a)$. The solution, as provided in Equations (IV. 27a) and (IV. 27a), was derived by Sih et al. [205]:

$$\mathrm{h}_l(x,a) = \frac{1}{\sqrt{\pi a}}\sqrt{\frac{a-x}{a+x}} \qquad \text{(Left tip)} \tag{IV. 27a}$$

$$\mathrm{h}_s(x,a) = \frac{1}{\sqrt{\pi a}}\sqrt{\frac{a+x}{a-x}} \qquad \text{(Straight tip)} \tag{IV.27b}$$

In the scenario involving a lateral crack within a sheet that is semi-infinite along the x direction and infinite along the y direction, similar to the configuration in Figure IV. 5a, Sih [206] introduced Equation (IV. 28) as a means to calculate $\mathrm{h}(x,a)$:

$$\mathrm{h}(x,a) = \frac{1}{\sqrt{\pi a[1-(x/a)^2]}}\left[1.3 - 0.3\left(\frac{x}{a}\right)^{5/4}\right] \tag{IV. 28}$$

IV.3 Fracture toughness

The critical stress intensity factor linked to a crack within a flat sheet is contingent upon whether the sheet is in a state of plane strain or plane stress. Consequently, the sheet's thickness assumes a significant role in influencing this critical stress intensity factor (also known as fracture toughness).

In general, the fracture toughness under plane stress is expressed by the symbol Kc. In a state of plane strain, it is expressed by the symbol $\mathrm{K_{Ic}}$. The relationship between $\mathrm{K_c}$ and $\mathrm{K_{Ic}}$ can be established by[207]:

$$\mathrm{K_c} = \mathrm{K_{Ic}}\sqrt{1+\frac{1.4}{t^2}\left(\frac{\mathrm{K_{Ic}}}{\sigma_{ys}}\right)^4} \tag{IV. 29}$$

According to standard E399[208], a test to evaluate $\mathrm{K_{Ic}}$ is valid only if the condition of Equation (IV. 30) is satisfied:

$$t > 2.5\left(\frac{\mathrm{K_{Ic}}}{\sigma_{ys}}\right)^2 \tag{IV. 30}$$

V. Propagation Rate Laws

V.1 Paris law

The Paris law[209] represents the simplest and most often used way to evaluate the rate of propagation of a fatigue crack. It is given by:

$$\frac{da}{dN} = C\Delta \mathrm{K}^{\mathrm{n}} = C(\mathrm{K}_{\max} - \mathrm{K}_{\min})^{\mathrm{n}} \quad \text{(IV. 31)}$$

In Equation (IV. 31), the parameters C and n are material-dependent. The exponent n is dimensionless, while the coefficient C has units of $Pa^{-n} \cdot m^{1-n/2}$ when following the International System of Units [210]. It is important to note that in this equation, we take $\mathrm{K}_{\min} = 0$ when $\sigma_{\min} < 0$.

Paris's law produces a linear appearance when plotted on a bi-logarithmic scale graph.

The load ratio (expressed as $R_s = \sigma_{\min}/\sigma_{\max} = \mathrm{K}_{\min}/\mathrm{K}_{\max}$) also influences the propagation rate. Paris's law does not explicitly incorporate the load ratio R_s. As noted by [211], if we intend to apply Paris's law for a specific load ratio, we need to determine the parameter C corresponding to that particular load ratio value.

V.2 Walker's Law

Walker's law [154], given by Equation (IV. 32), explicitly takes into account the charge ratio R_s:

$$\frac{da}{dN} = C_0\left[\frac{\Delta \mathrm{K}}{(1-R_s)^{1-m}}\right] \quad \text{(IV. 32)}$$

where C_0 is the same coefficient of the Paris law, for the load ratio $R_s = 0$. The parameter m has already been introduced in chapter III, Section V. It also appears in Equation (III. 20).

V.3 Forman's equation

Similar to Paris's law, Walker's law produces a linear curve when plotted on a log-log graph. However, this linear curve tends to underestimate the propagation rate when ΔK approaches the material's fracture toughness. To address this issue, Forman et al. [212] introduced Equation (IV. 33) as a remedy.

$$\frac{da}{dN} = \frac{C(\Delta \mathrm{K})^n}{(1-R_s)\mathrm{K}_{\mathrm{c}} - \Delta \mathrm{K}} = \frac{C(\Delta \mathrm{K})^n}{(1-R_s)(\mathrm{K}_{\mathrm{c}} - \mathrm{K}_{\max})} \quad \text{(IV. 33)}$$

There exists a threshold value, denoted as $\Delta \mathrm{K}_{th}$ (with " th " signifying threshold), below which crack propagation does not occur. When ΔK closely approaches $\Delta \mathrm{K}_{th}$, the Paris, Walker, and Forman laws tend to overestimate the rate of crack propagation. In contrast, the equation known as NASGRO [213] can accurately describe crack propagation rates in all scenarios: whether ΔK is near the threshold, falls within the average range, or approaches the fracture toughness of the material. These three scenarios correspond to regions I, II, and III of Figure IV. 8, respectively, on the da/dN propagation rate curve.

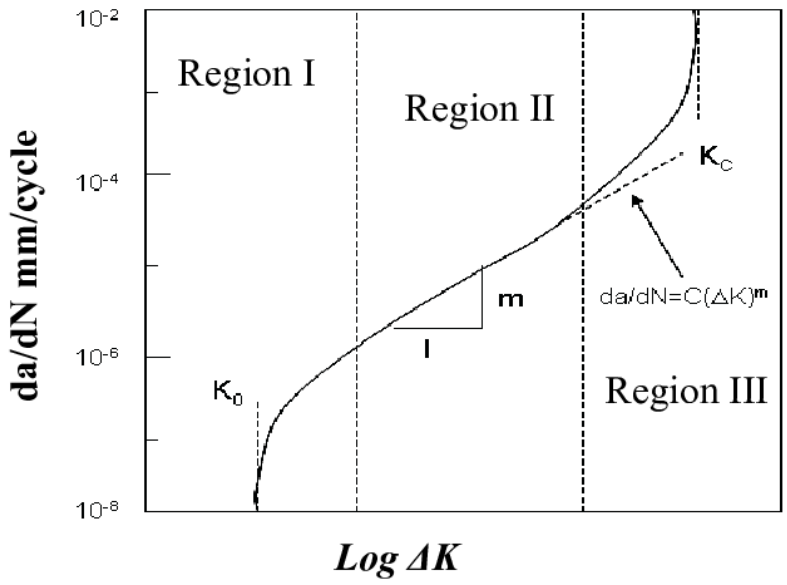

Figure IV. 8 the da/dN propagation rate curve[214].

VI. Shape And Size of The Plastic Zone

According to Broek [197] and Gdoutos [215], it is possible to deduce the shape of the plastic zone by associating σ_1, σ_2 and σ_3 provided by Equation (IV. 15),(IV. 16), and (IV. 17) to the von Mises flow criterion, given by:

$$(\sigma_1 - \sigma_2)^2 + (\sigma_2 - \sigma_3)^2 + (\sigma_3 - \sigma_1)^2 = 2\sigma_{ys}^2 \qquad \text{(IV. 34)}$$

As a result of this association, we obtain Equation (IV. 35a) whose graphic representation is in Figure IV. 9.

$$r_y(\theta) = \frac{1}{4\pi}\left(\frac{K_I}{\sigma_{ys}}\right)^2\left[1 + \cos\theta + \frac{3}{2}\sin^2\theta\right] \qquad \text{(Plane stress)} \qquad \text{(IV. 35a)}$$

$$r_y(\theta) = \frac{1}{4\pi}\left(\frac{K_I}{\sigma_{ys}}\right)^2\left[(1-2\nu)^2(1+\cos\theta) + \frac{3}{2}\sin^2\theta\right] \qquad \text{(Plane strain)} \qquad \text{(IV.35b)}$$

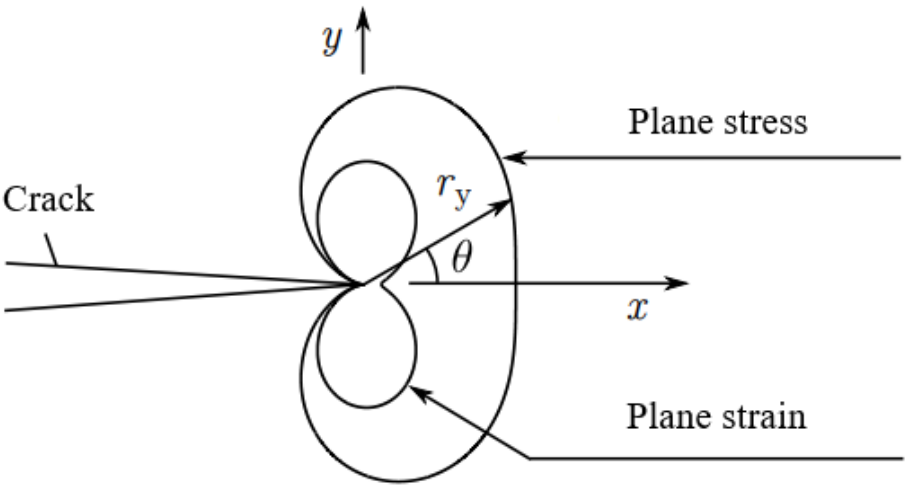

Figure IV. 9 Shape of the plastic zone, according to the von Mises plastic flow criterion[197, 215].

For the angle $\theta = 0$ and Poisson's ratio $\nu = 1/3$, Equation (IV. 35a) gives [215]:

$$r_y(0) = \frac{1}{2\pi}\left(\frac{K_I}{\sigma_{ys}}\right)^2 \qquad \text{(Plane stress)} \qquad \text{(IV. 36a)}$$

$$r_y(0) = \frac{1}{18\pi}\left(\frac{K_I}{\sigma_{ys}}\right)^2 \qquad \text{(Plane strain)} \qquad \text{(IV. 36b)}$$

According to [197], it is possible to obtain Equation (IV. 36a) from Equation (IV. 36a), considering a plastic restriction factor $\alpha = 3$:

$$r_y = \frac{1}{2\pi}\left(\frac{K_I}{\alpha\sigma_{ys}}\right)^2 = \frac{1}{2\pi}\left(\frac{K_I}{3\sigma_{ys}}\right)^2 = \frac{1}{18\pi}\left(\frac{K_I}{\sigma_{ys}}\right)^2 \qquad \text{(Plane stress)} \qquad \text{(III. 39)}$$

According to the same author, Irwin [216] considers $\alpha = 1.68$, which gives the result often mentioned in the literature:

$$r_y = \frac{1}{2\pi}\left(\frac{K_I}{\alpha\sigma_{ys}}\right)^2 = \frac{1}{2\pi}\left(\frac{K_I}{1.68\sigma_{ys}}\right)^2 \approx \frac{1}{6\pi}\left(\frac{K_I}{\sigma_{ys}}\right)^2 \qquad \text{(Plane strain)} \qquad \text{(IV. 37)}$$

Equation (IV. 36a) can also be derived from Equation (IV. 9) when we set $\theta = 0$, $\sigma_{yy} = \sigma_{ys}$, and $r = r_y$. By following this approach, we are essentially considering a stress distribution pattern originating from a linear-elastic deformation regime, akin to what's depicted in Figure IV. 10. However, it's crucial to acknowledge that in proximity to the crack tip, the actual deformation regime is elastoplastic. Consequently, the gray area illustrated in Figure IV. 10 should not exist since it is physically implausible for the stress level to surpass the yield strength σ_{ys}. To uphold the equilibrium of internal forces within the material, the stress σ_{yy} beyond r_y is actually higher than what Equation (IV. 9) predicts. As a result, the true extent of the plastic zone exceeds ry.

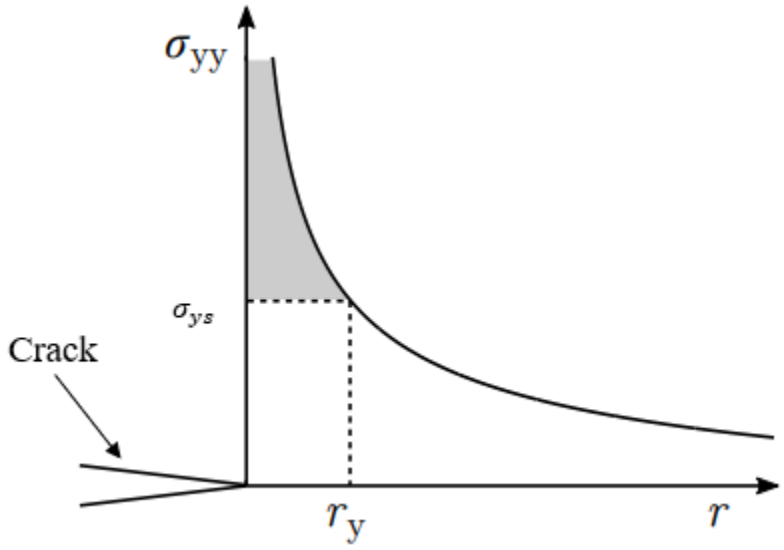

Figure IV. 10 Determining the extent of the plastic zone based on the stress distribution generated by a purely linear-elastic deformation regime [197].

VII. Crack Closure Effect

This section explains the crack closure effect, discovered by Elber [217]. It is important to understand this effect to implement the strip-yield method of crack propagation simulation.

Consider a crack subjected to cyclic external loading, fluctuating between two fixed values, σ_{min} and σ_{max}. Under these loading conditions, the stress intensity factor increases as the crack extends, as it is directly related to the square root of the crack length (as seen in, for instance, Equation (IV. 18)). It's worth recalling that the size of the plastically deformed region (covered in Section VI) is proportionate to the square of the stress intensity factor. Consequently, it can be deduced that if the loading maintains a constant amplitude within the range of σ_{min} to σ_{max}, it results in the development of a boundary consisting of plastic zones, akin to what's depicted in Figure IV. 11.

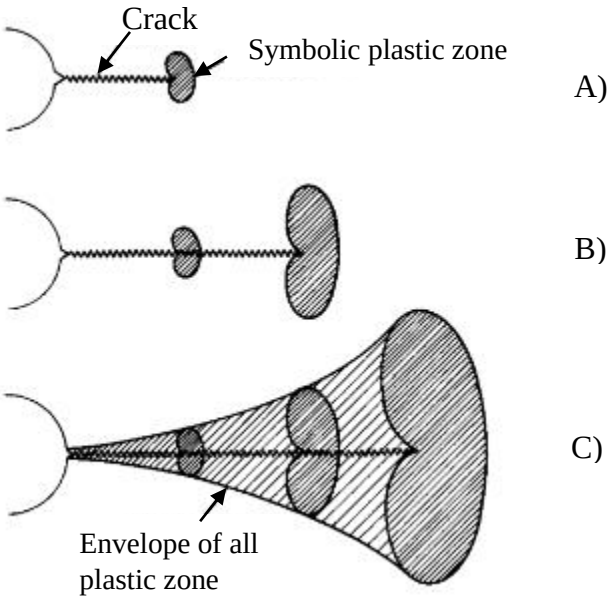

Figure IV. 11 Formation of the envelope of plastic zones under the crack surfaces [217].

In Figure IV. 12, the left side illustrates a fatigue crack (subjected to loading between $\sigma_{\min}$ and $\sigma_{\max}$) along with its associated boundary of plastic zones. On the right side of the same figure, we observe a cut created by an ideally thin saw, meaning a saw with negligible thickness that can cut without inducing plastic deformation. This sawn portion is subsequently exposed to a loading at $\sigma_{\max}$, leading to the formation of an identical plastic zone as what occurs when a fatigue crack propagates. The lengths of the fatigue crack and the saw cut are identical in both scenarios. The primary distinction between these two cases lies in the presence of the envelope of plastic zones on the fracture surfaces of the fatigue crack.

It is noticeable that, under the same loading condition denoted as σ, the separation between the fracture surfaces is less in the instance of the fatigue crack. This dissimilarity between the two case is elucidated by the expression $\delta = \delta_{cs} - \delta_{ff}$, with the variables depicted in Figure IV. 12. Consequently, one can infer that in the context of fatigue cracking, the fracture surfaces will come into contact before the external loading σ is entirely relieved.

Elber [217] postulated that a fatigue crack is capable of advancing solely when the fracture surfaces are entirely apart. Consequently, a fatigue crack emerging from the saw cut depicted on the right side of Figure IV. 12 is expected to exhibit a greater propagation rate compared to the fatigue crack presented on the left side of the same figure.

Elber [217] proposed an important modification to the Paris law. Such modification is shown in Equation (IV. 38a):

$$\frac{da}{dN} = C_{eff}\Delta K_{eff}^{n} \qquad \text{(IV. 38a)}$$

$$\Delta K_{eff} = \begin{cases} K_{max} - K_{op} & (\text{for } K_{min} < K_{op}) \\ K_{max} - K_{min} & (\text{for } K_{op} < K_{min}) \end{cases} \qquad \text{(IV.38b)}$$

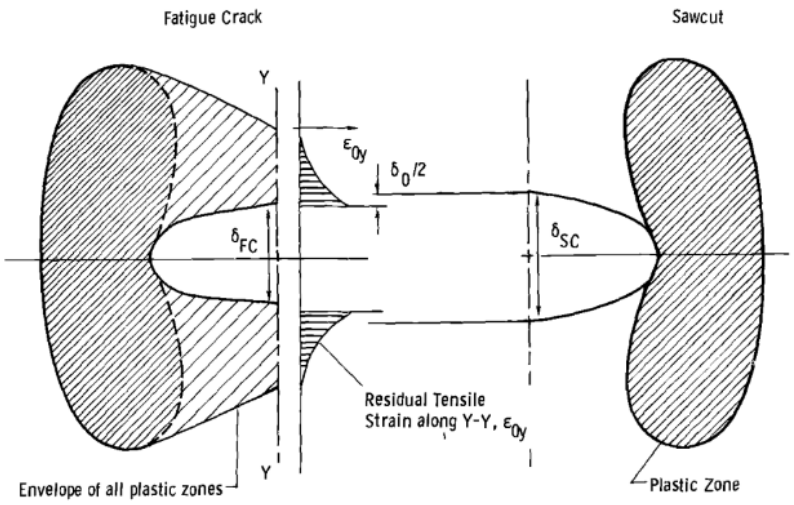

Figure IV. 12 Regions of plastic deformation in the near of a fatigue crack compared to those near a saw cut[217].

where K_{op} is the stress intensity factor corresponding to σ_{op}, which is the minimum loading to completely separate the fracture surfaces.

It is convenient to write Equation (IV. 38a) in terms of U [217]:

$$\frac{da}{dN} = C_{eff}(U\Delta K)^n \tag{IV. 39a}$$

$$U = \frac{\sigma_{max} - \sigma_{op}}{\sigma_{max} - \sigma_{min}} = \frac{\Delta\sigma_{eff}}{\Delta\sigma} = \frac{K_{max} - K_{op}}{K_{max} - K_{min}} = \frac{\Delta K_{eff}}{\Delta K} \tag{IV. 39b}$$

The association of Equations (IV. 31), (IV. 38a) and (IV. 39a) allows us to write:

$$C_{eff} = C\left[\frac{\Delta K}{\Delta K_{eff}}\right]^n = \frac{C}{U^n} \tag{IV. 40}$$

In Equation (IV. 40), the parameters C and U vary according to the charge ratio R_s. On the other hand, the coefficient C_{eff} remains constant for a given material (it is independent of R_s, as mentioned by Song et al.[218]).

For constant amplitude loading conditions, σ_{op} can be evaluated using Equation (IV. 41) [213, 219]:

$$\frac{\sigma_{op}}{\sigma_{max}} = \frac{K_{op}}{K_{max}} = \begin{cases} A_0 + A_1R_s + A_2{R_s}^2 + A_3{R_s}^3 & (R_s \geq 0) \\ A_0 + A_1R_s & (-1 \leq R_s < 0) \end{cases} \tag{IV. 41}$$

For $\sigma_{op} \geq \sigma_{min}$, the coefficients A_0, A_1, A_2 and A_3 can be evaluated by Equation (IV. 42a). They depend on the ratio σ_{min}/σ_0 and the restriction factor α.

$$A_0 = \left(0.825 - 0.34\propto + 0.05\propto^2\right)\left[\cos\left(\frac{\pi}{2}\frac{\sigma_{max}}{\sigma_0}\right)\right] \tag{IV. 42a}$$

$$A_1 = (0.415 - 0.071 \propto) \frac{\sigma_{\max}}{\sigma_0} \quad \text{(IV. 42b)}$$

$$A_2 = 1 - A_0 - A_1 - A_3 \quad \text{(IV. 42c)}$$

$$A_3 = 2A_0 + A_1 - 1 \quad \text{(IV. 42d)}$$

σ_0 represents the material's flow stress, incorporating the influence of work hardening. When the loading exhibits variable amplitudes, the determination of σ_{op} becomes considerably more intricate. One of the aims of this chapter is to delve into this specific scenario.

The application of the flow band method requires the use of the flow stress σ_0 whose value will vary due to the work hardening of the material. It can be approximated as the average between the yield strength σ_{ys} and the ultimate tensile strength σ_u[220, 221]

$$\sigma_0 = \frac{\sigma_{ys} + \sigma_u}{2} \quad \text{(IV. 43)}$$

Let $\sigma_{\max}$ be the maximum stress observed in a direction of practical interest (generally the y direction) in the plastic zone. The restriction factor is the ratio between $\sigma_{\max}$ and the flow stress σ_0:

$$\propto = \frac{\sigma_{\max}}{\sigma_0} \quad \text{(IV. 44)}$$

VIII. The Extended Finite Element Method (X-FEM)

The origin of the eXtended Finite Element Method (X-FEM) can be traced back to industrial challenges involving the three-dimensional propagation of cracks, aimed at predicting the structural integrity of components. Despite having been around for several decades, the conventional finite element method combined with remeshing has yet to completely fulfill the demands of the industry.

The X-FEM method was initially introduced by Belytschko and Black [222] and Dolbow [223], and subsequently, Daux et al. [224] made modifications and applied it to various crack analysis problems. The numerical X-FEM model is created through a two-step process: initially, generating a mesh for the domain geometry without considering the presence of cracks or other discontinuities, and then enhancing the finite element approximation by incorporating suitable functions to represent any imperfections. In the ensuing sections, we will explore the fundamentals of the X-FEM formulation[225].

VIII.1 Basics of X-FEM formulation

Numerous methods have been devised to incorporate unique solution features into the approximation space (The partition of unity method (PUM)[226], partition of unity unite element method (PUFEM)[227]). The extended finite element method (XFEM) is one such technique that involves the inclusion of specific enrichment functions within a standard approximation space. Consequently, the approximation takes the following form[228]:

$$u^h(x) = \sum_i N_i(x) u_i + \text{enrichment terms} \quad \text{(IV. 45)}$$

Here, $N_i(x)$ typically represents classical finite element shape functions. This type of approximation is referred to as externally enriched.

VIII.2 Enrichment

In theory, enrichment can be seen as a concept that enhances the attainable degree of completeness. In practical computational terms, it might primarily focus on improving the accuracy of the approximation by incorporating information derived from the analytical solution.

We shall commence with the traditional representation of a field variable **u** in the context of a finite element method:

$$\mathbf{u} = \sum_{j=1}^{n} \mathbf{N}_j \bar{\mathbf{u}}_j \tag{IV. 46}$$

Alternatively, in a more suitable form with respect to the m basis functions p:

$$\mathbf{u} = \mathbf{p}^T \mathbf{a} = \sum_{k=1}^{m} p_k \mathbf{a}_k \tag{IV. 47}$$

Here, the unknowns $\mathbf{a}_k$ are calculated based on the approximation values at nodal points.

In the case of one- and two-dimensional problems, the basis function can be established with varying levels of completeness:

$$\begin{cases} 1D: \begin{cases} \mathbf{p}^T = \{1, x\} & \text{1st order} \\ \mathbf{p}^T = \{1, x, x^2\} & \text{2st order} \end{cases} \\ 2D: \begin{cases} \mathbf{p}^T = \{1, x, y\} & \text{1st order} \\ \mathbf{p}^T = \{1, x, y, x^2, xy, y^2\} & \text{2st order} \end{cases} \end{cases} \tag{IV. 48}$$

The fundamental concept behind enrichment is to modify Equations. (IV. 46) or (IV. 47) into a more suitable form to improve the construction of the approximation. This enhancement can be linked to the consistency level of the approximation or its ability to replicate a complex field of interest accurately.

Enriching an approximation can generally be accomplished through two methods: either by enriching the basis vector (referred to as intrinsic enrichment) or by enhancing the approximation itself (referred to as extrinsic enrichment). Subsequent sections will delve into both of these approaches.

VIII.2.1 intrinsic enrichment

In this approach, the objective is to improve the approximation described in Equation (IV. 47) by modifying the basis function p to introduce additional terms that fulfill a specific requirement for accurately replicating a complex field [229]. For example, when dealing with a first-order standard linear basis function $\mathbf{p}^{\mathbf{lin}} = \{1, x, y\}$, new enrichment terms $\mathbf{p}^{\mathbf{enr}} = \{f_1, f_2\}$ are introduced as follows:

$$\mathrm{p} = \{\mathbf{p}^{\mathbf{lin}}, \mathbf{p}^{\mathbf{enr}}\} = \{1, x, y, f_1, f_2\} \tag{IV. 49}$$

To delve deeper into the notion of enrichment, let's explore the classical problem involving cracks. The asymptotic displacement field in the vicinity of the crack tip can be expressed as follows:

$$u_x = \frac{1}{\mu}\sqrt{\frac{r}{2\pi}}\left(\mathrm{K_I}\cos\frac{\theta}{2}(\kappa - \cos\theta) + \mathrm{K_{II}}\sin\frac{\theta}{2}(\kappa + \cos\theta + 2)\right) \quad \text{(IV. 50)}$$

$$u_x = \frac{1}{\mu}\sqrt{\frac{r}{2\pi}}\left(\mathrm{K_I}\sin\frac{\theta}{2}(\kappa - \cos\theta) - \mathrm{K_{II}}\cos\frac{\theta}{2}(\kappa + \cos\theta - 2)\right) \quad \text{(IV. 51)}$$

Here, r and θ are specified as illustrated in Figure IV. 13, and $\mathrm{K_I}$ and $\mathrm{K_{II}}$ represent the stress intensity factors for mode I and mode II, respectively.

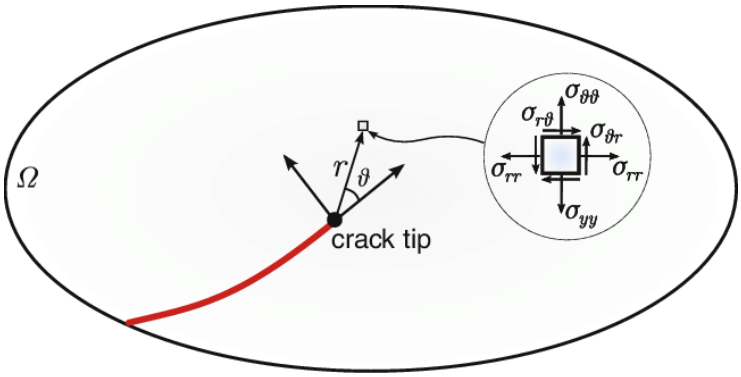

Figure IV. 13 Polar coordinates within the coordinate system of the crack tip. [230]

It can be demonstrated that the asymptotic displacement field in the vicinity of the crack tip can be described using the following basis function $\mathbf{p}(x)$, which is defined in the polar coordinate system.

$$\mathbf{p}^{\boldsymbol{T}}(\boldsymbol{x}) = [P_1, P_2, P_3, P_4] = \left[\sqrt{r}\sin\frac{\theta}{2}, \sqrt{r}\cos\frac{\theta}{2}, \sqrt{r}\sin\theta\sin\frac{\theta}{2}, \sqrt{r}\sin\theta\cos\frac{\theta}{2}\right] \quad \text{(IV. 52)}$$

The foundation function for the overall solution should encompass both the constant and linear components:

$$\mathbf{p}^{\boldsymbol{T}}(\boldsymbol{x}) = \left[1, x, y, \sqrt{r}\sin\frac{\theta}{2}, \sqrt{r}\cos\frac{\theta}{2}, \sqrt{r}\sin\theta\sin\frac{\theta}{2}, \sqrt{r}\sin\theta\cos\frac{\theta}{2}\right] \quad \text{(IV. 53)}$$

This is a recognizable basis function that has been employed in fracture analysis through the meshless Element-Free Galerkin (EFG) method in the past[231].

$$\mathbf{u}^h(\boldsymbol{x}) = \mathbf{p}^{\boldsymbol{T}}(\boldsymbol{x})\mathbf{a}(\boldsymbol{x}) \quad \text{(IV. 54)}$$

Here, $\mathbf{a}(\boldsymbol{x})$ represents a coefficient vector derived using one of the least-squares techniques aimed at minimizing the overall approximation error. Depending on whether the weighted least squares (WLS) or moving least squares (MLS) techniques are employed, the vector $\mathbf{a}(\boldsymbol{x})$ can either be treated as constants or variables, respectively.[232]

VIII.2.2 Extrinsic enrichment

An alternative method of enrichment is rooted in what's known as extrinsic enrichment. This approach utilizes extrinsic bases $p_k(x)$ to elevate the level of completeness.

$$\mathbf{u}^h(\boldsymbol{x}) = \sum_{\boldsymbol{j=1}}^{\boldsymbol{n}} \mathrm{N}_{\boldsymbol{j}}(\boldsymbol{x})\mathbf{u}_{\boldsymbol{j}} + \sum_{\boldsymbol{k=1}}^{\boldsymbol{m}} p_k(x)\mathbf{a}_{\boldsymbol{k}} \qquad \text{(IV. 55)}$$

Here, $\mathbf{a}_{\boldsymbol{k}}$ represents additional unknowns or degrees of freedom linked to the enriched solution. In a comprehensive partition of unity enrichment, Equation (IV. 55) is reformulated as:

$$\mathbf{u}^h(\boldsymbol{x}) = \sum_{\boldsymbol{j=1}}^{\boldsymbol{n}} \mathrm{N}_{\boldsymbol{j}}(\boldsymbol{x})\mathbf{u}_{\boldsymbol{j}} + \sum_{\boldsymbol{k=1}}^{\boldsymbol{m}} f_k^{pu}(x)p(x)\mathbf{a}_{\boldsymbol{k}} \qquad \text{(IV. 56)}$$

Here, $f_k^{pu}(x)$ represents a collection of partition of unity functions established within the support domain of the partition of unity enrichment Ω_{pu}, as depicted in Figure IV. 14.

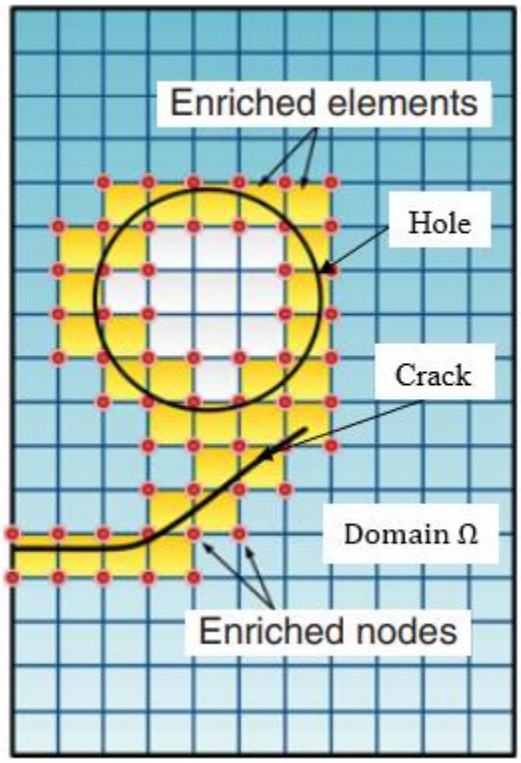

Figure IV. 14 Specification of the support domain for enrichment[233] (modified).

VIII.3 Approximation using the XFEM

Let's consider a point x within a finite element model, and suppose there exists a discontinuity within an arbitrary domain that has been discretized into n-node finite elements. In the XFEM, the following approximation is employed to compute the displacement at point x within the domain[222]:

$$\mathbf{u}^h(\boldsymbol{x}) = \mathbf{u}^{\mathbf{FE}} + \mathbf{u}^{\mathbf{enr}} = \sum_{j=1}^{n} \mathrm{N}_j(\boldsymbol{x})\mathbf{u}_j + \sum_{k=1}^{m} \mathrm{N}_k(\boldsymbol{x})\boldsymbol{\psi}(\boldsymbol{x})\mathbf{a}_k \qquad \text{(IV. 57)}$$

Here, $\mathbf{u}_j$ represents the vector of standard nodal degrees of freedom in the finite element method, $\mathbf{a}_k$ stands for the additional degrees of freedom incorporated into the conventional finite element model, and $\boldsymbol{\psi}(\boldsymbol{x})$ denotes the discontinuous enrichment function defined for the nodes within the influence (support) domain of the discontinuity.

The influence domain linked to a node situated along an edge encompasses the elements that include that specific node. Conversely, for an interior node, typically within higher-order elements, the influence domain corresponds to the element that surrounds the node. Figure IV. 15 provides a visual representation of the influence domain definitions for a node positioned at the edges of elements (a corner node) and an internal node.

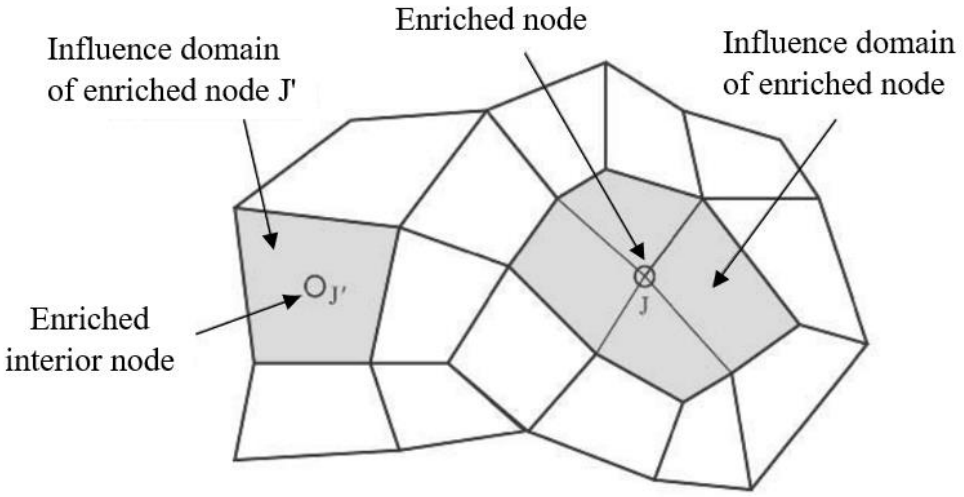

Figure IV. 15 Support domains for an edge node J and an interior node J' within a generic FE mesh[234].

In Equation (IV. 57), the initial term on the right-hand side represents the conventional finite element approach for computing the displacement field. Meanwhile, the second term encompasses the enrichment approximation, which factors in the presence of any discontinuities.

In the presence of *np* multiple discontinuities within a finite element, the expression (IV. 57) can be extended as follows:

$$\mathbf{u}^h(\boldsymbol{x}) = \mathbf{u}^{\mathbf{FE}} + \mathbf{u}^{\mathbf{enr}} = \sum_{j=1}^{n} \mathrm{N}_j(\boldsymbol{x})\mathbf{u}_j + \sum_{l=1}^{np}\sum_{k=1}^{m} \mathrm{N}_k(\boldsymbol{x})\boldsymbol{\psi}^l(\boldsymbol{x})\mathbf{a}_k^l \qquad \text{(IV. 58)}$$

VIII.3.1 The Heaviside functions

Various interpretations of the Heaviside function have emerged over time. The initial form of the Heaviside function, denoted as $H(\xi)$, can be described as a step function.

$$H(\xi) = \begin{cases} 1 & \forall \xi > 0 \\ 0 & \forall \xi < 0 \end{cases} \qquad \text{(IV. 59)}$$

the approximation (IV. 57) can be read as follows:

$$\mathbf{u}^h(\boldsymbol{x}) = \sum_{\boldsymbol{j=1}}^{\boldsymbol{n}} \mathrm{N}_{\boldsymbol{j}}(\boldsymbol{x})\mathbf{u}_{\boldsymbol{j}} + \sum_{\boldsymbol{k=1}}^{\boldsymbol{m}} \mathrm{N}_{\boldsymbol{k}}(\boldsymbol{x})H(\xi)\mathbf{a}_{\boldsymbol{k}} \tag{IV. 60}$$

To ascertain whether the approximation (IV. 60) constitutes an interpolation, we can compute the value of the field variable $\mathbf{u}(\boldsymbol{x})$ at an enriched node i using the following expression:

$$\mathbf{u}^h(\boldsymbol{x_i}) = \mathbf{u}_{\boldsymbol{i}} + H(\xi_i)\mathbf{a}_{\boldsymbol{i}} \tag{IV. 61}$$

VIII.3.2 The Crack modeling

Moës et al. [228] suggested a rearrangement of Equation (IV. 57) for modeling crack surfaces and tips in the extended finite element method, as shown below:

$$\begin{aligned}\mathbf{u}^h(\boldsymbol{x}) = &\sum_{\boldsymbol{j=1}}^{\boldsymbol{n}} \mathrm{N}_{\boldsymbol{j}}(\boldsymbol{x})\mathbf{u}_{\boldsymbol{j}} + \sum_{\boldsymbol{h=1}}^{\boldsymbol{m}} \mathrm{N}_{\boldsymbol{h}}(\boldsymbol{x})H\big(\xi(x)\big)\mathbf{a}_{\boldsymbol{h}} \\ &+ \sum_{\boldsymbol{k=1}}^{\boldsymbol{mt_1}} \mathrm{N}_{\boldsymbol{k}}(\boldsymbol{x})\left(\sum_{\boldsymbol{l=1}}^{\boldsymbol{mf}} \boldsymbol{F}_{\boldsymbol{l}}^{\boldsymbol{1}}(\boldsymbol{x})\mathbf{b}_{\boldsymbol{k}}^{\boldsymbol{l1}}\right) \\ &+ \sum_{\boldsymbol{k=1}}^{\boldsymbol{mt_2}} \mathrm{N}_{\boldsymbol{k}}(\boldsymbol{x})\left(\sum_{\boldsymbol{l=1}}^{\boldsymbol{mf}} \boldsymbol{F}_{\boldsymbol{l}}^{\boldsymbol{2}}(\boldsymbol{x})\mathbf{b}_{\boldsymbol{k}}^{\boldsymbol{l2}}\right)\end{aligned} \tag{IV. 62}$$

In this equation, m represents the collection of nodes within the support domain of crack faces (excluding crack tips), while mt_1 and mt_2 denote the sets of nodes related to the influence domains of crack tips 1 and 2, respectively. $\mathbf{u}_{\boldsymbol{j}}$ signifies the nodal displacements (standard degrees of freedom). $\mathbf{a}_{\boldsymbol{h}}$, $\mathbf{b}_{\boldsymbol{k}}^{\boldsymbol{l1}}$, and $\mathbf{b}_{\boldsymbol{k}}^{\boldsymbol{l2}}$ are vectors of supplementary nodal degrees of freedom utilized for modeling crack faces and the two crack tips, respectively. Additionally, $\boldsymbol{F}_{\boldsymbol{l}}^{\boldsymbol{i}}(\boldsymbol{x})$, where $i = 1, 2$, represents the enrichment functions specific to crack tips.

VIII.3.3 Definition of the level set function

Let's consider a domain Ω that is partitioned into two distinct and non-overlapping subdomains, Ω_1 and Ω_2, both of which share a common interface Γ, as depicted in
Figure IV. **16**. The level set function $\phi(x)$ is defined as follows:

$$\phi(x) = \begin{cases} > 0 & x \in \Omega_1 \\ = 0 & x \in \Gamma \\ < 0 & x \in \Omega_2 \end{cases} \tag{IV. 63}$$

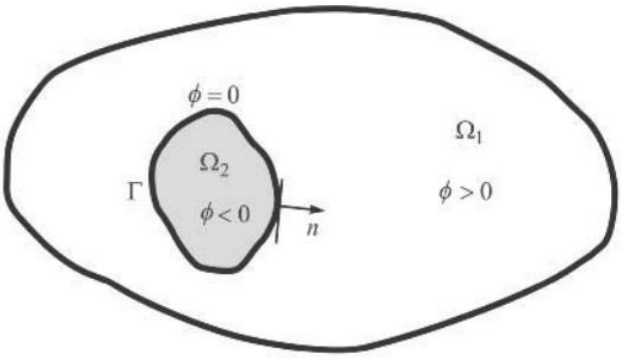

Figure IV. 16 the level set function definition[234].

One way to understand Equation (IV. 63) is to consider that the interface Γ corresponds to the contour where the level set function $\phi(x)$ equals zero.

VIII.4 Modeling anisotropic materials using XFEM

The overall approach employed for isotropic extended finite elements can be extended to tackle anisotropic problems by incorporating anisotropic enrichment functions into an anisotropic finite element framework. This involves the introduction of generalized Heaviside functions and anisotropic enrichment functions as additional degrees of freedom, alongside the standard finite element model, at specific nodes near the discontinuities.

VIII.4.1 Governing equation

The equilibrium equation's strong form can be expressed as follows:

$$\nabla . \sigma + \mathrm{f}^b = 0 \quad \text{in } \Omega \tag{IV. 64}$$

Accompanied by the subsequent boundary conditions:

$$\sigma \cdot \mathrm{n} = \mathrm{f}^t \qquad \text{on } \Gamma_t\text{: external traction} \tag{IV. 65}$$

$$\mathbf{u} = \bar{\mathbf{u}} \qquad \text{on } \Gamma_\mathrm{u}\text{: prescribed displacement} \tag{IV. 66}$$

$$\sigma \cdot \mathrm{n} = 0 \qquad \text{on } \Gamma_\mathrm{c}\text{: traction free crack} \tag{IV. 67}$$

Here, Γ_t, Γ_u, and Γ_c denote the boundaries associated with traction, displacement, and cracks, respectively. In this context, σ represents the stress tensor, while f^b and f^t represent the body force and external traction vectors, respectively.

The variational representation of the boundary value problem can be defined as follows:

$$W^{\mathrm{int}} = W^{\mathrm{ext}} \tag{IV. 68}$$

Or

$$\int_\Omega \sigma \cdot \delta\varepsilon \, \mathrm{d}\Omega = \int_\Omega \mathrm{f}^b \cdot \delta \mathrm{u} \, \mathrm{d}\Omega + \int_\Omega \mathrm{f}^t \cdot \delta \mathrm{u} \, \mathrm{d}\Gamma \tag{IV. 69}$$

VIII.4.2 XFEM discretization

Let's examine a body in a state of equilibrium, subject to boundary conditions in the form of tractions and displacements, which also involves the presence of a crack, as illustrated in Figure IV. 17.

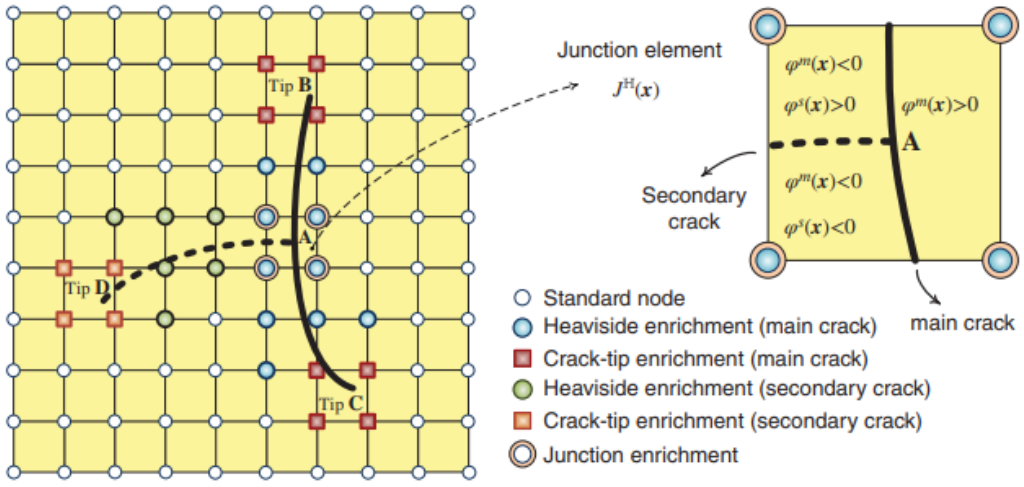

Figure IV. 17 crack in an orthotropic domain

The discretization of Equation (IV. 69) through the XFEM approach, as indicated in Equation (IV. 63), leads to the formation of a discrete set of linear equilibrium equations:

$$\mathbf{K}\mathbf{u}^h = \mathbf{f} \tag{IV. 70}$$

In this context, **K** represents the stiffness matrix, $\mathbf{u}^h$ is the vector encompassing degrees of nodal freedom, incorporating both classical and enriched ones, and **f** stands for the vector representing external forces. The computation of the global matrix and vectors involves the assembly of matrices and vectors from individual elements. Specifically, for each element, the matrices **K** and vector **f** are defined as follows:

$$k_{ij}^e = \begin{bmatrix} k_{ij}^{uu} & k_{ij}^{ua} & k_{ij}^{ub} \\ k_{ij}^{au} & k_{ij}^{aa} & k_{ij}^{ab} \\ k_{ij}^{bu} & k_{ij}^{ba} & k_{ij}^{bb} \end{bmatrix} \tag{IV. 71}$$

$$\mathrm{f}_i^e = \left\{\mathrm{f}_\mathrm{i}^\mathrm{u}\,\mathrm{f}_\mathrm{i}^\mathrm{a}\,\mathrm{f}_\mathrm{i}^{\mathrm{b1}}\,\mathrm{f}_\mathrm{i}^{\mathrm{b2}}\,\mathrm{f}_\mathrm{i}^{\mathrm{b3}}\,\mathrm{f}_\mathrm{i}^{\mathrm{b4}}\right\}^T \tag{IV. 72}$$

and $\mathbf{u}^h$ represents the vector containing nodal parameters:

$$\mathbf{u}^h = \{u.\,a.\,b_1 b_2 b_3\, b_4\}^T \tag{IV. 73}$$

With

$$k_{ij}^{rs} = \int_{\Omega^e} (\boldsymbol{B}_i^r)^T \boldsymbol{D}\boldsymbol{B}_j^S d\Omega \qquad (r,s = u,a,b) \tag{IV. 74}$$

$$f_i^u = \int_{\Gamma_t} N_i \mathbf{f}^t \mathrm{d}\Gamma + \int_{\Omega^e} N_i\, \mathbf{f}^b d\Omega \tag{IV. 75}$$

$$f_i^a = \int_{\Gamma_t} N_i H \mathbf{f}^t \mathrm{d}\Gamma + \int_{\Omega^e} N_i\, H \mathbf{f}^b d\Omega \tag{IV. 76}$$

$$f_i^{\alpha b} = \int_{\Gamma_t} N_i F_\alpha \mathbf{f}^t \mathrm{d}\Gamma + \int_{\Omega^e} N_i\, F_\alpha \mathbf{f}^b d\Omega \qquad (\alpha = 1,2,3\,and\,4) \tag{IV. 77}$$

Here, $\boldsymbol{B_i^u}$, $\boldsymbol{B_i^a}$, and $\boldsymbol{B_i^b}$ denote the derivatives of shape functions as defined in Equations (IV. 78), (IV. 79), and (IV. 80), respectively.

$$\boldsymbol{B_i^u} = \begin{bmatrix} N_{i,x} & 0 \\ 0 & N_{i,y} \\ N_{i,y} & N_{i,x} \end{bmatrix} \tag{IV. 78}$$

$$\boldsymbol{B_i^a} = \begin{bmatrix} (N_i H)_{,x} & 0 \\ 0 & (N_i H)_{,y} \\ (N_i H)_{,y} & (N_i H)_{,x} \end{bmatrix} \tag{IV. 79}$$

$$\boldsymbol{B_i^b} = \left[B_i^{b1} B_i^{b2} B_i^{b3} B_i^{b4}\right] \tag{IV. 80}$$

Enrichment functions for crack tips are derived from the analytical solution for displacement in the vicinity of the crack tip.

$$\{F_l(r,\theta)\}_{l=1}^{4} = \left\{\sqrt{r}\cos\frac{\theta_1}{2}\sqrt{g_1(\theta)}, \sqrt{r}\cos\frac{\theta_2}{2}\sqrt{g_2(\theta)}, \sqrt{r}\sin\frac{\theta_1}{2}\sqrt{g_1(\theta)}, \right. \\ \left. , \sqrt{r}\sin\frac{\theta_2}{2}\sqrt{g_2(\theta)}\right\} \tag{IV. 81}$$

Equation (IV. 81) is not directly applicable in isotropic materials since it can result in undefined (0/0) expressions[235]. An immediate solution is to utilize the conventional isotropic enrichment functions instead.

$$\{F_l(r,\theta)\}_{l=1}^{4} = \left\{\sqrt{r}\cos\frac{\theta}{2}, \sqrt{r}\sin\frac{\theta}{2}\cos\frac{\theta}{2}, \sqrt{r}\sin\theta\sin\frac{\theta}{2}\right\} \tag{IV. 82}$$

VIII.4.3 Stress Intensity Factor (SIF) calculations

The stress intensity factor (SIF) is a crucial parameter that characterizes the fracture behavior of a crack tip. In this context, we employ the domain integral method introduced by [236] to assess the stress intensity factors under mixed mode (modes I, II, and III illustrated in Figure IV. 18) conditions in homogeneous orthotropic materials.

The conventional path-independent J integral for the cracked body is formally defined as [237]:

$$J = \int_{\Gamma}\left[W_S\delta_{1j} - \sigma_{ij}\frac{\partial u_j}{\partial x_1}\right]\mathbf{n}_j d\Gamma \tag{IV. 83}$$

Here, $\mathbf{n}_j$ represents the jth component of the outward unit normal to Γ, δ_{1j} is the Kronecker delta, W_S stands for the strain energy density for linear elastic materials, and Γ refers to an arbitrary contour surrounding the crack tip, ensuring that it encompasses no other cracks or discontinuities.

Equation (IV. 83) is not particularly suitable for finite element solutions. An alternative expression of the J integral can be derived by employing the divergence theorem in the context of the domain integral approach, as introduced by [238].

$$J = -\int_A \left[W_S \delta_{1j} - \sigma_{ij} \frac{\partial u_j}{\partial x_1}\right] \frac{\partial q}{\partial x_j} d\Gamma \qquad \text{(IV. 84)}$$

Here, A represents the area encompassing the crack tip, which is the inner region of Γ, and q is a function that varies smoothly. Γ is typically considered as a circular or rectangular area, centered at the crack tip.

Following the proposals by Dolbow[223] and Moës et al. [228], the finite element model employs a straightforward function, q, which linearly transitions from $q = 1$ at the crack tip to $q = 0$ at the outer boundary Γ (refer to Figure IV. 19). Consequently, elements situated away from the boundary can be disregarded. It's important to note that the value within the parentheses in Equation (IV. 84) need not be calculated within the region where q remains constant, leading to a vanishing gradient. From a numerical perspective, despite the often-high stress gradient in elements containing a crack tip, it is more appropriate to avoid positioning the contour within elements that encompass a crack tip [235].

The interaction integral method, which relies on establishing an auxiliary state, is employed to derive mixed-mode stress intensity factors. Consider two equilibrium conditions: state 1 represents the actual state, while state 2 corresponds to an auxiliary state tailored to the problem's geometry.

The selection of auxiliary stress and strain states should ensure the fulfillment of both the equilibrium equation and the absence of traction on the crack surface within region A. One possible choice is to employ the displacement and stress fields near the crack tip as described by Sih et al. [239] and Asadpoure et al. [235].

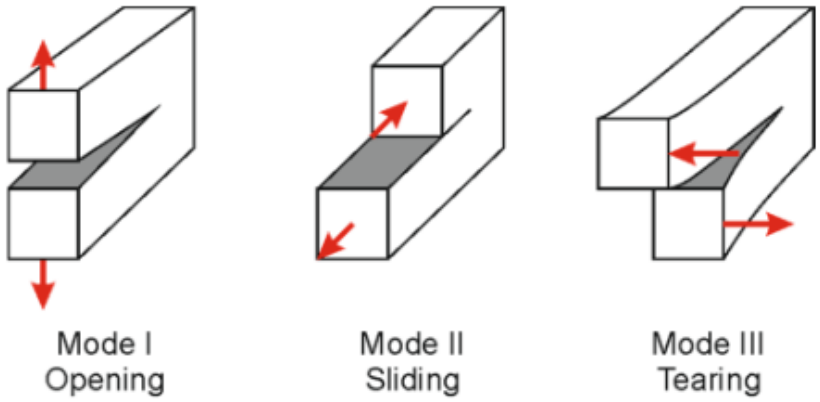

Figure IV. 18 The three different modes of fracture [240].

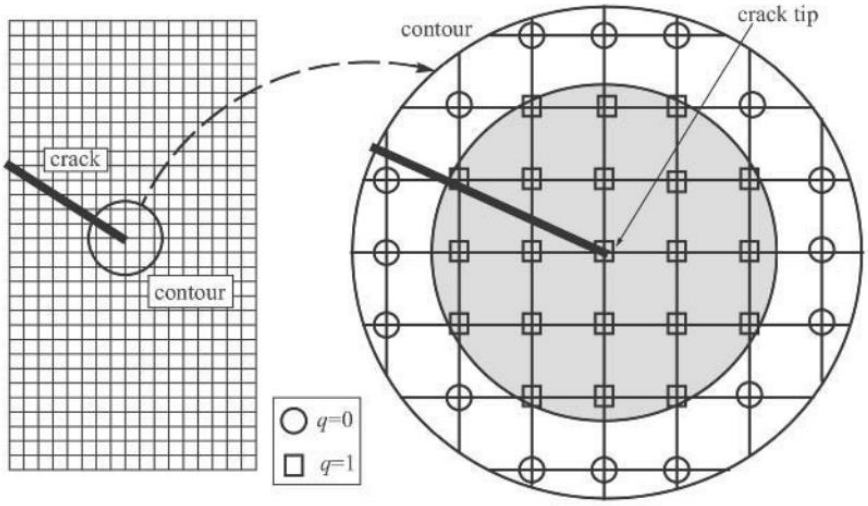

Figure IV. 19 Values of the function q at the nodes [228].

$$\sigma_{11}^{aux} = \frac{K_I^{aux}}{\sqrt{2\pi r}} Re\left[\frac{S_1 S_2}{S_1 - S_2}\left\{\frac{S_2}{\sqrt{\cos\theta + S_2 \sin\theta}} - \frac{S_1}{\sqrt{\cos\theta + S_1 \sin\theta}}\right\}\right] + \frac{K_{II}^{aux}}{\sqrt{2\pi r}} Re\left[\frac{1}{S_1 - S_2}\left\{\frac{S_2^2}{\sqrt{\cos\theta + S_2 \sin\theta}} - \frac{S_1^2}{\sqrt{\cos\theta + S_1 \sin\theta}}\right\}\right] \quad \text{(IV. 85)}$$

$$\sigma_{22}^{aux} = \frac{K_I^{aux}}{\sqrt{2\pi r}} Re\left[\frac{1}{S_1 - S_2}\left\{\frac{S_2}{\sqrt{\cos\theta + S_2 \sin\theta}} - \frac{S_1}{\sqrt{\cos\theta + S_1 \sin\theta}}\right\}\right] + \frac{K_{II}^{aux}}{\sqrt{2\pi r}} Re\left[\frac{1}{S_1 - S_2}\left\{\frac{1}{\sqrt{\cos\theta + S_2 \sin\theta}} - \frac{1}{\sqrt{\cos\theta + S_1 \sin\theta}}\right\}\right] \quad \text{(IV. 86)}$$

$$\sigma_{12}^{aux} = \frac{K_I^{aux}}{\sqrt{2\pi r}} Re\left[\frac{S_1 S_2}{S_1 - S_2}\left\{\frac{1}{\sqrt{\cos\theta + S_2 \sin\theta}} - \frac{1}{\sqrt{\cos\theta + S_1 \sin\theta}}\right\}\right] + \frac{K_{II}^{aux}}{\sqrt{2\pi r}} Re\left[\frac{1}{S_1 - S_2}\left\{\frac{s_1}{\sqrt{\cos\theta + S_1 \sin\theta}} - \frac{S_2}{\sqrt{\cos\theta + S_2 \sin\theta}}\right\}\right] \quad \text{(IV. 87)}$$

$$u_1^{aux} = K_I^{aux}\sqrt{\frac{2r}{\pi}} Re\left[\frac{1}{S_1 - S_2}\left\{S_1 P_2\sqrt{\cos\theta + S_2 \sin\theta} - S_2 P_1\sqrt{\cos\theta + S_1 \sin\theta}\right\}\right] + K_{II}^{aux}\sqrt{\frac{2r}{\pi}} Re\left[\frac{1}{S_1 - S_2}\left\{P_2\sqrt{\cos\theta + S_2 \sin\theta} - P_1\sqrt{\cos\theta + S_1 \sin\theta}\right\}\right] \quad \text{(IV. 88)}$$

$$u_2^{aux} = K_I^{aux}\sqrt{\frac{2r}{\pi}} Re\left[\frac{1}{S_1 - S_2}\left\{S_1 q_2\sqrt{\cos\theta + S_2 \sin\theta} - S_2 q_1\sqrt{\cos\theta + S_1 \sin\theta}\right\}\right] + K_{II}^{aux}\sqrt{\frac{2r}{\pi}} Re\left[\frac{1}{S_1 - S_2}\left\{q_2\sqrt{\cos\theta + S_2 \sin\theta} - q_1\sqrt{\cos\theta + S_1 \sin\theta}\right\}\right] \quad \text{(IV. 89)}$$

In the equation, the "aux" superscript represents the auxiliary state, while S_1 and S_2 denote material parameters at the crack tip, which are determined by solving the characteristic equation of the anisotropic stress function in a homogeneous partial differential equation[241].

By combining the actual and auxiliary states to compute the J integral, we can express it as follows:

$$J = J^{act} + J^{aux} + M \tag{IV. 90}$$

In this equation, J represents the superposition state, while J^{act} and J^{aux} represent the J integrals for the actual and auxiliary states, respectively, with:

$$M = \int_A \left[\sigma_{ij}\frac{\partial u_1^{aux}}{\partial x_1} + \sigma_{ij}^{aux}\frac{\partial u_i}{\partial x_1} - W^M\delta_{ij}\right]\frac{\partial q}{\partial x_j}dA \tag{IV. 91}$$

where $W^M = 0.5\left(\sigma_{ij}\varepsilon_{ij}^{aux} + \sigma_{ij}^{aux}\varepsilon_{ij}\right)$ corresponds to linear elastic conditions.

The strain of the auxiliary field can be selected based on either the strain-stress relationship, $\varepsilon_{ij}^{aux} = C_{ijkl}\sigma_{kl}^{aux}$, or as the symmetric part of the displacement gradient, $\varepsilon_{ij}^{aux} = 0.5\left(u_{i,j}^{aux} + u_{j,i}^{aux}\right)$; these choices are compatible with each other as long as the material is homogeneous and C_{ijkl} has a consistent value in the domain. After performing some manipulations[225, 235]:

$$M = 2t_{11}K_IK_{II}^{aux} + t_{12}(K_IK_{II}^{aux} + K_I^{xau}K_{II}) + 2t_{22}K_{II}K_{II}^{aux} \tag{IV. 92}$$

Where:

$$t_{11} = \frac{c_{22}}{2}\,Im\left(\frac{S_1 + S_2}{S_1S_2}\right) \tag{IV. 93}$$

$$t_{12} = -\frac{c_{22}}{2}Im\left(\frac{1}{S_1S_2}\right) + \frac{c_{11}}{2}Im(S_1S_2) \tag{IV. 94}$$

$$t_{22} = \frac{c_{11}}{2}Im(S_1S_2) \tag{IV. 95}$$

The stress intensity factor can be determined by considering two states and solving a system of linear algebraic equations. These two states are state 1, where $K_I^{aux} = 1, K_{II}^{aux} = 0$, and state 2, where $K_I^{aux} = 0, K_{II}^{aux} = 1$. By calculating M from both equations (IV. 91) and (IV. 92) and solving the system of linear algebraic equations, we obtain the actual mixed-mode stress intensity factors associated with state 1 and state 2 [225, 235]:

$$M^{(1)} = 2t_{11}K_I + t_{12} \tag{IV. 96}$$

$$M^{(2)} = t_{12}K_I + 2t_{22}K_{II} \tag{IV. 97}$$

IX. Conclusion

Cracking is a significant issue that wind turbine blades encounter during their operation under various loads induced by wind, gravity, and other forces. In this chapter, we provided an overview of cracks and introduced the necessary mathematical equations, starting with stress concentration around the fracture. We also explored the stress intensity factor, a crucial parameter in fracture analysis, as it determines the stress at the crack tip and provides insight into the crack's propensity to propagate and its direction of propagation. Additionally, we defined fracture propagation and presented several methods for calculating crack propagation.

One of the key topics covered in Chapter Four is the Extended Finite Element Method (XFEM), which is particularly relevant for studying fractures and their propagation. We explained how XFEM can be applied to analyze crack expansion in anisotropic materials.

In conclusion, it is imperative to emphasize the importance of ongoing research and learning about fracture phenomena in wind turbines. This area of study is vital given its relevance to the broader field. Therefore, we stress the significance of continued exploration of wind turbine fractures to mitigate associated issues and potential disasters.

CHAPTER V

RESULTS AND DISCUSSION

I. Introduction

The wind turbine blade holds a prominent position within the realm of renewable energy systems due to its crucial role in generating power for a wide range of applications, including industrial, agricultural, and residential use. The production of a wind turbine involves several essential steps:

Firstly, the blade's design process is initiated, focusing on enhancing its aerodynamic performance. Next, an in-depth analysis of the blade's structure is conducted, involving the selection of suitable materials for manufacturing. This material choice often seeks to strike a balance between cost-effectiveness and high durability. The material selection process is informed by a comprehensive examination of vibrations to ensure the material's ability to withstand cyclic loads during operation. Furthermore, a fatigue analysis is performed to determine the blade's expected lifespan before it undergoes manufacturing. Lastly, a fracture analysis is conducted to assess the material's resistance to crack propagation, as extensively discussed in the preceding four chapters of this thesis. Figure V. 1 shows the study flow for wind turbine optimization.

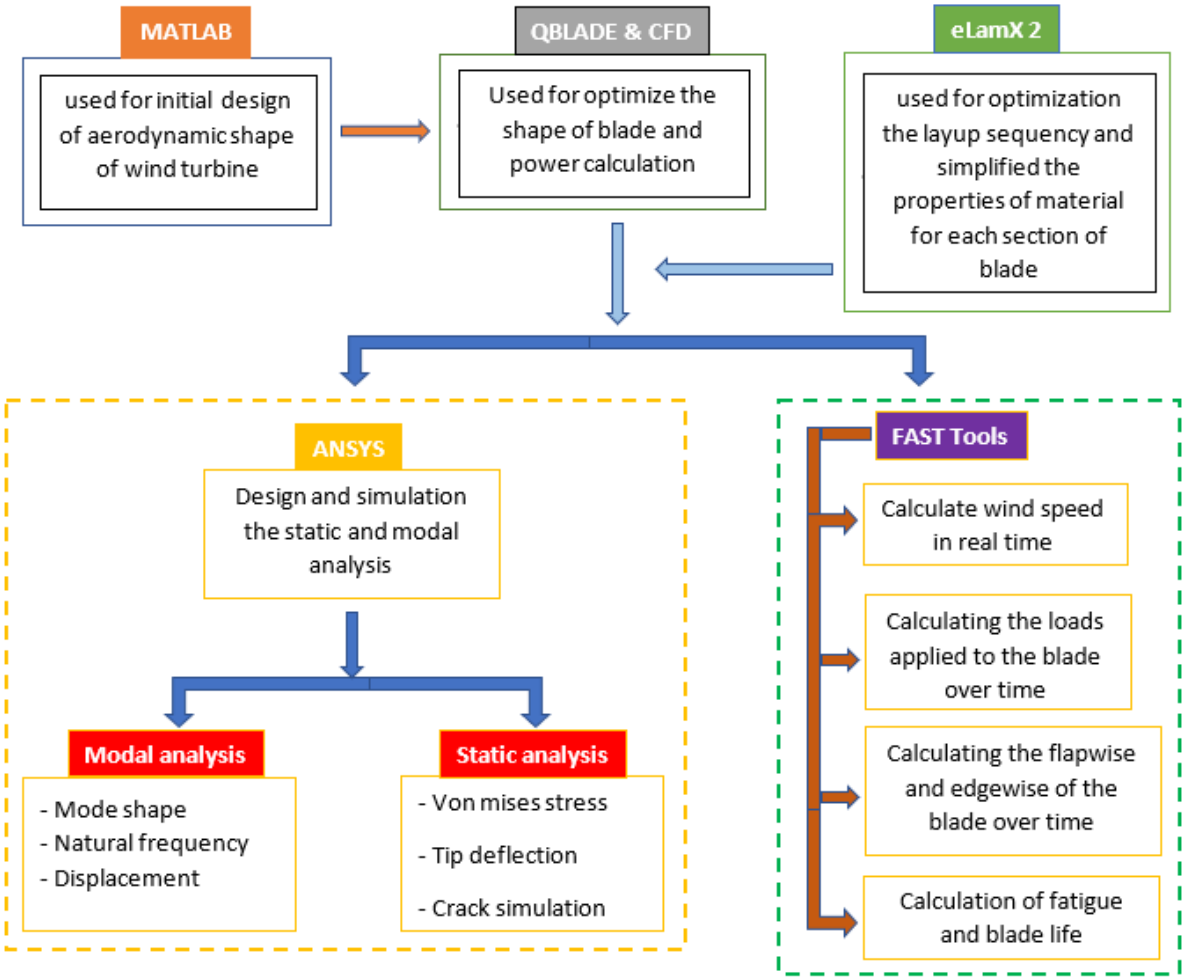

Figure V. 1 flow chart to study and optimize the blade

II. Wind Turbine Blade Design and Optimization

The process of blade design stands as a pivotal phase in the comprehensive examination of wind turbines. Blade design comprises multiple essential stages, with a primary focus on selecting the suitable airfoil. This choice of airfoil plays a fundamental role in shaping the external aerodynamics of the blade, ultimately facilitating the generation of the required power output.

In a subsequent phase, meticulous calculations are carried out to determine both the chord length and the angle of twist. These parameters hold significant influence over the external configuration of the blade and bear primary responsibility for both its aerodynamic profile and the power harnessed from it.

II.1 Select the blade airfoil

Selecting the optimal airfoil for a wind turbine blade presents a complex task, hinging on various factors like blade length, power requirements, and the Reynolds number, predominantly influenced by blade dimensions such as height and length. Additionally, the choice of airfoil significantly impacts the structural integrity and longevity of the blade. Consequently, there is no one-size-fits-all method for airfoil selection, and it typically necessitates a combination of experimentation and simulation.

Nonetheless, certain standards and criteria exist for comparing airfoils and determining the most suitable among them, such as evaluating the lift-to-drag coefficient ratio. In this research, our focal point centers on enhancing small wind turbine blades, tailored for providing electricity to residences and small agricultural operations. As such, we've opted for a 5-kW wind turbine, aligning with the required specifications. Consequently, the selection of the appropriate airfoil for smaller blades, like NACA4412, NACA4415, NACA4418, and NACA4421, as detailed in the initial chapter, becomes paramount.

The Reynolds number experiences variations relative to both the chord (c) and radius (r) parameters. Consequently, determining an initial value to initiate the calculation process can be challenging. To streamline the calculation process for a 5 kW Horizontal Axis Wind Turbine (HAWT) featuring a 5-meter rotor diameter, an average Reynolds number is employed. This approach aims to simplify the process. Notably, at the tip chord of 0.106 meters, the Reynolds number registers at approximately 450,000. For the computation of lift and drag coefficients, the XFoil software was harnessed. XFoil is integrated into QBlade, and the ensuing outcomes are visually depicted in the Figure V. 2 below.

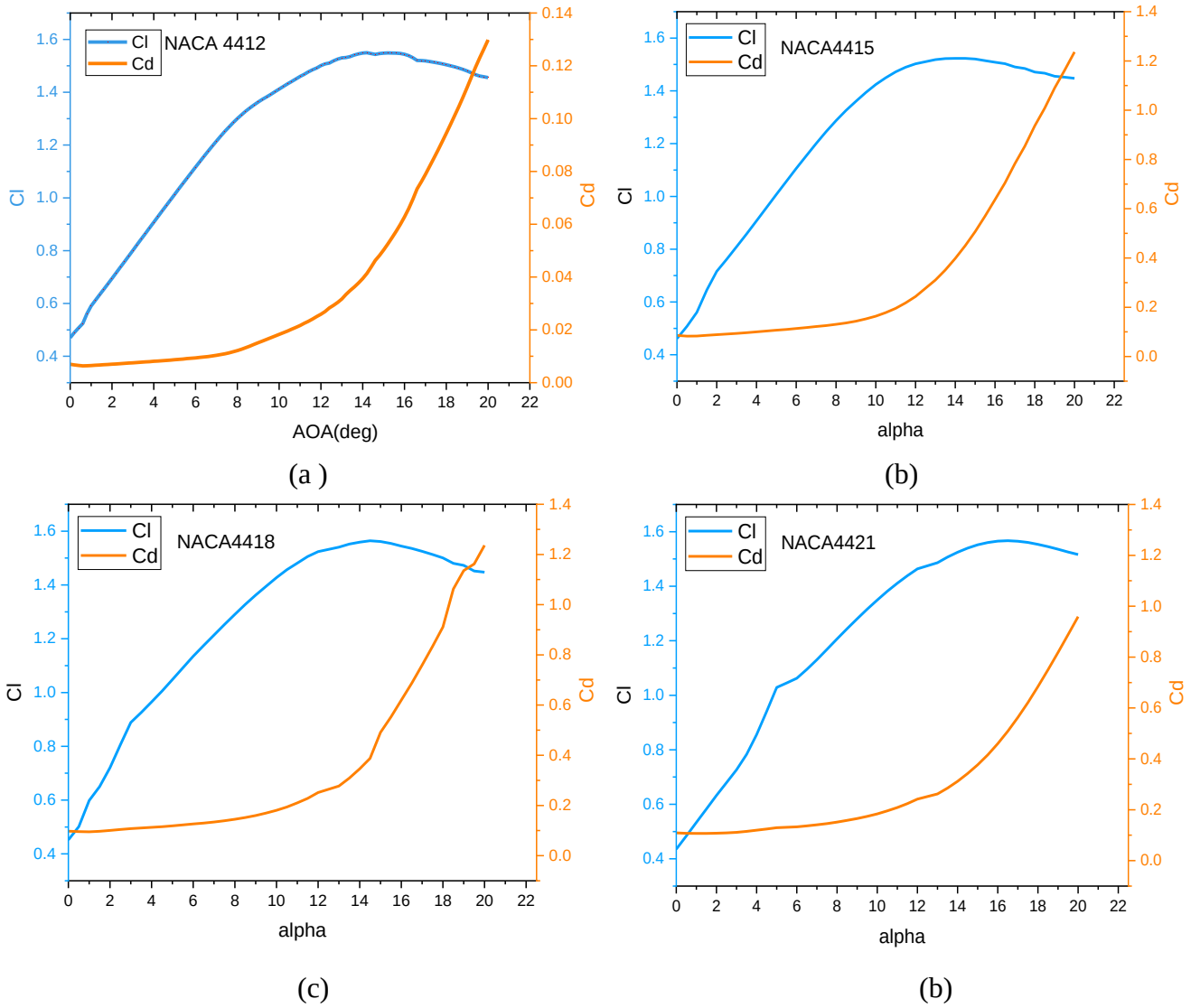

Figure V. 2 Cl and Cd for a) NACA4415, b) NACA4415, c) NACA4418, and d) NACA4421

In Figure V. 3, we observe a comparison of lift and drag coefficients among the analyzed airfoils. Notably, the NACA4415 airfoils exhibit the highest lift coefficient at an angle of attack of 15, whereas the NACA4418 airfoils display the lowest drag coefficient at the same angle of attack.

Figure V. 4 illustrates the comparison of the lift coefficient to drag coefficient ratio for evaluating the suitability of various airfoils for the blade being examined.

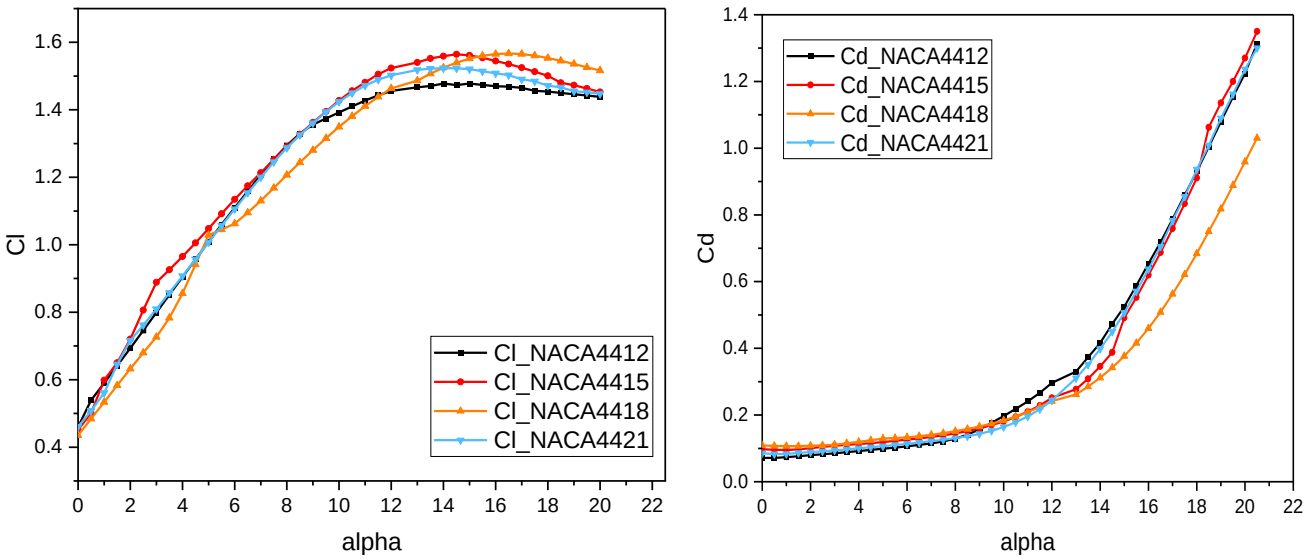

(a) (b)

Figure V. 3 comparison of a) the lift, and b) the drag coefficients among the analyzed airfoils

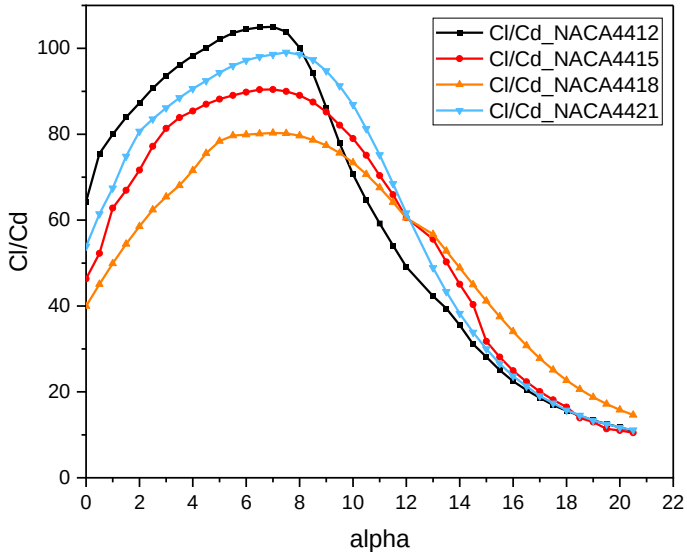

Figure V. 4 Cl/Cd for the studied airfoils

Figure V. 4 clearly illustrates that when comparing the curves, the NACA4412 airfoil stands out with the highest value of the coefficient ratio Cl/Cd. Therefore, it is the airfoil of choice for our blade design, as it achieves the maximum Cl/Cd ratio, reaching 119 at an angle of attack (AOA) of 6°. This angle is considered the design or optimal angle of attack, with a corresponding lift coefficient of $C_{l,design}$= 1.12.

II.2 Blade initial design

Once we've identified the suitable airfoil in the previous stage, the next critical step in designing the initial wind turbine blade shape involves defining both the chord length and the twist angle. For this purpose, we employ the Betz equations within a custom MATLAB program, allowing us to compute the chord length (c) and twist angle (θ). In order to derive the blade's initial shape, we need to establish specific design parameters, including the average wind speed, the design rotational speed, and the number of blade section set at 10 for our analysis (refer to Figure I. 20), among other parameters detailed in Table V. 1.

Table V. 1 Initial design parameters of 5 kW small wind turbine.

Design parameter	Value	Unit
Rated power	5	[kW]
Design Wind speed	10.5	m/s]
Number of blades	3	[-]
Design tip speed ratio	6	[-]
Design angle of attack	6	[°]
Rotor radius	2.5	[m]
Design rotational speed	240	[rpm]
Density of air	1.22	[Kg/m^3]
Airfoil type	NACA4412	[-]

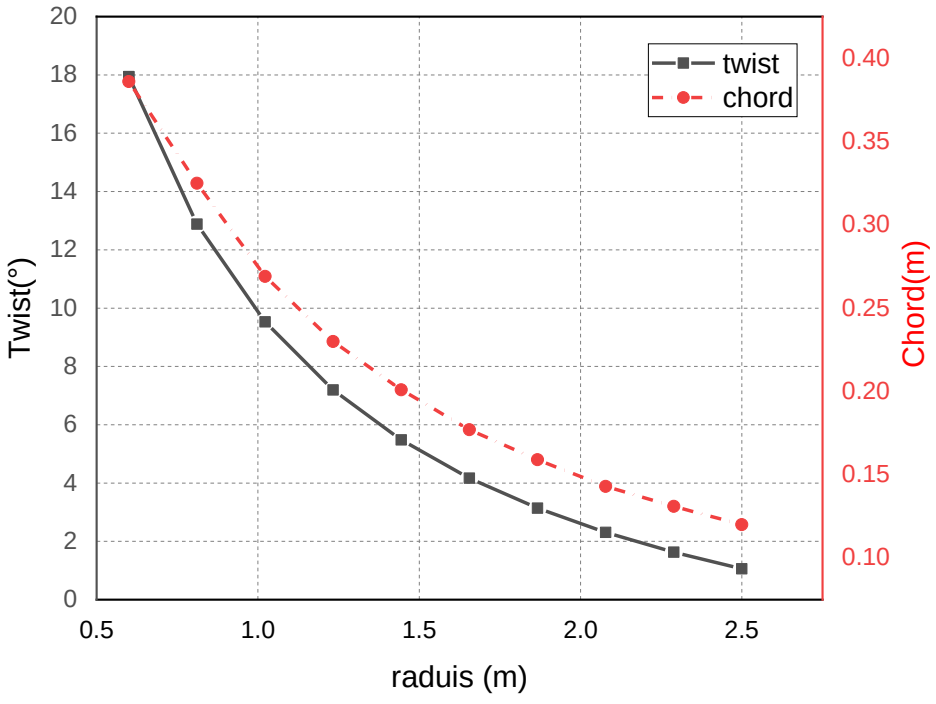

Figure V. 5 Chord and Twist angle distribution of the 2.5m small wind turbine blade

The wind turbine blade's chord distribution and twist angle, obtained using the Betz equation and a MATLAB program, are illustrated in Figure V. 5. The key specifications include a root chord length of 386 mm, a tip chord length of 120 mm, a hub length of 200 mm, an 80 mm root diameter, a 200 mm length from root to blade neck, and a twist angle that decreases from 18° at the root chord to 1° at the tip chord. These specifications are summarized in Table V. 2. Figure V. 6 displays the impact of the twist angle and chord on the airfoil in blade design.

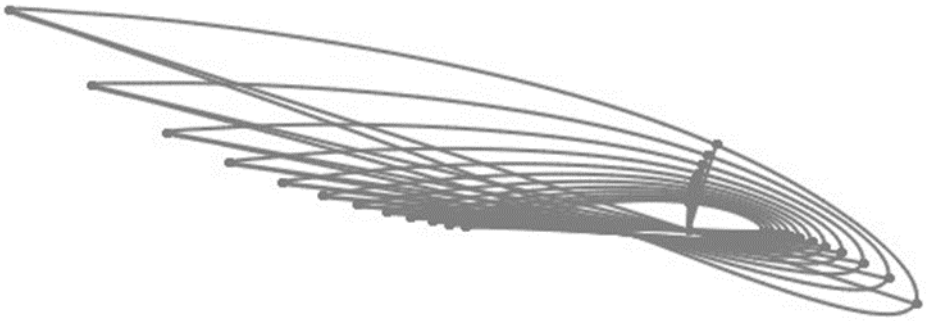

Figure V. 6 Chord and twisted airfoil NACA4412

Table V. 2 design Specifications of 2.5m small blade

Parameter	**specification**
Root chord length	0.386 m
Tip chord length	0.120 m
Blade length	2.5 m
Root diameter	0.080 m
Hub length	0.200 m
Hub to neck length	0.200 m

II.3 Blade optimization design

To achieve the optimal aerodynamic blade design, we will employ the QBlade program[242], which relies on BEM theory for its computations. This program is instrumental in optimizing blade shape and determining aerodynamic loads. The primary goal of the wind turbine blade's optimization process is to discover the most efficient design for maximizing power generation. While the Betz method guided the initial design of the chord and twist angle, one drawback is its lack of linearity in these design aspects. Therefore, this analysis aims to optimize the blade through a linearization approach. The optimization process is to fix the chord and twist angle values linearly decrease from the blade root to the tip using the following equations:

$$c_{i,n} = c_{t,0} + \left(0.7c_{r,0} - c_{t,0}\right)\frac{(n-1)}{N}\frac{r_i}{R} \qquad n = 1,2,\dots,N+1 \tag{V. 1}$$

$$\theta_{i,n} = \theta_{t,0} + \left(\theta_{r,0} - \theta_{t,0}\right)\frac{(n-1)}{N}\frac{r_i}{R} \qquad n = 1,2,\dots,N+1 \tag{V. 2}$$

where n is the number of linearized chord lines, $c_{i,n}$is the chord of the blade element section at the nth linearized chord line, $\theta_{i,n}$is the twist angle of the blade element section at the nth linearized twist line. $c_{t,0}$, $c_{r,0}$ and $\theta_{t,0}$, $\theta_{r,0}$are the chords and twist at the blade tip and root of the preliminary blade respectively, and N is the number of nth linearized line divisions for our study equal 4. Figure V. 7 show the preliminary and linear design of the chord and twist.

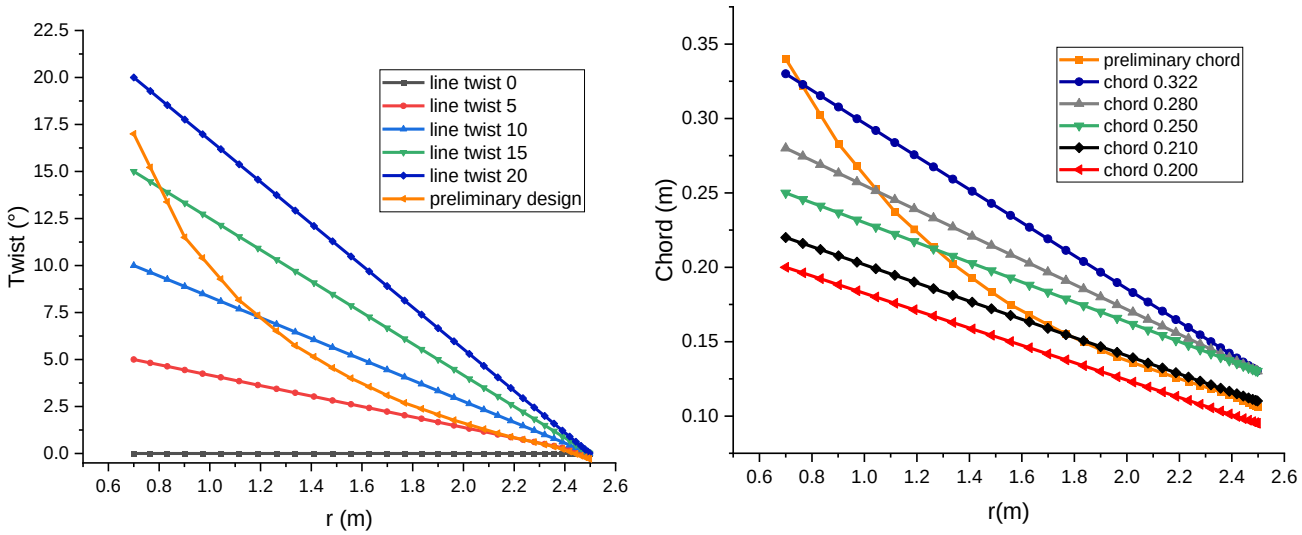

(a) (b)

Figure V. 7 (a) blade twist and (b) blade chord of the preliminary and linearization

After setting the division number to N=4, as shown in Figure V. 7 (a) and (b), it becomes evident how to linearize the chord and twist angle. To simplify and optimize the design, we first determine the ideal chord and subsequently use this chord value to select the optimal twist angle. Figure V. 8 illustrates the power and power coefficient comparisons between the preliminary and linear designs.

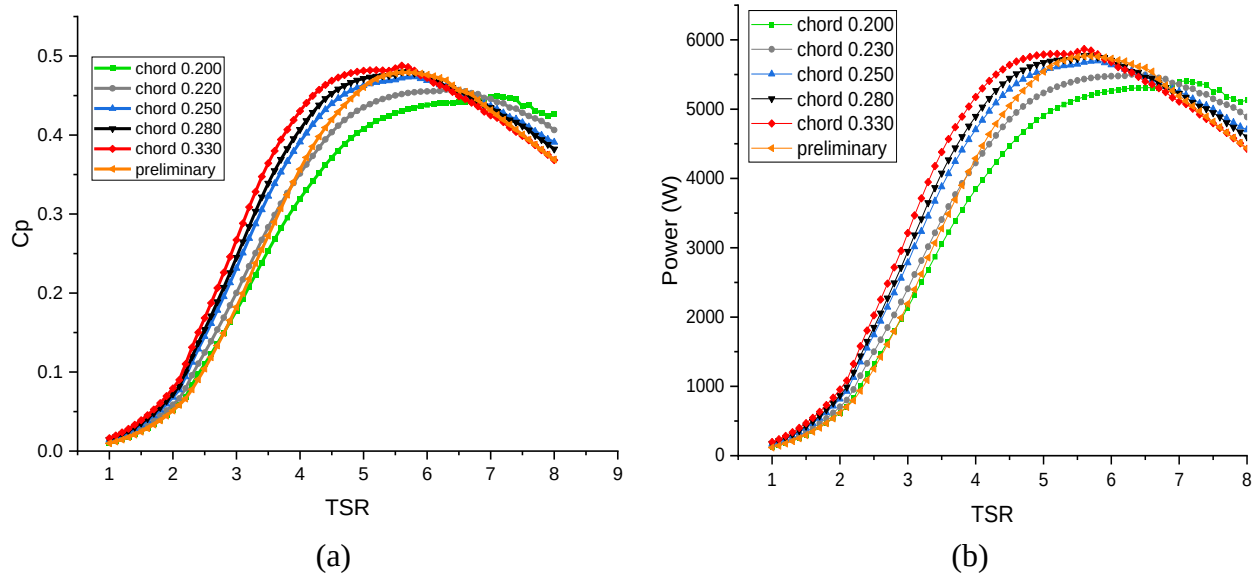

(a) (b)

Figure V. 8 (a) power coefficient and (b) wind turbine power of preliminary and linearization chord.

As depicted in Figure V. 8, there is a noticeable variation in power concerning Tip Speed Ratio (TSR) across different chord values. Notably, the maximum power output occurs at a low TSR with a chord length of 0.330. Consequently, given this chord's favorable power and power coefficient characteristics, it serves as a suitable choice for designing the optimal blade. Subsequently, we will determine the optimal twist angle to complement the blade. Figure V. 9 shows the power and power coefficient of a linear twist angle.

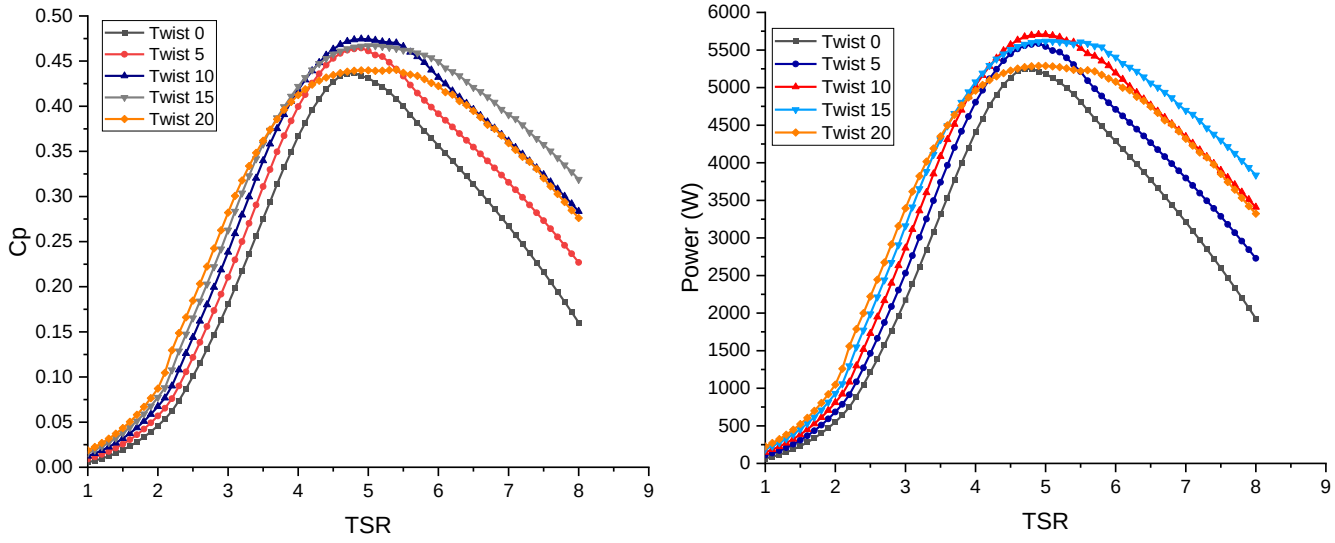

(a) (b)

Figure V. 9 (a) power coefficient, and (b) wind turbine power of the linearization twist

According to the obtained results, we can say that the optimal linear chord is 0.330 and the optimal linear twist angle is 10°, therefore we can consider these two values in the design of the wind turbine blade. To complete the design process, we must specify the rest of the design parameters, such as the design rotational speed and the design pitch. Figure V. 10 shows the design rotation speed, and Figure V. 11 shows the design pitch angle.

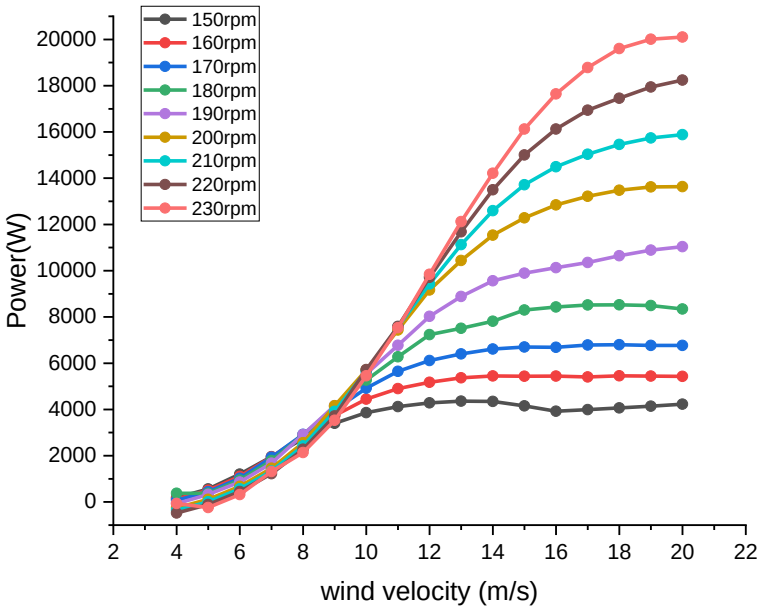

Figure V. 10 design rotational speed of optimal wind turbine blade

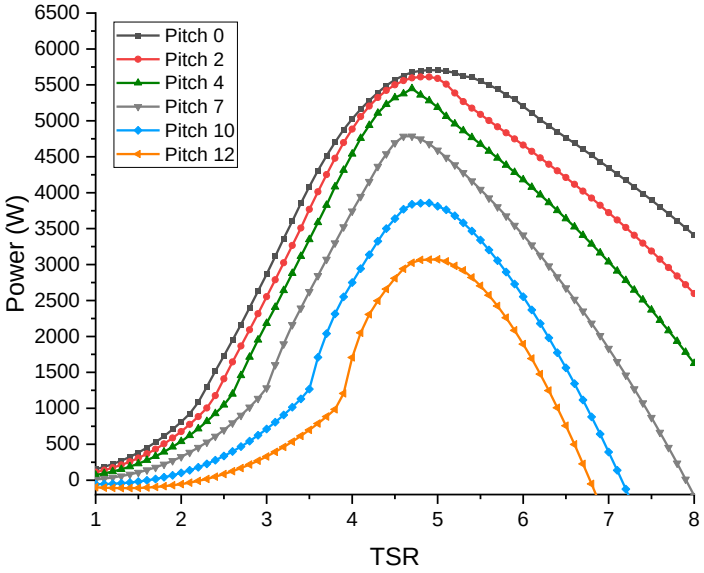

Figure V. 11 design pitch angle of wind turbine

Examining Figure V. 10, which presents the wind turbine's power output across various rotational speeds, reveals that the most suitable rotational speed for our design is 160 rpm. Furthermore, Figure V. 11, illustrating power variations with pitch angle adjustments, distinctly indicates that the optimal angle for

maximum power generation is 0 degrees. In conclusion, the optimal design parameters for the 5-kW wind turbine are succinctly summarized in Table V. 3.

Table V. 3 Optimal Design Parameter of Wind Turbine Blade

Blade parameter	**Parameter value**	**Unite**
Rated Pawer	5	kW
Rotor Diameter	5	m
Rotational Design Speed	160	RPM
Root Chord Length	0.330	m
Tip Chord Length	0.120	m
Number of Blade	3	-
Design Wind Speed	10	m/s
Design Tip Speed Ratio	5	-
Airfoil	NACA4412	-

Now that we have established the appropriate chord and twist angle, we can conduct a tailored comparison between the initial blade design and the enhanced version. As depicted in Figure V. 12, a noticeable disparity exists between the initial design, following the parabolic curve prescribed by Betz theory (BEM), and the new improved design. The improved design, founded on a linearization approach, exhibits a straight-line configuration from root to tip for both the chord and twist angle.

Figure V. 13 showcases the power coefficient and power curve for both the initial and optimized wind turbine designs. The observation drawn from Figure V. 13 reveals an augmentation in the power coefficient for the improved design. This increase occurs at lower TSR ranging from 1 to 4, aligning closely with the initial design at intermediate TSR values. Furthermore, the power coefficient experiences a surge at TSR values exceeding 6. This underscores the significance of the enhanced design, which elevates the power coefficient at both low and high rotational speeds, resulting in an average improvement of up to 8%.

The findings presented in Figure V. 13 lead to the conclusion that the design enhancement has a pronounced impact on increasing the wind turbine's power, notably at moderate wind speeds starting from 8 m/s. Furthermore, the power improvement at the rated wind speed reaches 7%, a notable enhancement when compared to the initial design.

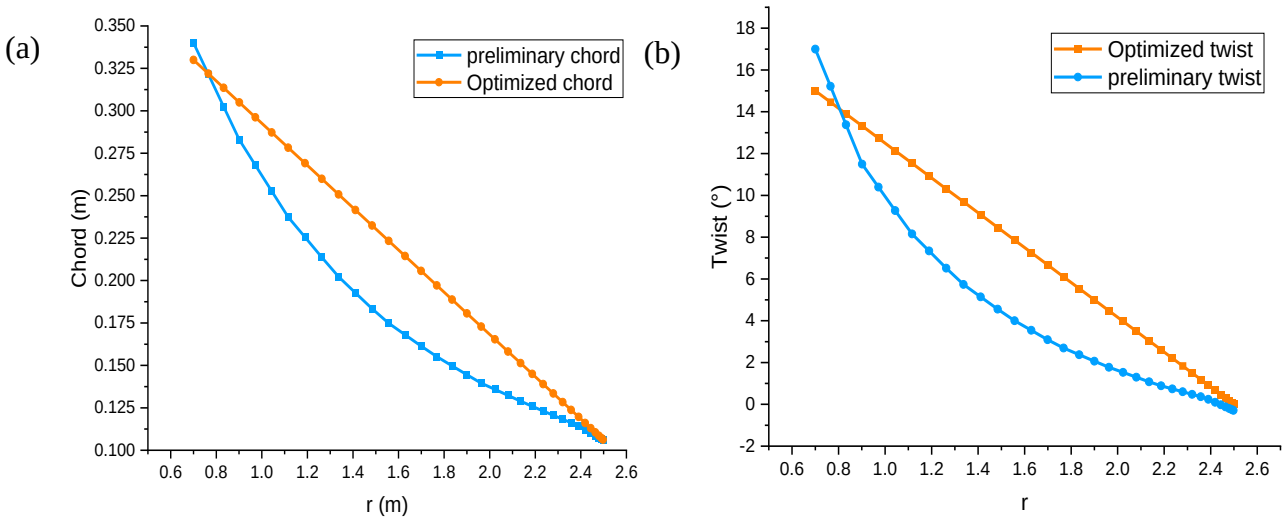

Figure V. 12 Blade distribution (a) chord Length and (b) twist angle

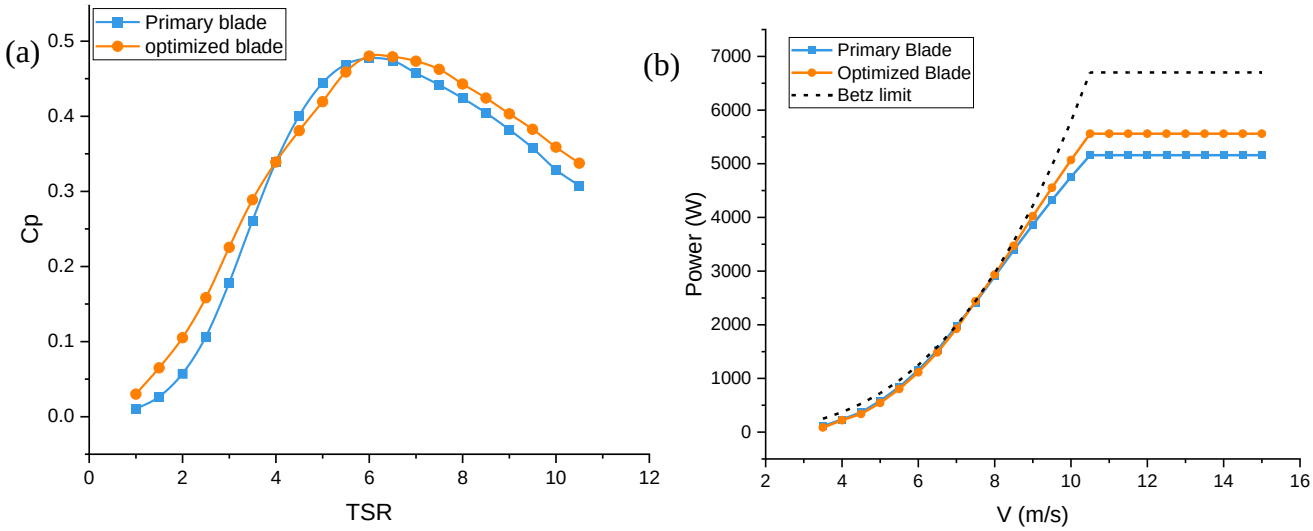

Figure V. 13 (a) power coefficient with tip speed ratio, (b) Power output with wind speed.

To conclude, we have detailed the wind turbine blade design process and outlined the essential stages involved. Additionally, we have introduced a method for enhancing the blade, specifically through linear adjustments in the chord and twist. As demonstrated earlier, these modifications have yielded highly favorable outcomes in the enhancement of the 5-kW wind turbine blade according to our approach. Figure V. 14 illustrates the three-dimensional representation of the final improved model, showcasing the culmination of our design efforts.

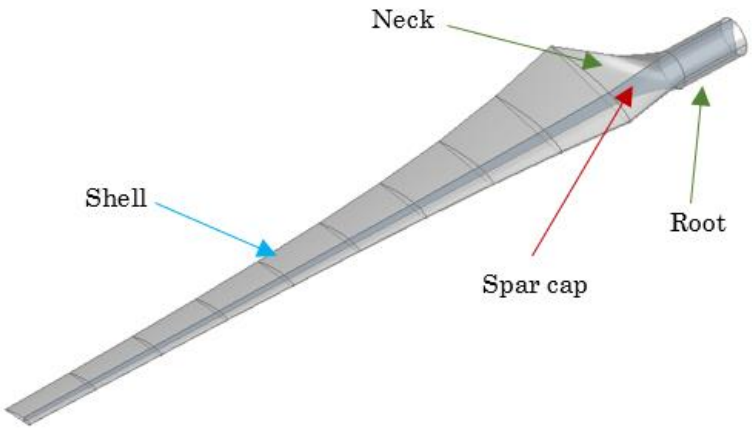

Figure V. 14 3D geometry of 2.5m small wind turbine blade

II.4 CFD simulation of wind turbine blade

Our approach in this study focuses on the comprehensive modeling and simulation of a wind turbine blade in three dimensions (3D). This approach enables us to capture the intricate 3D airflow effects around a wind turbine rotor during rotation. Presently, Ansys fluent is Computational Fluid Dynamics (CFD) stands as a highly effective tool for aiding design and decision-making processes in both small and large-scale wind projects. In essence, it is essential to validate numerical simulations of wind turbines through comparison elements to affirm the accuracy of the derived results. In this context, we employed CFD models to establish these comparison elements, which were subsequently juxtaposed with outcomes derived from the Blade Element Momentum (BEM) theory. The findings of this comparative investigation will be pivotal in further exploring various mechanical and aerodynamic factors that influence wind turbines. Furthermore, the comparative work conducted has opened the doors to initiate an analytical examination of the airflow dynamics engendered by the rotational movement of wind turbine rotor blades. The utilization of a solid-rotating fluid coupling has enabled us to scrutinize the behavior of the fluid medium as the wind turbine rotates. To conduct a CFD simulation, a series of essential steps must be followed, as delineated in Figure V. 15. These steps collectively contribute to our comprehensive analysis and understanding of wind turbine performance.

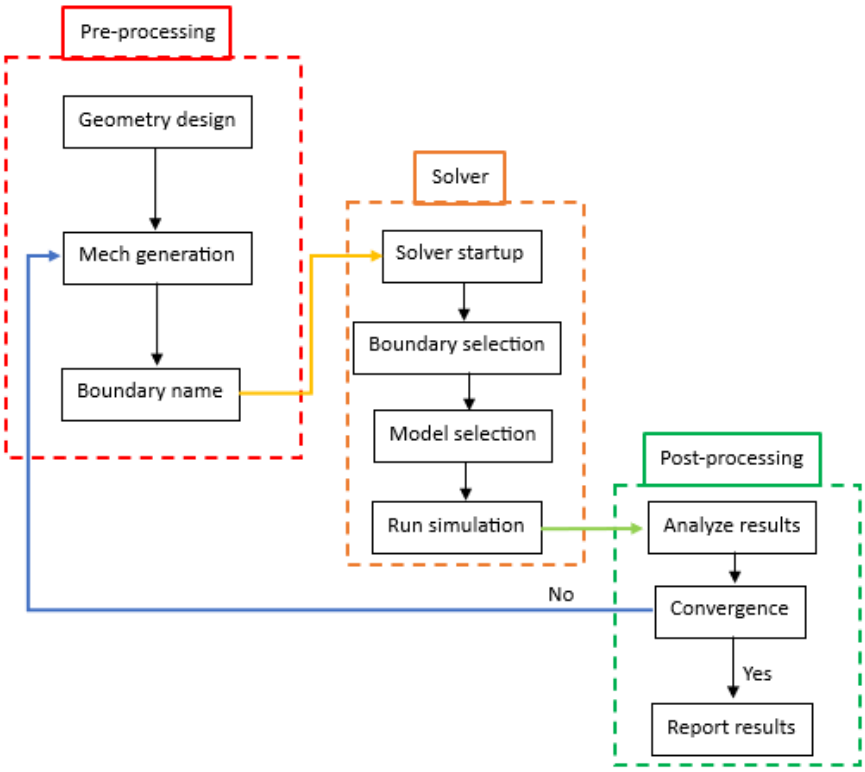

Figure V. 15 flowchart of CFD simulation

II.4.1 The simulation domain and boundary condition

The rotor geometry under investigation represents a straight 5 kW wind turbine blade positioned at a 0° pitch angle. Notably, this study excludes the consideration of both the nacelle and the turbine axis. The coupling takes into account only one blade rotation, assuming rotational periodicity along the radial surfaces as the boundary conditions. The remaining boundary conditions, collectively referred to as external factors in Figure V. 16b, and Figure V. 17 , have been formulated based on subsonic far-field principles.

To provide a visual context, Figure V. 16a presents a 3D representation of the computational domain. An expansion angle in the longitudinal direction has been incorporated to prevent the alignment of fluid velocity with the external boundary conditions Figure V. 16b features a scaled diagram of the computational domain. This adjustment ensures that the fluid behavior within the domain is accurately represented.

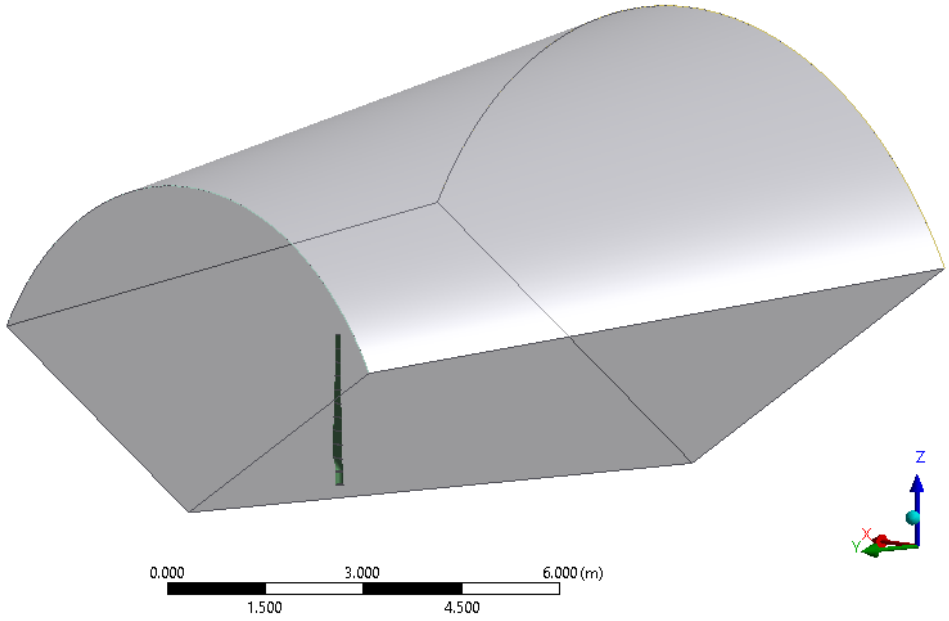

(a)

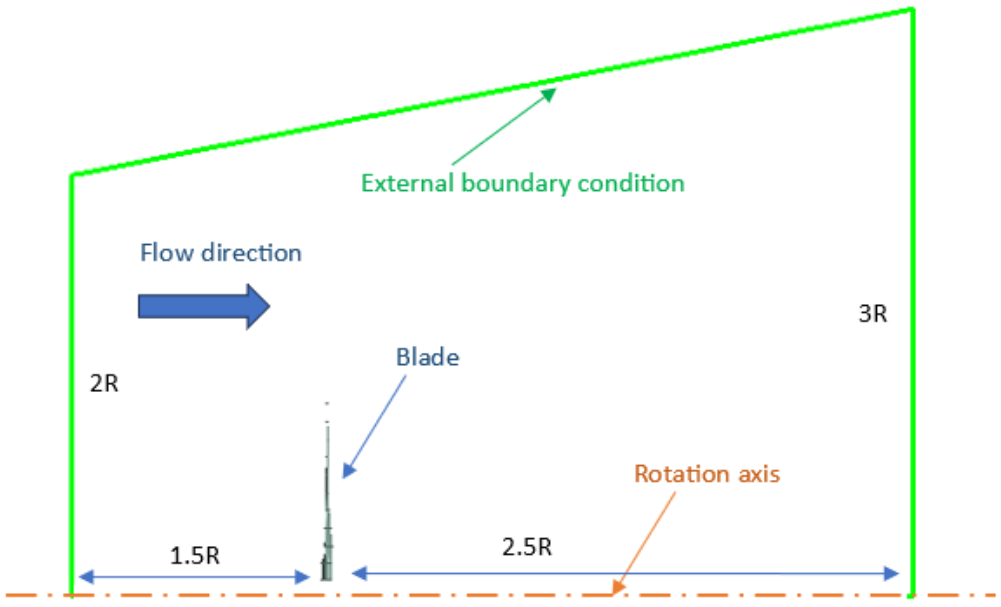

(b)

Figure V. 16 wind turbine Geometry domain (a) 3D views Computational domain, and (b) Scaled sketch of the computational domain.

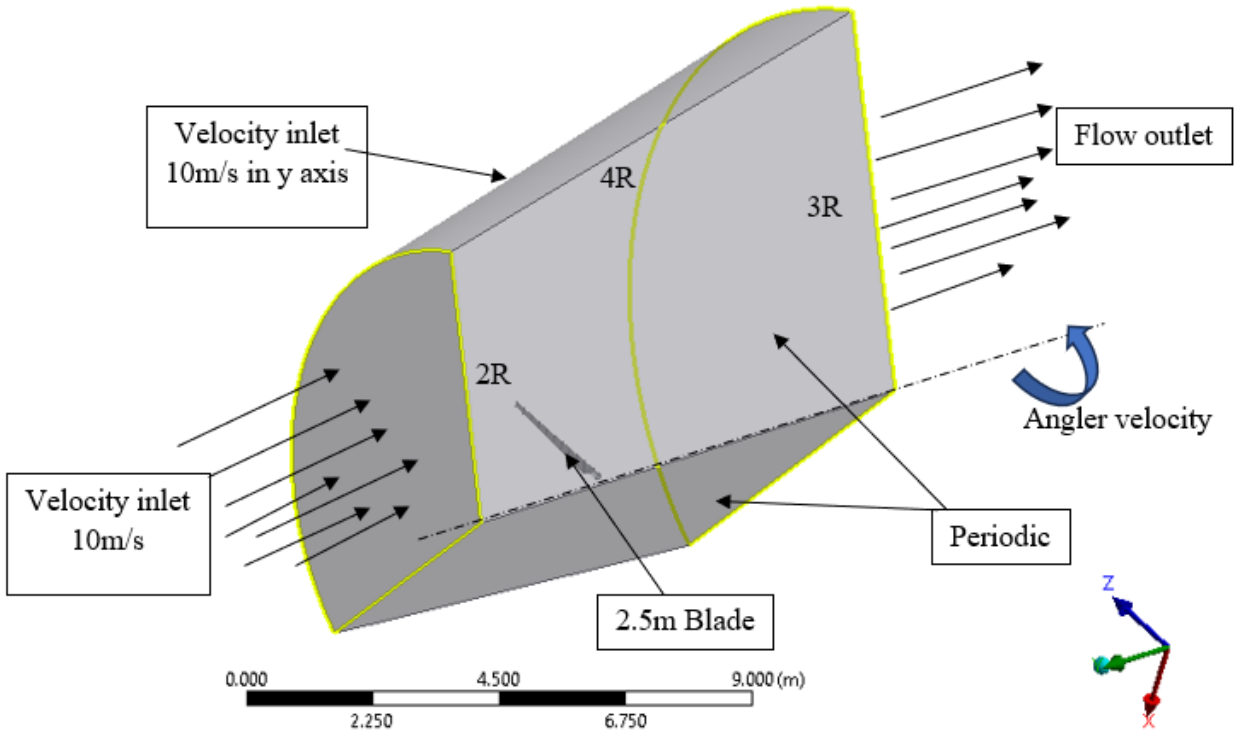

Figure V. 17 Boundary condition of the blade domain

In this problem, the blade is considered as a wall, and the area around the blade is considered as a fluid. The wall is used to direct airflow and to provide energy to the fluid passing around the blade. The two sides are considered periodic, and the upper and front sides are considered an inlet for the wind speed. The wind speed is 10 m/s and moves along the y-axis. At the exit face of the simulation domain, an outlet flow was used for the boundary conditions.

II.4.2 Mesh of computational domain

In a complex CFD problem, a significant amount of time is devoted to configuring the computational domain to ensure a well-distributed mesh throughout the entire volume, as depicted in Figure V. 18(a-b). In such scenarios, determining the optimal thickness for the prism layer covering the blade geometry and selecting the appropriate cell sizes on the blade walls can be a time-consuming and challenging task. In our specific case, the prism layers, illustrated in Figure V. 19, have a thickness of 10 mm and were created using the structured mesh technique. This widely-used technique in CFD software is employed to accurately model wall effects. The remainder of the simulation domain utilizes tetrahedron elements, as seen in Figure V. 19, with a concentration of these elements following the rotor's shape to ensure an accurate representation of fluid flow in this region.

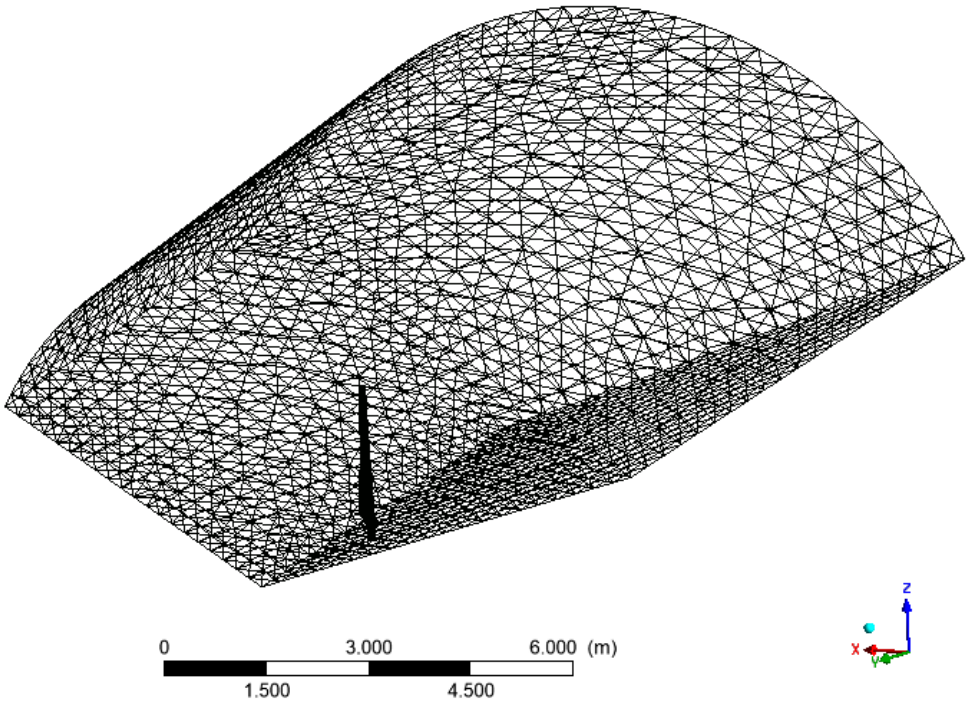

(a)

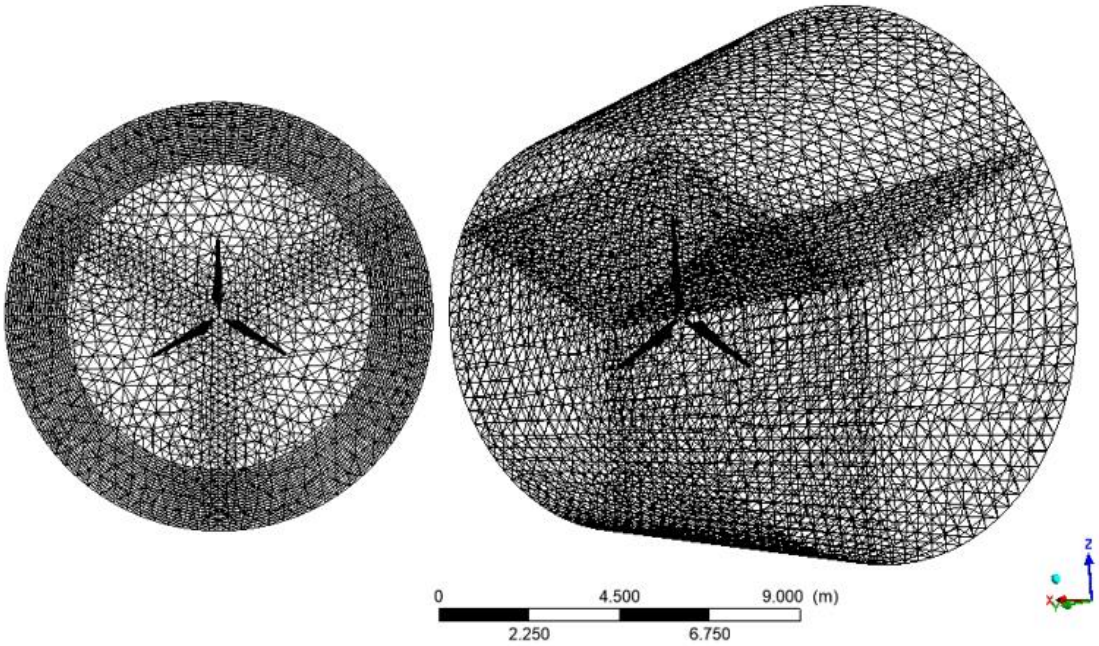

(b)

Figure V. 18 Computational domain meshing (a) simplified domain, and (b) full domain

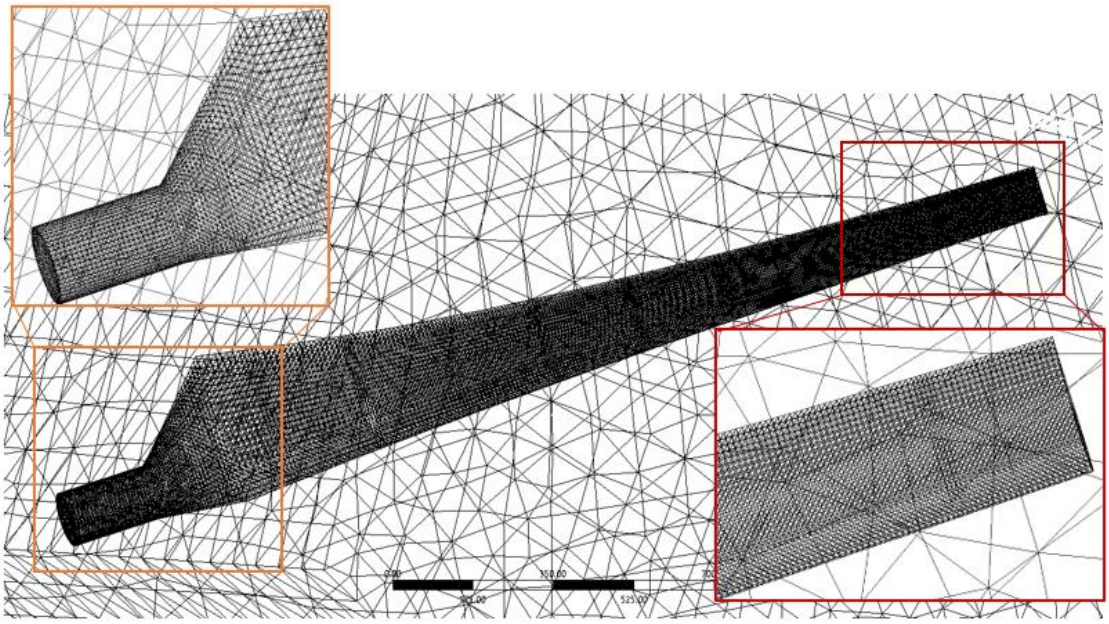

Figure V. 19 the mesh near the blade surface

II.4.3 CFD simulation results

In this section, we will outline some of the key findings obtained from the CFD simulation, including parameters like velocity and pressure resulting from the interaction between air particles and the blade's surface, along with other significant outcomes.

II.4.3.1 Velocity vector

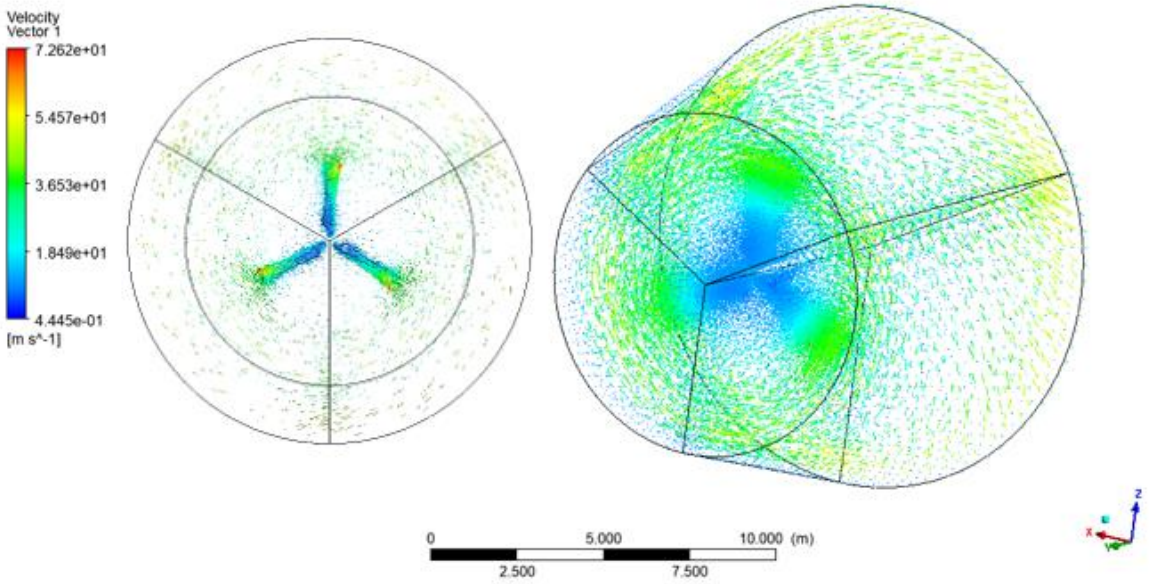

(a)

Figure V. 20a provides a visualization of velocity vectors surrounding the wind turbine blade. Understanding the directions of these velocity vectors is crucial for discerning the airflow patterns around the blade, particularly the fluctuations occurring at the blade tip. As evident in Figure V. 20b, the vector direction at the blade tip traces a circular path, a consequence of the blade's rotational motion interacting with the wind.

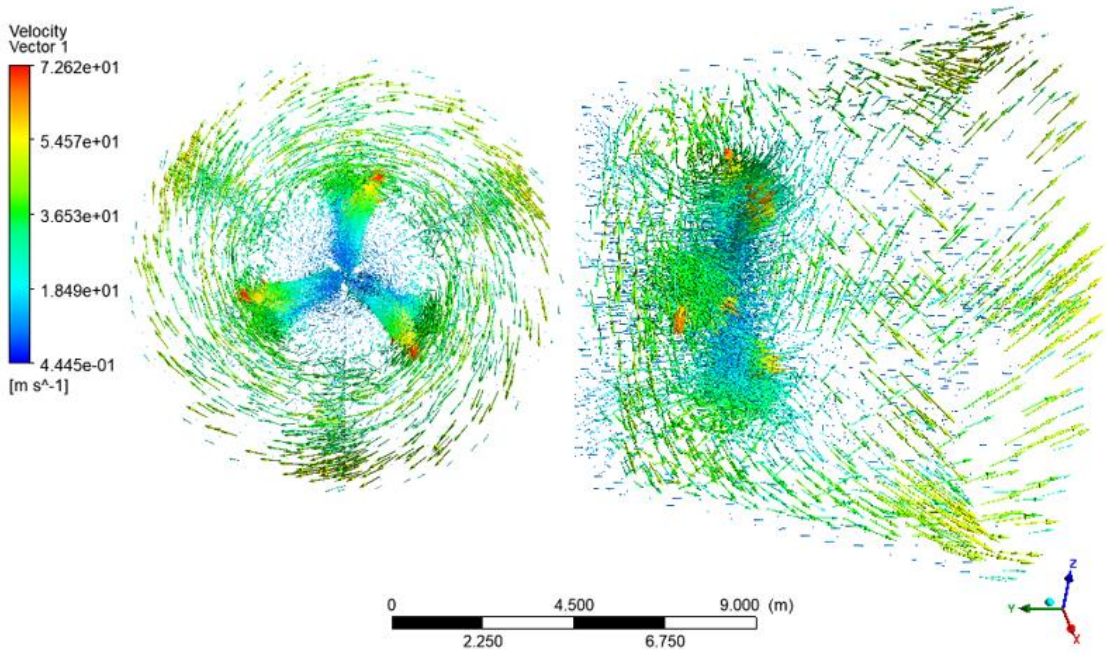

(b)

Figure V. 20 velocity vector of Computational domain (a) domain zooms out, and (b) domain zoom in

II.4.3.2 Streamline around blade

Figure V. 21a presents the streamlines resulting from the wind turbine blade's rotation within an airflow, representing the fluid flow field. Streamlines are the imaginary lines that depict the paths followed by fluid particles as they traverse the flow, ultimately converging or diverging. These lines offer valuable insights into fluid flow behavior and characteristics, including regions of elevated turbulence or vortex formation. The streamlined wind turbine blade was utilized to investigate and visually represent fluid flow patterns. As it is clearly visible in Figure V. 21b, the streamlines are when the current passes through the blade, and as we can see, along the length of the blade there are no disturbances in the fluid except in the neck area, and the reason for this is that it is a transitional area between the root and the shell. In Figure V. 22, we will take three sections along the blade span r/R=0.3, r/R=0.6, and r/R=0.9 so that it is easier for us to see the streamline. Flow separation can be more effectively comprehended by examining the friction streamlines along the blade surfaces (refer to Figure V. 23). Friction streamlines along the blade surface at a speed of 10 m/s, illustrating regions of flow separation on both the pressure side and the suction side.

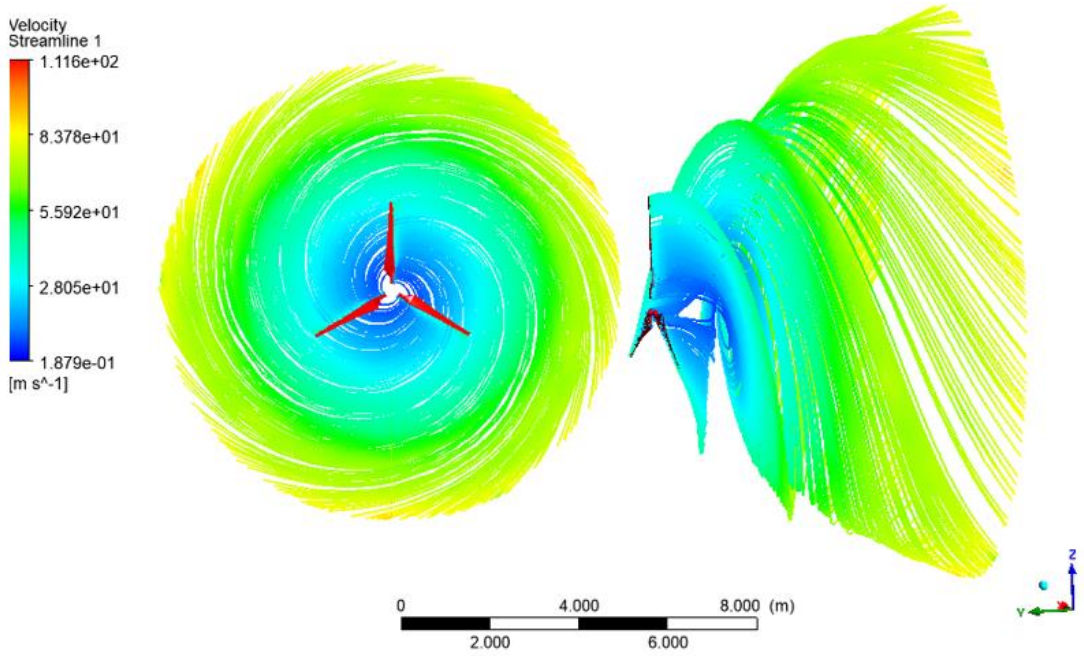

(a)

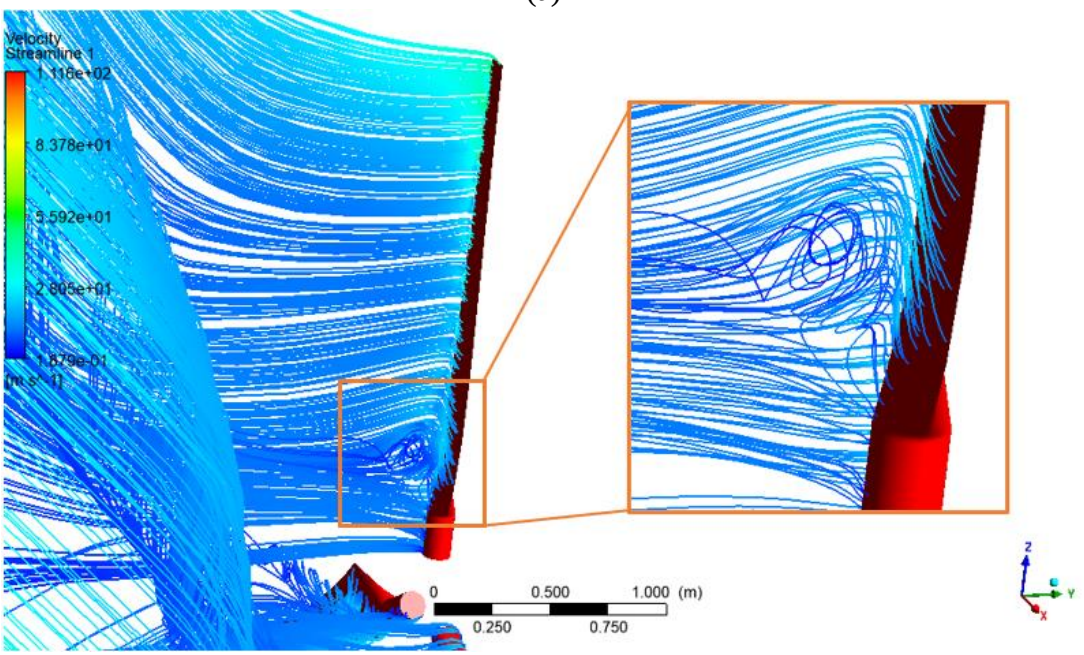

(b)

Figure V. 21 streamlines resulting from the wind turbine blade (a) view of the blade domain, (b) streamline of blade transitional area.

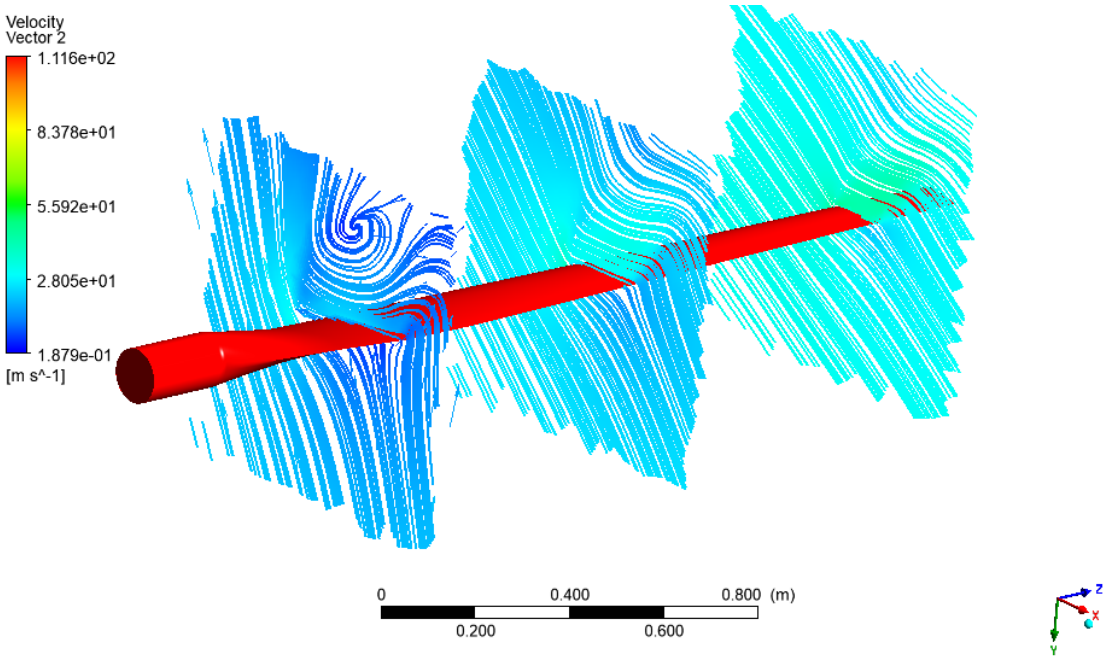

Figure V. 22 streamline at blade span r/R=0.3, r/R=0.6, and r/R=0.9.

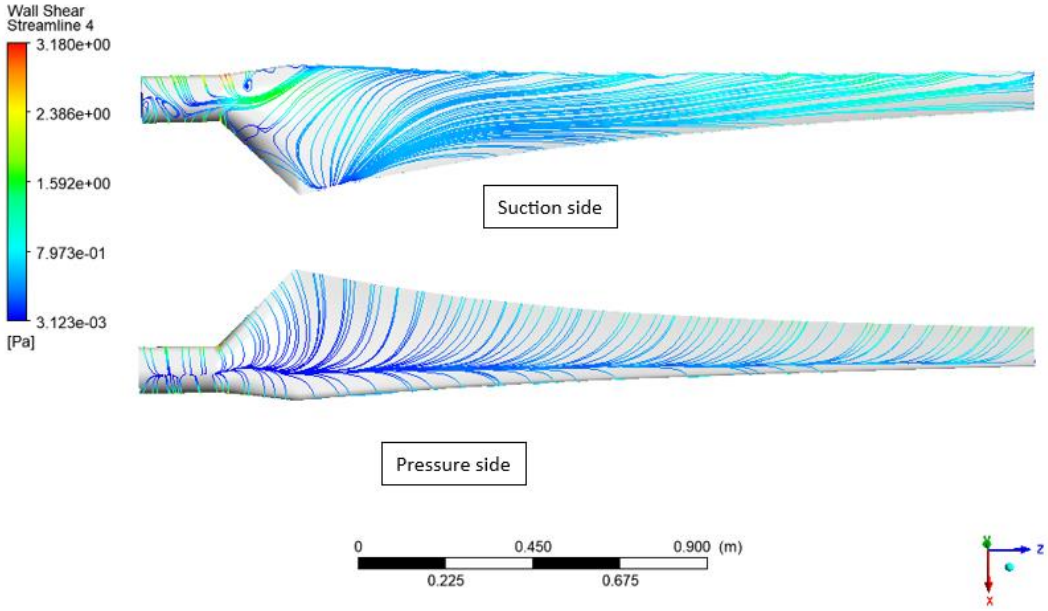

Figure V. 23 Friction streamlines along the blade surface

II.4.4 Wind turbine blade velocity and pressure

One of the important results to analyze and compute in CFD simulations is velocity and pressure. In our research, pressure is of particular significance as it induces blade deflection during operation, stemming from the collision of air particles due to the surrounding wind speed. Figure V. 24 displays the velocity distribution along the blade resulting from its rotation and interaction with the wind. Additionally, Figure V. 25 illustrates the pressure distribution along both ends of the blade, including the pressure side and suction side.

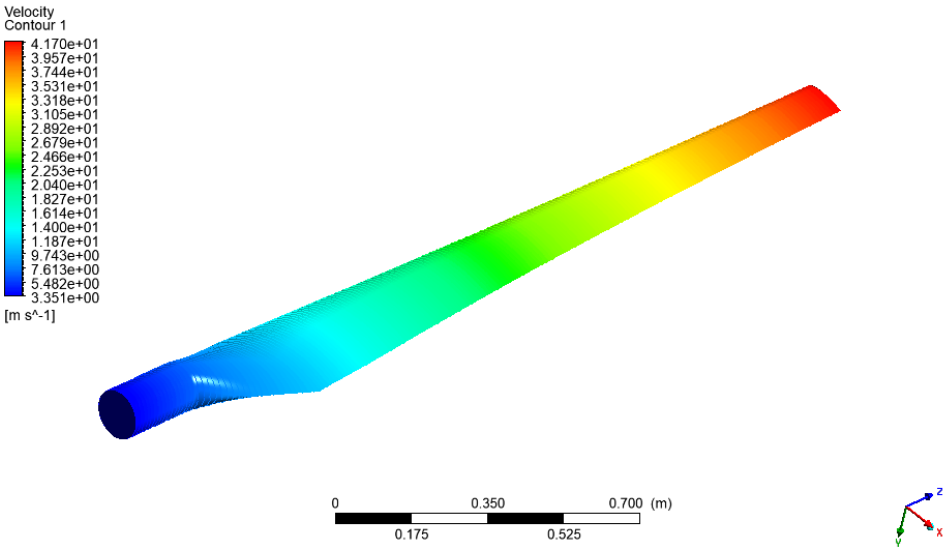

Figure V. 24 velocity contour at the blade surface.

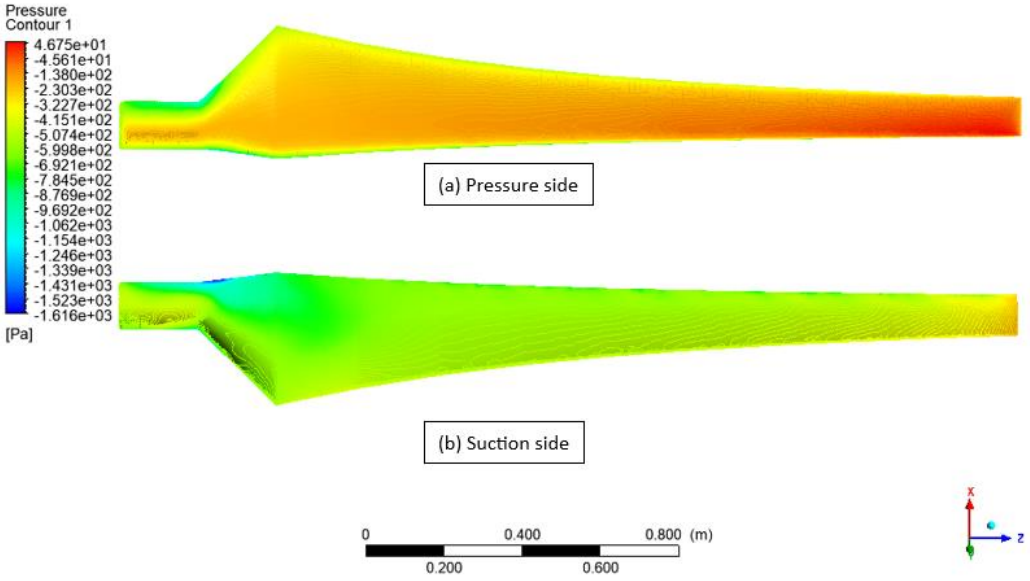

Figure V. 25 pressure contour at a) pressure side, and b) suction side.

To gain a more comprehensive understanding of the wind speed and pressure distribution surrounding the wind turbine blade, we will focus on three segments positioned evenly along the blade span: r/R = 0.3, r/R = 0.6, and r/R = 0.9. These segments provide detailed insights into the airflow patterns around the rotating blade. Figure V. 26 illustrates the locations of these three sections under examination. Additionally, Figure V. 27a displays the wind speed distribution, while Figure V. 27b showcases the pressure distribution around the blade at these specified sections.

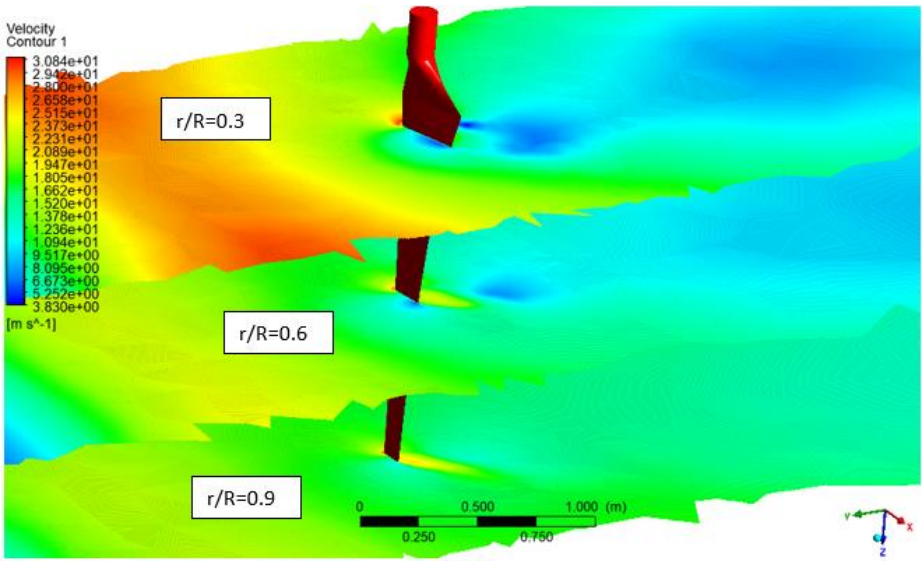

Figure V. 26 locations of three sections: r/R = 0.3, r/R = 0.6, and r/R = 0.9

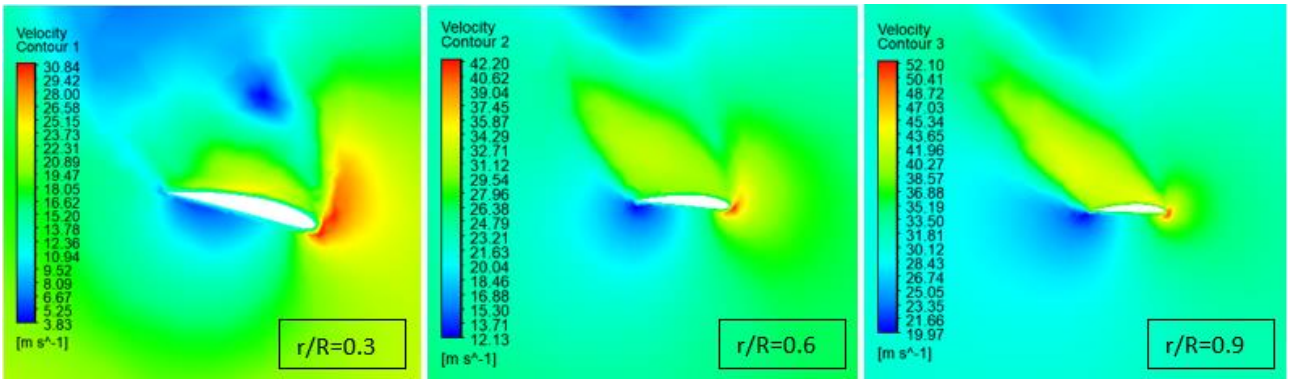

(a)

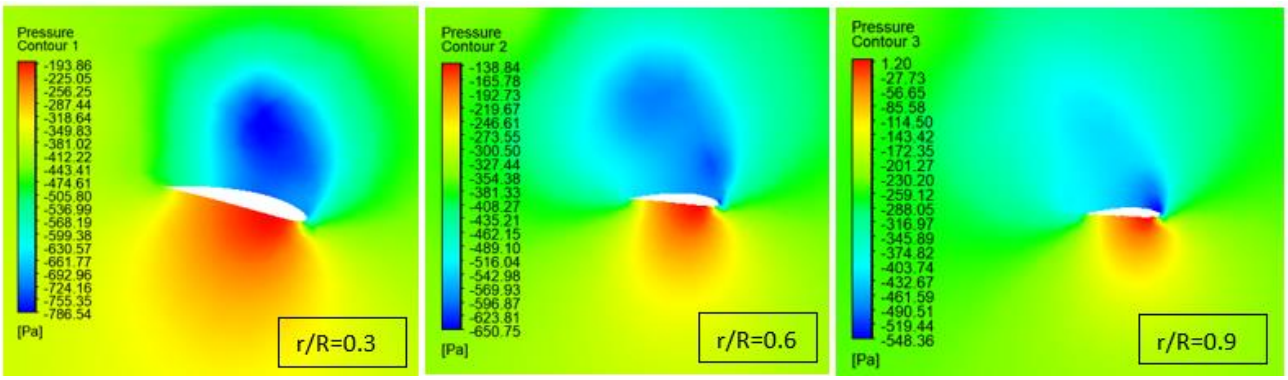

(b)

Figure V. 27 blade section contour of (a) velocity, and (b) pressure at r/R=0.3, r/R=0.6, and r/R=0.9.

Examining the contours, we observe a zone of elevated pressure at the leading edge, known as the stagnation point, and a region of reduced pressure on the upper surface of the airfoil. According to the Bernoulli equation, low pressure coincides with high velocity and conversely. On the lower surface of the airfoil, the pressure exceeded that of the incoming flow stream, resulting in an upward force acting perpendicular to the incoming flow stream, effectively lifting the airfoil.

II.4.5 Load and performance of the wind turbine rotor

To calculate aerodynamic loads, the Computational Fluid Dynamics (CFD) method was employed due to its ability to simulate the 3D model, accounting for external factors such as blade tip vortices. Ansys Fluent software was utilized for simulating the wind turbine, and a comparison was made with the results obtained from the Blade Element Momentum (BEM) theory to validate the findings. In Figure V. 28, you can observe the distribution of tangential and normal force coefficients. A comparison was conducted between CFD simulations and the BEM theory in seven different sections along the blade.

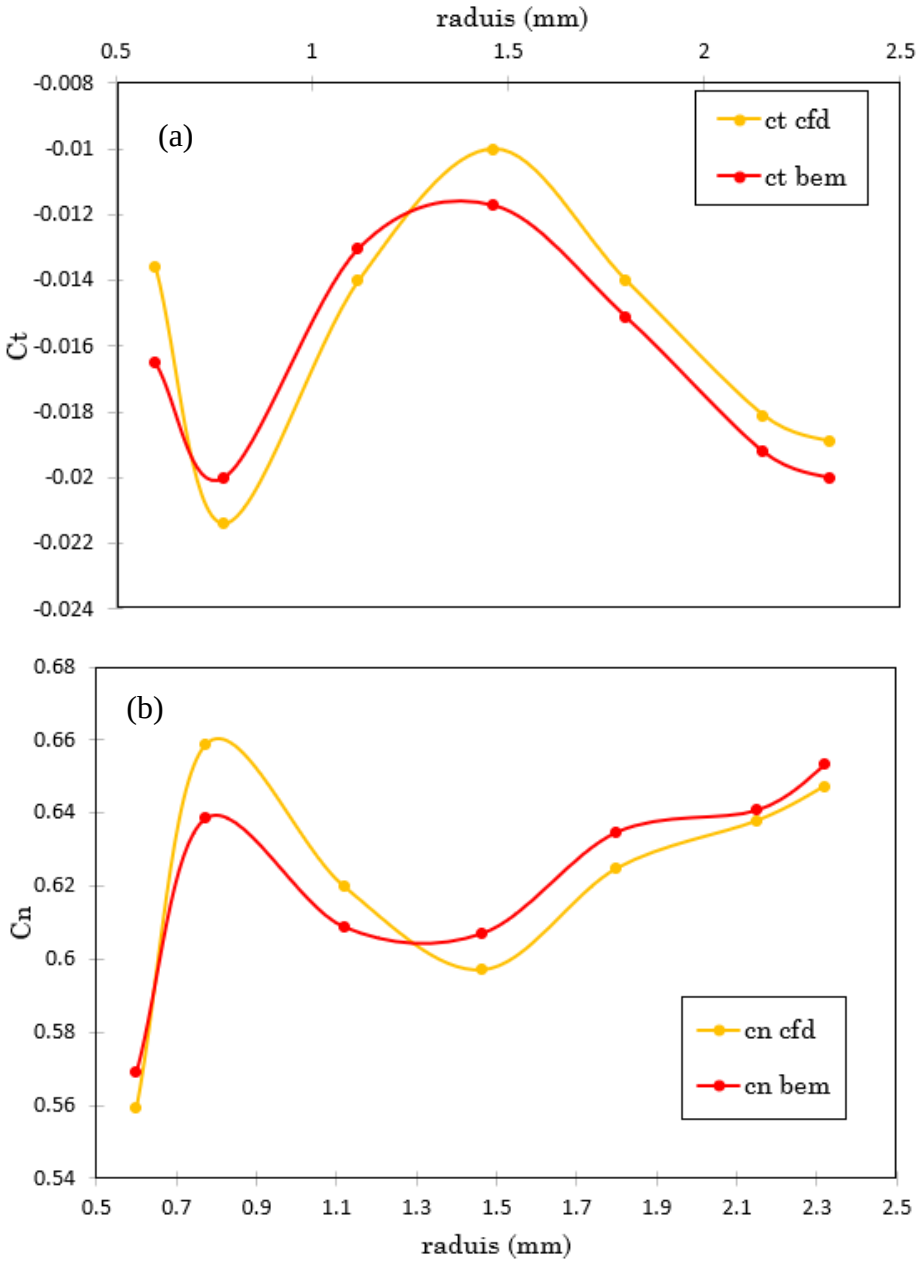

Figure V. 28 distribution of (a) tangential, and (b) normal force coefficients along the blade

As depicted in Figure V. 28a and Figure V. 28.b, the results are closely aligned, and any discrepancies can be attributed to the differences in calculation methods. CFD analyzes a 3D model, which is influenced by factors such as the number of elements and nodes, while the BEM method simplifies the blade as an ideal 1D rotating disk. The lift and drag forces were computed based on the BEM method applied to the blade, yielding values of 380.2 N and 7.9 N, respectively. Additionally, the gravitational force and centrifugal forces were determined to be 241.32 N and 1544.88 N, respectively. Figure V. 29 also presents a comparison between CFD and BEM regarding power results as a function of wind speed. It's evident from the findings that, for all the wind speeds investigated, the maximum percentage difference remained below 1.5%.

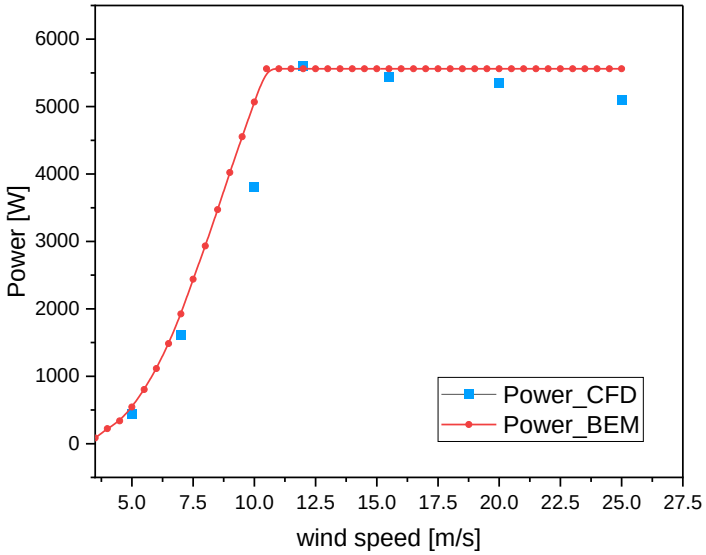

Figure V. 29 comparison of CFD and BEM of the power as a function of wind speed

III. Blade Deflection and Vibration Analysis

The primary objective of this section of the thesis is to enhance the material used in blade manufacturing. The initial step involves selecting a material to focus on, followed by the enhancement process.

III.1 Initial FE model of blade

In this study, the Finite Element (FE) method, implemented through ANSYS software, was utilized to simulate the 5-kW wind turbine blade. The wind turbine blade featured a composite sandwich structure composed of E-Glass (fiberglass epoxy) material. To construct the shell, a combination of tri-axial and unidirectional layers was employed. Following the establishment of local coordinates for the structure, the fiber orientation was defined based on these coordinates. In this context, the Z-axis represented a rotation angle of 0°, extending along the blade towards the tip.

III.1.1 E-glass /MY750 material properties

To mitigate blade tip deflection and enhance blade resilience against extreme wind forces, the blade was constructed using E-glass/MY750 material. Theoretically, the fiber volume fraction of V_f = 0.6 provides the highest stiffness-to-weight ratio (E/ρ). The calculated mass of this model's blade was 24.6 kg, which

closely matches the experimental result of 24.7 kg [243]. The mechanical properties of this material are detailed in Table V. 4 [244].

Table V. 4 Mechanical properties of material E-glass /MY750epoxy

Properties		**value**
Young's modulus	E_{xx} (GPa)	45.6
	E_{yy} (GPa)	16.2
	E_{zz} (GPa)	16.2
Poisson's ratio	υ_{xy}	0.27
	υ_{zx}	0.27
	υ_{yz}	0.33
Shear modulus	G_{xy} (GPa)	5.83
	G_{zx} (GPa)	5.83
	G_{yz} (GPa)	3.69
Density	ρ (kg/m^3)	2000

III.1.2 Initial model mesh

Figure V. 30 depicts the finite element model utilized for calculating stresses and deflections resulting from variations in wind speed. The blade underwent meshing using shell element 281, specifically designed for composite materials. Each element comprises eight nodes, each with six degrees of freedom (DOF). A grid convergence test was carried out to ascertain the optimal mesh, ensuring an error rate of under 2%. The final FE model consists of 4515 elements and 21536 nodes.

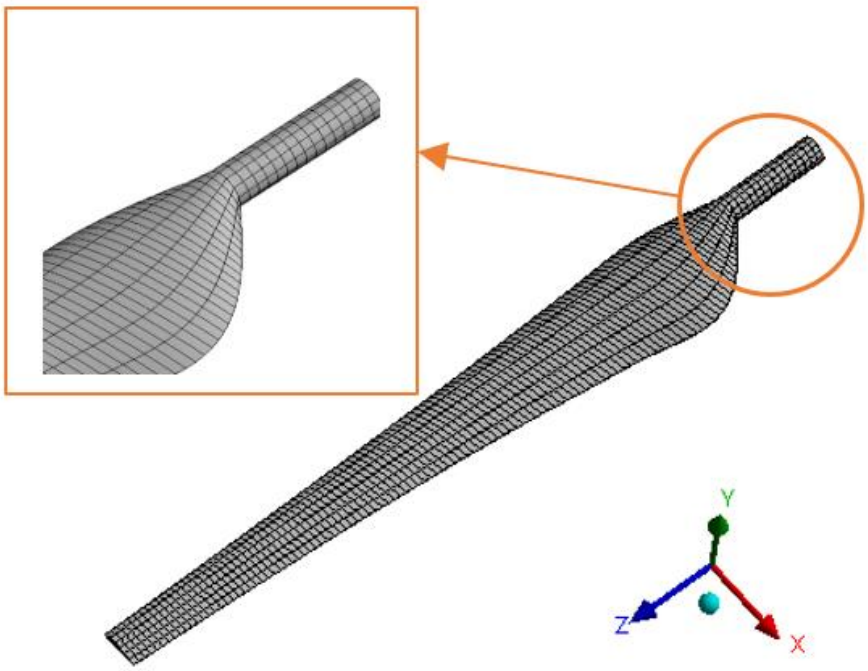

Figure V. 30 FE model Mesh of blade

III.1.3 Boundary conditions

Figure V. 31 illustrates the boundary conditions applied to the wind turbine blade. At the root side, the blade is securely fixed, and the influence of the gravitational force acting at the center of the blade's mass is accounted for The blade experiences several forces, including centrifugal force due to rotation, aerodynamic pressure load on the blade's shell, and the force of gravity. Negligible forces, such as those arising from mechanical brake activation and gyroscopic effects, have been omitted due to their minimal impact.

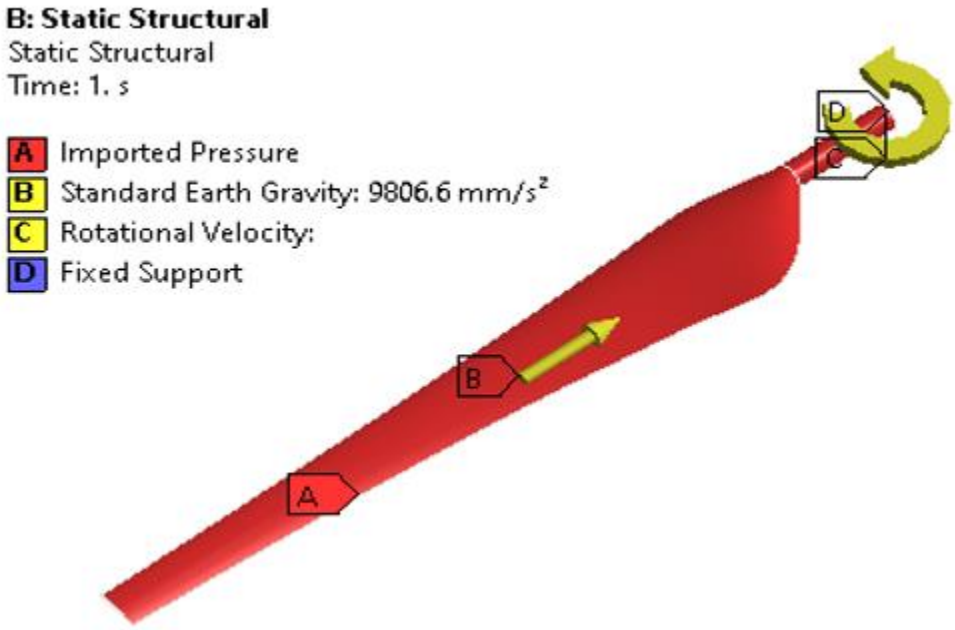

Figure V. 31 boundary conditions applied to the wind turbine blade

III.1.4 Free vibration of the blade model

To assess the results accurately, it's important to consider the convergence criterion. Achieving an optimal number of elements involves gradually refining the mesh. Figure V. 32 illustrates the outcome of mesh convergence in relation to the stabilization of mode 1 and mode 2. As shown in Figure V. 32, convergence is achieved with 2,300 or more elements and 19,066 nodes.

A free vibration analysis was conducted for the FE model, and Table V. 5 presents the natural frequencies of the blade, compared to findings from previous studies.

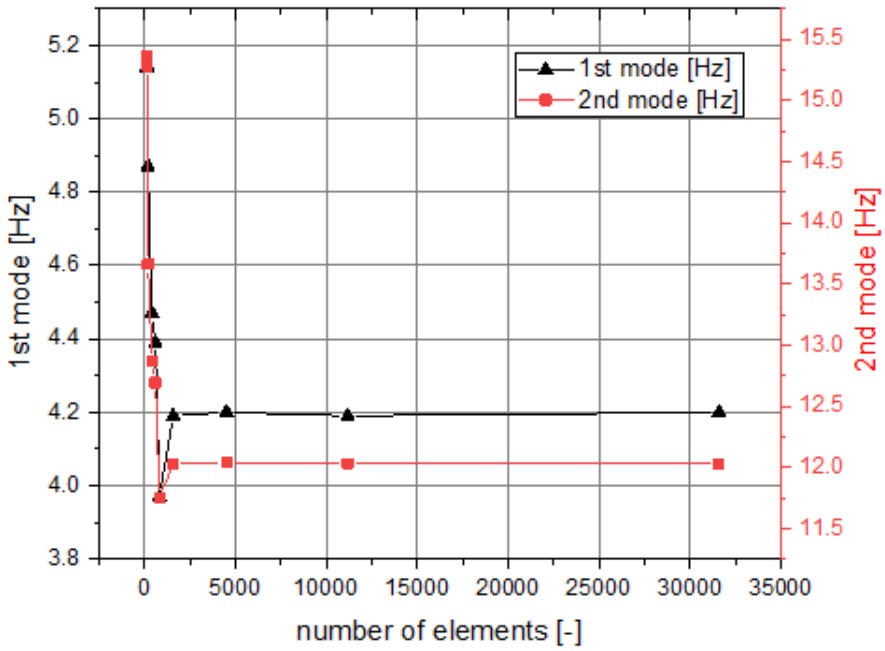

Figure V. 32 mesh convergence of mode 1 and mode 2

Table V. 5 Natural frequency of the wind turbine blade

Mode	Bechly and Clausen [243] (Experimental)	Rajadurai et al.[245]	Bechly and Clausen [246]	Present study
1	4.18	4.14	5.3	4.2
2	10.0	10.14	12.4	12.03
3	-	-	-	26.09
4	-	-	-	47.95
5	-	-	-	58.29

The five frequencies were determined through finite element analysis. We compared the first and second fundamental frequencies with experimental results [243]and finite element analysis results from previous studies [245] [246]. The results of the free blade vibration analysis indicate that the model aligns well with experimental studies and produces favorable outcomes.

III.1.5 Deflection of the blade at the specified loads

Computational fluid mechanics (CFD) was employed to compute the aerodynamic loads acting on the blade's surface. A new 3D model was created using ANSYS-Fluent software, and this model was coupled with the structural dynamics (SD) model, resulting in a fluid-structure interaction (FSI) analysis to determine the stresses and deflections experienced by the blade. The numerical calculation of deflections at the trailing and leading edges of the blade was compared with experimental results, as depicted in Figure V. 33. It was determined that the numerical and experimental approaches yielded deflections of 133 mm and 195 mm, respectively. This resulted in a difference of approximately 11% in flapwise deflection and about 31% in deflection at the trailing and leading edges. The disparities between the numerical and experimental results can be attributed to the approximation of material properties in the numerical model.

Nevertheless, a high level of agreement was achieved between the numerical and experimental outcomes [18]. Figure V. 34 illustrates the maximum flapwise deflection of the wind turbine blade.

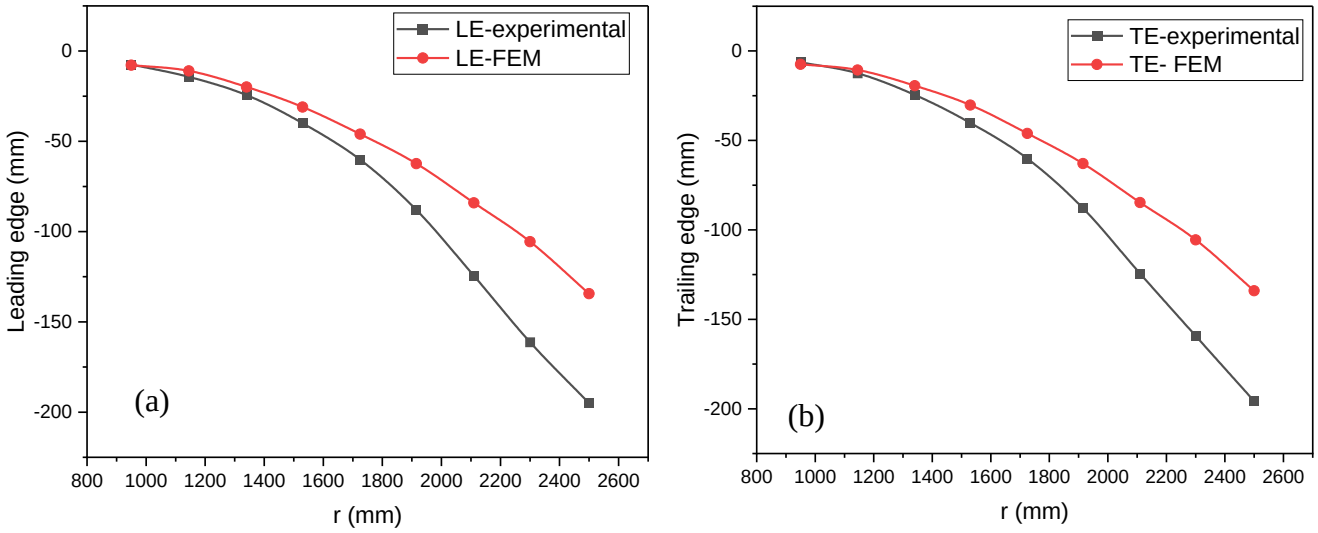

Figure V. 33 The blade deflection of (a) Leading Edge (LE), and (b) Trailing Edge (TE)

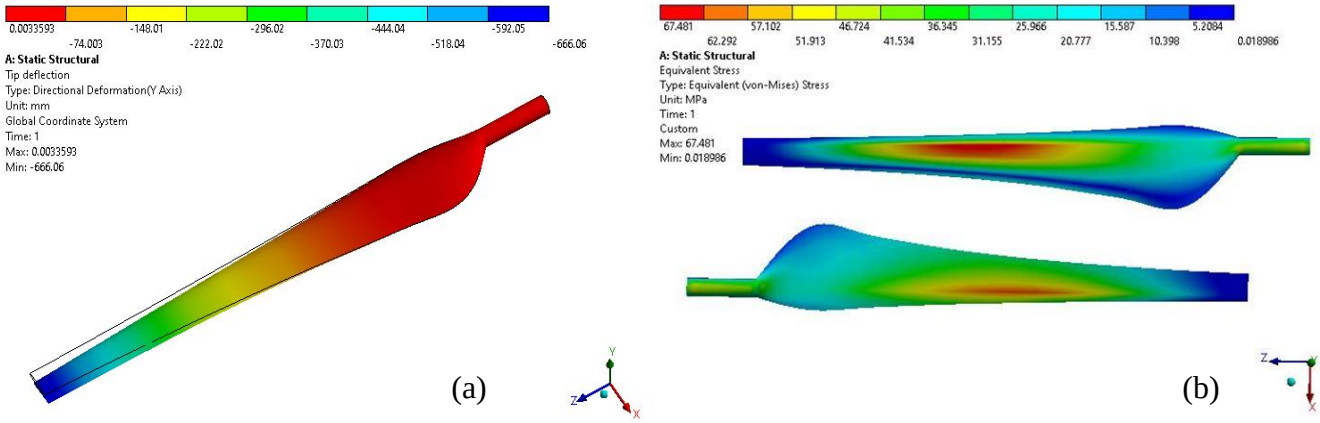

Figure V. 34 (a) The maximum flapwise deflection and (b) the maximum stress distribution of the wind turbine blade

III.2 Optimize FE model of blade

Following the examination of the initial blade structure, it is essential to proceed with a refinement and enhancement process for the model. As the second step towards material improvement for the blade, we will initially consider three materials for evaluation and select the most suitable one among them.

III.2.1 Blade's Material and lay-up sequence

Wind turbine blades can be crafted from a variety of materials, with some common options being E-glass/epoxy, S-glass/epoxy, carbon/epoxy, braided composites, aluminum, and more. Given the wide range of materials employed in blade manufacturing, this study focuses on optimizing the blade structure using the most typical materials. The objective is to achieve an optimized blade design that combines high

stiffness with minimal weight, ultimately reducing wind turbine costs and enhancing performance. Table V. 6 outlines the properties of the three selected materials used for optimizing the wind turbine blade.

Table V. 6 composite material properties of wind turbine blade

Material	E-glass/ Epoxy [247]	Carbon/ Epoxy [247]	Braided Composite [247, 248]
E_1 (GPa)	48.7	136.7	62.8
E_2 (GPa)	16.8	8.2	62.8
G_{12} (GPa)	5.83	4.45	9.68
G_{23} (GPa)	6	2.91	7.97
υ_{12}	0.28	0.29	0.33
υ_{23}	0.20	0.42	0.40
X_T (MPa)	1170	1604	460
X_C (MPa)	977	1305	420.4
Y_T (MPa)	30.5	40.5	526.2
Y_C (MPa)	114	239.7	420.4
ρ(kg/m3)	2000	1518	1800

The blade of a small wind turbine comprises four fundamental sections: the root, the neck, the shell, and the shear web. Each section of the blade features distinct layer thickness and fiber orientation. Determining the appropriate fiber orientation and laminate thickness is crucial to simplify manufacturing processes and enhance structural stiffness. The lay-up sequence, orientation, and laminate thickness have been optimized for the selected composite materials. Table V. 7 outlines the sequence of layers in the blade, while Figure V. 35 provides a 3D model of the wind turbine blade materials. Each section is color-coded, reflecting variations in composite material thickness and fiber orientation, as detailed in Table V. 7.

Table V. 7 The lay-up sequence of 2.5 m small wind turbine

Section name	Location (m)	Shell layup	thickness(m)	shear web layup	thickness(m)
1	0.200-0.400	[(±45)3/08/(±45)]s	0.0064	[(±45)3/09/(±45)]s	0.0070
2	0.400-0.600	[(±45)3/07/(±45)]s	0.0058	[(±45)3/08/(±45)]s	0.0064
3	0.600-0.811	[(±45)3/06/(±45)]s	0.0052	[(±45)3/07/(±45)]s	0.0058
4	0.811-1.022	[(±45)2/06/(±45)]s	0.0048	[(±45)3/06/(±45)]s	0.0052
5	1.022-1.233	[(±45)2/05/(±45)]s	0.0042	[(±45)2/06/(±45)]s	0.0048
6	1.233-1.444	[(±45)2/04/(±45)]s	0.0036	[(±45)2/05/(±45)]s	0.0042
7	1.444-1.655	[(±45)2/03/(±45)]s	0.0030	[(±45)2/04/(±45)]s	0.0036
8	1.655-1.866	[(±45)2/02/(±45)]s	0.0024	[(±45)2/03/(±45)]s	0.0030
9	1.866-2.077	[(±45)/02/(±45)]s	0.0020	[(±45)2/02/(±45)]s	0.0024
10	2.077-2.288	[(±45)/01/(±45)]s	0.0014	[(±45)/02/(±45)]s	0.0020
11	2.288-2.500	[(±45)/01/(±45)]	0.0007	[(±45)/01/(±45)]s	0.0014

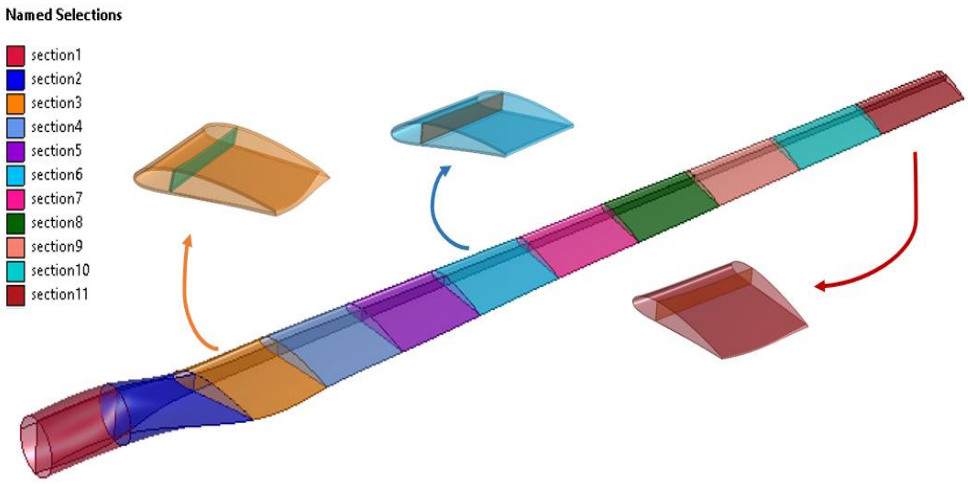

Figure V. 35 3D FEM of the composite blade section

III.2.2 FE Structural analysis

The finite element model of the wind turbine blade was established using Ansys software for investigating the steady-state structural problem. This simulation is designed to optimize the materials of the wind turbine blade by analyzing the tip deflection, von Mises stress, and deformation resulting from applied aerodynamic loads. The aerodynamic loads were calculated using QBlade software, which operates on the basis of the BEM theory. Table V. 8 provides an overview of the results for the applied loads on the wind turbine blade.

Table V. 8 The load applied on the FE model

$Z\ (m)$	$\Delta Z\ [m]$	$F_T[N/m]$	$F_N[N/m]$
0.200	0.200	-1.535	2.930
0.400	0.200	-4.415	8.825
0.600	0.200	27.610	57.455
0.811	0.211	38.052	81.014
1.022	0.211	36.047	93.246
1.233	0.211	35.260	106.279
1.444	0.211	34.701	120.023
1.655	0.211	34.492	134.815
1.866	0.211	33.881	147.971
2.077	0.211	32.781	161.331
2.288	0.211	29.654	172.156
2.500	0.212	9.8160	81.7452

III.2.3 Boundary conditions of blade

The wind turbine blade is anchored at its root side, leading to the assumption that all degrees of freedom (DOF) are constrained at the root. Conversely, at the tip, the blade is left unrestricted to move freely. The blade maintains a consistent rotational speed throughout the analysis. Pressure is uniformly distributed over the blade's shell, but the loads were computed using the BEM theory, applied at the center of each

section of the blade. The gravitational force is applied at the blade's center of gravity. Figure V. 36 illustrates the loads and boundary conditions imposed on the blade.

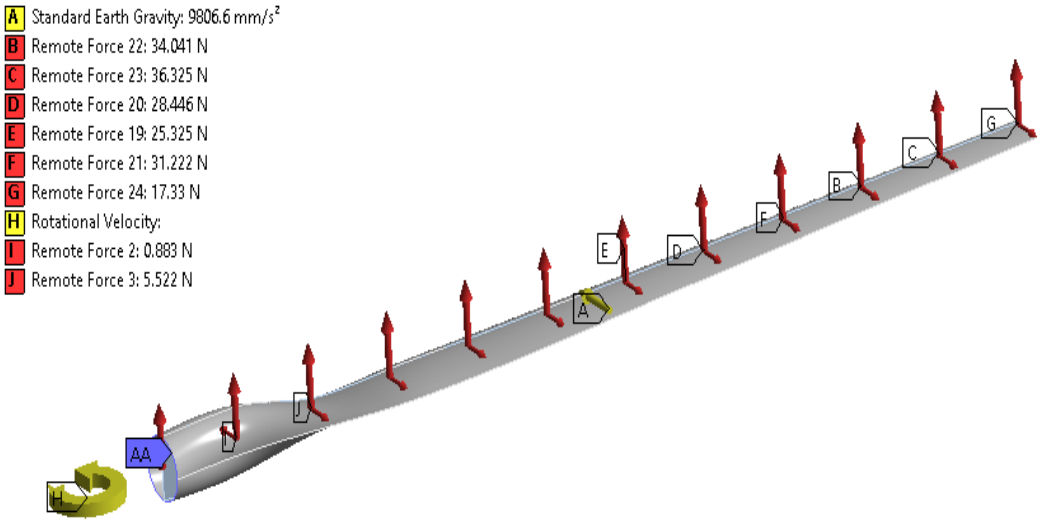

Figure V. 36 Loads and boundary conditions Applied on blade

III.2.4 Mesh generation and convergence

When a wind turbine blade operates, it experiences various loads that result in bending and deflection of the blade. Simulating a wind turbine blade requires selecting an appropriate mesh that accurately represents the geometry and material composition. In this study, the blade was meshed using shell element 281, specifically designed for composite materials. Each element comprises eight nodes, with each node having six degrees of freedom (DOF). A mesh convergence test was conducted for the wind turbine blade to determine the most suitable mesh, and the results are presented in Table V. 9 and Figure V. 37.

Table V. 9 wind turbine blade mesh convergence

Mesh segments	No. nodes	No. elements	Max. total deflection [mm]	Difference
1	19824	3694	18.392	-
2	26722	7431	18.371	-0.021
3	34624	11385	18.365	-0.006
4	45857	15124	18.361	-0.004
5	74154	24475	18.356	-0.005
6	108789	35970	18.354	-0.002
7	225602	75053	18.358	0.004

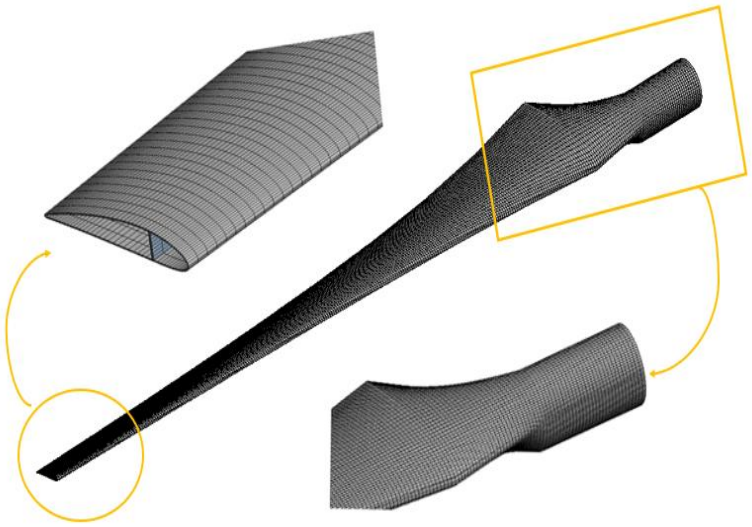

Figure V. 37 FE model wind turbine mesh

III.2.5 Steady-State Analysis of Wind Turbine Blade

The steady-state finite element model was employed to analyze the variation in blade tip deflection and Von Mises stresses for the three proposed materials, aiming to identify the optimal material in terms of strength that results in the minimum tip deflection. Additionally, this analysis helps identify stress concentration zones within the blade structure, enabling improvements to enhance structural strength and achieve an optimal, robust structure. Figure V. 38 illustrate the distribution of Von Mises stresses for the three selected materials, while Figure V. 39 depict the deflection distribution (tip deflection) of the wind turbine blade using different materials.

To validate the chosen approach for blade analysis, a comparison was made between the results obtained from QBlade software and ANSYS software in terms of tip deflection and Von Mises stresses. The comparison revealed a high level of agreement between the results obtained from QBlade and ANSYS software, as demonstrated in Table V. 10.

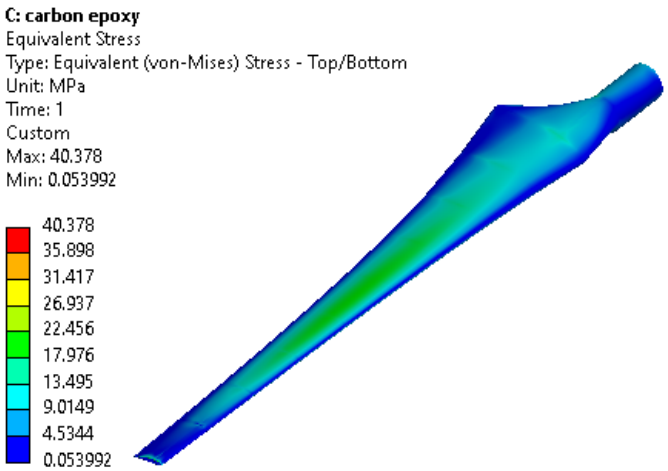

(a)

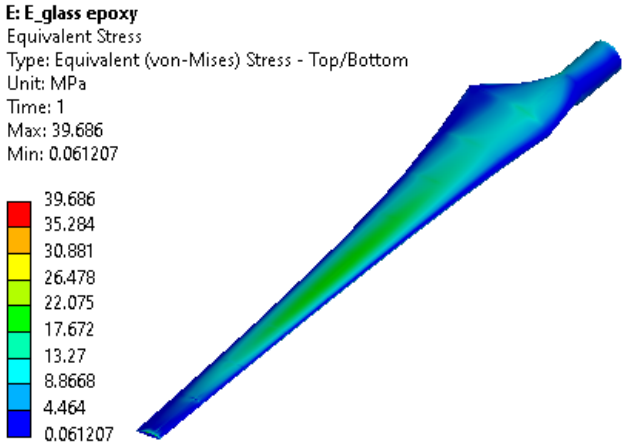

(b)

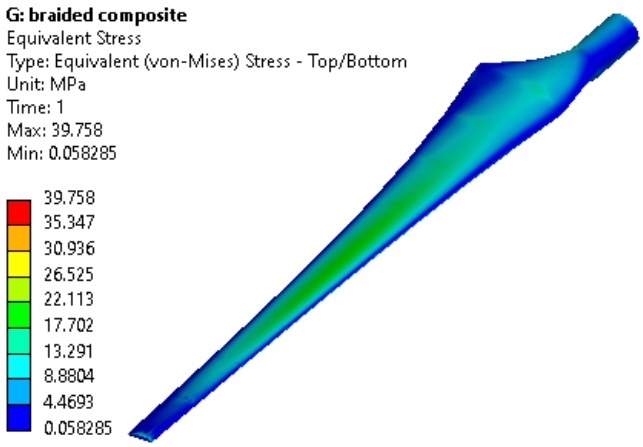

(c)

Figure V. 38 Distribution of Von Mises stress of (a) carbon/epoxy, (b) E-glass/epoxy, and (c) Braided composite

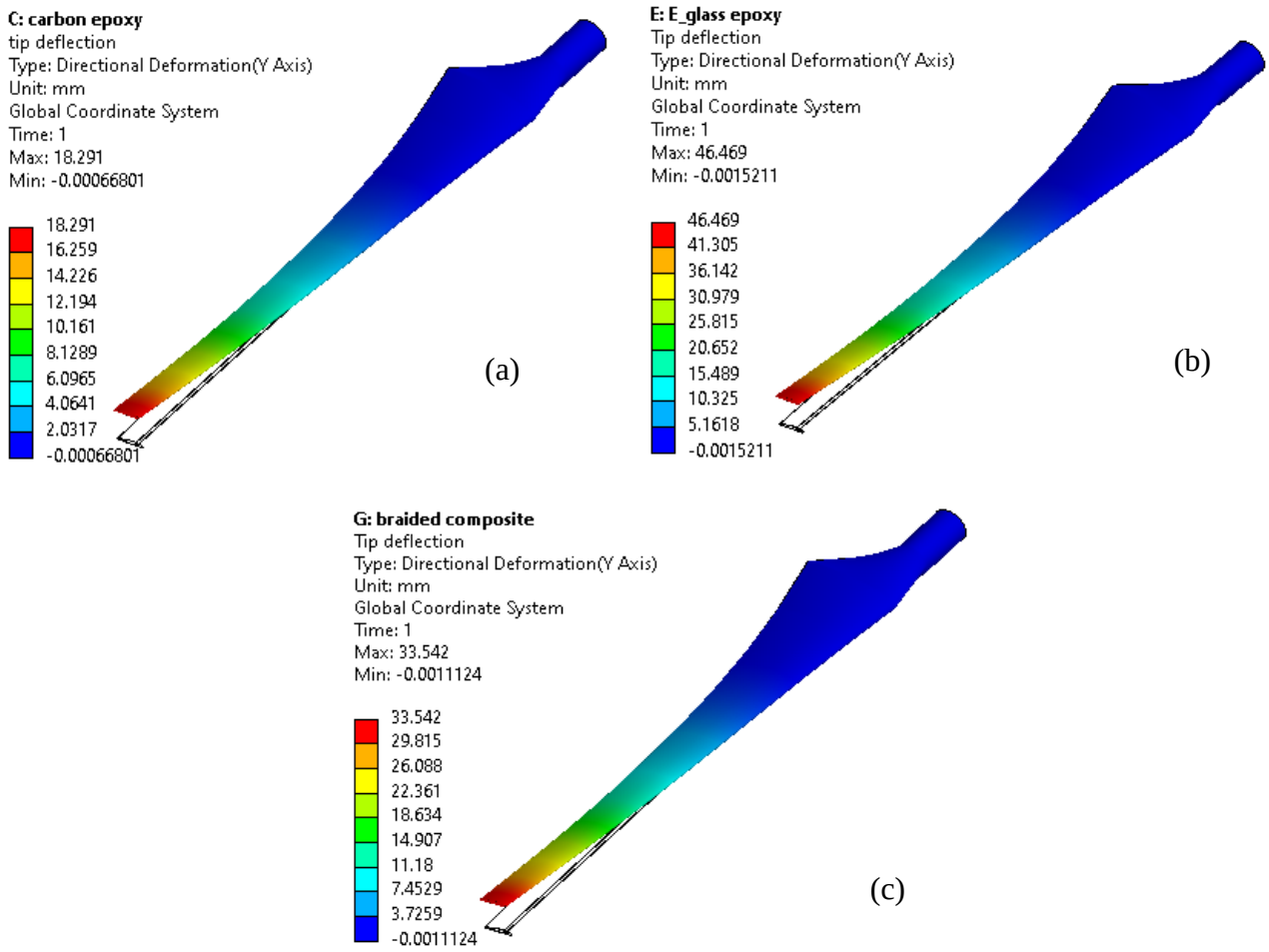

Figure V. 39 Tip deflection of (a) carbon/epoxy, (b) E-glass/epoxy, and (c) Braided composite

The deflection analysis revealed that the blade tends to bend in the direction of the lift forces, primarily due to the low-pressure region on this side. The Von-Mises stresses for the glass fibers and carbon fibers are 39.68 MPa and 40.37 MPa, respectively, both slightly higher than the Von-Mises stresses for the braided composite material, which is 39.75 MPa. It's worth noting that the highest stresses are concentrated in the middle section of the wind turbine blade length, indicating that the fiber distribution and thickness are well-suited for the structure.

As for tip deflection, Figure V. 39 displays noticeable differences among the three materials/models. The deflection for carbon fiber is 18.29 mm, glass fiber exhibits a deflection of 46.46 mm, and braided composite has a deflection of 33.54 mm. Importantly, all these deflection values remain within acceptable limits. The distance between the tower and the blade tip is approximately 400 mm, indicating that all three materials can be used effectively. However, E-glass stands out as the most suitable material due to its cost-effectiveness when compared to the other two materials.

Figure V. 40 provides insight into how blade deflections and Von-Mises stresses vary along the blade length. Additionally, Figure V. 41 illustrates the distribution of mass and stiffness along the blade length for all three materials under the same operational conditions.

Table V. 10 tip deflection and von mises comparison for different materials

	E-glass/epoxy			Braided composite			Carbon/ Epoxy		
	QBlade	**ANSYS**	**difference %**	**QBlade**	**ANSYS**	**difference %**	**QBlade**	**ANSYS**	**difference %**
Von mises stress [MPa]	38.51	39.68	2.94	39.20	39.75	1.38	39.96	40.37	1.015
Tip deflection[mm]	43.20	46.46	7.016	29.32	33.54	6.61	16.86	18.29	7.81

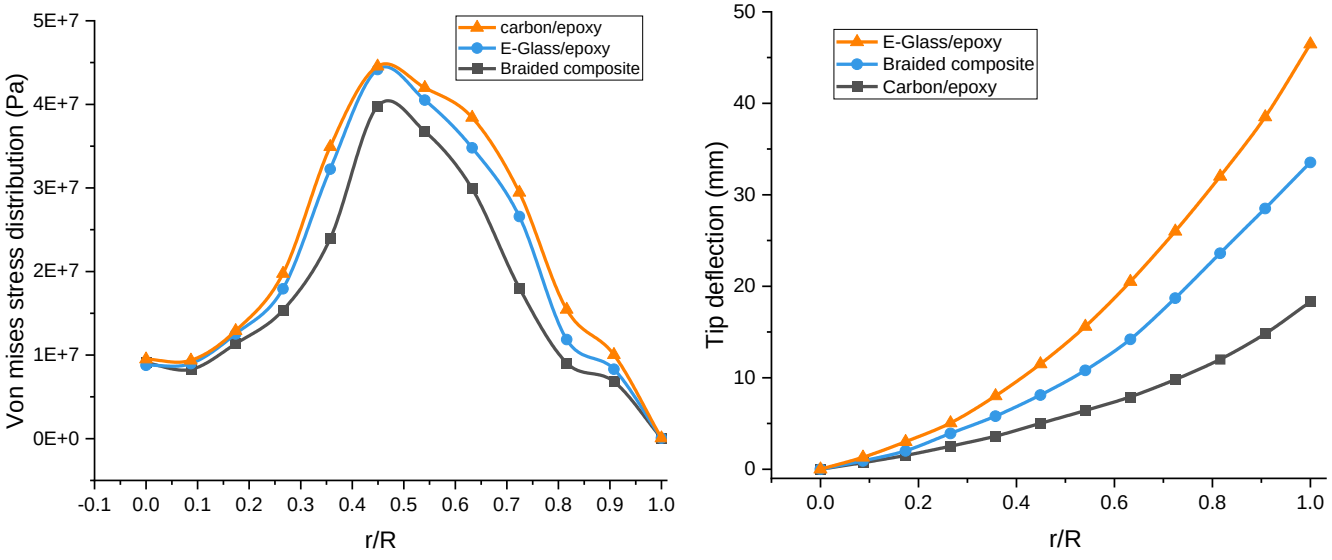

(a) (b)

Figure V. 40 Variation of (a) Von mises stress and (b) tip deflection along the blade

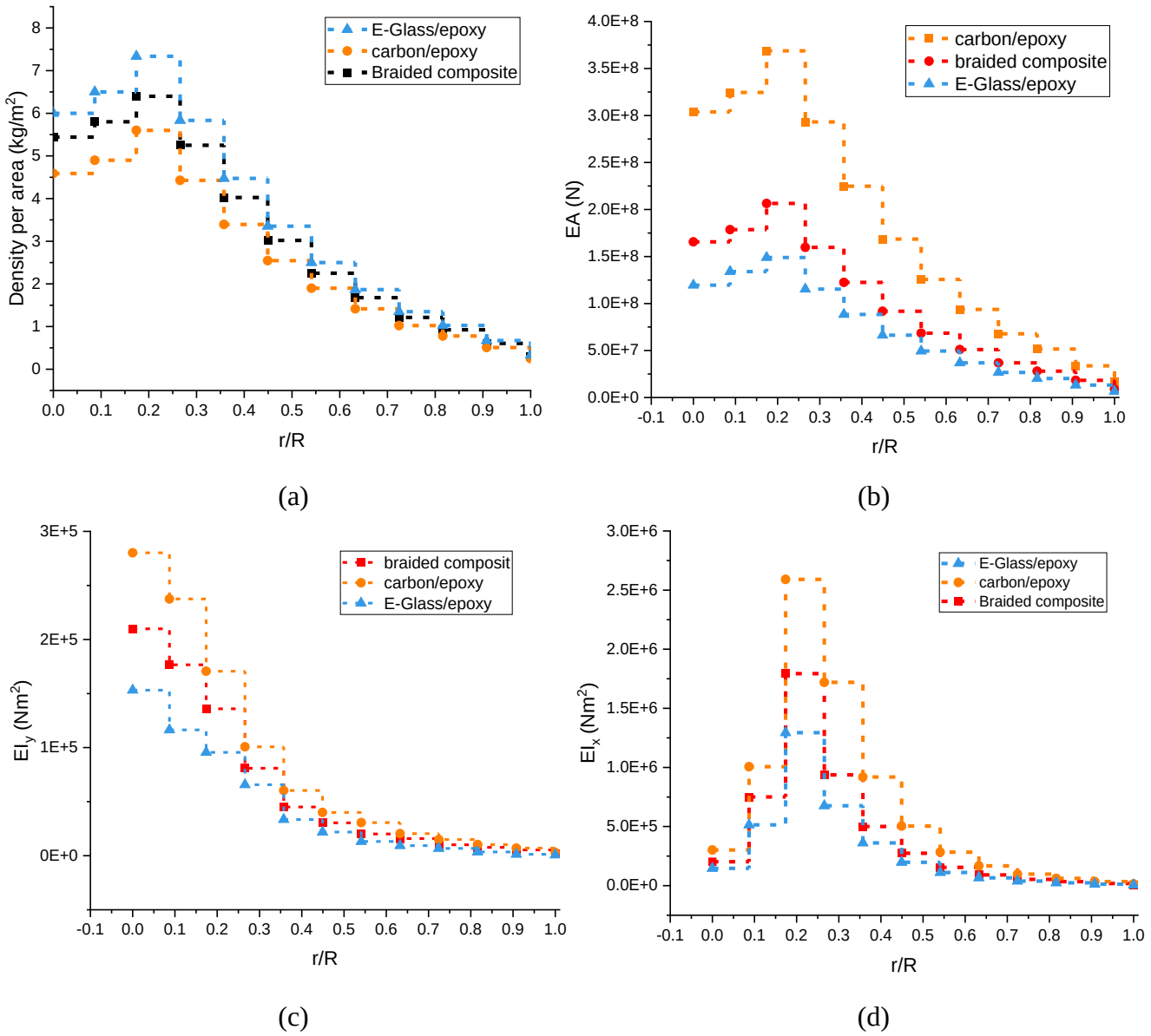

Figure V. 41 Distribute of (a) the density, (b) longitudinal stiffness, (c) Flapwise Stiffness, and (d) Edgewise Stiffness along the blade

The results from Figure V. 40a indicate that the highest stress values are concentrated at r/R = 0.5, which corresponds to the midpoint of the blade. This stress concentration occurs because the thickness distribution of the shell at the root is appropriately designed, leading to stress concentration in the middle of the blade, which is the region with the least damage and risk. On the other hand, Figure V. 40b reveals that the largest deflection occurs for E-glass, followed by the braided composite, and then carbon epoxy, in descending order of deflection magnitude. Figure V. 41 provide insights into the distribution of mass and stiffness along the wind turbine blade. The distribution is linear, with greater thickness at the root and gradually decreasing thickness towards the tip. This linear distribution aligns well with the layered composition of composite materials along the blade length, making it a suitable design for composite material layers.

III.2.6 Modal analysis of blade

In this section, we delve into the results of the modal analysis, focusing on the natural frequencies of the wind turbine blade. The primary goal of this analysis is to assess the compatibility of the aerodynamic shape design with the blade's structural characteristics, specifically examining the distribution of mass and stiffness along the blade's length. To achieve this, we selected an optimal mesh for the modal analysis based on the mesh used in the steady-state analysis, as illustrated in Figure V. 37. Figure V. 42 displays the natural frequencies and displacements for the first six mode shapes of the wind turbine blade, employing the selected materials. Additionally, Figure V. 43 to Figure V. 45 depict the first six mode shapes of the blade for the chosen materials. To validate our findings, we conducted a comparison between the results obtained from Ansys software and QBlade to determine the frequencies for various materials, as outlined in Table V. 11.

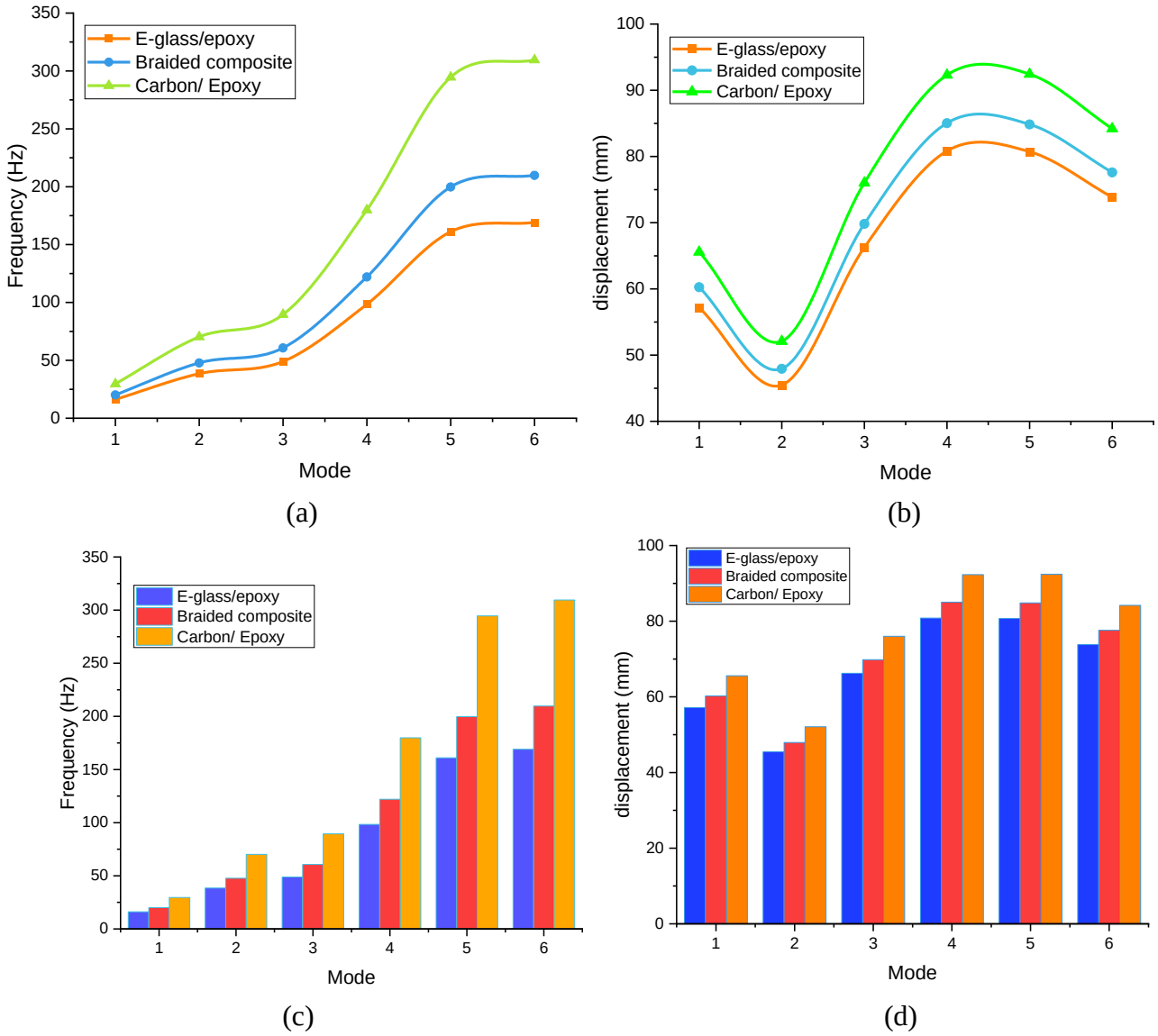

Figure V. 42 Variation of (a) natural frequency and (b) displacement with modes (c) Graph bar frequency with mode (d) Graph bar of displacement with mode

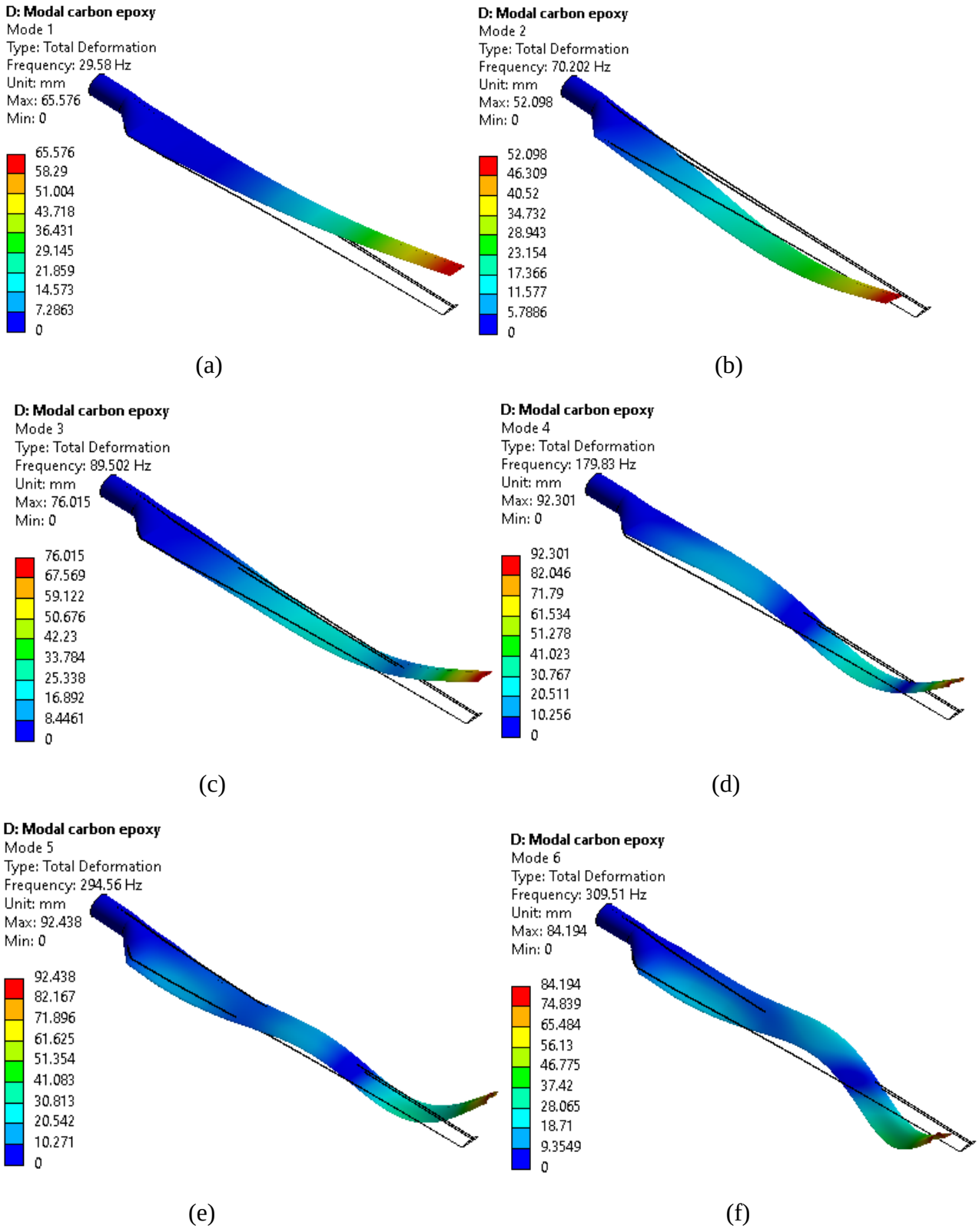

Figure V. 43 The first 6th mode shape of Carbon/Epoxy material. (a) 1st mode. (b) 2nd mode. (c) 3rd mode. (d) 4th mode. (e) 5th mode. (f) 6th mode.

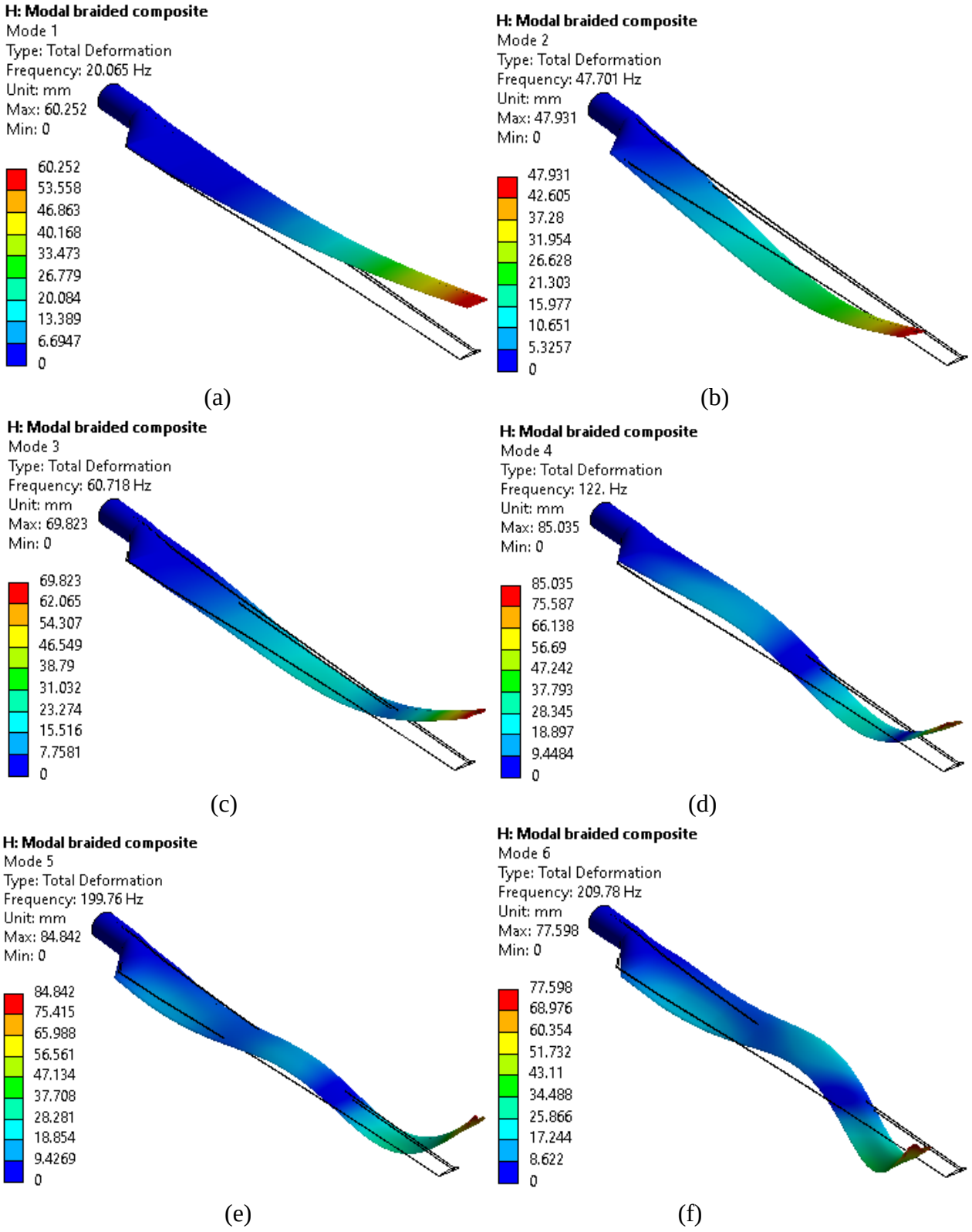

Figure V. 44 The first 6th mode shape of Braided composite material. (a) 1st mode. (b) 2nd mode. (c) 3rd mode. (d) 4th mode. (e) 5th mode. (f) 6th mode.

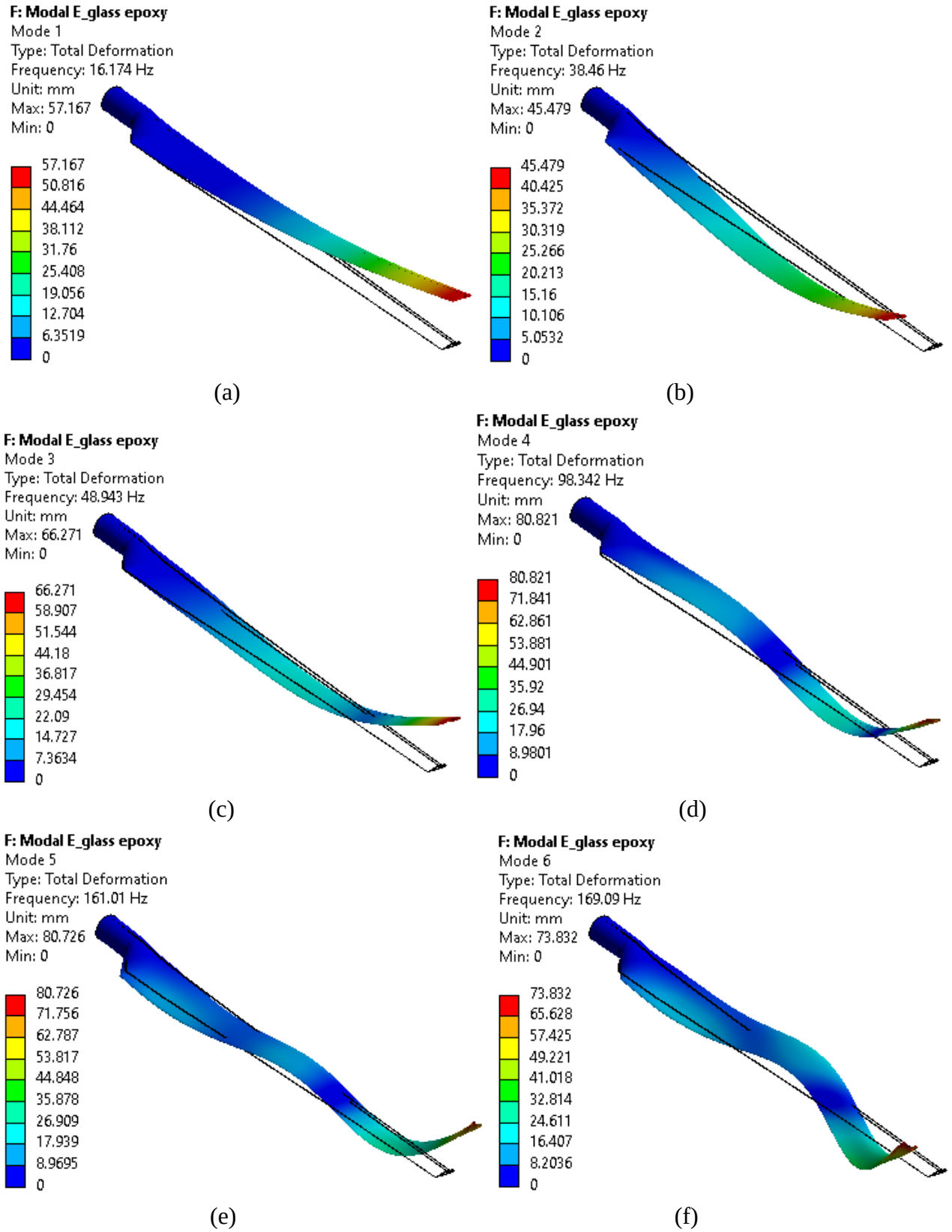

Figure V. 45 The first 6th mode shape of E-glass/epoxy material. (a) 1st mode. (b) 2nd mode. (c) 3rd mode. (d) 4th mode. (e) 5th mode. (f) 6th mode.

The structural stiffness of a wind turbine blade hinges significantly on material properties, particularly Young's modulus (E) and density (ρ). Consequently, the natural frequencies of the wind turbine structure primarily depend on the ratio ($\sqrt{E/\rho}$). Examining the results of the modal analysis presented in Figure 14-a, it's evident that the frequencies for the E-glass fiber material are lower than those for braided composite and carbon epoxy materials, indicating it is less resistant to vibrations. Despite this, the results for braided composite and E-glass material are relatively close due to the proximity of the ($\sqrt{E/\rho}$) ratio between them. In contrast, the carbon/epoxy material exhibits the highest natural frequencies among the materials, attributed to its superior ($\sqrt{E/\rho}$) ratio.

Figure V. 42b illustrates the displacement of the blade tip for the selected mode shapes of the three materials under study. It's apparent that carbon/epoxy material experiences the least displacement, owing to its high stiffness. Braided composite material follows, and E-glass/epoxy material exhibits the highest displacement. Notably, the highest displacement values occur in modes 4 and 5, signifying these two modes as critical and potentially problematic in blade design.

Table V. 11 The comparison of Frequencies using different materials

Mode	E-glass/Epoxy			Braided Composite			Carbon/ Epoxy		
	QBlade	ANSYS	difference %	QBlade	ANSYS	difference %	QBlade	ANSYS	difference %
1	15.13	16.17	6.43	19.80	20.06	1.30	28.29	29.58	4.36
2	36.19	38.46	5.90	48.32	47.70	1.30	74.11	70.20	5.57
3	45.39	48.94	7.25	63.41	60.71	4.45	92.20	89.50	3.02
4	99.56	98.34	1.24	130.59	122	7.04	185.14	179.83	2.95
5	165.82	161.01	2.99	196.43	199.76	1.67	289.23	294.56	1.81
6	172.93	169.09	2.27	221.15	209.78	5.42	315.67	309.51	1.99

III.3 Wind turbine blade under the static load

As part of the effort to further enhance the wind turbine blade's structural integrity, we will explore the possibility of changing the material type while also subjecting the blade to static loads. This thesis aims to compare the Finite Element (FE) model results with experimental data from studies conducted by [249] and [250]. To accomplish this, we will introduce three static loads/masses of varying magnitudes (3.3 kg, 6 kg, and 8.3 kg) near the blade's tip region to assess the maximum deflection of the blade tip.

III.3.1 Lay-up and material properties of the blade

In this study, we will explore the utilization of composite materials for crafting a wind turbine blade. To enhance the structural performance and minimize deflection, we will consider two distinct materials: glass fiber reinforced polymer (GFRP) and carbon fiber reinforced polymer (CFRP). These materials will be employed to construct Finite Element (FE) models, which will then be compared to experimental results to determine the most appropriate material for fabricating small wind turbine blades. The mechanical properties of GFRP and CFRP materials are detailed in Table V. 12 [251, 252].

Table V. 12 Mechanical properties of used material

Properties		GFRP	T300 CFRP
Young's modulus	E_{xx} (GPa)	44	136.7
	E_{yy} (GPa)	17	8.2
	E_{zz} (GPa)	16.7	8.2
Poisson's ratio	υ_{xy}	0.26	0.29
	υ_{zx}	0.26	0.42
	υ_{yz}	0.35	0.29
Shear modulus	G_{xy} (GPa)	3.49	4.45
	G_{zx} (GPa)	3.77	4.45
	G_{yz} (GPa)	3.46	2.91
Density	ρ (kg/m^3)	1800	1300

In constructing the Finite Element (FE) model for the blade composed of composite materials, it is crucial to establish the fiber orientation. For this study, we have chosen the following lay-up sequences for the shell fibers: $[0/90]_3$ for CFRP and $[0/90]_4$ for GFRP materials. Simultaneously, the spar cap employs a lay-up sequence of $[45/-45]_3$. Each ply has a thickness of 0.25 mm, and this determines the orientation along the length of the blade, corresponding to the z-axis (as depicted in Figure V. 46) representing the 0° orientation of the fiber lay-up sequence.

III.3.2 FE mode mesh

The Finite Element (FE) model of the wind turbine blade was simulated using the commercial Ansys software. The blade mesh employed the "shell 281" element, which is an eight-node element with six degrees of freedom (DOF) per node. Mesh convergence was achieved by ensuring the error rate did not exceed 1%. Once convergence was reached, the final FE model consisted of 17,820 elements and 18,205 nodes. You can observe the ultimate form of the FE mesh model in Figure V. 46.

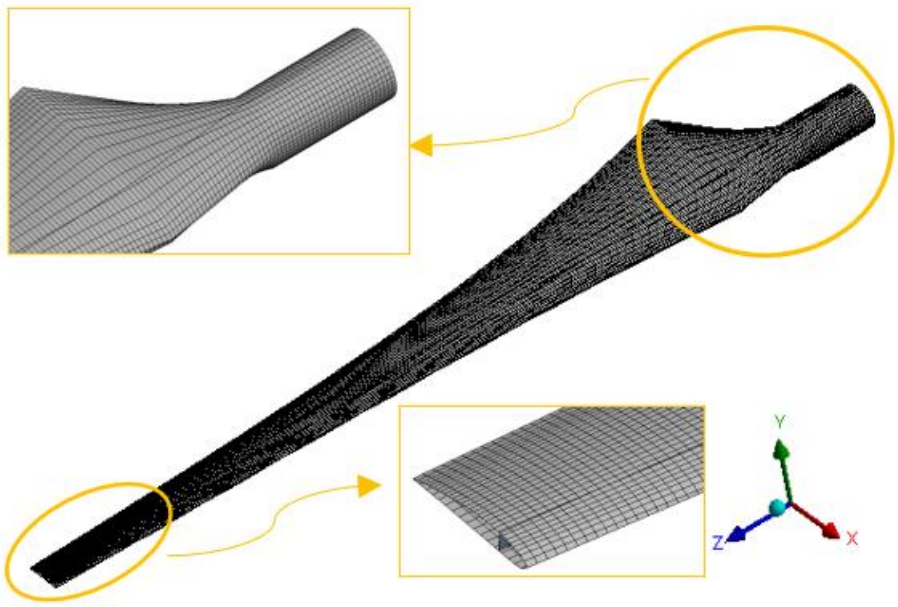

Figure V. 46 FE model mesh of blade

III.3.3 Blade boundary conditions

For the static analysis of the blade, the rotational speed will not be considered, and only the effect of gravity will be applied at the center of gravity of the blade. Furthermore, the blade will be fixed at the root side, which means all degrees of freedom will be constrained, and it will be free at the tip side. Additionally, there will be boundary conditions for the static loads applied to the blade, specifying the locations of their application. You can visualize the boundary conditions applied to the blade under static loads in Figure V. 47.

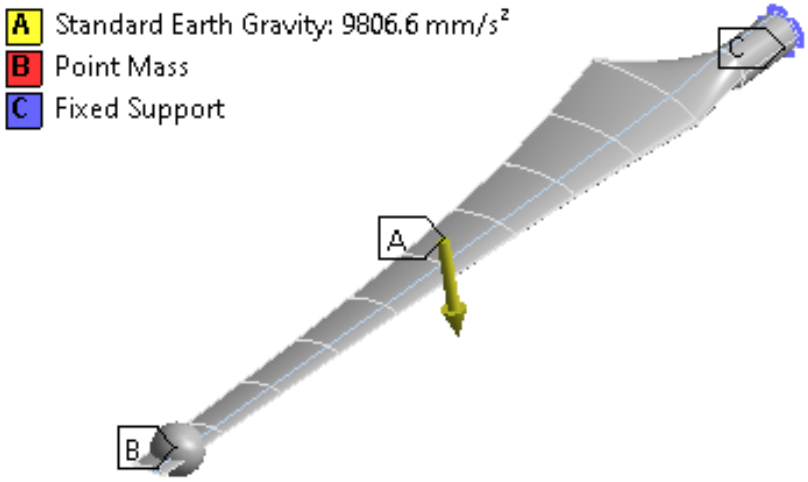

Figure V. 47 boundary condition of 2.5m steady-state blade

III.3.4 Deflection of the blade under the static loads

In the experimental study conducted by [249, 250], a wind turbine blade shell made of GFRP was fabricated and filled with H80 foam, with three different loads/masses (3.3 kg, 6 kg, and 8.3 kg) fixed near the blade tip to measure the maximum blade deflection. In our study, FE models were created using both GFRP and CFRP materials to optimize the blade structure. The H80 foam used in the previous experiment was replaced with the spar cap part to reduce mass, and the deflection behavior of the blade was analyzed.

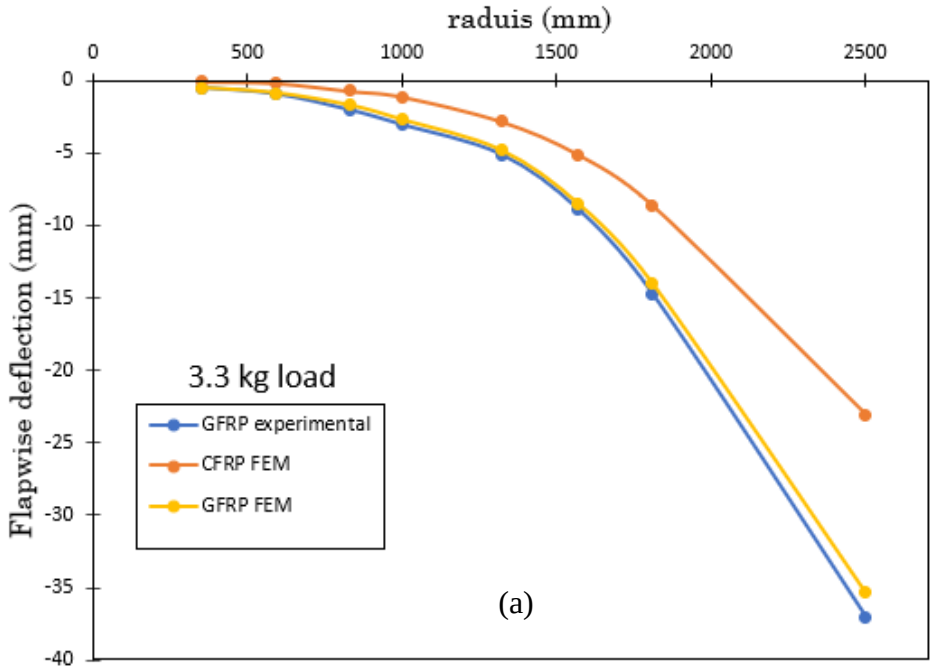

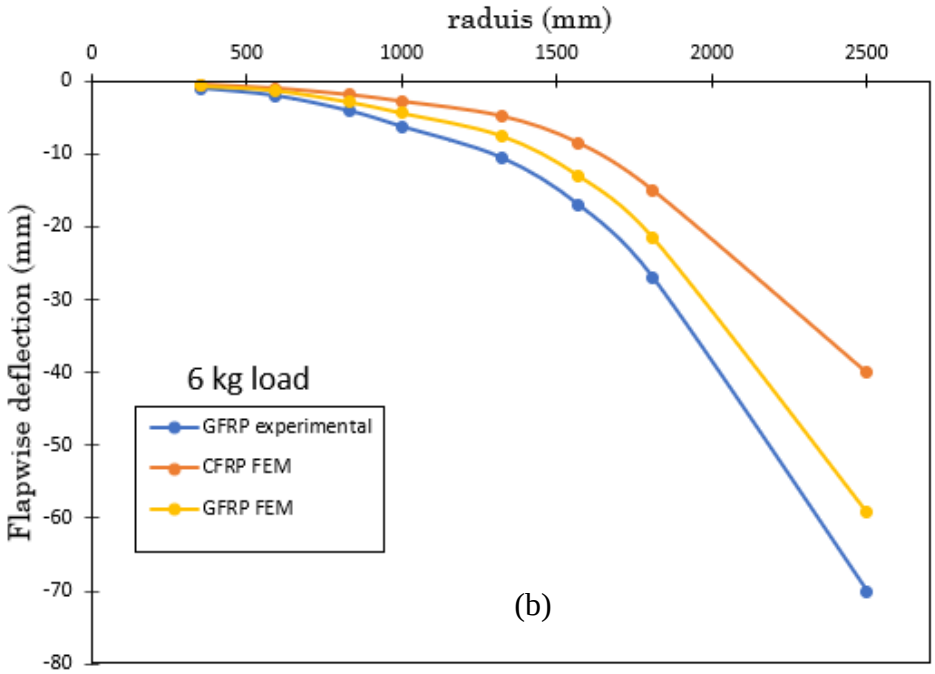

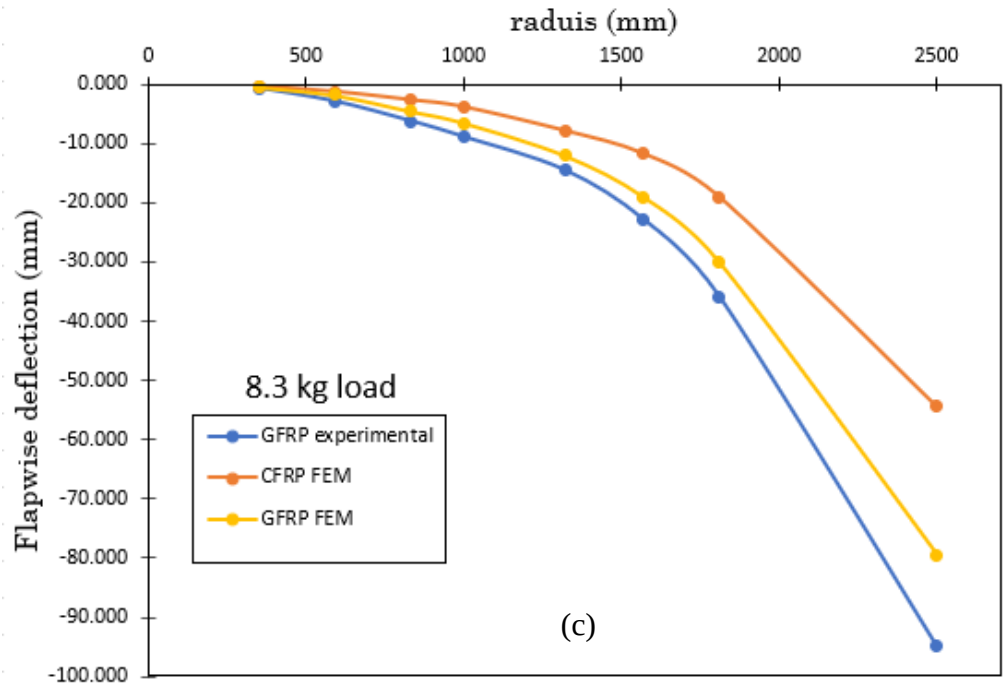

Figure V. 48 The blade flapwise deflection of a) 3.3 kg load and b) 6 kg load, and (c) 8.3 kg load.

The results, as shown in Figure V. 48, indicate that when applying a load of 3.3 kg, the maximum deflections for the CFRP and GFRP blades were 23.08 mm and 35.35 mm, respectively. These values are 37% and 4.5% less than the experimental deflection of 37 mm. When a load of 6 kg was applied, the deflections of the CFRP and GFRP blades were 40 mm and 59.18 mm, representing reductions of 42.85% and 15.45% compared to the experimental deflection of 70 mm. Finally, when an 8.3 kg load was applied, the maximum deflection of the CFRP blade was 54.42 mm, which is 42.61% less than the experimental result. The GFRP blade exhibited a deflection of 79.48 mm, which is 16.19% less than the experimental result of 94.83 mm.

Upon analyzing the results, it is evident that the blade made of CFRP material exhibits the lowest deflection for all different loads. In contrast, the deflection of the GFRP blade, when carrying a 3.3 kg load, closely aligns with the experimental results. However, the difference in deflection values becomes more pronounced when applying loads of 6 kg and 8.3 kg. This indicates that the improved blade structure shows better resistance when subjected to significant loads.

While the enhanced blade structure provides acceptable results in terms of deflection values, the most notable improvement is the reduction in blade mass, as illustrated in Figure V. 49. In the experimental study, the blade mass was 6.3 kg. In the FE model, the GFRP blade mass was reduced to 3.3 kg, marking a 47.86% reduction. On the other hand, the CFRP blade mass was reduced to 1.8 kg, which corresponds to a substantial 71.24% reduction compared to the experimental blade mass.

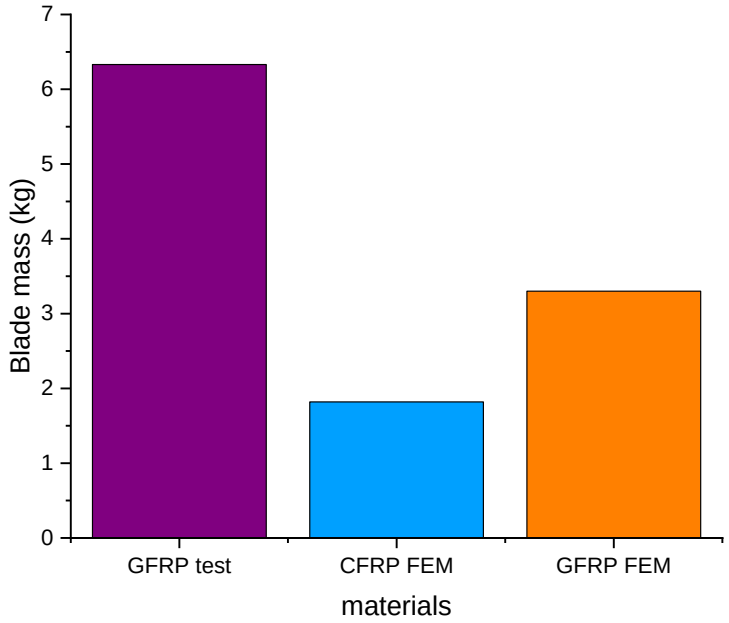

Figure V. 49 Mass of the wind turbine blade

IV. Fatigue Analysis of Wind Turbine Blade

To assess the impact of wind loads on the wind turbine blade, an aeroelastic simulation will be conducted using the FAST software (version 7). This simulation will utilize the geometry parameters of the optimized blade as a starting point. To simplify the load modeling process and streamline calculations, the simplified load model (SLM) will be adopted. The SLM is chosen for its simplicity and the use of primary loads with high safety factors. The first step objective of this simulation is to analyze blade fatigue by calculating the loads that induce fatigue in the blade.

IV.1 fatigue load calculation for SLM case A

Figure V. 50a illustrates the flapwise moment of the wind turbine blade at a design wind speed of 10.5 m/s. The fatigue loads under normal wind conditions are presented in Table V. 13. The simplified load model (SLM) approach assumes constant fatigue loads at a design speed. However, in actual operation, the blade's fatigue loads vary over time, influenced by operational periods, rest, and maintenance.

The SLM approach represents these varying fatigue loads using a constant sinusoidal field, with the maximum flapwise moment calculated at 1.5 times ΔM_{yB}, equal to 952.38.

To validate the flapwise moment results, a comparison was made between the results obtained by the SLM approach and the aeroelastic simulation conducted in FAST software. Figure V. 50b depicts this comparison, showing that the SLM predicts a constant flapwise moment over time, while FAST simulation results exhibit fluctuations. These fluctuations are due to changes in instantaneous wind speed and are closer to reality since fatigue loads typically vary rather than remain constant.

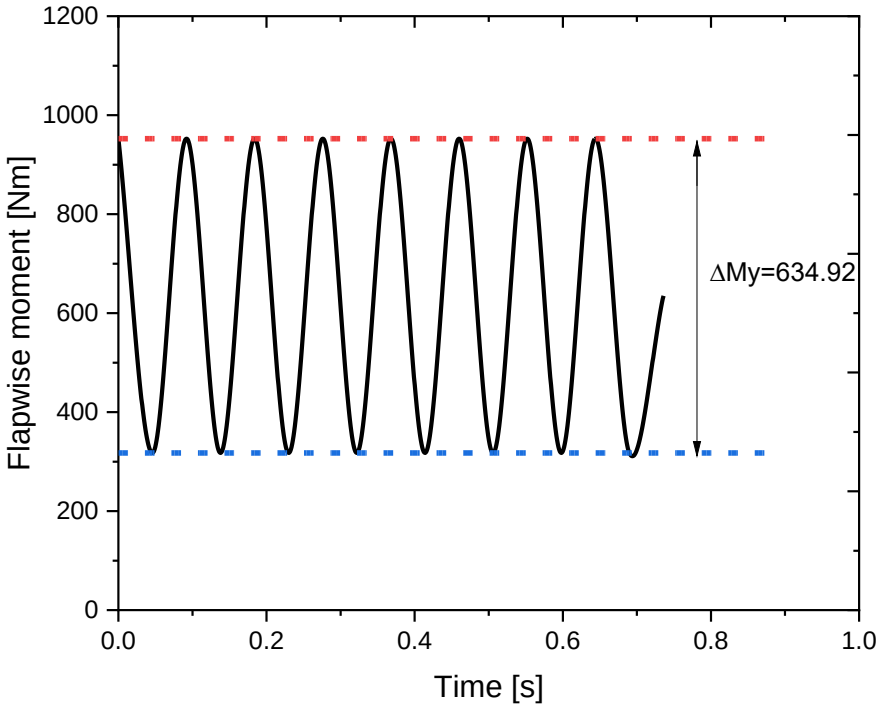

(a)

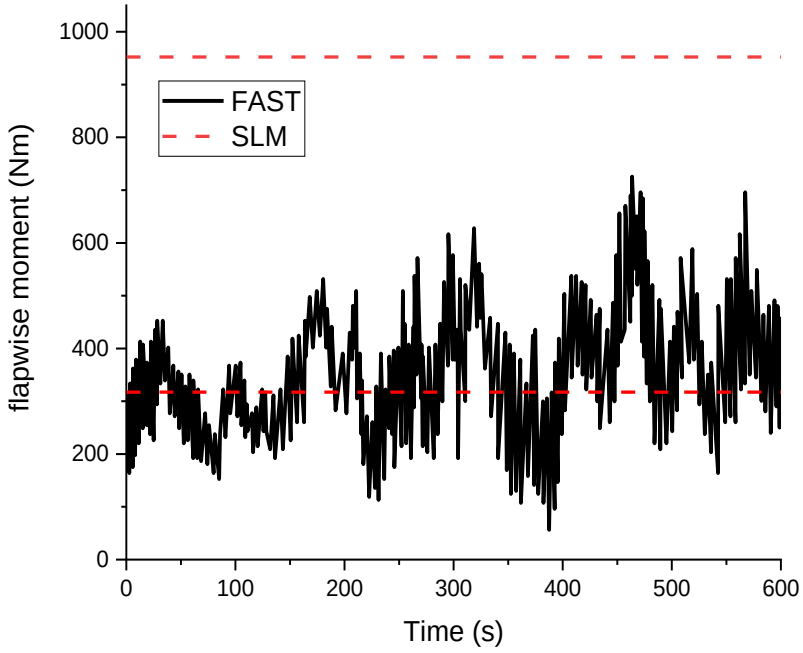

(b)

Figure V. 50 flapwise moment of blade (a) the SLM sinusoidal range, and (b) comparison between SLM and FAST simulation

Table V. 13 The fatigue Loads at normal wind conditions (10.5 m/s).

Loads type	SLM	FAST
Centrifugal force(kN)	27.49	23.83
Flapwise bending (Nm)	635	742
Edgewise bending (Nm)	531	1268
Design torque Q_{design}(Nm)	317	295

IV.2 Extreme wind load for SLM (case H)

In the "case H" of the SLM approach, the blade is considered safe if the von Mises stress is below the allowable stress limit. Table V. 14 presents the equivalent stress values for GFRP and CFRP blades, which are 19.23 MPa and 26.84 MPa, respectively. Since these equivalent stress values are lower than the allowable stress limit, it indicates that the blade will remain safe under extreme wind loads.

To validate the results obtained using the SLM method, a simulation was conducted using ANSYS software. Initially, CFD was employed to study the effect of airflow at a wind speed of 52.5 m/s, calculating the pressure applied to the blade surface. Subsequently, this pressure data was used in the FE model to assess the stress at the root zone. Figure V. 51a and Figure V. 51 illustrate the distribution of von Mises stress on blades made from CFRP and GFRP materials.

From Figure V. 51a and Figure V. 51b, it is evident that the average von Mises stress at the root of GFRP and CFRP blades is 20.58 MPa and 35.31 MPa, respectively. This convergence between the results obtained from the SLM "case H" and ANSYS simulations in the distribution of von Mises stresses at the root zone suggests that the SLM results can be relied upon to verify the blade's safety when subjected to extreme wind loads.

Table V. 14 Extreme wind condition load case H of SLM

Material	Allowable Stress Limit (MPa)	Calculated equivalent Stress (MPa)	Conclusion
GFRP	151.52	19.23	SAFE
CFRP	248.48	26.84	SAFE

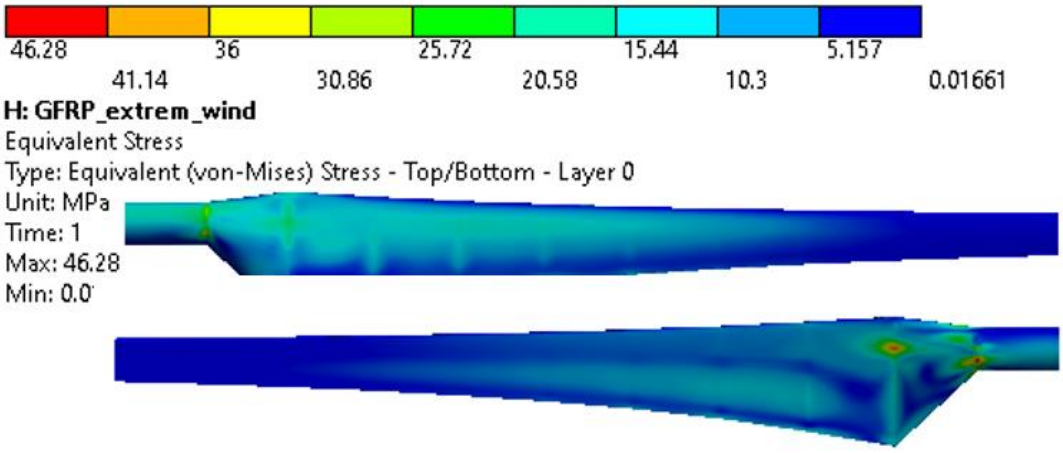

(a)

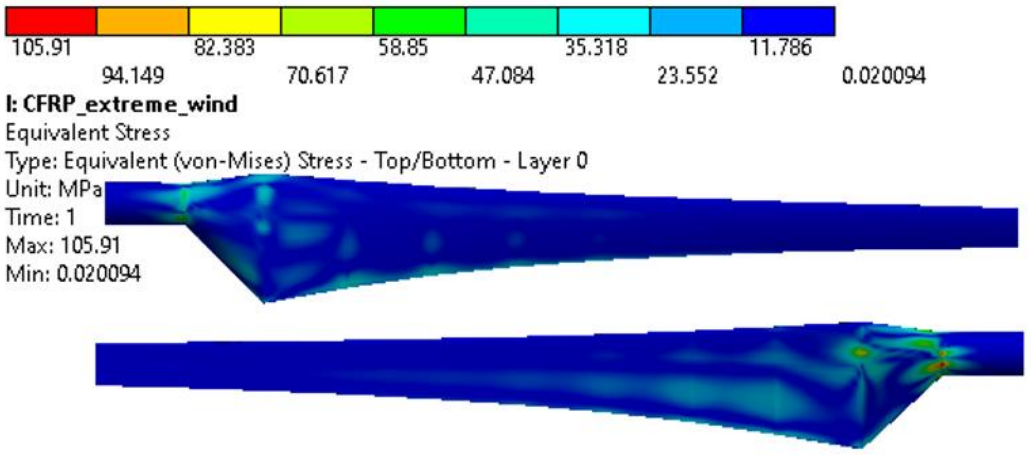

(b)

Figure V. 51 The von-Mises stress distribution of extreme wind conditions (a) GFRP material and (b) CFRP material

IV.3 FAST Aeroelastic simulation for fatigue

In the simulation, the wind load was generated using TurbSim and then input into the InflowWind FAST module. QBlade includes a computational tool for generating these wind fields through stochastic temporospatial simulation. In this study, the following parameters were employed: a complete turbulent wind field was generated using the Kaimal spectral model and the power law wind profile. The mean wind velocity at the hub height was set at 10 m/s, and it exhibited turbulence characteristics according to IEC characteristic B, representing a turbulence intensity of 14%. The wind field grid size was configured as 10 m × 10 m. A simulation duration of 600 seconds was selected to obtain results for a 10-minute interval, excluding the initial 20 seconds to permit the dissipation of transient effects associated with starting from a stationary state. The output time step of 0.25 seconds, equivalent to a sampling frequency of 4 Hz, was chosen to ensure accurate frequency domain processing of the time-domain data. Figure V. 52 displays a spatial wind field map for four instants captured during the 600-second simulation with an average speed of 10 m/s.

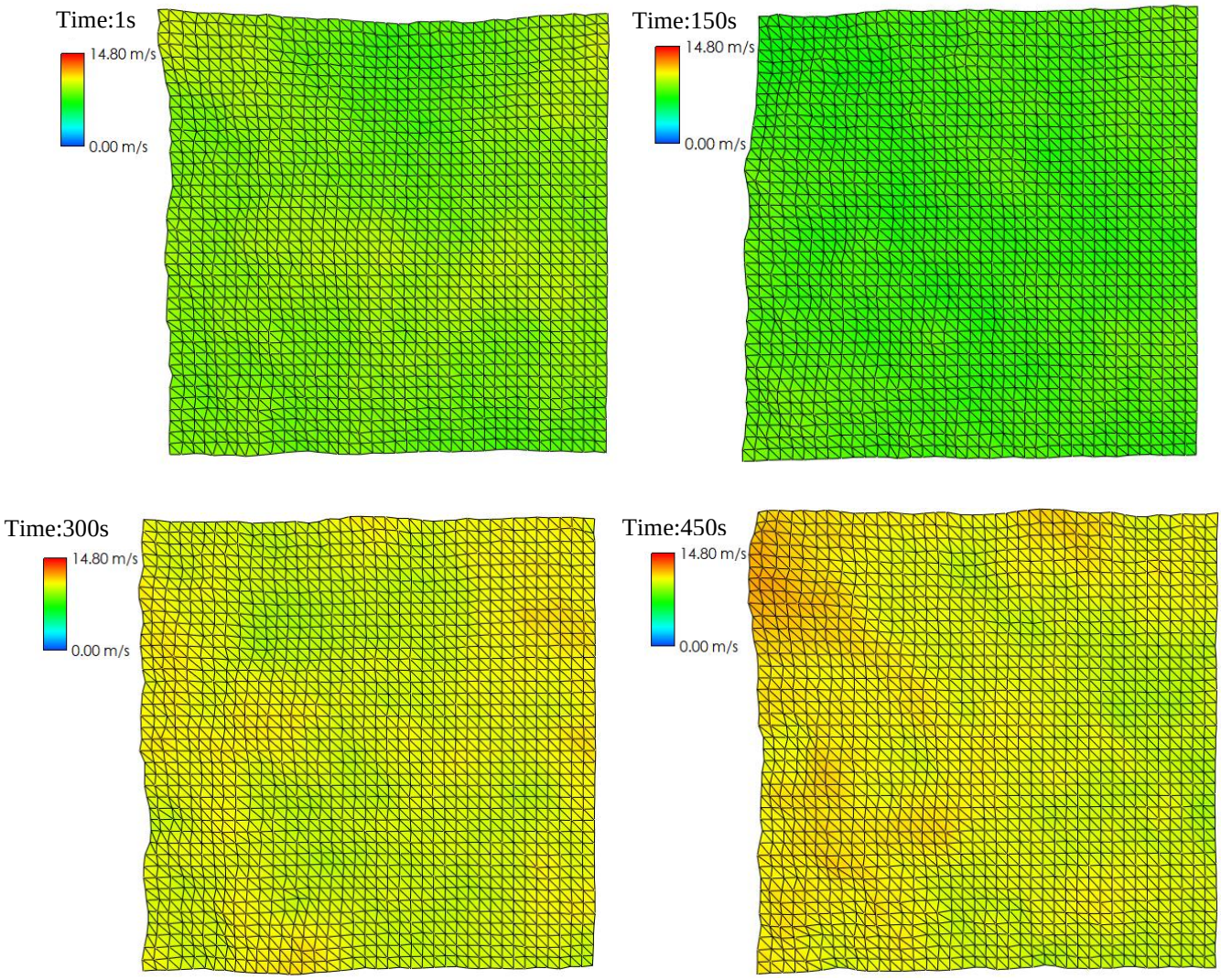

Figure V. 52 Wind field simulation at different time steps

As evident from the wind field map, there is a variation in wind intensity at the rotor as time progresses. Wind field maps were captured at intervals of 1s, 150s, 300s, and 450s to illustrate the changes in wind intensity over time. However, it is worth noting that during the 600s duration, the wind intensity would be comparable to that observed at the 1s time period.

Figure V. 53 displays a time series of wind velocity fluctuations in the horizontal directions (x-directions). These fluctuations show variations around 10 m/s in the x-direction, the wind velocity equal to zero in both the y- and z-directions.

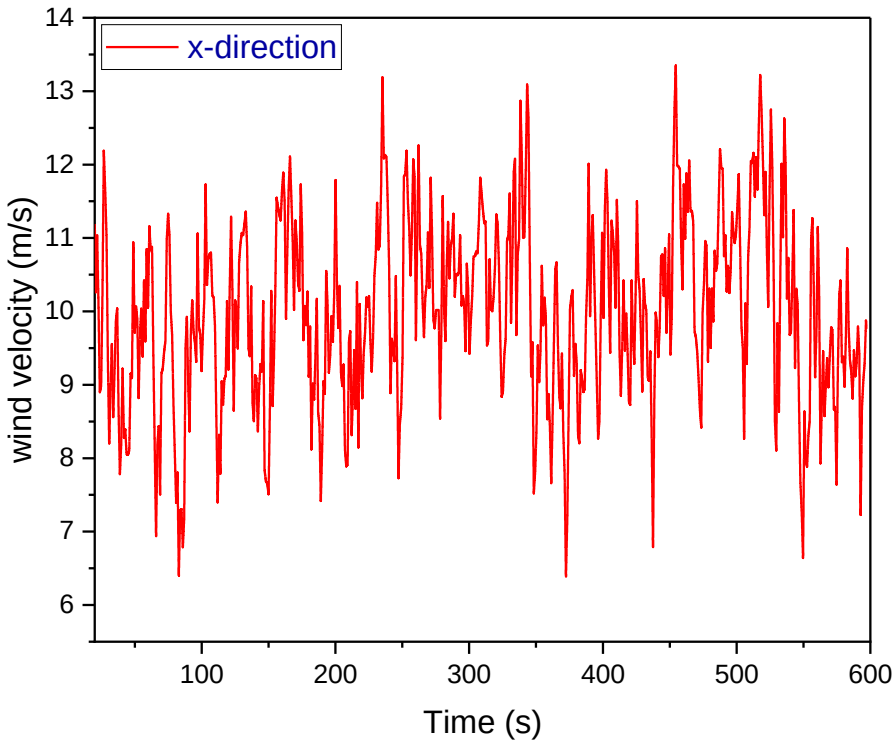

Figure V. 53 variation of wind field with time

The temporal variation in wind speed, as seen in the aeroelastic simulation, and its inherent instability, which occurs at a fixed average value, add a level of realism to the calculation of fatigue loads applied to the blade. This approach allows for a more accurate prediction of the blade's lifespan, taking into account the frequency of wind fluctuations. However, it doesn't consider scenarios of wind cessation or maintenance intervals, which could extend the blade's lifespan further. Given that the wind turbine blade is anchored at the root side, axial and tangential loads applied to the blade vary over time, as depicted in Figure V. 54. These variations result in flapwise and edgewise moments, both subject to temporal fluctuations as shown in Figure V. 55. These dynamic loads ultimately lead to deflections at the blade's tip, which also vary over time, as illustrated in Figure V. 56. These cyclic loads induce fatigue in the blade material, increasing the risk of structural failure. The same figures clearly indicate that the choice of material used does not have a significant or discernible effect on the loads or the power extracted from the blade. These factors are primarily related to the aerodynamic design of the blade rather than the material of its structure.

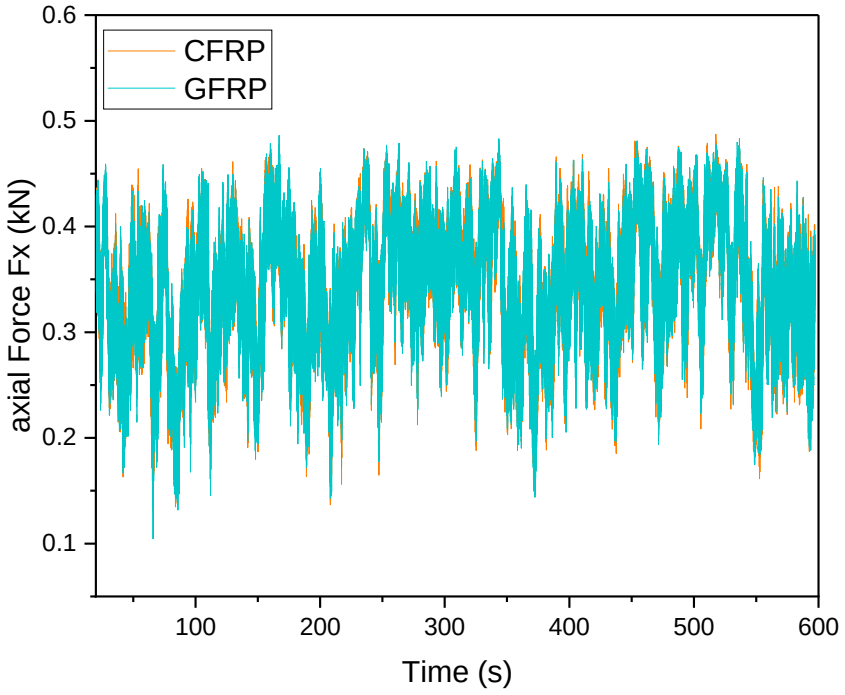

(a)

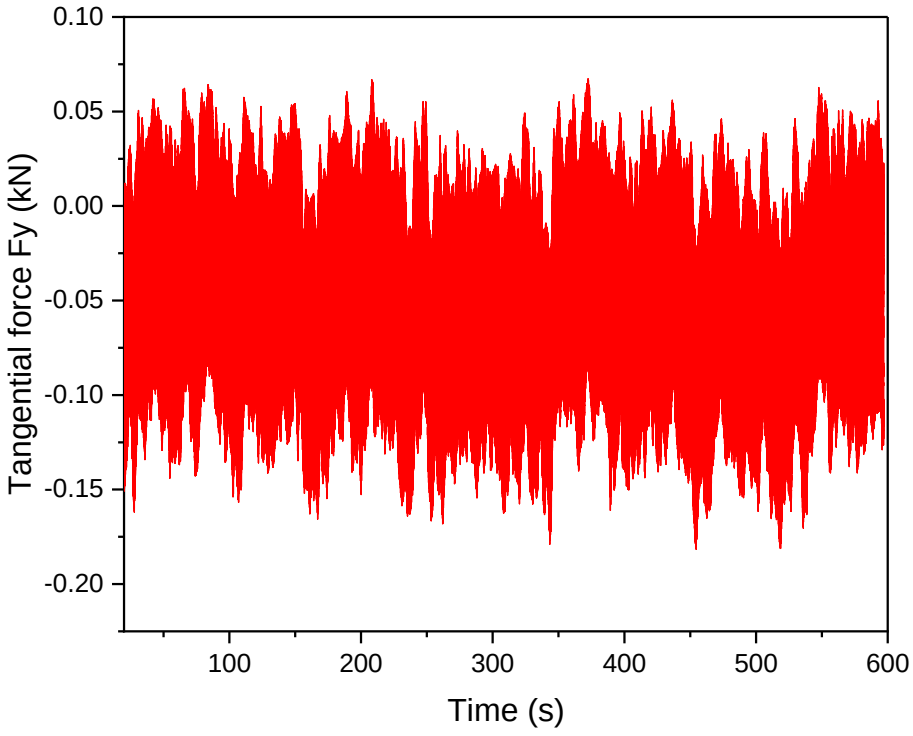

(b)

Figure V. 54 fluctuating loads applied on the blade (a) axial force, and (b) force tangential

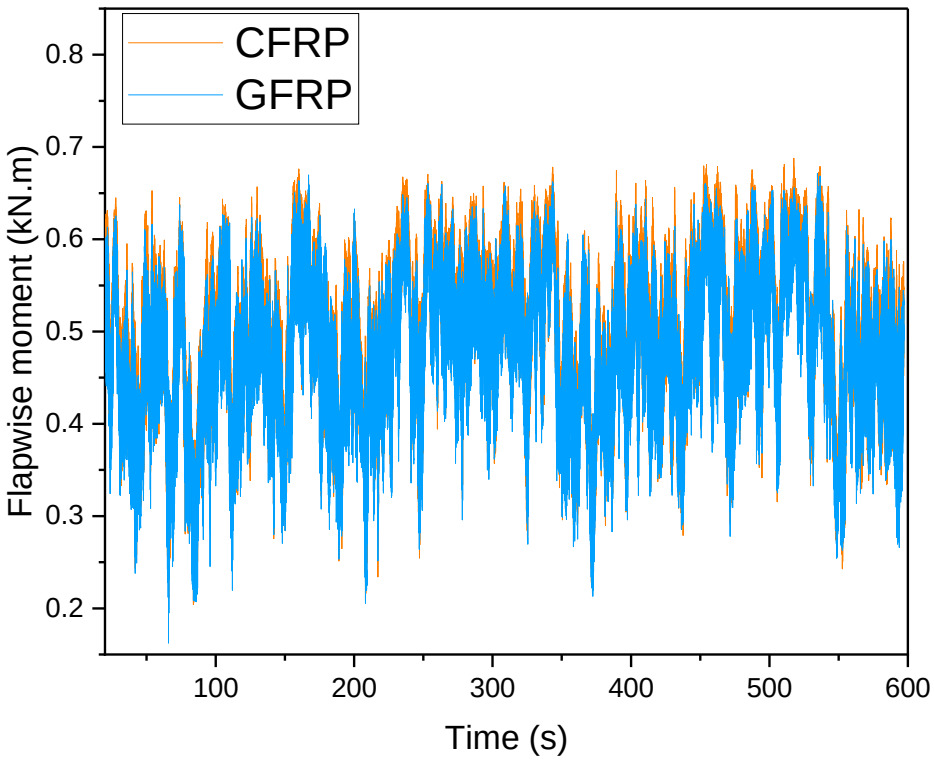

(a)

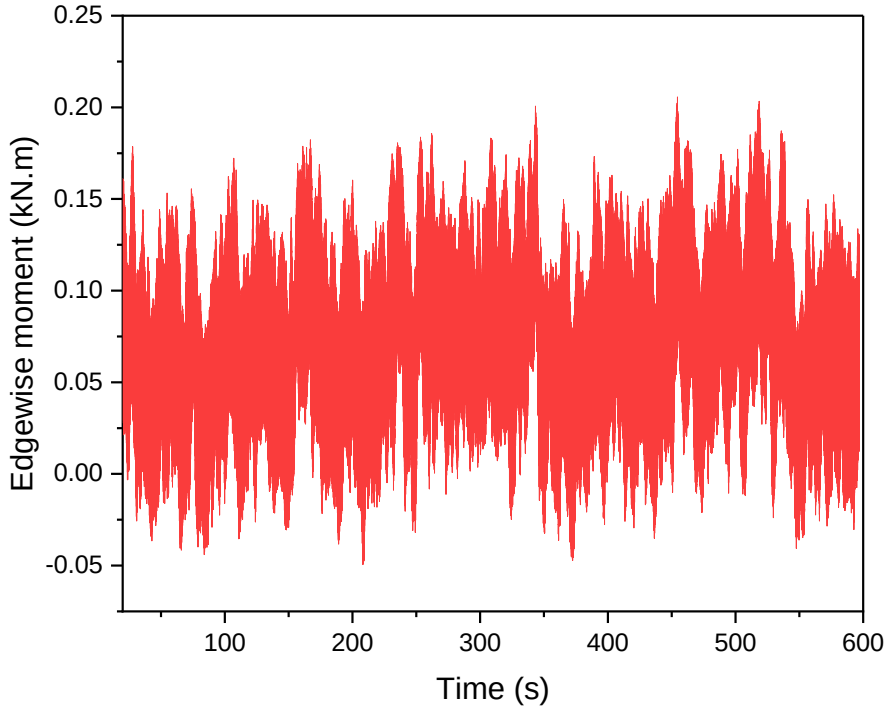

(b)

Figure V. 55 moment applied on the blade (a) flapwise moment, and (b) edgewise moment.

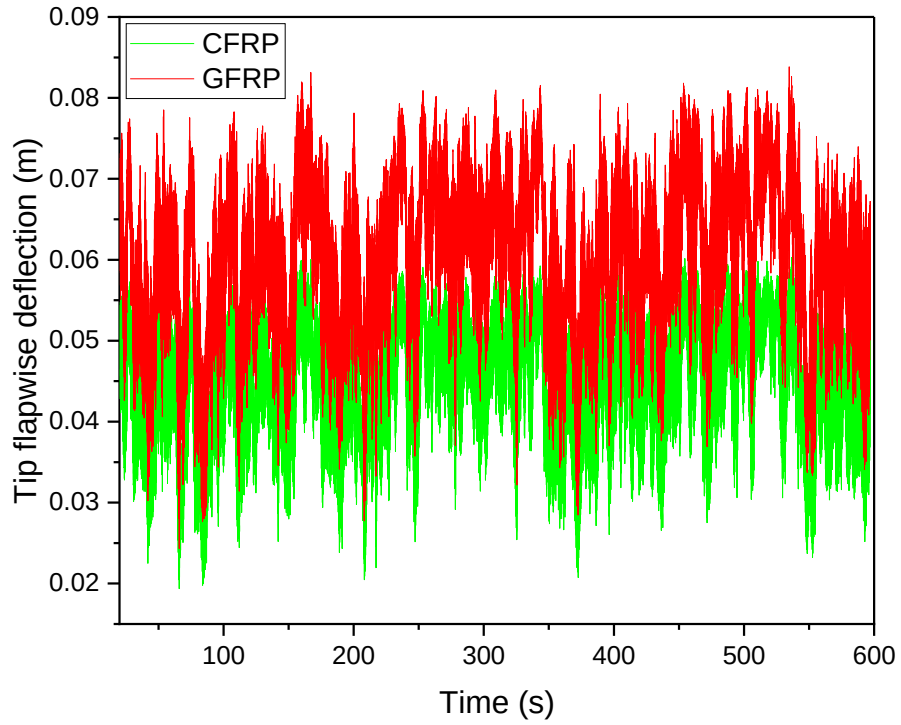

(a)

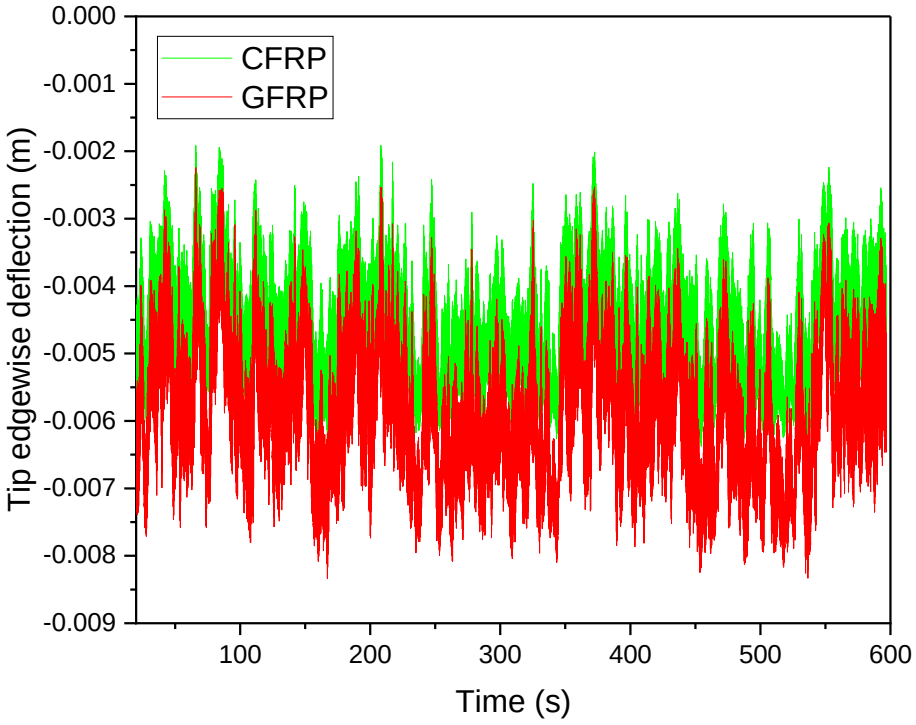

(b)

Figure V. 56 blade tip deflection of (a) flapwise direction, and (b) edgewise direction.

Indeed, wind speed exhibits a continuous and fluctuating pattern, as illustrated in Figure V. 53. The power harnessed by the wind turbine depends on the wind speed it encounters, causing the turbine's rotation. Consequently, when representing the harnessed power over time, it fluctuates reciprocally, resembling the pattern in
Figure V. 57. Conversely, if we depict power concerning wind speed over time, it forms clusters of closely spaced points due to wind speed fluctuations (both increases and decreases), as exemplified in Figure V. 58. Similarly, the power coefficient is influenced by the wind's instability, marked by its periodic shifts in a manner that is dependent on the geographical location where the blade is positioned, as demonstrated in Figure V. 59. Indeed, the power output from the analyzed model demonstrates a considerable range, reaching its peak at 13 kW when the wind speed hits 13 m/s, and decreasing to 0.5 kW during low wind speed conditions.

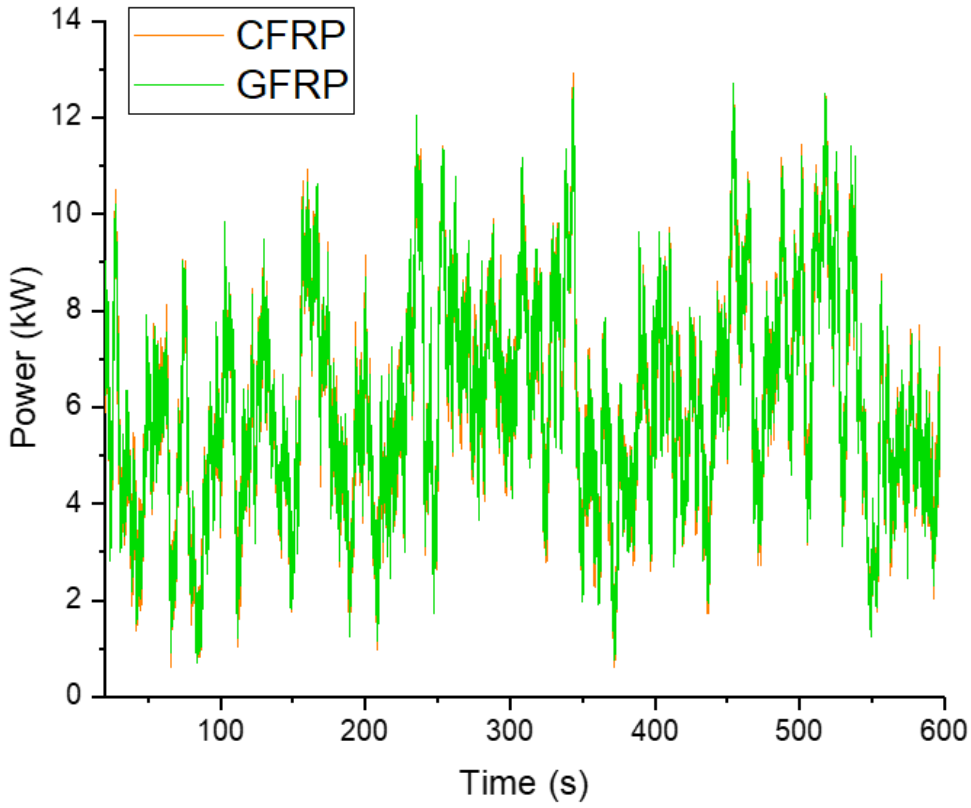

Figure V. 57 output Power of wind turbine dependent with time

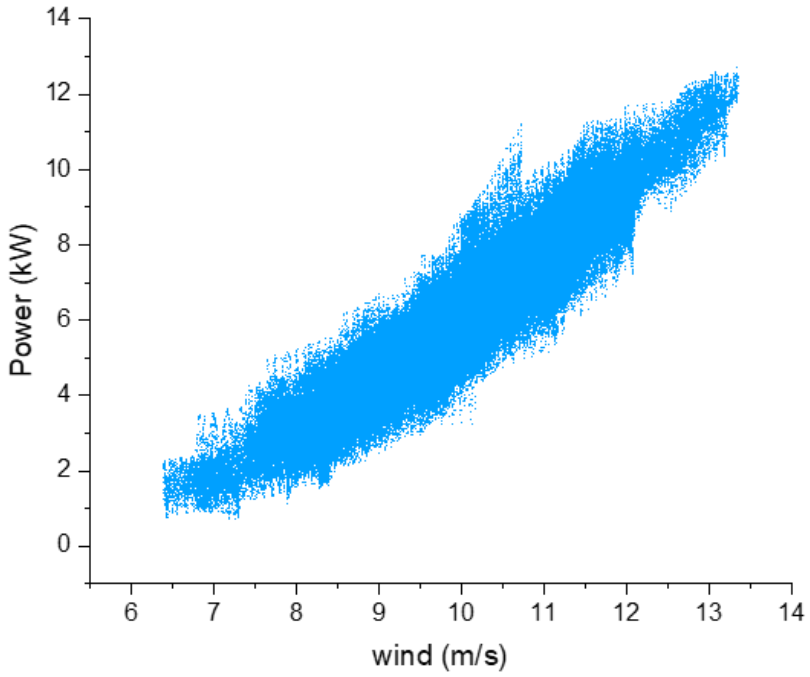

Figure V. 58 variation in power of wind turbine in function of wind speed

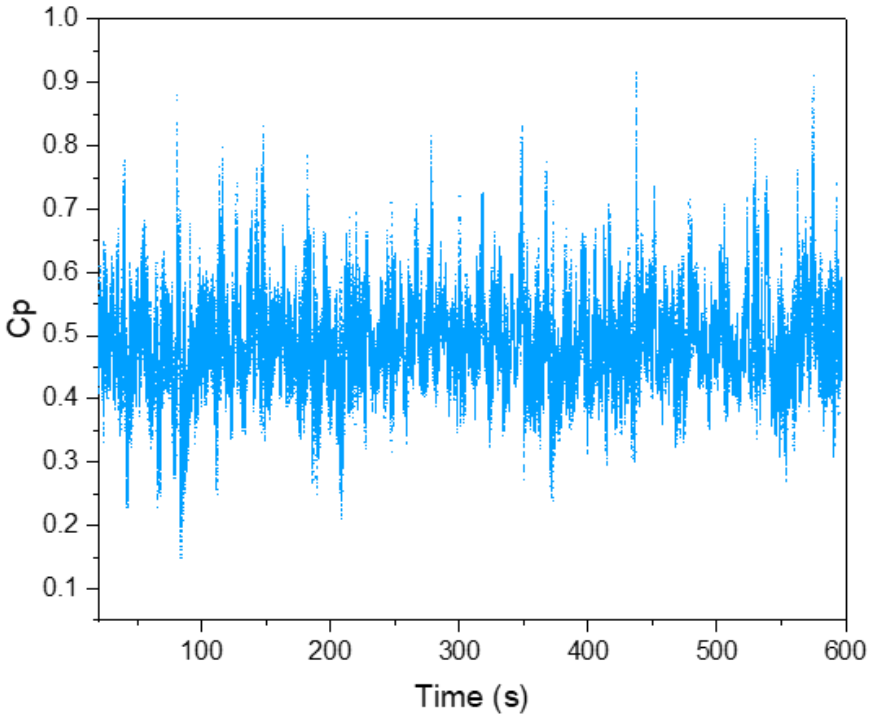

Figure V. 59 variation of output power coefficient with time

IV.4 Damage analyses and blade life

To predict blade damage, Miner's law was applied. The GFRP material has an S-N slope parameter β of 0.106 [253], while the CFRP material has a parameter less than 0.085 [254]. Using equation (III. 37), it was determined that the number of cycles to reach failure for the GFRP blade is $N_{f,GFRP} = 2.06\text{x}10^9$ cycles, and for the CFRP blade, it is $N_{f,CFRP} = 8.84 \times 10^{10}$cycles.

The damage of the GFRP blade was calculated using the SLM approach and was found to be $D_{SLM,GFRP} = 3.68 > 1$, which is greater than 1. This indicates that the wind turbine blade will fail before reaching the design life. On the other hand, the damage of the CFRP blade is $D_{SLM,CFRP} = 8.59 \times 10^{-2}$, which is less than one, implying that the blade will exceed the required design life.

Additionally, the damage was predicted using M-Life in FAST software, resulting in a damage value of $D_{FAST,GFRP} = 2.01$ for the GFRP blade and $D_{FAST,CFRP} = 4.27 \times 10^{-2}$ for the CFRP blade.

Based on the SLM approach, a GFRP blade is expected to withstand periodic fatigue loads for approximately 5.5 years, while a CFRP blade is projected to have a lifespan of more than 20 years. In the aerodynamic simulation conducted using FAST software, a GFRP blade is estimated to withstand loads for about 10.25 years, while a CFRP blade is predicted to have a very long life exceeding 20 years. Table V. 15 provides a comparison of the results obtained from both the SLM and FAST approaches with the experimental results of a wind turbine blade.

Table V. 15 Fatigue damage load and blade life for different methods and materials.

Method	materials	SLM	FAST	Measured [255]
Fatigue damage loads (Nm)		634	195	71
Blade fatigue life (years)	GFRP	5.5	10.25	9.18
	CFRP	over 20	over 20	-

Based on the previous results, it can be concluded that the SLM method provides the most conservative (safest) estimates, followed by aeroelastic simulations, with the measured results being the least conservative. Interestingly, all established methods predict a lifetime for the GFRP material that is less than the design life of 20 years, while the CFRP material is projected to have a fatigue life of more than 20 years.

V. Blade Fracture Analysis

In contemporary wind turbine design, the blades are fabricated from composite materials. Under normal operating conditions, these blades experience repeated loads, which may result in failure and the formation of cracks. The exploration of cracks and fractures in composite materials remains an active area of study and advancement. This thesis seeks to investigate the spread of cracks within composite materials by scrutinizing the stress distribution on wind turbine blades. Figure V. 60 illustrates the procedural steps involved in simulating cracks within the ANSYS program.

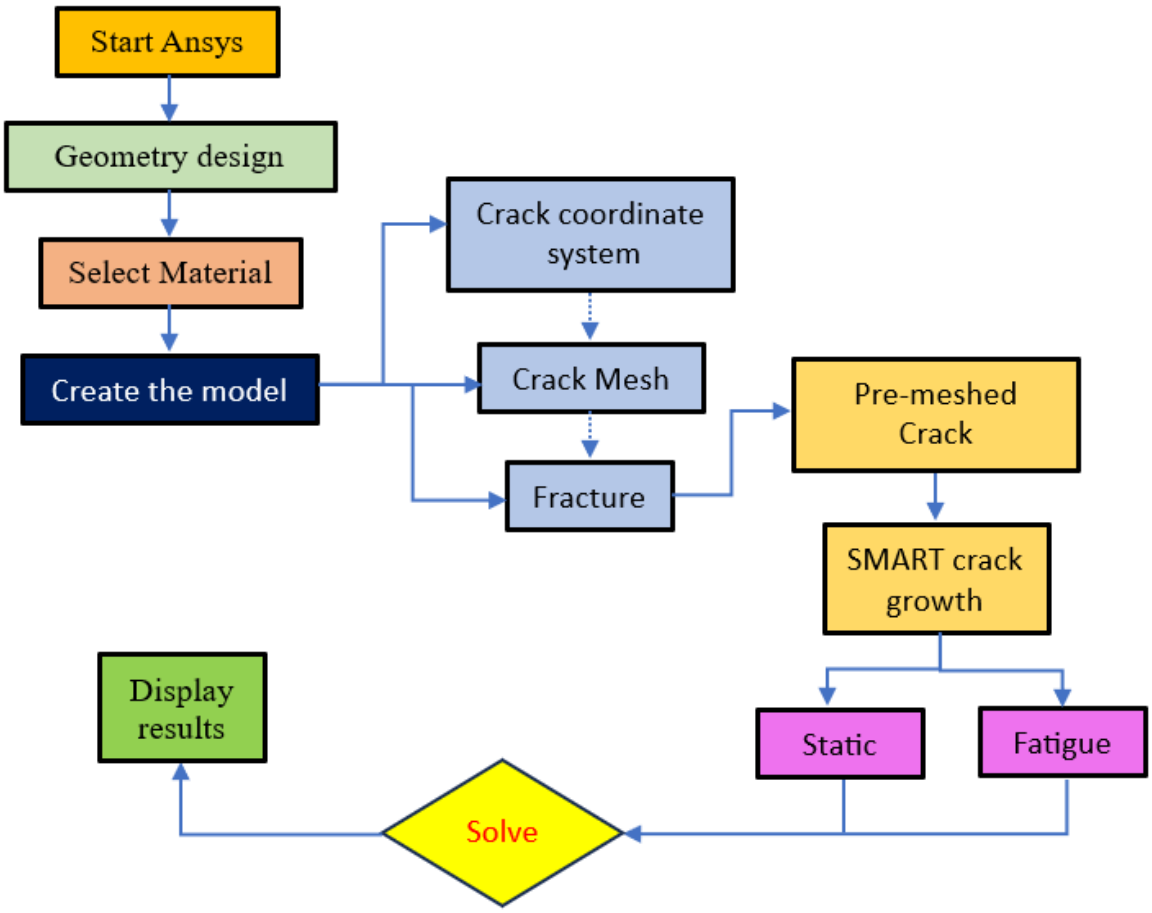

Figure V. 60 ANSYS flowchart for crack simulations

V.1 The Crack Location in Blade

Cracks tend to manifest in regions subjected to elevated stress levels. To anticipate the probable crack locations or predict where cracking is likely to transpire, it is imperative to commence with a stress analysis of the blade. According to the outcomes of the preceding stress analysis section IV.2, it has been established that the region with the greatest stress magnitude is situated at the blade's root area, as this serves as the point of attachment for the blade, making it the most vulnerable area to cracks. Figure V. 61 provides a visual representation of crack locations on a small wind turbine blade.

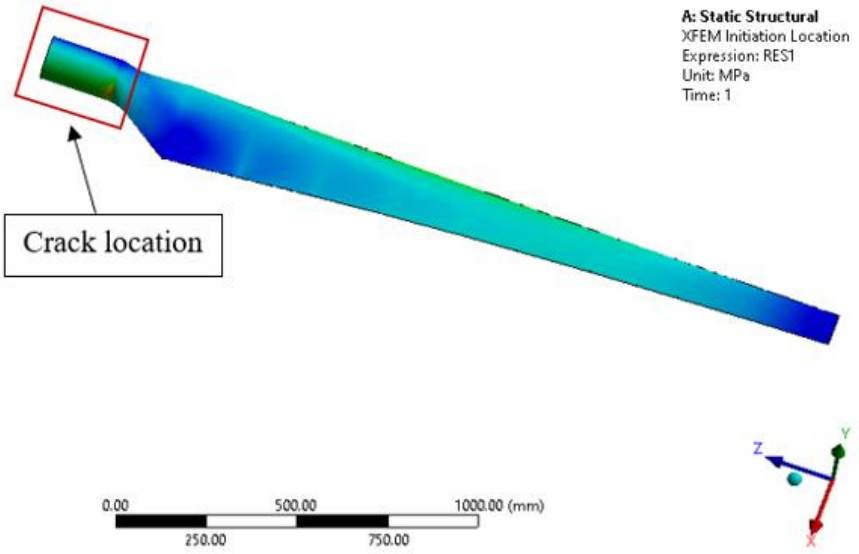

Figure V. 61 crack location in wind turbine blade

V.2 Mesh of Cracked Blade

Achieving the most precise simulation outcome hinges on the number of nodes and elements utilized. Thus, it is crucial to validate result convergence by comparing current values with their previous counterparts, ensuring the study's accuracy. In this investigation, we attained a convergence rate not exceeding 1%. Regarding the crack mesh, the crack front was divided into 30 nodes, and we established 6 mesh contours around the crack to compute the *J* integral, with a 5 mm maximum contour radius and a circumferential division of 6, as displayed in Figure V. 62b. Figure V. 62a illustrates the ultimate mesh configuration adopted in this research, which comprises 102,391 nodes and 49456 elements.

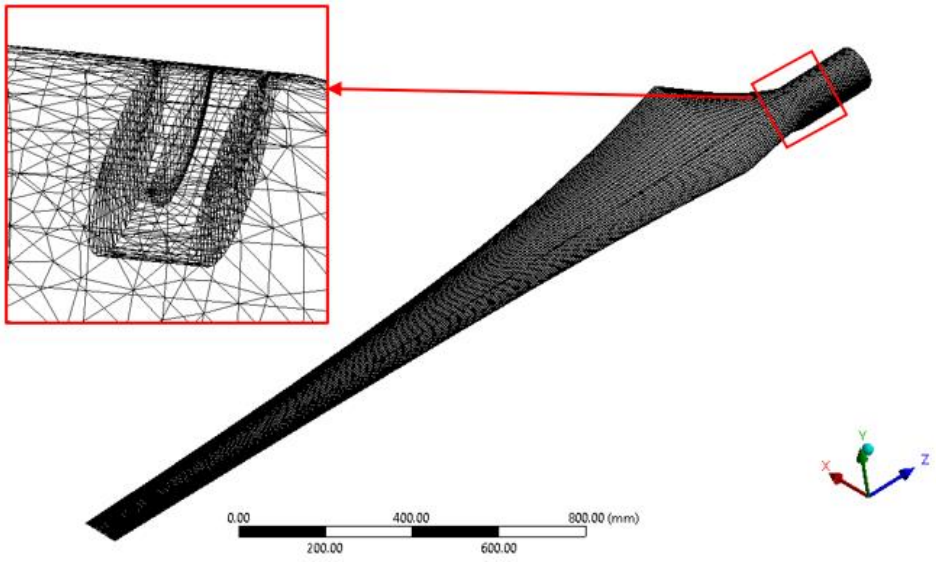

(a)

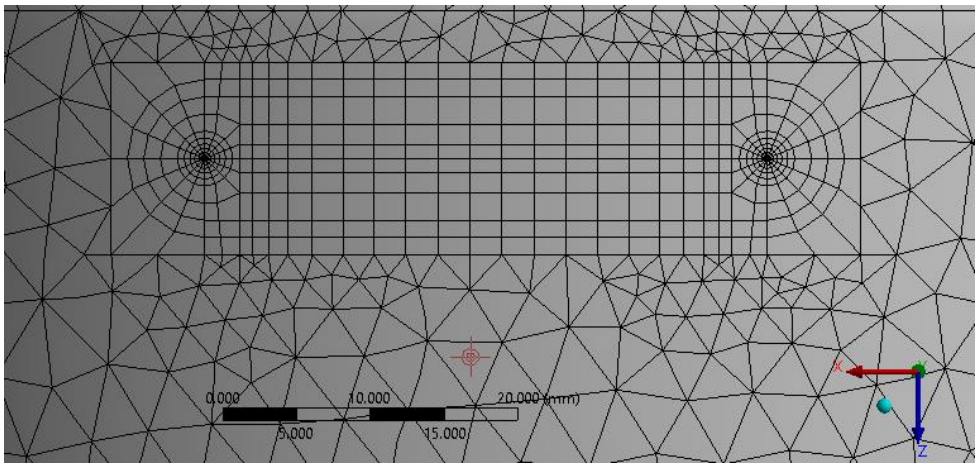

(b)

Figure V. 62 Mesh of initial cracked blade (a) full size blade mesh, and (b) crack mesh.

V.3 Boundary Conditions of blade

After the blade is installed, it is firmly anchored at the root, causing all degrees of freedom (DOFs) to be constrained at this end, while leaving the tip unconstrained. We applied a wind force of 10 m/s to the blade's surface to induce deflection and calculate Stress Intensity Factors (SIFs) based on the crack size variation. Figure V. 63 provides a depiction of the boundary conditions that were imposed on the wind turbine blade.

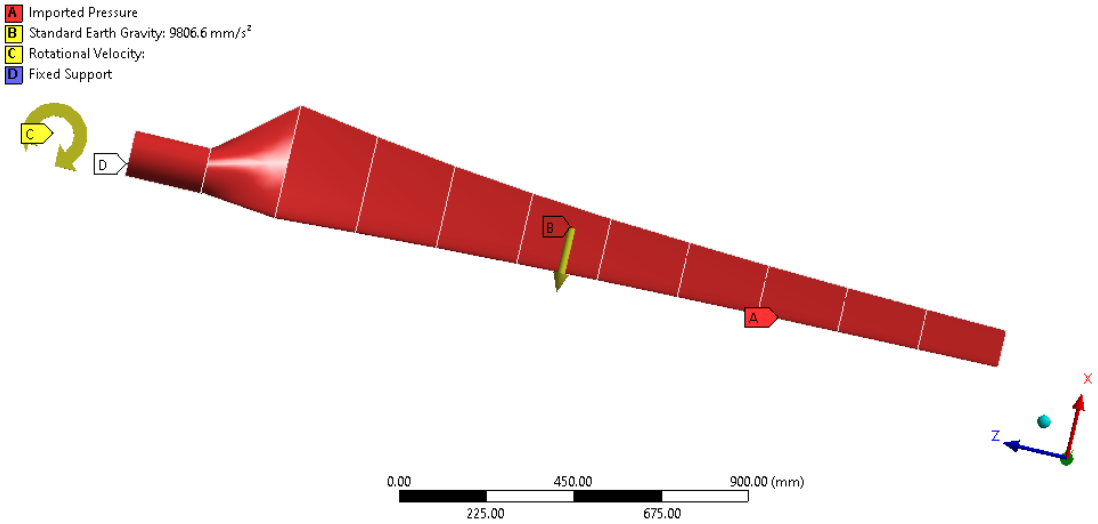

Figure V. 63 boundary conditions of blade

V.4 Crack analysis results

In this thesis, simulations of wind turbine blades were conducted using the XFEM method to analyze stresses and deflections with and without cracks. All analyses were carried out under constant loads to facilitate result comparison and to investigate the impact of crack length on blade deflection. Figure V. 64 demonstrates a clear trend of increasing stresses with longer crack lengths. Stress levels in the blade

without any crack were measured at 3.53 MPa, whereas in the blade with a crack length of a/D = 0.4, it escalated to 7.77 MPa. This rise is attributed to stress concentration at the crack tip, which promotes crack propagation. Figure V. 65 depicts how blade deflection increases as a result of crack propagation. The deflection for a crack-free blade was 5.12 mm, whereas for a blade with a crack of a/D = 0.4, it measured 5.22 mm, signaling a heightened risk of blade failure. Figure V. 66 and Figure V. 67 illustrates the correlation between front crack length and stress intensity factor SIF for mode I, and mode II at each initial crack length. This correlation signifies that longer cracks induce greater stress concentrations at the crack tip, thereby accelerating the crack propagation process.

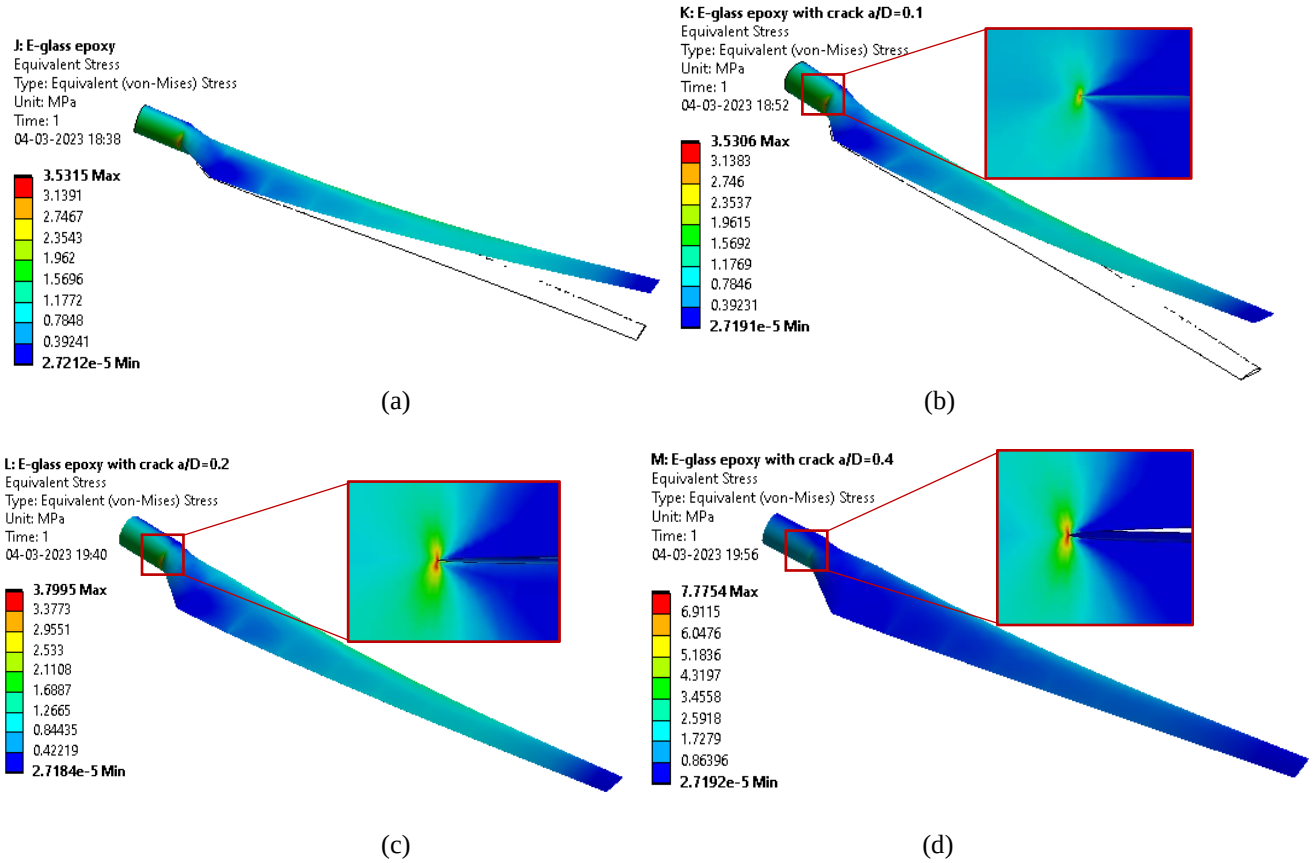

Figure V. 64 The stress of blade (a) without crack (b) with crack a/D = 0.1 (c) with crack a/D = 0.2 (d) with crack a/D = 0.4

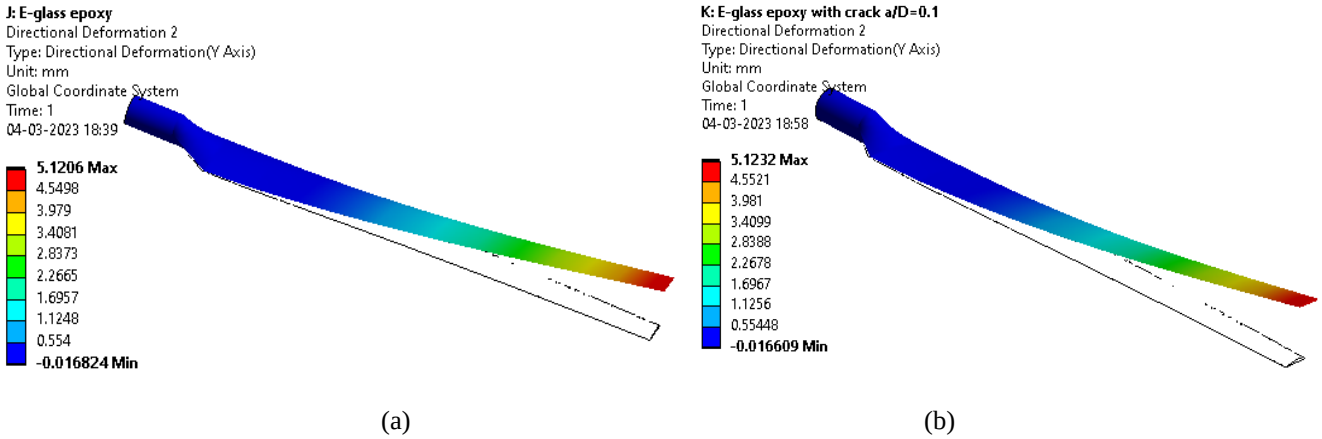

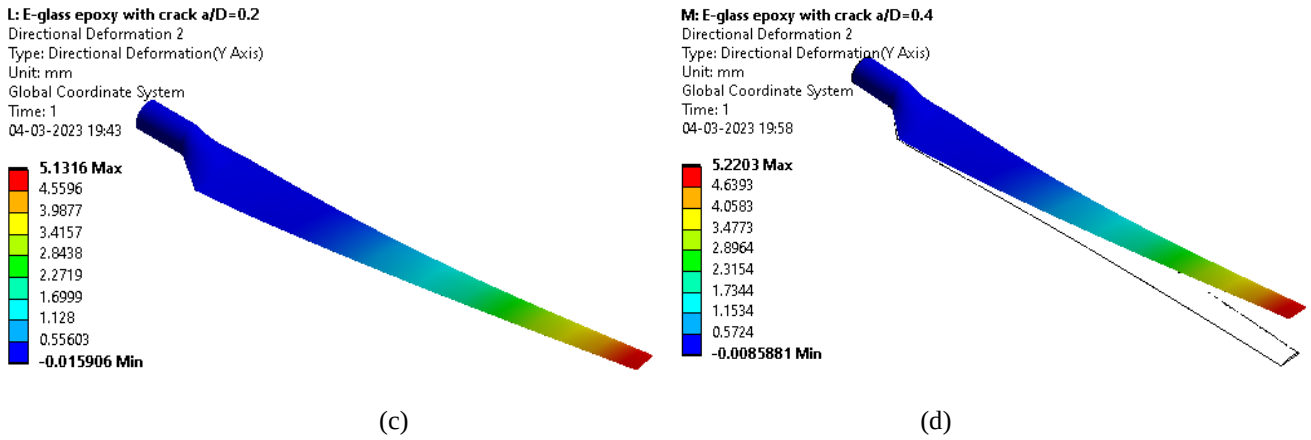

(c) (d)

Figure V. 65 Deflection of the blade (a) without crack (b) with crack a/D = 0.1 (c) with crack a/D = 0.2 (d) with crack a/D = 0.4

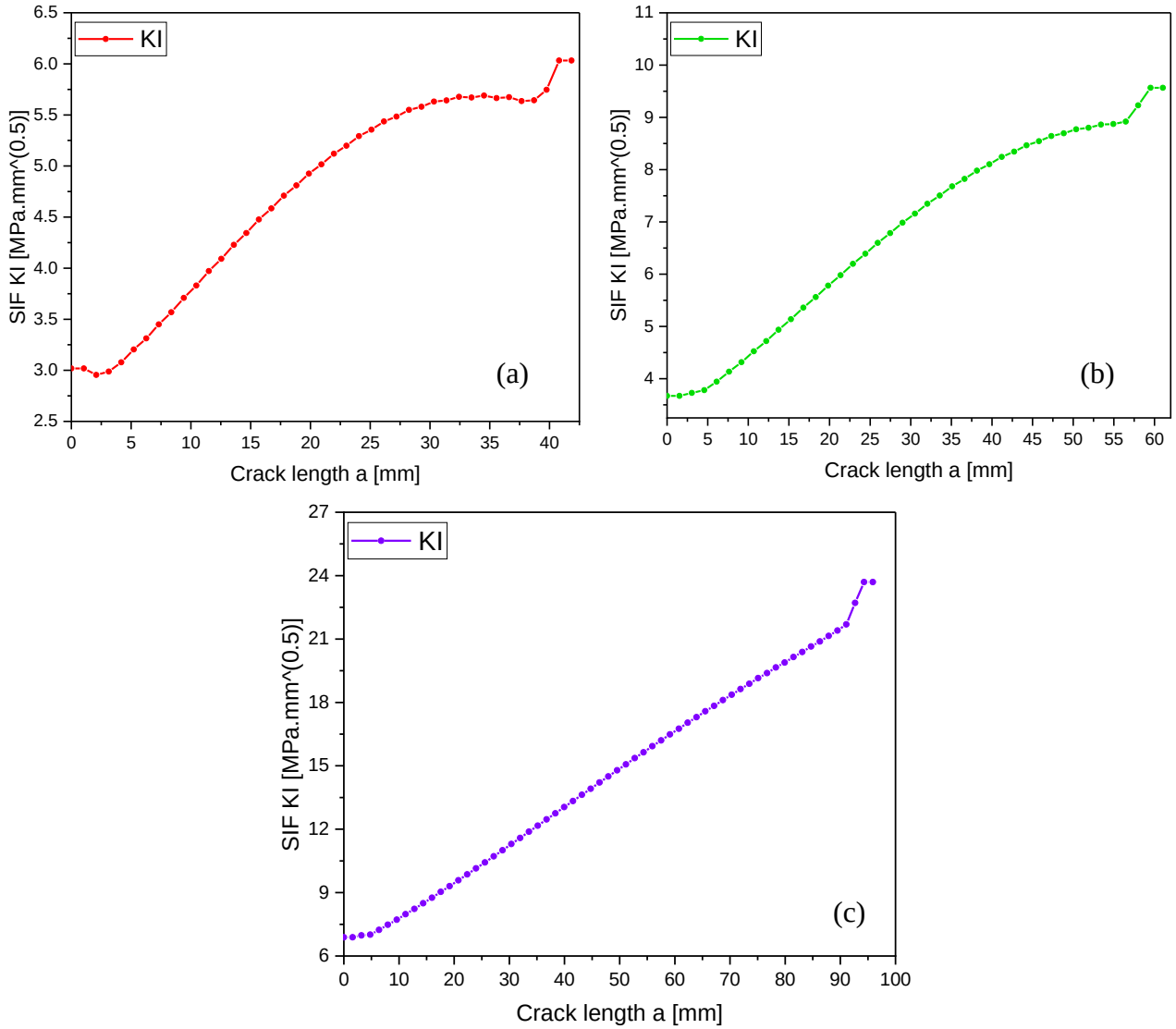

Figure V. 66 Stress intensity factors KI with crack length of (a) a/D = 0.1, (b) a/D = 0.2, (c) a/D = 0.4

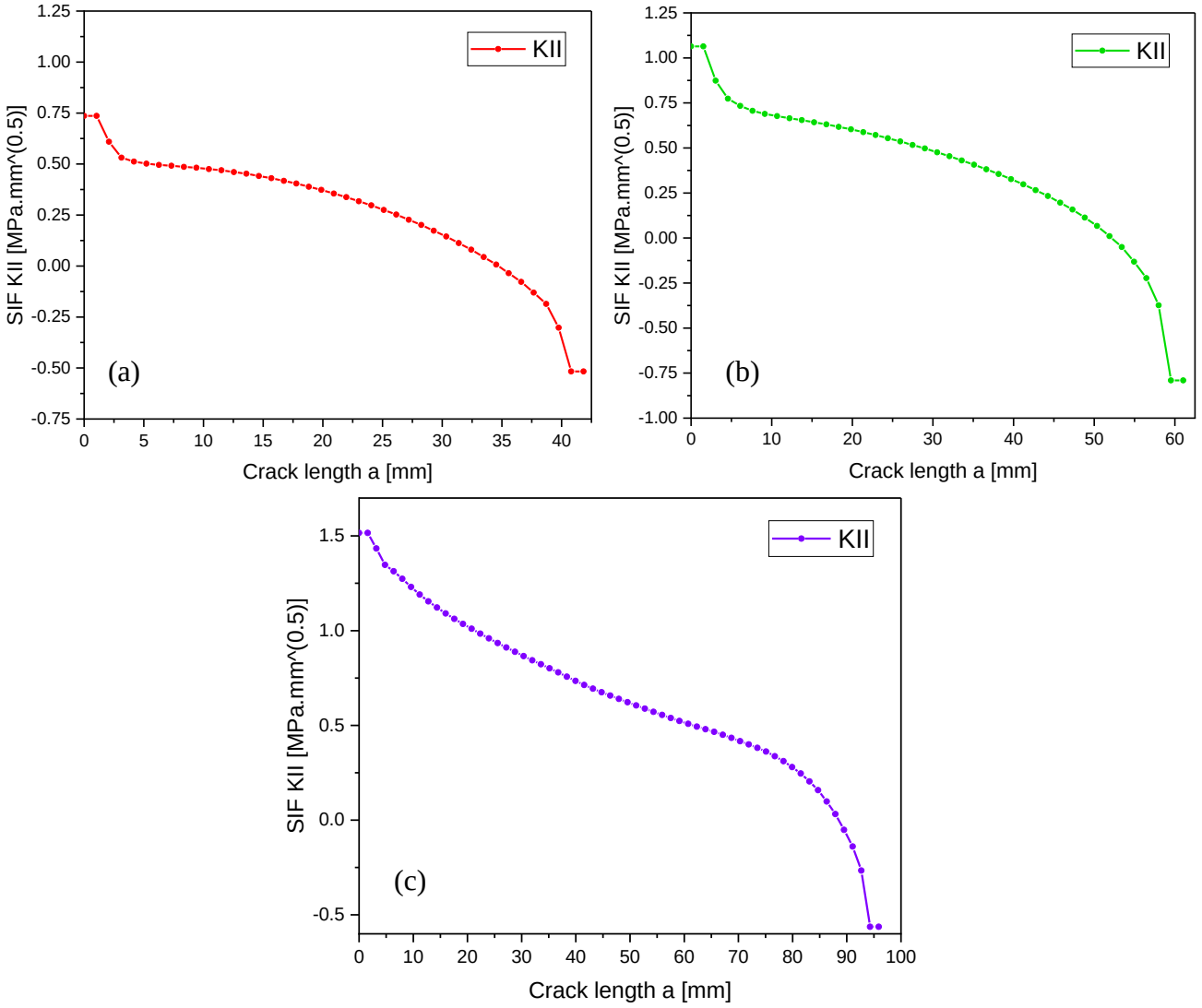

Figure V. 67 Stress intensity factors KII with crack length of (a) a/D = 0.1, (b) a/D = 0.2, (c) a/D = 0.4

The stress intensity factor (SIF) is a crucial parameter in evaluating stress levels and their distribution in the vicinity of a crack's tip. SIFs are also essential for assessing the likelihood of crack propagation and its growth. Given that wind turbine blades are typically subjected to a combination of loading conditions, it is imperative to compute SIFs for each of the three crack modes: opening, sliding, and tearing, as illustrated in Figure IV. 18. This comprehensive analysis ensures a thorough understanding of how different loading modes affect crack behavior.

Figure V. 68 shows the results of the SIF distribution along the crack front for the mode III. As evident from the findings presented in previous results, the elongation of a crack exerts a discernible impact on the stress levels, deflection at the blade tip, and the stress intensity factors at the crack's leading edge. An expansion in crack size invariably leads to elevated stresses, ultimately resulting in blade deflection until failure becomes imminent. It is worth noting that all the preceding results were generated through static crack propagation analysis utilizing the ACT tool integrated into the ANSYS program, referred to as "XFEM Initiation and Propagation," as illustrated in Figure V. 69.

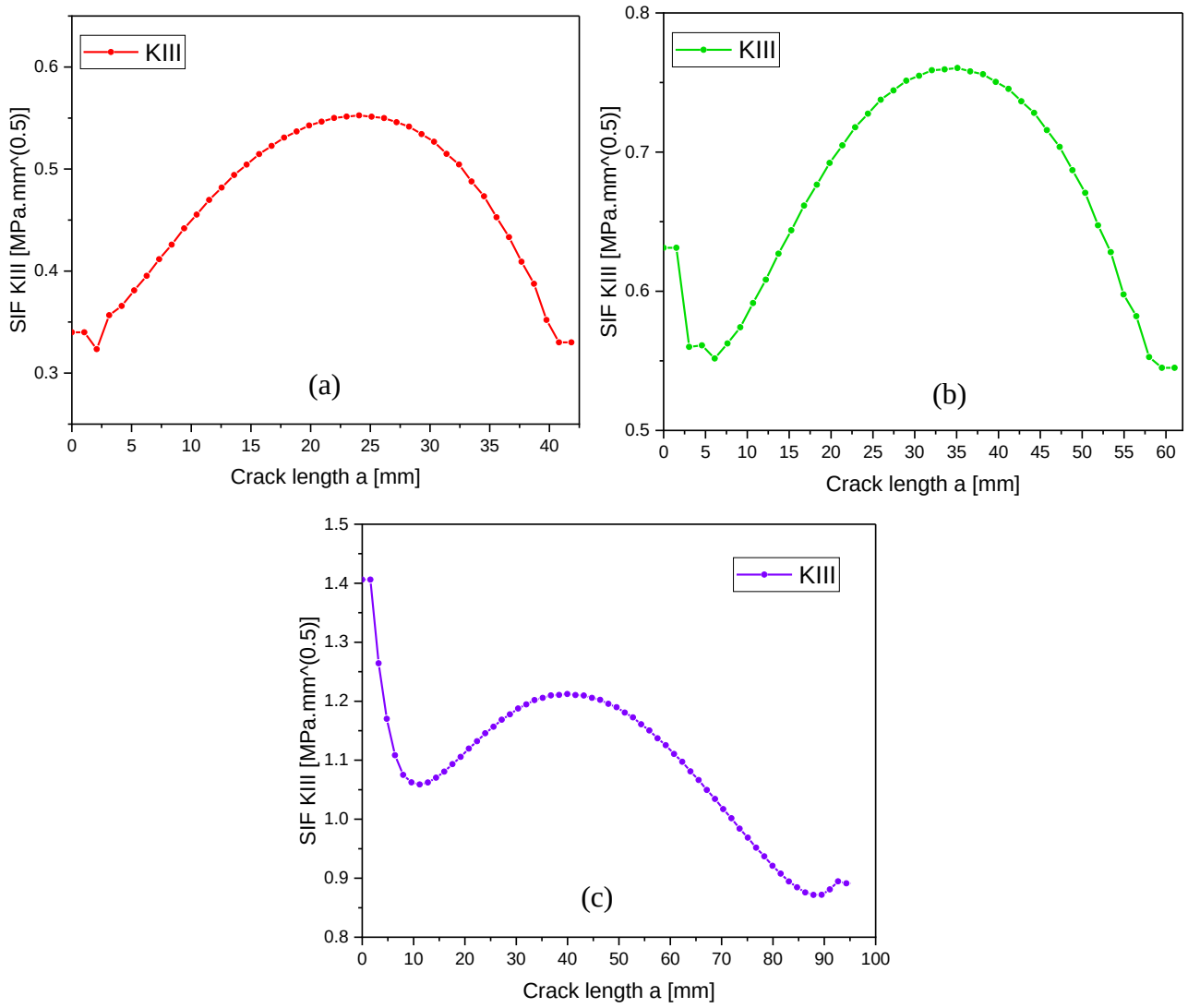

Figure V. 68 Stress intensity factors KIII with crack length of (a) a/D = 0.1, (b) a/D = 0.2, (c) a/D = 0.4

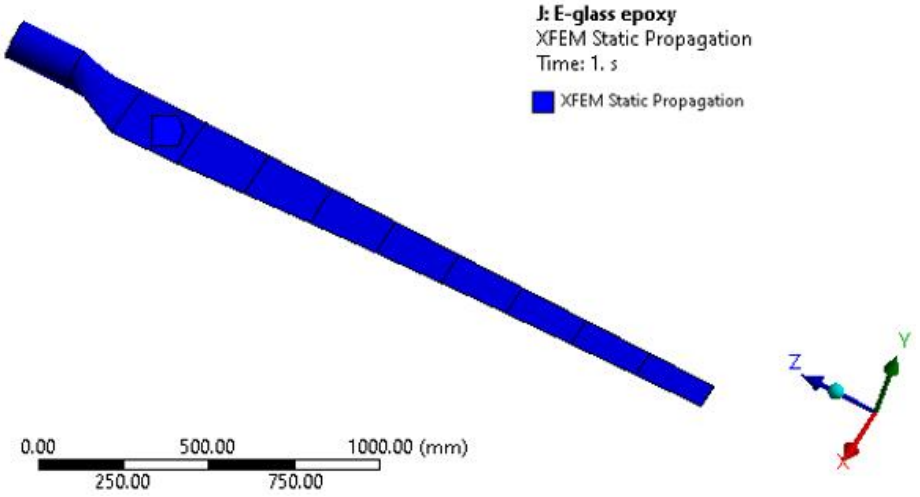

Figure V. 69 XFEM static propagation model.

V.5 Vibration crack analysis

Analyzing the fracture of full structural objects through experimental means can be challenging due to the expense and the specialized tools required. For instance, investigating the fracture of a wind turbine blade can be cost-prohibitive and complex. To address this issue, a modern, efficient, and cost-effective approach has been developed, involving the analysis of vibrations in structures containing cracks. In this study, we will utilize this method to validate the impact of cracks on vibrations, and the outcomes are presented in Figure V. 70.

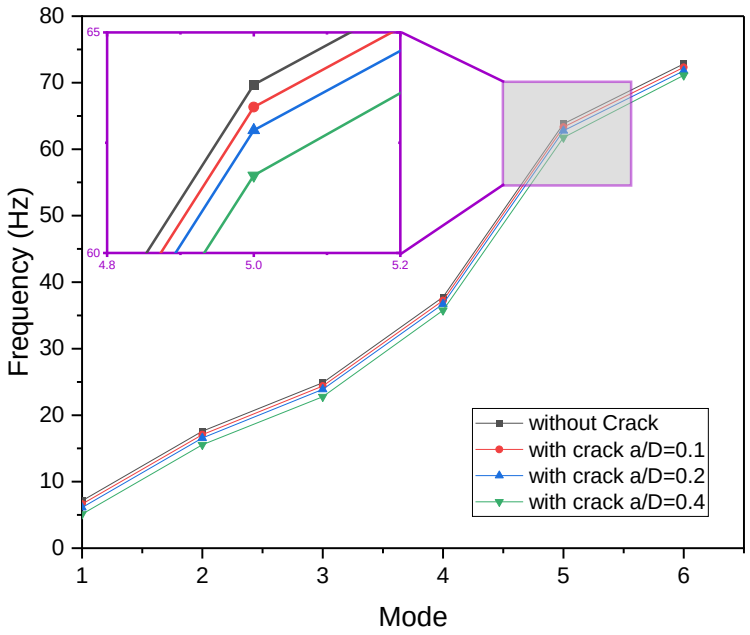

Figure V. 70 frequency with mode shape of blade without crack, and crack length a/D = 0.1, a/D = 0.2, a/D = 0.4

Observing the frequency results and their corresponding mode shapes for the blade without a crack and with various crack lengths (a/D = 0.1, a/D = 0.2, a/D = 0.4), it's evident that there are disparities in the frequency values among each model. These differences can be attributed to the presence of the crack at the blade root. This analysis strongly suggests that the vibration analysis has effectively detected the presence of a crack within the blade.

V.6 Conclusion

In conclusion, this chapter has provided a comprehensive analysis of the wind turbine blade's performance and durability under various conditions and using different materials. Key findings and takeaways from this chapter include:

1. Material Selection: The study considered various materials for the wind turbine blade, including GFRP and CFRP. Material properties such as Young's modulus and density were crucial factors in determining the blade's natural frequencies and stiffness.
2. Finite Element Analysis (FEA): FEA was employed to simulate the structural behavior of the wind turbine blade. Mesh convergence tests were conducted to determine the optimal mesh density for accurate results.

3. Modal Analysis: The natural frequencies and mode shapes of the blade were analyzed to assess its dynamic behavior. Comparisons with experimental data and other numerical simulations demonstrated good agreement.
4. Static Loads: Static loads were applied to the blade to evaluate its deflection and structural integrity. The results indicated that the CFRP blade exhibited reduced deflection and mass compared to the GFRP blade.
5. Aeroelastic Simulation: Aeroelastic simulations were performed to assess the wind turbine blade's performance under varying wind conditions. The results showed that the power output varied with wind speed and that the blade's lifespan depended on material properties and fatigue calculations.
6. Fatigue Analysis: Miner's law was applied to predict blade damage and estimate the remaining lifespan. The CFRP blade was found to have a significantly longer fatigue life compared to the GFRP blade.
7. Comparison of Methods: The study compared the results obtained from different approaches, including SLM, aeroelastic simulations, and experimental data. While SLM provided conservative estimates, aeroelastic simulations yielded fewer conservative results, with measured data being the least conservative.
8. Material Impact: The choice of material had a significant impact on the blade's performance and longevity. CFRP material outperformed GFRP in terms of fatigue life and deflection under load.
9. The study has demonstrated the significant influence of crack length on stress distribution, blade deflection, and stress intensity factors (SIFs). By examining various crack lengths (a/D = 0.1, a/D = 0.2, a/D = 0.4), it was apparent that the presence of a crack at the blade root significantly altered the blade's vibrational characteristics, leading to discernible differences in frequency values.
10. The application of the XFEM method, combined with vibration analysis, has proven to be a valuable and cost-effective tool for studying crack behavior in wind turbine blades.

In summary, this chapter has provided valuable insights into the structural analysis, dynamic behavior, and fatigue life prediction of wind turbine blades. The results highlight the importance of material selection and the application of different analysis methods to ensure the reliability and longevity of wind turbine systems.

GENERAL CONCLUSION

I. General Conclusion

wind energy is a promising and environmentally friendly source of power. However, it's important to recognize that technology is not static and continues to evolve. One crucial aspect of this evolution is extending the lifespan and efficiency of wind turbine rotors. By improving the durability and performance of these critical components, we can further enhance the sustainability and economic viability of wind energy. This underscores the importance of ongoing research and development in the field to harness the full potential of wind power in addressing climate change and our energy needs.

In this thesis, we have taken a multifaceted approach to enhance the performance of wind turbine blades. Our efforts encompassed both aerodynamic and structural aspects of the blades, with the goal of increasing power generation while ensuring durability and reliability. Through a thorough analysis of structural properties and material behaviors, we have devised strategies to improve blade efficiency and longevity. By optimizing the blade's aerodynamic design and addressing concerns like vibration, fatigue, and cracking, our research has made valuable contributions to the development of more effective and sustainable wind turbine blades for renewable energy systems.

In the first chapter, we provided a thorough review of the existing literature on horizontal-axis turbine blades. Additionally, we introduced the fundamental principles of small wind turbine blade design, incorporating the theories of Blade Element Momentum (BEM) and Computational Fluid Dynamics (CFD) to analyze blade performance.

In the second chapter, our focus shifted towards the investigation of wind turbine blade vibration. This included the determination of natural frequencies and mode shapes to better understand and enhance blade performance. Addressing vibration-related issues is essential for improving both the design and operation of wind turbine blades.

The third chapter delved into the critical aspect of fatigue, a central theme of this thesis. We offered an in-depth exploration of fatigue, particularly concerning wind turbine blades. Additionally, we enhanced blade design to prolong fatigue life and streamlined the fatigue equations related to small wind turbine blades. This was achieved through the introduction of the Simplified Load Model (SLM) method and the utilization of the FAST tool to infer fatigue.

In Chapter Four, we provided a comprehensive examination of cracks that can develop in wind turbine blades due to prolonged exposure to various loads and environmental conditions. We introduced the eXtended Finite Element Method (XFEM) as a specialized tool for studying cracks, allowing us to gain insights into crack initiation timing and propagation within the blade structure.

Finally, in the fifth and concluding chapter, we synthesized the results from our analyses in the previous chapters. This consolidation aimed to enhance the clarity and coherence of the findings. In summary, our results can be summarized as follows:

- The linearization design of the chord and the twist angle can be adopted to simplify the design of the blade, and it gets more power at a lower wind speed.
- This thesis has made significant strides in enhancing the aerodynamic performance of wind turbines, resulting in an improved model. The optimal design achieved a power coefficient of 0.47 when the

Tip Speed Ratio (TSR) was set to 6. In practical terms, this represents an 8% increase in efficiency compared to the initial design. Moreover, the optimized wind turbine's power output increased by 7% at rated wind speeds. These advancements signify a substantial improvement in wind turbine performance and energy generation potential. Also, the aerodynamic loads using CFD and BEM were compared for the improved shape. Where, it was found that the results of both methods are compatible, and it can be relied upon them to find the aerodynamic loads

- A new finite element model was developed for a 5-kW small wind turbine blade, using the optimized design. The results of this analysis revealed that the minimum tip deflection, measuring 18.29 mm, was achieved when employing carbon fiber material. In contrast, the tip deflection was 33.54 mm for the Braided composite and 46.46 mm for the E-glass material. Consequently, it can be concluded that carbon fiber is the most favorable material in terms of minimizing deflection.
- In the modal analysis, it was observed that wind turbine blades made from E-glass exhibited the lowest natural frequencies, with values of 16.17 Hz for the first mode and 38.46 Hz for the second mode. In contrast, blades constructed from carbon fiber material had the highest natural frequencies, measuring 29.58 Hz for the first mode and 70.20 Hz for the second mode.
- Under various static mass/loads (3.3 kg, 6 kg, and 8.3 kg), the GFRP blade exhibited deflections of 35.35 mm, 59.18 mm, and 79.48 mm, respectively. These deflection values indicate how the blade responds to different loads and provide insights into its structural behavior under varying conditions.
- When subjected the blade to various static mass/loads (3.3 kg, 6 kg, and 8.3 kg), the deflections of the GFRP blade measured 35.35 mm, 59.18 mm, and 79.48 mm, respectively. In contrast, the CFRP blade exhibited deflections of 23.08 mm, 40 mm, and 54.42 mm under the same loads. Notably, the optimized CFRP blade displayed reduced deflections by 37%, 42.85%, and 42.61% for the respective loads of 3.3 kg, 6 kg, and 8.3 kg. On the other hand, the optimized GFRP blade showed deflection reductions of 4.5%, 15.45%, and 16.19% for the same load conditions. Additionally, the optimized blade structures, whether made from CFRP or GFRP materials, experienced significant mass reductions of 71.24% and 47.86%, respectively. Importantly, both optimized blade variants, CFRP and GFRP, were determined to be structurally safe under extreme wind loads, confirming their reliability and suitability for use.
- The assessment of blade damage was conducted using both the SLM approach and FAST software. A comparison of the results from these two methods revealed a percentage difference of 45.3% for GFRP and 50.29% for CFRP. According to the SLM approach, the expected lifespan of a wind turbine blade constructed from GFRP is estimated to be 5.5 years, whereas the FAST software results suggest a longer life of 10.25 years. Conversely, for a blade fabricated from CFRP material, both the SLM approach and FAST software projections indicate a lifespan exceeding 20 years, emphasizing the superior durability of CFRP blades.
- the stresses of the blade without cracking were 3.79 MPa, which is less than the stresses of the blade with cracks 7.77 MPa. At the same time, the deflection of a blade without a crack was 5.12 mm, while it had a slight effect at a crack of a/D = 0.4 by 5.22 mm.
- the SIFs were calculated using the XFEM method, and it was found that the highest value is at a/D = 0.4, which is KI = 23.69 MPa.mm^(0.5), KII = 1.5 MPa.mm^(0.5), and KIII = 1.4 MPa.mm^(0.5).

Future works

In future research, there are several important areas that merit further investigation. One such area involves the utilization of nanotechnology to enhance composite materials, which could potentially lead to improvements in the efficiency of small wind turbines. Additionally, addressing issues related to noise generated by wind turbine rotation is crucial for mitigating its impact on the environment and surrounding communities.

Furthermore, the geographical locations of wind turbines vary, subjecting them to different climatic conditions, whether hot or cold. Hence, a comprehensive study on how climate influences the dynamic characteristics of wind turbine blades is essential, as it can help optimize blade designs for specific environmental conditions.

Certainly, studying the dynamic behavior of wind turbine blades when subjected to wind shock loads and considering the application of gyroscopic loads is a promising avenue for future research. This research could provide valuable insights into how wind turbine blades respond to sudden changes in wind conditions and the resulting stresses on the blade's root zone, as well as how gyroscopic effects influence blade deflection. Understanding these dynamics can lead to improved designs and enhanced reliability for wind turbine systems.

REFERENCES

References

[1] E. Hau, *Wind turbines: fundamentals, technologies, application, economics*. Springer Science & Business Media, 2013.

[2] M. O. Hansen, *Aerodynamics of wind turbines*. Routledge, 2015.

[3] J. F. Manwell, J. G. McGowan, and A. L. Rogers, *Wind energy explained: theory, design and application*. John Wiley & Sons, 2010.

[4] B. Energy, "Renewables 2017 Global Status Report," *Renewable Energy Policy Network for the 21st Century. Paris: REN21,* 2016.

[5] WWEA. "World Wind Energy Association " https://wwindea.org/information-2/statistics-news/ (accessed Mar 2022, Mar 2022).

[6] J. K. Kaldellis and D. Zafirakis, "The wind energy (r) evolution: A short review of a long history," *Renewable energy,* vol. 36, no. 7, pp. 1887-1901, 2011.

[7] B. Kim, W. Kim, S. Lee, S. Bae, and Y. Lee, "Developement and verification of a performance based optimal design software for wind turbine blades," *Renewable energy,* vol. 54, pp. 166-172, 2013.

[8] A. Jameson and L. Martinelli, "Aerodynamic shape optimization techniques based on control theory," *Computational Mathematics Driven by Industrial Problems: Lectures given at the 1st Session of the Centro Internazionale Matematico Estivo (CIME) held in Martina Franca, Italy, June 21–27, 1999,* pp. 151-221, 2007.

[9] R. E. Wilson and P. B. Lissaman, "Applied aerodynamics of wind power machines," *National Science Foundation,* 1974.

[10] M. Pandey, K. Pandey, and T. Ojha, "An analytical approach to optimum design and peak performance prediction for horizontal axis wind turbines," *Journal of Wind Engineering and Industrial Aerodynamics,* vol. 32, no. 3, pp. 247-262, 1989.

[11] T. Burton, N. Jenkins, D. Sharpe, and E. Bossanyi, *Wind energy handbook*. John Wiley & Sons, 2011.

[12] E. Hoogedoorn, G. B. Jacobs, and A. Beyene, "Aero-elastic behavior of a flexible blade for wind turbine application: A 2D computational study," *Energy,* vol. 35, no. 2, pp. 778-785, 2010.

[13] P. Pratumnopharat and P. S. Leung, "Validation of various windmill brake state models used by blade element momentum calculation," *Renewable energy,* vol. 36, no. 11, pp. 3222-3227, 2011.

[14] K. Kishinami, H. Taniguchi, J. Suzuki, H. Ibano, T. Kazunou, and M. Turuhami, "Theoretical and experimental study on the aerodynamic characteristics of a horizontal axis wind turbine," *Energy,* vol. 30, no. 11-12, pp. 2089-2100, 2005.

[15] M. J. Lampinen, V. W. Kotiaho, and M. El Haj Assad, "Application of axial fan theory to horizontal-axis wind turbine," *International journal of energy research,* vol. 30, no. 13, pp. 1093-1107, 2006.

[16] V. Nelson, "Wind Power," in *Electric Power Generation, Transmission, and Distribution: The Electric Power Engineering Handbook*: CRC Press, 2018, pp. 1-1-1-23.

[17] N. Tenguria, N. Mittal, and S. Ahmed, "Investigation of blade performance of horizontal axis wind turbine based on blade element momentum theory (BEMT) using NACA airfoils," *International Journal of engineering, science and technology,* vol. 2, no. 12, 2010.

[18] R. Lanzafame and M. Messina, "Horizontal axis wind turbine working at maximum power coefficient continuously," *Renewable Energy,* vol. 35, no. 1, pp. 301-306, 2010.

[19] J. R. P. Vaz, J. T. Pinho, and A. L. A. Mesquita, "An extension of BEM method applied to horizontal-axis wind turbine design," *Renewable Energy,* vol. 36, no. 6, pp. 1734-1740, 2011.

[20] M. Birajdar, S. Kale, and S. Sapali, "Effects of design parameters on aerodynamic performance of new profile small wind turbine blades," in *ASME International Mechanical Engineering Congress and Exposition*, 2015, vol. 57472: American Society of Mechanical Engineers, p. V07BT09A049.

[21] A. Sedaghat and M. Mirhosseini, "Aerodynamic design of a 300 kW horizontal axis wind turbine for province of Semnan," *Energy conversion and management,* vol. 63, pp. 87-94, 2012.

[22] A. Sharifi and M. Nobari, "Prediction of optimum section pitch angle distribution along wind turbine blades," *Energy Conversion and Management,* vol. 67, pp. 342-350, 2013.

[23] A. Sedaghat, M. E. H. Assad, and M. Gaith, "Aerodynamics performance of continuously variable speed horizontal axis wind turbine with optimal blades," *Energy,* vol. 77, pp. 752-759, 2014.

[24] Z. N. Ashrafi, M. Ghaderi, and A. Sedaghat, "Parametric study on off-design aerodynamic performance of a horizontal axis wind turbine blade and proposed pitch control," *Energy Conversion and Management,* vol. 93, pp. 349-356, 2015.

[25] D. G. Shepherd, "Historical development of the windmill," Cornell Univ., Ithaca, NY (USA). Dept. of Mechanical and Aerospace Engineering, 1990.

[26] M. Ragheb, "History of harnessing wind power," in *Wind Energy Engineering*: Elsevier, 2017, pp. 127-143.

[27] J. Vestergaard, L. Brandstrup, and R. D. Goddard, "A brief history of the wind turbine industries in Denmark and the United States," in *Academy of international business (Southeast USA Chapter) Conference proceedings*, 2004, vol. 2, pp. 322-7.

[28] X. Wang, Z. Dong, P. Yan, J. Zhang, and G. Qian, "Wind energy environments and dunefield activity in the Chinese deserts," *Geomorphology,* vol. 65, no. 1-2, pp. 33-48, 2005.

[29] M. Rahman, Z. C. Ong, W. T. Chong, S. Julai, and S. Y. Khoo, "Performance enhancement of wind turbine systems with vibration control: A review," *Renewable and Sustainable Energy Reviews,* vol. 51, pp. 43-54, 2015.

[30] S. Aubrun, A. Leroy, and P. Devinant, "A review of wind turbine-oriented active flow control strategies," *Experiments in Fluids,* vol. 58, pp. 1-21, 2017.

[31] B. Yaniktepe, M. Savrun, and T. Koroglu, "Current status of wind energy and wind energy policy in Turkey," *Energy Conversion and Management,* vol. 72, pp. 103-110, 2013.

[32] P. H. Wirsching, "Probability-based fatigue design criteria for offshore structures," *Final Report, API,* 1983.

[33] W. G. Byers, M. J. Marley, J. Mohammadi, R. J. Nielsen, and S. Sarkani, "Fatigue reliability reassessment applications: State-of-the-art paper," *Journal of Structural Engineering,* vol. 123, no. 3, pp. 277-285, 1997.

[34] A. M. Freudenthal, J. M. Garretts, and M. Shinozuka, "The analysis of structural safety," *Journal of the Structural Division,* vol. 92, no. 1, pp. 267-326, 1966.

[35] A. Murty, U. Gupta, and A. Radha, "A new approach to fatigue strength distribution for fatigue reliability evaluation," *International journal of fatigue,* vol. 17, no. 2, pp. 85-89, 1995.

[36] N. Cosack and M. Kühn, "An approach for fatigue load monitoring without load measurement devices," in *European Wind Energy Conference, Marseille, France,* 2009.

[37] C. W. Kensche, "Fatigue of composites for wind turbines," *International journal of fatigue,* vol. 28, no. 10, pp. 1363-1374, 2006.

[38] Y. J. Jang, C. W. Choi, J. H. Lee, and K. W. Kang, "Development of fatigue life prediction method and effect of 10-minute mean wind speed distribution on fatigue life of small wind turbine composite blade," *Renewable Energy,* vol. 79, pp. 187-198, 2015.

[39] Y. Du, S. Zhou, X. Jing, Y. Peng, H. Wu, and N. Kwok, "Damage detection techniques for wind turbine blades: A review," *Mechanical Systems and Signal Processing,* vol. 141, p. 106445, 2020.
[40] A. Rezaeiha, R. Pereira, and M. Kotsonis, "Fluctuations of angle of attack and lift coefficient and the resultant fatigue loads for a large horizontal axis wind turbine," *Renewable Energy,* vol. 114, pp. 904-916, 2017.
[41] Y. Bazilevs, A. Korobenko, X. Deng, and J. Yan, "Fluid–structure interaction modeling for fatigue-damage prediction in full-scale wind-turbine blades," *Journal of Applied Mechanics,* vol. 83, no. 6, 2016.
[42] H. G. Lee, M. G. Kang, and J. Park, "Fatigue failure of a composite wind turbine blade at its root end," *Composite Structures,* vol. 133, pp. 878-885, 2015.
[43] C. Rubiella, C. A. Hessabi, and A. S. Fallah, "State of the art in fatigue modelling of composite wind turbine blades," *International Journal of Fatigue,* vol. 117, pp. 230-245, 2018.
[44] M. M. Shokrieh and R. Rafiee, "Simulation of fatigue failure in a full composite wind turbine blade," *Composite structures,* vol. 74, no. 3, pp. 332-342, 2006.
[45] N. Dervilis *et al.*, "On damage diagnosis for a wind turbine blade using pattern recognition," *Journal of sound and vibration,* vol. 333, no. 6, pp. 1833-1850, 2014.
[46] E. J. N. Menezes, A. M. Araújo, and N. S. B. Da Silva, "A review on wind turbine control and its associated methods," *Journal of cleaner production,* vol. 174, pp. 945-953, 2018.
[47] K. Dai, A. Bergot, C. Liang, W.-N. Xiang, and Z. Huang, "Environmental issues associated with wind energy–A review," *Renewable energy,* vol. 75, pp. 911-921, 2015.
[48] T. Ishugah, Y. Li, R. Wang, and J. Kiplagat, "Advances in wind energy resource exploitation in urban environment: A review," *Renewable and sustainable energy reviews,* vol. 37, pp. 613-626, 2014.
[49] G. J. Herbert, S. Iniyan, and D. Amutha, "A review of technical issues on the development of wind farms," *Renewable and Sustainable Energy Reviews,* vol. 32, pp. 619-641, 2014.
[50] Y. Guo, S. Sheng, C. Phillips, J. Keller, P. Veers, and L. Williams, "A methodology for reliability assessment and prognosis of bearing axial cracking in wind turbine gearboxes," *Renewable and Sustainable Energy Reviews,* vol. 127, p. 109888, 2020.
[51] A. Joshuva and V. Sugumaran, "Crack detection and localization on wind turbine blade using machine learning algorithms: A data mining approach," *Structural Durability & Health Monitoring,* vol. 13, no. 2, p. 181, 2019.
[52] A. Greco, S. Sheng, J. Keller, and A. Erdemir, "Material wear and fatigue in wind turbine systems," *Wear,* vol. 302, no. 1-2, pp. 1583-1591, 2013.
[53] V. Igwemezie, A. Mehmanparast, and A. Kolios, "Materials selection for XL wind turbine support structures: A corrosion-fatigue perspective," *Marine Structures,* vol. 61, pp. 381-397, 2018.
[54] G. R. Kalagi, R. Patil, and N. Nayak, "Experimental study on mechanical properties of natural fiber reinforced polymer composite materials for wind turbine blades," *Materials Today: Proceedings,* vol. 5, no. 1, pp. 2588-2596, 2018.
[55] M. Appadurai and E. F. I. Raj, "Finite element analysis of composite wind turbine blades," in *2021 7th international conference on electrical energy systems (ICEES)*, 2021: IEEE, pp. 585-589.
[56] M. Tarfaoui, M. Nachtane, and H. Boudounit, "Finite element analysis of composite offshore wind turbine blades under operating conditions," *Journal of Thermal Science and Engineering Applications,* vol. 12, no. 1, 2020.

[57] Y. Wang, C. Soutis, A. Hajdaei, and P. Hogg, "Finite element analysis of composite T-joints used in wind turbine blades," *Plastics, Rubber and Composites*, vol. 44, no. 3, pp. 87-97, 2015.
[58] H. Boudounit, M. Tarfaoui, D. Saifaoui, and M. Nachtane, "Structural analysis of offshore wind turbine blades using finite element method," *Wind Engineering*, vol. 44, no. 2, pp. 168-180, 2020.
[59] F. M. Jensen and K. Branner, "Introduction to wind turbine blade design," in *Advances in wind turbine blade design and materials*: Elsevier, 2023, pp. 3-53.
[60] B. Byrne and G. Houlsby, "Foundations for offshore wind turbines," *Philosophical Transactions of the Royal Society of London. Series A: Mathematical, Physical and Engineering Sciences*, vol. 361, no. 1813, pp. 2909-2930, 2003.
[61] X. Wu *et al.*, "Foundations of offshore wind turbines: A review," *Renewable and Sustainable Energy Reviews*, vol. 104, pp. 379-393, 2019.
[62] D. Snieckus. "Chinese OEM's 2.5MW machines to power Entre-Tille-et-Venelle wind farm in France set to be switched-on in 2020." https://www.rechargenews.com/wind/envision-turbines-in-french-debut-as-trig-buys-onshore-project/2-1-588762?lantern_redirect=true (accessed 27/05/023, 2023).
[63] A. Smaïli and C. Masson, "On the rotor effects upon nacelle anemometry for wind turbines," *Wind Engineering*, vol. 28, no. 6, pp. 695-713, 2004.
[64] M. R. Islam, Y. Guo, and J. Zhu, "A review of offshore wind turbine nacelle: Technical challenges, and research and developmental trends," *Renewable and Sustainable Energy Reviews*, vol. 33, pp. 161-176, 2014.
[65] E. Al-Ahmar, M. Benbouzid, Y. Amirat, and S. B. Elghali, "DFIG-based wind turbine fault diagnosis using a specific discrete wavelet transform," in *2008 18th International Conference on Electrical Machines*, 2008: IEEE, pp. 1-6.
[66] N. Lavars. "Surprising study shows how wind turbines can work better behind hills." https://newatlas.com/energy/study-wind-turbines-behind-hills/ (accessed June 16, 2021).
[67] F. Miceli. "Wind farms construction." WordPress. https://www.windfarmbop.com/wind-turbine-tower/ (accessed 2023).
[68] N. Luo, Y. Vidal, and L. Acho, *Wind turbine control and monitoring*. Springer, 2014.
[69] E. W. E. Association, *Wind energy-the facts: a guide to the technology, economics and future of wind power*. Routledge, 2012.
[70] A. Cherubini, A. Papini, R. Vertechy, and M. Fontana, "Airborne Wind Energy Systems: A review of the technologies," *Renewable and Sustainable Energy Reviews*, vol. 51, pp. 1461-1476, 2015.
[71] S. Nikolova and A. Causevski, "Vulnerability of renewable energy production to climate change," *BALWOIS, Water Observation and Information System for Decision Support 2010*, pp. 25-29, 2010.
[72] S. Pishgar-Komleh, A. Keyhani, and P. Sefeedpari, "Wind speed and power density analysis based on Weibull and Rayleigh distributions (a case study: Firouzkooh county of Iran)," *Renewable and sustainable energy reviews*, vol. 42, pp. 313-322, 2015.
[73] D. Goodfield *et al.*, "The suitability of the IEC 61400-2 wind model for small wind turbines operating in the built environment," *Renewable Energy and Environmental Sustainability*, vol. 2, p. Article Number 31, 2017.
[74] W. Wang and Y. Bai, "Investigation on installation of offshore wind turbines," *Journal of Marine Science and Application*, vol. 9, no. 2, pp. 175-180, 2010.

[75] S. Manson and W. Morgan, "National advisory committee for aeronautics," *J. Appl. Phys,* vol. 14, no. 8, pp. 399-405, 1943.
[76] W. Timmer, "An overview of NACA 6-digit airfoil series characteristics with reference to airfoils for large wind turbine blades," in *47th AIAA aerospace sciences meeting including the new horizons forum and aerospace exposition*, 2009, p. 268.
[77] U. Mamadaminov, "Review of airfoil structures for wind turbine blades," *Department of Electrical Engineering and Renewable Energy REE,* vol. 515, pp. 1-8, 2013.
[78] M. Miller, "The multi-objective design of flatback wind turbine airfoils," Carleton University, 2017.
[79] A. Muratoglu and M. I. Yuce, "Design of a river hydrokinetic turbine using optimization and CFD simulations," *Journal of Energy Engineering,* vol. 143, no. 4, p. 04017009, 2017.
[80] H. Zhonghua, S. Wenping, G. Yongwei, and C. Jing, "Design and verification of airfoil families for large-size wind turbine blades," *Applied Mathematics and Mechanics (English Edition),* vol. 37, no. S1, pp. S67-S84, 2016.
[81] W. Timmer and R. Van Rooij, "Summary of the Delft University wind turbine dedicated airfoils," *J. Sol. Energy Eng.,* vol. 125, no. 4, pp. 488-496, 2003.
[82] J. G. Leishman, "Wing Shapes & Nomenclature," *Introduction to Aerospace Flight Vehicles*, 2023.
[83] K. Yang, "Geometry design optimization of a wind turbine blade considering effects on aerodynamic performance by linearization," *Energies,* vol. 13, no. 9, p. 2320, 2020.
[84] H. A. Madsen, C. Bak, M. Døssing, R. Mikkelsen, and S. Øye, "Validation and modification of the blade element momentum theory based on comparisons with actuator disc simulations," *Wind Energy: An International Journal for Progress and Applications in Wind Power Conversion Technology,* vol. 13, no. 4, pp. 373-389, 2010.
[85] R. MacNeill and D. Verstraete, "Blade element momentum theory extended to model low Reynolds number propeller performance," *The Aeronautical Journal,* vol. 121, no. 1240, pp. 835-857, 2017.
[86] Z. Sun, J. Chen, W. Z. Shen, and W. J. Zhu, "Improved blade element momentum theory for wind turbine aerodynamic computations," *Renewable energy,* vol. 96, pp. 824-831, 2016.
[87] M. Bilgili and A. Yasar, "Performance evaluation of a horizontal axis wind turbine in operation," *International Journal of Green Energy,* vol. 14, no. 12, pp. 1048-1056, 2017.
[88] O. Ajayi, "Application of automotive alternators in small wind turbines," 2012.
[89] Q. Chen, Y. Li, and J. E. Seem, "Bumpless transfer-based inter-region controller switching of wind turbines for reducing power and load fluctuation," *IEEE Transactions on Sustainable Energy,* vol. 7, no. 1, pp. 23-31, 2015.
[90] B. Sanderse, S. Van der Pijl, and B. Koren, "Review of computational fluid dynamics for wind turbine wake aerodynamics," *Wind energy,* vol. 14, no. 7, pp. 799-819, 2011.
[91] E. M. Marshall and A. Bakker, "Computational fluid mixing," *Handbook of industrial mixing: science and practice*, pp. 257-343, 2003.
[92] D. Vučina, I. Marinić-Kragić, and Z. Milas, "Numerical models for robust shape optimization of wind turbine blades," *Renewable Energy,* vol. 87, pp. 849-862, 2016.
[93] F. Menter, "Zonal two equation kw turbulence models for aerodynamic flows," in *23rd fluid dynamics, plasmadynamics, and lasers conference*, 1993, p. 2906.
[94] P. A. Durbin and B. P. Reif, *Statistical theory and modeling for turbulent flows*. John Wiley & Sons, 2011.

[95] C. Yorke and G. Coleman, "Assessment of common turbulence models for an idealised adverse pressure gradient flow," *European Journal of Mechanics-B/Fluids*, vol. 23, no. 2, pp. 319-337, 2004.
[96] C. L. Rumsey and S. X. Ying, "Prediction of high lift: review of present CFD capability," *Progress in Aerospace Sciences*, vol. 38, no. 2, pp. 145-180, 2002.
[97] M. C. Jacob Moore, Agnes d'Entremont, Joan Kowalski, and Douglas Miller. "Viscous Damped Harmonic Forced Vibrations." U.S. National Science Foundation. http://mechanicsmap.psu.edu/websites/16_one_dof_vibrations/16-5_viscous_damped_harmonic/16-5_viscous_damped_harmonic.html (accessed 2023).
[98] T. D. Ashwill and S. Gershin, "A Nastran-Based Computer Program For Structural Dynamic Analysis Of Horizontal Axis Wind Turbines," Sandia National Lab.(SNL-NM), Albuquerque, NM (United States), 2011.
[99] P. E. JUSTIN KAUWALE. "Vibration for the Machine Design & Materials P.E. Exam." Engineering Pro Guides. https://www.engproguides.com/machine-vibration.html (accessed 2023).
[100] K. Tartibu, "A simplified analysis of the vibration of variable length blade as might be used in wind turbine systems," Cape Peninsula University of Technology, 2008.
[101] W. Thomson, *Theory of vibration with applications*. CrC Press, 1996.
[102] A. Nikolić and S. Šalinić, "A rigid multibody method for free vibration analysis of beams with variable axial parameters," *Journal of Vibration and Control*, vol. 23, no. 1, pp. 131-146, 2017.
[103] M. Mahmoud, "Natural frequency of axially functionally graded, tapered cantilever beams with tip masses," *Engineering Structures*, vol. 187, pp. 34-42, 2019.
[104] H. Rabiee and S. Galehdari, "Modal numerical analysis of helicopter rotor sample using Holzer-Myklestad method," *Journal of Stress Analysis*, vol. 3, no. 1, pp. 111-121, 2018.
[105] N. Myklestad, "A new method of calculating natural modes of uncoupled bending vibration of airplane wings and other types of beams," *Journal of the Aeronautical Sciences*, vol. 11, no. 2, pp. 153-162, 1944.
[106] R. R. Craig Jr and A. J. Kurdila, *Fundamentals of structural dynamics*. John Wiley & Sons, 2006.
[107] D. J. Ewins, *Modal testing: theory, practice and application*. John Wiley & Sons, 2009.
[108] W. J. Bottega, *Engineering vibrations*. CRC Press, 2014.
[109] R. R. Craig Jr and S. E. Benzley, "Structural dynamics, an introduction to computer methods," 1982.
[110] H. Anton and C. Rorres, *Elementary linear algebra: applications version*. John Wiley & Sons, 2013.
[111] M. Petyt, *Introduction to finite element vibration analysis*. Cambridge university press, 2010.
[112] S. Adhikari, "Damping modelling using generalized proportional damping," *Journal of Sound and Vibration*, vol. 293, no. 1-2, pp. 156-170, 2006.
[113] S. Adhikari and A. S. Phani, "Rayleigh's classical damping revisited," in *International Conference on Civil Engineering in the New Millennium: Opportunities and Challenges*, 2007.
[114] T. Caughey and M. E. O'Kelly, "Classical normal modes in damped linear dynamic systems," *Journal of Applied Mechanics*, vol. 32, no. 3, pp. 583-588, 1965.
[115] D. J. Inman, *Vibration with control*. John Wiley & Sons, 2017.
[116] ScienceDirect. https://www.sciencedirect.com/search?qs=fatigue%20wind%20turbine (accessed 08/2023, 2023).
[117] J. Lemaitre, *A course on damage mechanics*. Springer Science & Business Media, 2012.

[118] A. Alavudeen, N. Venkateshwaran, and J. W. Jappes, *A textbook of engineering materials and metallurgy*. Firewall Media, 2006.
[119] J. A. Collins, H. R. Busby, and G. H. Staab, *Mechanical design of machine elements and machines: a failure prevention perspective*. John Wiley & Sons, 2009.
[120] Y.-L. Lee, *Fatigue testing and analysis: theory and practice*. Butterworth-Heinemann, 2005.
[121] S. Khan, A. Vyshnevskyy, and J. Mosler, "Low cycle lifetime assessment of Al2024 alloy," *International Journal of Fatigue*, vol. 32, no. 8, pp. 1270-1277, 2010.
[122] E. Haibach, *Betriebsfeste Bauteile: Ermittlung und Nachweis der Betriebsfestigkeit, konstruktive und unternehmerische Gesichtspunkte*. Springer-Verlag, 2013.
[123] J. E. Shigley, C. R. Mischke, and T. H. Brown Jr, *Standard handbook of machine design*. McGraw-Hill Education, 2004.
[124] C. Bathias and P. C. Paris, "Gigacycle fatigue of metallic aircraft components," *International Journal of Fatigue*, vol. 32, no. 6, pp. 894-897, 2010.
[125] J. Lemaitre, J.-L. Chaboche, A. Benallal, and R. Desmorat, *Mécanique des matériaux solides-3e éd*. Dunod, 2020.
[126] H. E. Boyer, *Atlas of fatigue curves*. Asm International, 1985.
[127] J. Polák, "Cyclic deformation, crack initiation, and low-cycle fatigue," 2023.
[128] A. F. Grandt Jr, *Fundamentals of structural integrity: damage tolerant design and nondestructive evaluation*. John Wiley & Sons, 2003.
[129] B. OH, "The exponential law of endurance tests," in *Proc Am Soc Test Mater*, 1910, vol. 10, pp. 625-630.
[130] T. Lagoda, *Lifetime estimation of welded joints*. Springer Science & Business Media, 2008.
[131] C. Stromeyer, "The determination of fatigue limits under alternating stress conditions," *Proceedings of the Royal Society of London. Series A, Containing Papers of a Mathematical and Physical Character*, vol. 90, no. 620, pp. 411-425, 1914.
[132] A. Palmgren, "Die lebensdauer von kugellagern. z. vdi 68," *S339–S341*, 1924.
[133] W. Weibull, W. Weibull, S. Physicist, W. Weibull, S. Physicien, and W. Weibull, *A statistical representation of fatigue failures in solids*. Elander, 1949.
[134] F. Stüssi, *Die Theorie des Dauerfestigkeit und die Versuche von August Wöhler*. Verlag VSB, 1955.
[135] E. Castillo and A. Fernández-Canteli, *A unified statistical methodology for modeling fatigue damage*. Springer Science & Business Media, 2009.
[136] H. Karaouni, "Nouveaux outils pour la conception fiable des structures," 2001.
[137] C. Lalanne, "Fatigue Damage: Mechanical Vibration and Shock Analysis, Volume," *ISTE Ltd, London*, 2014.
[138] H. Okamura, S. Sakai, and I. Susuki, "Cumulative fatigue damage under random loads," *Fatigue & Fracture of Engineering Materials & Structures*, vol. 1, no. 4, pp. 409-419, 1979.
[139] M. Matsuishi and T. Endo, "Fatigue of metals subjected to varying stress," *Japan Society of Mechanical Engineers, Fukuoka, Japan*, vol. 68, no. 2, pp. 37-40, 1968.
[140] Y. Kondo, "Fatigue under variable amplitude loading," 2003.
[141] S. D. Downing and D. Socie, "Simple rainflow counting algorithms," *International journal of fatigue*, vol. 4, no. 1, pp. 31-40, 1982.
[142] R. Stelzer, B. Carlton, and S. Mazzoni, "Comparison of cycle counting methods for potential liquefaction and structural fatigue assessment," in *17th World Conference on Earthquake Engineering, 17WCEE*, 2020.

[143] C. H. McInnes and P. Meehan, "Equivalence of four-point and three-point rainflow cycle counting algorithms," *International journal of fatigue,* vol. 30, no. 3, pp. 547-559, 2008.
[144] Y.-L. Lee, M. E. Barkey, and H.-T. Kang, *Metal fatigue analysis handbook: practical problem-solving techniques for computer-aided engineering*. Elsevier, 2011.
[145] P. P. Milella, *Fatigue and corrosion in metals*. Springer Science & Business Media, 2012.
[146] A. S. o. T. Materials, "Standard practices for cycle counting in fatigue analysis," 2005.
[147] G. Sendeckyj, "Constant life diagrams—a historical review," *International journal of fatigue,* vol. 23, no. 4, pp. 347-353, 2001.
[148] M. Design, "An Integrated Approach," *RL Norton, pg,* vol. 73, 2007.
[149] A. Ince and G. Glinka, "A modification of Morrow and Smith–Watson–Topper mean stress correction models," *Fatigue & Fracture of Engineering Materials & Structures,* vol. 34, no. 11, pp. 854-867, 2011.
[150] J. Goodman, *Mechanics applied to engineering*. Longmans, Green, 1919.
[151] W. Gerber, "Bestimmung der zulossigenin eisen construcionen, 1874," *Z. Bayer Arch. Ing Ver,* vol. 6, pp. 101-110.
[152] C. R. Soderberg, "Closure to "Discussions of 'Factor of Safety and Working Stress'"(1930, Trans. ASME, 52 (2), pp. 22–27)," *Transactions of the American Society of Mechanical Engineers,* vol. 52, no. 2, pp. 27-28, 1930.
[153] J. Morrow, "Fatigue properties of metals," *Fatigue design handbook,* vol. 4, pp. 21-30, 1968.
[154] K. Walker, "The effect of stress ratio during crack propagation and fatigue for 2024-T3 and 7075-T6 aluminum," 1970.
[155] N. E. Dowling, "Mean stress effects in stress-life and strain-life fatigue," SAE Technical Paper, 0148-7191, 2004.
[156] J. Herbert and F. John, "Optimized goodman diagram for the analysisof fiberglass composites used in wind turbine blades," in *2005ASME Wind Energy Symposium*, 2005: ASME/AIAA, AIAA-2005-0196.
[157] T. Sekercioglu, "A new approach to the positive mean stress diagram in mechanical design," *Materialwissenschaft und Werkstofftechnik,* vol. 40, no. 9, pp. 713-717, 2009.
[158] J. Kauzlarich, "The palmgren-miner rule derived," in *Tribology Series*, vol. 14: Elsevier, 1989, pp. 175-179.
[159] L. Pook, "The Cracked Situation," *Metal Fatigue: What It Is, Why It Matters,* pp. 101-133, 2007.
[160] A. Fatemi and L. Yang, "Cumulative fatigue damage and life prediction theories: a survey of the state of the art for homogeneous materials," *International journal of fatigue,* vol. 20, no. 1, pp. 9-34, 1998.
[161] M. Spotts, T. Shoup, L. Hornberger, and D. O. Kazmer, "Design of Machine Elements," ed, 2004.
[162] E. Avellone, T. Baumeister III, and H. Saunders, "Marks standard handbook for mechanical engineers," 1993.
[163] M. A. Karataş and H. Gökkaya, "A review on machinability of carbon fiber reinforced polymer (CFRP) and glass fiber reinforced polymer (GFRP) composite materials," *Defence Technology,* vol. 14, no. 4, pp. 318-326, 2018.
[164] A. Kelly, "The nature of composite materials," *Scientific American,* vol. 217, no. 3, pp. 160-179, 1967.
[165] J. McGowan *et al.*, "A review of materials degradation in utility scale wind turbines," *Energy Materials,* vol. 2, no. 1, pp. 41-64, 2007.

[166] N. R. Council, *Assessment of research needs for wind turbine rotor materials technology*. National Academies Press, 1991.
[167] R. B. Hoadley, *Understanding wood: a craftsman's guide to wood technology*. Taunton press, 2000.
[168] M. F. d. S. de Moura, A. M. B. de Morais, and A. G. de Magalhães, *Materiais compósitos: materiais, fabrico e comportamento mecânico*. 2005.
[169] J. M. Jonkman and M. L. Buhl, *FAST user's guide*. National Renewable Energy Laboratory Golden, CO, USA, 2005.
[170] A. Manjock, "Evaluation Report: Design Codes FAST and ADAMS® for Load Calculations of Onshore Wind Turbines–Report No. 72042," *Germanischer Lloyd WindEnergie GmbH, Humburg, Germany,* 2005.
[171] I. B. Løken, "Dynamic Response and Fatigue of Offshore Wind Turbines-Effect of Foundation Type and Modelling Method Using Software FAST," NTNU, 2017.
[172] R. Damiani, J. Jonkman, and G. Hayman, "SubDyn user's guide and theory manual," National Renewable Energy Lab.(NREL), Golden, CO (United States), 2015.
[173] J. M. Jonkman, M. Buhl, and F. U. s. Guide, "National Renewable Energy Laboratory," *Golden, Colorado,* 2005.
[174] B. Jonkman and J. Jonkman, "FAST v8. 16.00 a-bjj," *National Renewable Energy Laboratory,* vol. 1355, 2016.
[175] G. Bir, "User's guide to BModes (software for computing rotating Beam-coupled Modes)," National Renewable Energy Lab.(NREL), Golden, CO (United States), 2005.
[176] B. Jonkman, "Turbsim user's guide v2. 00.00," *Natl. Renew. Energy Lab,* 2014.
[177] J. M. Jonkman, G. Hayman, B. Jonkman, R. Damiani, and R. Murray, "AeroDyn v15 user's guide and theory manual," *NREL Draft Report,* p. 46, 2015.
[178] J. M. Jonkman, A. Robertson, and G. J. Hayman, "HydroDyn user's guide and theory manual," *National Renewable Energy Laboratory,* 2014.
[179] A. Peña and O. Rathmann, "Atmospheric stability-dependent infinite wind-farm models and the wake-decay coefficient," *Wind Energy,* vol. 17, no. 8, pp. 1269-1285, 2014.
[180] G. Hayman, "MLife theory manual for version 1.00," *National Renewable Energy Laboratory, Golden, CO,* vol. 74, no. 75, p. 106, 2012.
[181] G. Freebury and W. Musial, "Determining equivalent damage loading for full-scale wind turbine blade fatigue tests," in *2000 ASME wind energy symposium*, 2000, p. 50.
[182] I. 61400-2, "Wind turbines—Part 2. Design requirements for small wind turbines," ed: International Electrotechnical Commission (IEC) Geneva, Switzerland, 2006.
[183] G. Lloyd and G. Hamburg, "Guideline for the certification of wind turbines," *July 1st,* 2010.
[184] D. Wood and D. Wood, "Using the IEC simple load model for small wind turbines," *Small Wind Turbines: Analysis, Design, and Application,* pp. 169-198, 2011.
[185] C. Zhang, H.-P. Chen, and T.-L. Huang, "Fatigue damage assessment of wind turbine composite blades using corrected blade element momentum theory," *Measurement,* vol. 129, pp. 102-111, 2018.
[186] Z. Zeng and A. Fatemi, "Elasto-plastic stress and strain behaviour at notch roots under monotonic and cyclic loadings," *The Journal of Strain Analysis for Engineering Design,* vol. 36, no. 3, pp. 287-300, 2001.
[187] H. Neuber, "Theory of stress concentration for shear-strained prismatical bodies with arbitrary nonlinear stress-strain law," 1961.

[188] T. Topper, R. Wetzel, and J. Morrow, "Neubers rule applied to fatigue of notched specimens," *J MATER*, vol. 4, no. 1, pp. 200-209, 1969.
[189] W. D. Pilkey, D. F. Pilkey, and Z. Bi, *Peterson's stress concentration factors*. John Wiley & Sons, 2020.
[190] P. Kuhn and H. F. Hardrath, "An engineering method for estimating notch-size effect in fatigue tests on steel," 1952.
[191] M. L. Williams, "On the stress distribution at the base of a stationary crack," 1957.
[192] J. Tong, "T-stress and its implications for crack growth," *Engineering Fracture Mechanics*, vol. 69, no. 12, pp. 1325-1337, 2002.
[193] F. IRWIN GR, "Handbuch der Physik, 6," ed: Springer, Berlin, 1958.
[194] R. W. Hertzberg, R. P. Vinci, and J. L. Hertzberg, *Deformation and fracture mechanics of engineering materials*. John Wiley & Sons, 2020.
[195] T. L. Anderson, *Fracture mechanics: fundamentals and applications*. CRC press, 2017.
[196] T. Fett, *Stress Intensity Factors-T-Stresses-Weight Functions. Supplement Volume*. KIT Scientific Publishing, 2014.
[197] D. Broek, *Elementary engineering fracture mechanics*. Springer Science & Business Media, 2012.
[198] B. J. Goodno and J. M. Gere, *Mechanics of materials*. Cengage Learning, 2020.
[199] H. Petroski and J. Achenbach, "Computation of the weight function from a stress intensity factor," *Engineering Fracture Mechanics*, vol. 10, no. 2, pp. 257-266, 1978.
[200] E. H. Miyaura, "Efeito das tensões residuais sobre a propagação de trincas em juntas soldadas por FSW," University of Campinas Campinas, 2012.
[201] H. Tada, P. C. Paris, and G. R. Irwin, "The stress analysis of cracks," *Handbook, Del Research Corporation*, vol. 34, no. 1973, 1973.
[202] I. Jones, "A wide range weight function for a single edge cracked geometry with clamped ends," *International journal of fracture*, vol. 89, pp. 1-18, 1998.
[203] R. Bao, X. Zhang, and N. A. Yahaya, "Evaluating stress intensity factors due to weld residual stresses by the weight function and finite element methods," *Engineering Fracture Mechanics*, vol. 77, no. 13, pp. 2550-2566, 2010.
[204] H. Bueckner, "Novel principle for the computation of stress intensity factors," *Zeitschrift fuer Angewandte Mathematik & Mechanik*, vol. 50, no. 9, 1970.
[205] G. C. Sih, P. Paris, and F. Erdogan, "Crack-tip, stress-intensity factors for plane extension and plate bending problems," 1962.
[206] G. Sih, "Handbook of stress intensity factors: Institute of Fracture and Solid Mechanics," *Lehigh University, Bethlehem*, 1973.
[207] G. Irwin, "Fracture mode transition for a crack traversing a plate," 1960.
[208] A. I. C. E. o. Fatigue and F. S. E. o. F. Mechanics, *Standard Test Method for Linear-elastic Plane-strain Fracture Toughness K [Ic] of Metallic Materials*. ASTM international, 2013.
[209] P. PC, "A rational analytic theory of fatigue," *Trends Engin*, vol. 13, pp. 9-14, 1961.
[210] J. Harter, "AFGROW users guide and technical manual. Air Vehicles Directorate, Air Force Research Laboratory OH," AFRL-VA-WP-TR-2003, June 2003 [available for download at http://afgrow …, 2003.
[211] F. Taheri, D. Trask, and N. Pegg, "Experimental and analytical investigation of fatigue characteristics of 350WT steel under constant and variable amplitude loadings," *Marine Structures*, vol. 16, no. 1, pp. 69-91, 2003.

[212] R. G. Forman, V. Kearney, and R. Engle, "Numerical analysis of crack propagation in cyclic-loaded structures," 1967.
[213] F. NASGRO, "mechanics and fatigue crack growth analysis software (version 6.0), reference manual," *NASA Johnson Space Center and Southwest Research Institute,* 2010.
[214] S. Beden, S. Abdullah, A. Ariffin, and N. Al-Asady, "Fatigue crack growth simulation of aluminium alloy under spectrum loadings," *Materials & Design,* vol. 31, no. 7, pp. 3449-3456, 2010.
[215] E. E. Gdoutos, *Fracture mechanics: an introduction*. Springer Nature, 2020.
[216] G. Irwin, "Plastic zone near a crack and fracture toughness," 1997.
[217] W. Elber, "The significance of fatigue crack closure," 1971.
[218] S. Xin, H.-p. LI, J.-p. SHAO, J.-z. ZHANG, Y.-h. WANG, and X.-d. YU, "Validity of three engineering models for fatigue crack growth rate affected by compressive loading in LY12M aluminum alloy," *Transactions of Nonferrous Metals Society of China,* vol. 22, pp. s27-s32, 2012.
[219] J. C. Newman Jr, "A crack opening stress equation for fatigue crack growth," *International Journal of fracture,* vol. 24, 1984.
[220] Y. Yamada, B. Ziegler, and J. Newman Jr, "Application of a strip-yield model to predict crack growth under variable-amplitude and spectrum loading–Part 1: Compact specimens," *Engineering fracture mechanics,* vol. 78, no. 14, pp. 2597-2608, 2011.
[221] J. Dominguez, "Fatigue crack growth under variable amplitude loading," *Handbook of fatigue crack propagation in metallic structures,* p. 955, 1994.
[222] T. Belytschko and T. Black, "Elastic crack growth in finite elements with minimal remeshing," *International journal for numerical methods in engineering,* vol. 45, no. 5, pp. 601-620, 1999.
[223] J. E. Dolbow, *An extended finite element method with discontinuous enrichment for applied mechanics*. Northwestern university, 1999.
[224] C. Daux, N. Moës, J. Dolbow, N. Sukumar, and T. Belytschko, "Arbitrary branched and intersecting cracks with the extended finite element method," *International journal for numerical methods in engineering,* vol. 48, no. 12, pp. 1741-1760, 2000.
[225] A. Asadpoure, S. Mohammadi, and A. Vafai, "Crack analysis in orthotropic media using the extended finite element method," *Thin-Walled Structures,* vol. 44, no. 9, pp. 1031-1038, 2006.
[226] I. Babuška and J. M. Melenk, "The partition of unity method," *International journal for numerical methods in engineering,* vol. 40, no. 4, pp. 727-758, 1997.
[227] J. M. Melenk and I. Babuška, "The partition of unity finite element method: basic theory and applications," *Computer methods in applied mechanics and engineering,* vol. 139, no. 1-4, pp. 289-314, 1996.
[228] N. Moës, J. Dolbow, and T. Belytschko, "A finite element method for crack growth without remeshing," *International journal for numerical methods in engineering,* vol. 46, no. 1, pp. 131-150, 1999.
[229] T. P. Fries and T. Belytschko, "The intrinsic XFEM: a method for arbitrary discontinuities without additional unknowns," *International journal for numerical methods in engineering,* vol. 68, no. 13, pp. 1358-1385, 2006.
[230] M. Georgioudakis, N. D. Lagaros, and M. Papadrakakis, "Reliability-based shape design optimization of structures subjected to fatigue," *Engineering and Applied Sciences Optimization: Dedicated to the Memory of Professor MG Karlaftis,* pp. 451-488, 2015.
[231] T. Belytschko, Y. Y. Lu, and L. Gu, "Element-free Galerkin methods," *International journal for numerical methods in engineering,* vol. 37, no. 2, pp. 229-256, 1994.

[232] E. Onate, "A finite point method for analysis of fluid flow problems," in *Proc. of Int. Conf. on Finite Eements in Fluids-New trends and applications Venezia*, 1995, pp. 15-21.
[233] A. R. Khoei, *Extended finite element method: theory and applications*. John Wiley & Sons, 2014.
[234] S. Mohammadi, *Extended finite element method: for fracture analysis of structures*. John Wiley & Sons, 2008.
[235] A. Asadpoure, S. Mohammadi, and A. Vafai, "Modeling crack in orthotropic media using a coupled finite element and partition of unity methods," *Finite Elements in analysis and Design*, vol. 42, no. 13, pp. 1165-1175, 2006.
[236] J.-H. Kim and G. H. Paulino, "Mixed-mode fracture of orthotropic functionally graded materials using finite elements and the modified crack closure method," *Engineering Fracture Mechanics*, vol. 69, no. 14-16, pp. 1557-1586, 2002.
[237] J. R. Rice and G. Rosengren, "Plane strain deformation near a crack tip in a power-law hardening material," *Journal of the Mechanics and Physics of Solids*, vol. 16, no. 1, pp. 1-12, 1968.
[238] J.-H. Kim and G. H. Paulino, "The interaction integral for fracture of orthotropic functionally graded materials: evaluation of stress intensity factors," *International journal of solids and structures*, vol. 40, no. 15, pp. 3967-4001, 2003.
[239] G. C. Sih, P. Paris, and G. Irwin, "On cracks in rectilinearly anisotropic bodies," *International Journal of Fracture Mechanics*, vol. 1, pp. 189-203, 1965.
[240] E. Preiß, *Fracture toughness of freestanding metallic thin films studied by bulge testing*. FAU University Press, 2018.
[241] S. G. Lekhnitskii, S. Tsai, and T. Chéron, *Anisotropic plates*. Gordon and Breach New York, 1968.
[242] D. Marten and J. Wendler, "Qblade guidelines," *Ver. 0.6, Technical University of (TU Berlin), Berlin, Germany*, 2013.
[243] M. Bechly and P. Clausen, "Structural design of a composite wind turbine blade using finite element analysis," *Computers & Structures*, vol. 63, no. 3, pp. 639-646, 1997.
[244] P. D. Soden, M. J. Hinton, and A. Kaddour, "Lamina properties, lay-up configurations and loading conditions for a range of fibre reinforced composite laminates," in *Failure criteria in fibre-reinforced-polymer composites*: Elsevier, 2004, pp. 30-51.
[245] J. S. Rajadurai, T. Christopher, G. Thanigaiyarasu, and B. N. Rao, "Finite element analysis with an improved failure criterion for composite wind turbine blades," *Forschung im Ingenieurwesen*, vol. 72, no. 4, pp. 193-207, 2008.
[246] M. Bechly and P. Clausen, "The Dynamic Performance of a Composite Blade from a 5kW Wind Turbine. Part 1: Measured Blade Response," *Wind Engineering*, vol. 25, no. 3, pp. 133-148, 2001.
[247] S. Zhou and X. Wu, "Fatigue life prediction of composite laminates by fatigue master curves," *Journal of Materials Research*, vol. 8, no. 6, pp. 6094-6105, 2019, doi: https://doi.org/10.1016/j.jmrt.2019.10.003.
[248] X. Gao, L. Yuan, Y. Fu, X. Yao, and H. Yang, "Prediction of mechanical properties on 3D braided composites with void defects," *Composites Part B: Engineering*, vol. 197, p. 108164, 2020, doi: https://doi.org/10.1016/j.compositesb.2020.108164.
[249] M. Da Costa and P. Clausen, "Structural Analysis of a small wind turbine blade subjected to gyroscopic load," in *Journal of Physics: Conference Series*, 2020, vol. 1618, no. 4: IOP Publishing, p. 042006, doi: https://doi:10.1088/1742-6596/1618/4/042006.

[250] M. S. Costa, S. P. Evans, D. R. Bradney, and P. D. Clausen, "A method to optimise the materials layout of small wind turbine blades," *Renewable Energy and Environmental Sustainability,* vol. 2, p. 19, 2017, doi: https://doi.org/10.1051/rees/2017006.

[251] S. Korkiakoski, P. Brøndsted, E. Sarlin, and O. Saarela, "Influence of specimen type and reinforcement on measured tension–tension fatigue life of unidirectional GFRP laminates," *International Journal of Fatigue,* vol. 85, pp. 114-129, 2016, doi: https://doi.org/10.1016/j.ijfatigue.2015.12.008.

[252] S. Zhou and X. Wu, "Fatigue life prediction of composite laminates by fatigue master curves," *Journal of Materials Research and Technology,* vol. 8, no. 6, pp. 6094-6105, 2019, doi: https://doi.org/10.1016/j.jmrt.2019.10.003.

[253] J. F. Mandell, D. D. Samborsky, and D. S. Cairns, "Fatigue of composite materials and substructures for wind turbine blades," Sandia National Laboratories Albuquerque, California, Contractor Report SAND2002-077, 2002.

[254] S. Backe and F. Balle, "A novel short-time concept for fatigue life estimation of carbon (CFRP) and metal/carbon fiber reinforced polymer (MCFRP)," *International Journal of Fatigue,* vol. 116, pp. 317-322, 2018, doi: https://doi.org/10.1016/j.ijfatigue.2018.06.044.

[255] S. P. Evans, "Aeroelastic measurements, simulations, and fatigue predictions for small wind turbines operating in highly turbulent flow," PhD thesis, School of Engineering, The University of Newcastle, Australia, Newcastle, Australia, 2017.

ANNEXES

International Journal of Energy for a Clean Environment 24(5):53–66 (2023)

DESIGN OPTIMIZATION OF SMALL WIND TURBINE BLADE BASED ON STRUCTURAL AND FATIGUE LIFE ANALYSES

Khalil Deghoum,[1,2] Mohammed Tahar Gherbi,[2] Muhsin J. Jweeg,[3] Hakim S. Sultan,[4] Azher M. Abed,[5] Oday I. Abdullah,[6,7,8,*] & Necib Djilani[2]

[1]*UDERZA Laboratory, University of El Oued, 39000 El Oued, Algeria*

[2]*Department of Mechanical Engineering, University of El Oued, 39000 El Oued, Algeria*

[3]*College of Technical Engineering, Al-Farahidi University, Baghdad 10005, Iraq*

[4]*University of Warith Al-Anbiyaa, College of Engineering, Karbala, Iraq*

[5]*Air Conditioning and Refrigeration Techniques Engineering Department, Al-Mustaqbal University College, Iraq*

[6]*Energy Engineering Department, College of Engineering, University of Baghdad, Iraq*

[7]*Mechanical Engineering Department, College of Engineering, Gulf University, Sanad 26489, Bahrain*

[8]*Hamburg University of Technology (TUHH), Institute of Laser and Systems Technologies (iLAS), Harburger Schloßstraße 28, 21079, Hamburg, Germany*

*Address all correspondence to: Oday I. Abdullah, Hamburg University of Technology (TUHH), Institute of Laser and Systems Technologies (iLAS), Harburger Schloßstraße 28, 21079, Hamburg, Germany; Tel.: +49 40 428 78 21 86; Fax: +49 40 428 78 40 76, E-mail: oday.abdullah@tuhh.de

Original Manuscript Submitted: 9/14/2022; Final Draft Received: 10/11/2022

In this study, a horizontal axis wind turbine blade model with a power of 5 kW was designed using a new MATLAB code based on the blade element momentum theory. The three-dimensional finite-element method was used to simulate and validate the wind turbine blade under normal and extreme operating conditions in order to evaluate the stress and deflection effects. International Standard IEC 61400.2 was applied to obtain the fatigue loads, estimate the damage, and predict the life of the blade. Based on the optimization approach, the flap-wise deflections were reduced by 11% and the trailing and leading edges were reduced by 31%. Based on the optimized design of the blade, the mass of the blade was reduced by 22%. Furthermore, the fatigue life of the blade was investigated and analyzed, in which the simplified load model (SLM) and the aeroelastic FAST software program were employed to predict the lifetime of the blade. Finally, it was found that based on the SLM method the design life of a 5-kW blade is 20 years when carbon fiber material is used.

KEY WORDS: *small wind turbine, blade element momentum, fatigue life, International Standard IEC 61400.2, simplified load model*

NOMENCLATURE

B	blade number
C_D	drag coefficient
C_L	lift coefficient
C_N	normal force coefficient
C_T	tangential force coefficient
c	chord length (m)
D_B	blade damage
F_C	centrifugal force (N)
F_D	drag force (N)
F_G	gravitational force (N)
F_L	lift force (N)
F_N	normal force (N)
F_T	tangential force (N)
m_B	blade mass (kg)
N_F	number of cycles to failure
n	number of fatigue cycles
R	blade length (m)
$\bar{R}$	stress ratio
T_d	design life
U_{rel}	relative wind velocity (m/s)
U_0	wind velocity (m/s)

Greek Symbols

α	attack angle (°)
β	slope coefficient of the normalized *S-N* curve
γ_f	safety factor for the loads
γ_m	safety factor for the materials
θ	twist angle (°)
ρ	air density (kg/m^3)
σ_0	ultimate stress (MPa)
φ	inflow angle (°)
Ω	blade rotational speed (revolutions per minute)
ω	blade rotation angular velocity (rad/s)

1. INTRODUCTION

The world is moving toward reducing dependence on fossil fuels and increasing the usage of renewable energy sources (Magomadov et al., 2023). Wind is one of the most important sources of renewable energy employed to produce electricity in different sectors such as agriculture, industrial, supplying homes with electricity, etc. (Ani and Ndubueze, 2013; Rosato, 2018).

The blade is one of the most important components of a wind turbine. The effects of extreme wind and gravity are among the biggest problems engineers face when designing wind turbine blades with high durability and resistance to wind loads. In addition, in order to reduce the effect of gravity, the weight of the blade needs to be reduced. Composite materials have become important components in the manufacturing of wind blades due to their lightweight, high-strength, high-safety, and reliability characteristics, and the fact that they are recyclable and environmentally friendly (Song et al., 2011).

The study of wind turbine blade structures using the finite-element method (FEM) is a subject of interest to many researchers. Kim et al. (2021) coupled computational fluid dynamics (CFD) with a three-dimensional (3D) FEM model to investigate and optimize the wind turbine structure. Wu and Young (2012) studied the distribution and orientation of a fiber component using a wind turbine composite material based on finite elements

(FEs). Pourrajabian et al. (2016) optimized the blade of small wind turbines by studying the aero-structural design. Kim et al. (2009) studied the efficiency of large wind turbines under the influence of rotational and aerodynamic loads.

Despite the improvements made to wind turbine materials, machines operating for extended periods of time during work hours experience fatigue, which presents a complex problem. This fact has urged researchers to study wind turbines from this aspect. Kong et al. (2006) verified the fatigue life in a medium-scale wind turbine blade. Kensche (2006) reviewed the influence of the environment on a composite fiber material, studied the fatigue life of wind turbines, and presented the required *S-N* curve of the wind turbine material. Sutherland and Mandell (2004) used the Goodman diagram to infer the damage caused by the mean stresses applied to wind turbines. Sutherland and Kelley (1995) estimated the effect of wind farms on the fatigue damage experienced by wind turbines in Europe and the United States. The results showed fundamental differences. Shokrieh and Rafiee (2006) used a simulation to predict the fatigue failure of a composite material in a full blade model and extract the critical zone where the failure began.

Fatigue is an extremely complicated problem due to the loads applied to wind turbine blades. The International Electrotechnical Commission (IEC) has simplified a method (Standard IEC 61400-2) that employs a simplified load model (SLM) to analyze the applied loads on small wind turbines (IEC, 2013; Wood, 2009). The aim of this study was twofold. First, we studied the steady-state problem of a 5-kW small wind turbine blade made from a composite material (E-Glass/MY750 epoxy) under the influence of aerodynamic loads using CFD and FEM approaches. Second, we focused on the fatigue problem of small wind turbine blades using the SLM and IEC 61400-2 aeroelastic FAST software program simulation approach. Based on the results of these two approaches, we predicted the blade's life.

2. BLADE DESIGN AND FINITE-ELEMENT MODEL

The main parts of the blade in a small wind turbine are the root, neck, and shell. The root section is cylindrical with a metal flange to facilitate connection to the main hub using screws. The neck part attaches the root to the shell and is made of composite materials. The shell part is formed by twisting the airfoil from the root to the tip in order to distribute the wind speed pressure over the blade surface. The thickness of the blade decreases from the root to the tip and from the leading edge to the trailing edge.

In designing a wind blade, efficiency should be taken into account. Therefore, as a first and important step, an appropriate airfoil must be chosen. In this research study, in order to obtain high efficiency—i.e., a high ratio of $C_L/C_D = 129.37$ at angle $\alpha = 5.25°$—we selected the NACA 4412 airfoil (Haque et al., 2015). In addition, we applied the blade element momentum theory (BEMT) (Tenguria et al., 2010) to obtain the optimum aerodynamic design of the blade. Based on the BEMT, we calculated the following design parameters of the blade geometry: twist angle (θ), chord length (c), and angle of attack (α).

Using the MATLAB software program, we developed a new code based on the BEMT to find the optimum design for the blade. The first step in the design process was the selection of the design parameters. Table 1 lists the design parameters used in the case study of the wind turbine blade and Table 2 gives the design specifications that produced the optimum results according to the BEMT. Using this model, we calculated the blade mass as equal to 24.6 kg, which highly agreed with the experimental result of 24.7 kg (Bechly and Clausen, 1997).

In this study, we employed the FEM in the ANSYS software program to simulate the 5-kW wind turbine blade. Figure 1(a) represents the FE model used to compute the stresses and deflections due to the changes in wind speed. The blade was meshed using the element shell 281 for composite materials. The element consisted of eight nodes, in which each node had six degrees of freedom. A grid convergence test was conducted to determine the optimal mesh based on an error rate of less than 2%. The number of elements in the final FE model was 4515 and the number of nodes was 21,536. To reduce the tip deflection, improve the blade strength, and enable the blade to withstand extreme working conditions, we selected the E-Glass/MY750 composite material to build the blade. Theoretically, the fiber volume fraction ($V_f = 0.6$) gives the highest stiffness-to-weight (E/ρ) ratio (Mishnaevsky et al., 2017). The mechanical properties of the used

TABLE 1: The design parameters of the small wind turbine

Design parameter	Value
Rated power	5 kW
Wind speed	10.5 m/s
Number of blades	3
Design tip speed ratio	6
Design angle of attack	5.25°
Rotor radius	2.5 m
Design rotational speed	240 rpm
Air density	1.22 kg/m^3
Airfoil type	NACA4412

TABLE 2: Specifications design of the 5-kW wind turbine blade

Parameter	Specification
Root chord length	0.386 m
Tip chord length	0.120 m
Blade length	2.5 m
Root diameter	0.080 m
Hub length	0.300 m
Hub-to-neck length	0.300 m

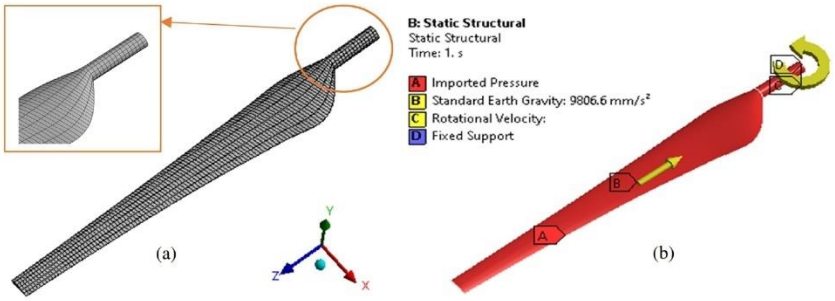

FIG. 1: FE model (a) and boundary conditions (b) of the blade

material are listed in Table 3 (Soden et al., 2004). Figure 1(b) illustrates the boundary conditions of the wind turbine blade, in which the root side was fixed and the effect of gravity force in the center of the blade mass was taken into consideration. The wind turbine blade was subjected to centrifugal force due to rotation, aerodynamic pressure load on the blade's shell, and gravity force; other forces such as the mechanical brake activation and gyroscopic forces were neglected since their effects are minimal.

CFD was used to calculate the aerodynamic loads applied to the blade surface. We developed a new 3D model using the ANSYS Fluent software program. We coupled the

TABLE 3: Mechanical properties of the material E-Glass/MY750 epoxy

Property	Value
Young's modulus	
E_{xx}	45.6 GPa
E_{yy}	16.2 GPa
Ezz	16.2 GPa
Poisson's ratio	
υ_{xy}	0.27
υ_{zx}	0.27
υ_{yz}	0.33
Shear modulus	
G_{xy}	5.83 GPa
G_{zx}	5.83 GPa
G_{yz}	3.69 GPa
Density	
ρ	2000 kg/m^3

CFD and structural dynamics models to investigate the fluid–structure interaction and find the stresses and deflections affecting the blade. Figure 2 shows the applied force and wind direction at each section of the blade, where α is the angle of attack; θ is the twist angle; φ is the inflow angle; and F_D, F_L, F_N, and F_T are the drag, lift, normal, and tangential forces, respectively. The finite-volume method was used to solve the Navier–Stokes equation (Bechmann et al., 2011) and calculate the coefficients of the normal (C_N), tangential (C_T), drag (C_D), and lift (C_L) forces. Finally, the results of the forces obtained using the BEMT and CFD were compared. The following equations were used to calculate the lift and drag forces (Rosato, 2018):

$$F_L = \frac{1}{2}\rho U_{\text{rel}}^2 c C_L \tag{1}$$

$$F_D = \frac{1}{2}\rho U_{\text{rel}}^2 c C_D \tag{2}$$

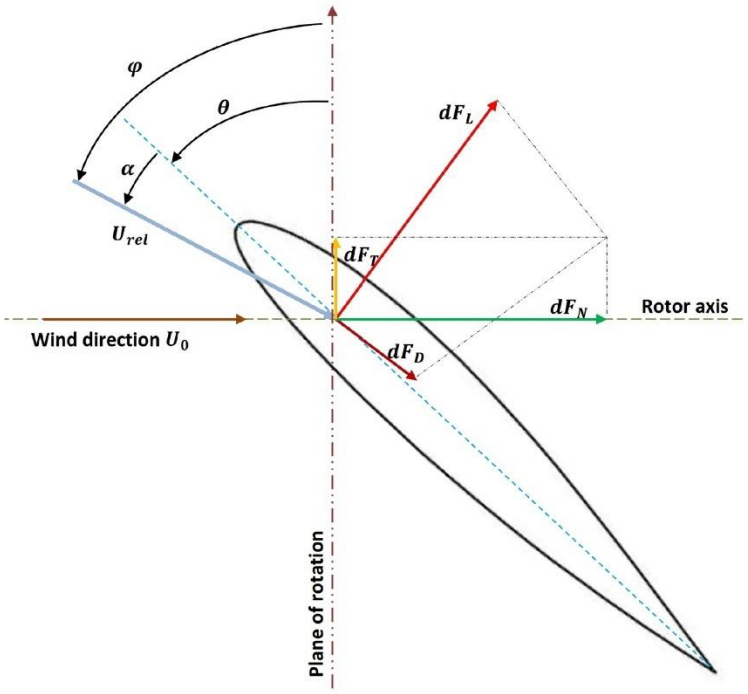

FIG. 2: The airfoil section with aerodynamic loads and wind direction

The following formulas were used to find the normal coefficient force:

$$C_N = \frac{F_N}{(1/2)\rho U_{\text{rel}}^2 c} \tag{3}$$

$$C_N = C_L \cos\varphi + C_D \sin\varphi \tag{4}$$

The following equations were used to obtain the coefficient of the tangential force:

$$C_T = \frac{F_T}{(1/2)\rho U_{\text{rel}}^2 c} \tag{5}$$

$$C_T = C_L \sin\varphi - C_D \cos\varphi \tag{6}$$

The relative wind velocity was obtained using the following equation (Liu et al., 2013):

$$U_{\text{rel}} = \sqrt{\left(\frac{\Omega R}{2}\right)^2 + (U_0)^2} \tag{7}$$

where c is the chord and U_0 is the wind velocity. To calculate the gravitational and centrifugal forces, we used the following equations (Rajadurai et al., 2008):

$$F_G = m_B g \tag{8}$$

$$F_C = m_B \omega^2 R \tag{9}$$

where m_B is the blade mass and ω is the angular velocity of the blade rotation. Figure 3 shows the results obtained for the coefficients of the tangential and normal forces at seven different sections along the blade based on BEMT and CFD. Based on the results, it was found that the lift and drag forces applied to the blade were equal to 380.2 and 7.9 N, respectively, while the gravitational and the centrifugal forces were equal to 241.32 and 1544.88 N, respectively.

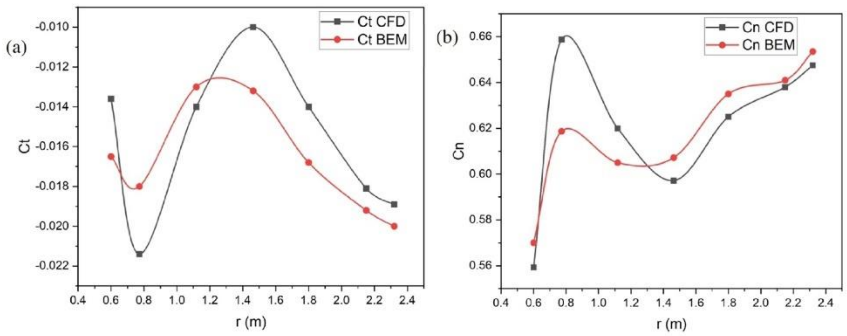

FIG. 3: The coefficients of the tangential (a) and normal (b) forces

The deflections of the trailing and leading edges of the blade were calculated numerically and compared with the experimental results, as shown in Fig. 4. It was found that the deflections based on the numerical and experimental approaches were 133 and 195 mm. The difference between the flap-wise deflections in the two studies was about 11% and the difference between the deflections in the trailing and leading edges was about 31%. The differences between the numerical and experimental results were due to the approximation of the material properties in the numerical model. High agreement was obtained between the numerical and experimental results (Bechly and Clausen, 1997). Figure 5(a) and 5(b) show the maximum flap-wise deflection and stress distribution of the wind turbine blade.

3. EXTREME WIND AND DAMAGE ANALYSES

Wind turbine blades are subjected to fatigue as a result of the wind loads; therefore, fatigue should be taken into consideration when designing blades in order to avoid pre-

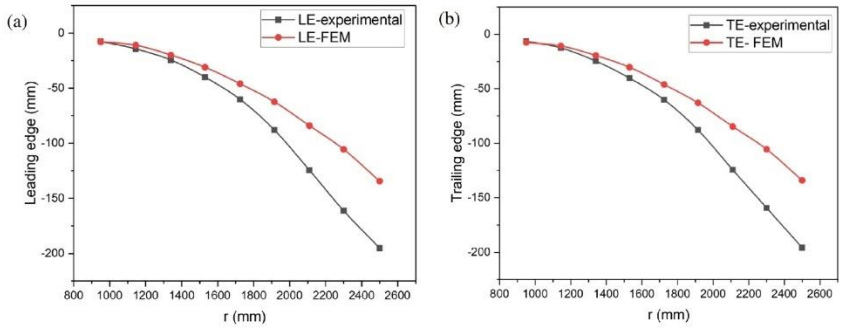

FIG. 4: Deflections of the leading edge (LE) (a) and trailing edge (TE) (b) along the blade length

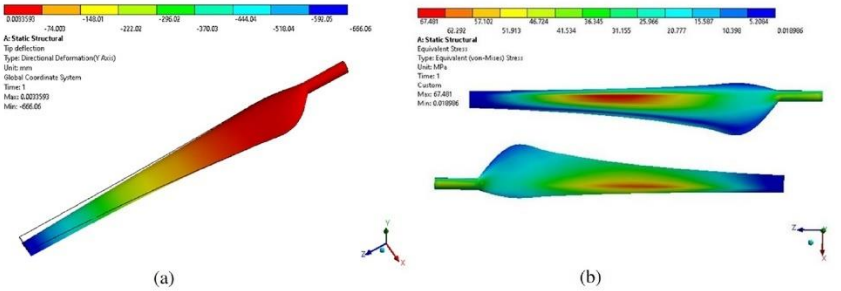

(a) (b)

FIG. 5: Maximum flap-wise deflection (a) and maximum stress distribution (b) of the wind turbine blade

mature failure. To study the loads causing fatigue in small wind turbines, IEC 61400-2 (IEC, 2013) presents three methods for calculating the loads: experimental measurements, aeroelastic simulations, and a SLM. In order to evaluate the impact of loads on wind turbine blades, the FAST software program (version 7), developed by the National Renewable Energy Laboratory (Corbus and Meadors, 2005), was employed in the aeroelastic simulation of the 5-kW wind turbine. The same design parameters (airfoil, blade length, rotation speed, etc.) were used to simulate the blade in the FAST software program. The ANSYS software program was used in the CFD numerical simulation to study the effect of airflow on the wind blade at an extreme wind speed of 52.5 m/s. In the next step, we exported the pressure distribution from the blade surface to the structural model to analyze the steady-state problem and compute the stresses and deformations. Figure 6(a) shows the distribution of von Mises stresses on the wind blade structure. It was found that the maximum stress at the extreme wind speed in the root region was

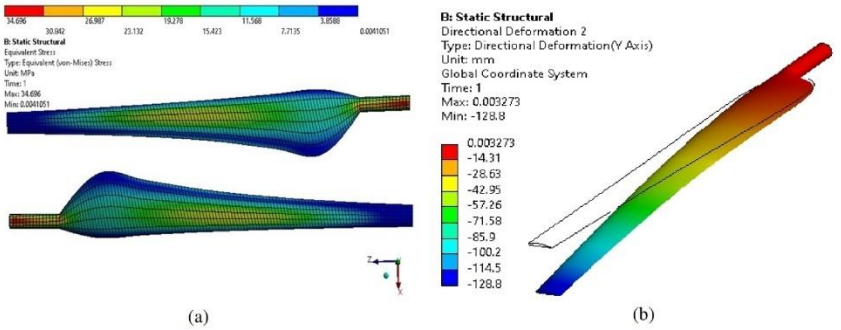

(a) (b)

FIG. 6: Stress distribution under extreme wind conditions (a) and flap-wise deflection of the blade (b)

about 34.69 MPa. Figure 6(b) shows the deflection of the blade under the extreme wind speed.

In order to assess the damage caused by the fatigue loads on the wind turbine blade, the IEC 61400-2 approach is recommended using Miner's method, which is based on cumulative damage. This method states that breakage occurs if the damage exceeds the allowable limit. The damage is calculated by the following equation (Zhang et al., 2018):

$$D_B = \sum_i \frac{n_i}{N_F(\gamma_f \gamma_m \sigma_B)} \leq 1 \tag{10}$$

where n_i is the number of performed cycles for bin i of the load characteristic spectrum; N_F is the number of cycles to failure, which is a variable function in terms of the stress level of fatigue cycles (σ_B); and γ_m and γ_f are the safety factors for the material and load, respectively (see Table 4). The number of cycles to failure has a relationship with the associated stress level. In the SLM, the number of fatigue cycles is calculated as follows:

$$n = \frac{B\Omega_{\text{design}} T_d}{60} = 7.59 \times 10^9 \tag{11}$$

where Ω_{design} is the rotational speed of 240 revolutions per minute (rpm); and T_d is the design life of the composite material of a wind turbine blade, which is estimated to be about 20 years (i.e., 6.31×10^8 s). In order to determine N_F, an *S-N* curve should be used. This curve presents the number of cycles to failure versus the maximum applied stress (the stress level of fatigue cycles, σ_B). At a constant stress ratio of $\bar{R} = \sigma_{\min}/\sigma_{\max}$, the *S-N* curve of the composite material decreases linearly (i.e., the relation between the stress and log N_F is linearly proportional). The number of cycles to failure (N_F) can be calculated by applying Basquin's equation (Rajadurai et al., 2008):

$$\frac{\sigma_B}{\sigma_0} = 1 - \beta \log_{10} N_F \tag{12}$$

TABLE 4: Fatigue damage load and blade life for the different methods

Method	SLM	FAST	Measured (Evans, 2017)
Fatigue damage loads (Nm)	634	195	71
Blade fatigue life (years)	0.1	4.13	9.18

where σ_B is the maximum applied stress (in which the associated stress level is 25.20 MPa); σ_0 is the ultimate strength of the blade's material; and β is the slope coefficient of the normalized *S-N* curve, which varies with different materials and is related to the stress ratio. To simulate the blade under the same operating conditions, we used the stress ratio of $R = 0.1$. For a wind turbine made of composite material, the value of parameter β is 0.106 (Mandell et al., 2002). From Eq. (12), we found that the allowable number of cycles to failure corresponds to a maximum working stress of $N_F = 3.93 \times 10^7$ cycles.

Based on Eq. (10), and assuming the wind turbine design life is 20 years, we found that the fatigue damage in the SLM was $D_{B,LSM} = 193 > 1$. Since the damage was greater than one, this means that the wind turbine blade would fail before reaching the design life. In addition, the M-Life in the FAST software predicted the damage as $D_{B,FAST} = 4.84$, which indicated that the blade would not resist the fatigue loads until the required period (20 years).

According to the SLM, the blade will withstand the cyclical fatigue loads for 0.1 years (i.e., the number of fatigue cycles is 3.79×10^7), which is equivalent to 37 days before breaking, and according to the aeroelastic simulation by FAST program, the blade will withstand loads for 4.13 years (i.e., 1.57×10^9 cycles). Table 4 compares the results obtained by the SLM and FAST methods as well as the experimental results obtained by Evans (2017).

According to the damage analysis, the blade life in the SLM is 0.1 years and the blade life of the experimental results is 9.18 years, which is approximately 92 times the blade life predicted by the SLM. However, the expected lifetime of the blade obtained based on the aeroelastic simulations is 4.13 years, which is approximately 41 times the life obtained by the SLM. The fatigue loads resulting from the aeroelastic simulation were more realistic compared to the SLM fatigue loads, which means that the simulation gave a good prediction of the damage to the wind blade under normal operating conditions.

It can be concluded that the SLM is the most conservative and safest approach, followed by the aeroelastic simulations, while the measured results are the least conservative approach. Somewhat disturbingly, all of the established methods predicted lifetimes that were less than the nominal design life of 20 years. The diminished design life results based on the three methods used were due to the continuous application of fatigue loads without taking into account that wind resources are sometimes unavailable or shutdown for long periods of time for maintenance or other plant-related problems; these factors may reduce the number of damage cycles on the blade. If all of the actual factors are taken into consideration with respect to the fatigue life, the design life of the blade approximately approaches 20 years.

According to SLM calculations, a material with an *S-N* slope of less than 0.085 must be certified for the blade to exceed the required design life of 20 years. Optimal fiberglass composites do not have *S-N* slopes of less than 0.1; therefore, carbon fiber materials must be used to keep the *S-N* slope lower than 0.085 (Backe and Balle, 2018). After choosing the proposed material, we found that the mass of the blade was reduced

by 22%, while the number of fatigue cycles to reach failure was estimated at around $N_F = 1.96 \times 10^{10}$. The damage caused by fatigue loads was $D_{B,LSM} = 3.87 \times 10^{-1} < 1$. This means that the blade will exceed the required design life when using carbon fiber material.

4. CONCLUSIONS AND REMARKS

The blade is one of the most important components in a wind turbine. Blades are mostly made of composite materials with a variable thickness along the blade length and a complex aerodynamic shape. In this research study, we built new numerical models of 5-kW wind turbine blades to find the optimal values of the design parameters. In addition, a new MATLAB code was developed based on the BEMT in order to optimize the wind turbine blade. In addition, the effect of the type of blade material (E-Glass/MY750 epoxy) on the results was considered. The results obtained can be summarized as follows:

1. Compared to other types of materials, the E-Glass/MY750 material reduced the flap- and edge-wise deflections by 11% and 31%, respectively.
2. Carbon fiber material can reduce the weight of wind turbine blades by 22%, which will also reduce the gravitational and centrifugal effects. In addition, using this type of material enhances the lifetime of the blade to 20 years.
3. We analyzed the fatigue problem based on Miner's method and using the SLM and aeroelastic approaches to calculate the number of fatigue cycles of the wind turbine blade.
4. The obtained numerical results proved the reliability and accuracy of the developed models compared with the results of other researchers.

In future research studies, the dynamic behavior of a wind turbine blade subjected to impact load (wind) should be investigated. In addition, the effect of gyroscopic motion on the fatigue in wind turbine blades influenced by the root zone during blade yaw should be taken into consideration.

REFERENCES

Ani, V.A. and Ndubueze, N.A., The Potential of Stand-Alone PV/Wind Hybrid Energy Systems for Power Supply to Remote Rural Areas in Nigeria, *Int. J. Energy Clean Environ.*, vol. **14**, no. 1, pp. 1–20, 2013. DOI: 10.1615/InterJEnerCleanEnv.2012004922

Backe, S. and Balle, F., A Novel Short-Time Concept for Fatigue Life Estimation of Carbon (CFRP) and Metal/Carbon Fiber Reinforced Polymer (MCFRP), *Int. J. Fatigue*, vol. **116**, no. 3, pp. 317–322, 2018.

Bechly, M. and Clausen, P., Structural Design of a Composite Wind Turbine Blade Using Finite Element Analysis, *Comput. Struct.*, vol. **63**, no. 3, pp. 639–646, 1997.

Bechmann, A., Sørensen, N.N., and Zahle, F., CFD Simulations of the MEXICO Rotor, *Wind Energy*, vol. **14**, no. 5, pp. 677–689, 2011.

Corbus, D. and Meadors, M., Small Wind Research Turbine, Technical Rep. NREL/TP-500-38550, National Renewable Energy Laboratory, Golden, CO, 2005.

Evans, S.P., Aeroelastic Measurements, Simulations, and Fatigue Predictions for Small Wind Turbines Operating in Highly Turbulent Flow, PhD, School of Engineering, The University of Newcastle, Australia, 2017.

Haque, M.N., Ali, M., and Ara, I., Experimental Investigation on the Performance of NACA 4412 Aerofoil with Curved Leading Edge Planform, *Procedia Eng*., vol. **105**, no. 2, pp. 232–240, 2015.

International Electrotechnical Commission (IEC), *IEC 61400-2: 2013-Wind Turbines. Part 2. Small Wind Turbines, Australia*, International Electrotechnical Commission, 2013.

Kensche, C.W., Fatigue of Composites for Wind Turbines, *Int. J. Fatigue*, vol. **28**, no. 10, pp. 1363–1374, 2006.

Kim, D.-M., Kim, D.-H., Park, K.-K., and Kim, Y.-S., Efficient Super-Element Structural Vibration Analyses of a Large Wind-Turbine Rotor Blade Considering Rotational and Aerodynamic Load Effects, *Trans. Korean Soc. Noise Vib. Eng*., vol. **19**, no. 7, pp. 651–658, 2009.

Kim, T., Nagai, H., Uda, N., and Ohya, Y., Fundamental Effect of Vibrational Mode on Vortex-Induced Vibration in a Brimmed Diffuser for a Wind Turbine, *Int. J. Energy Clean Environ*., vol. **22**, no. 4, pp. 1–32, 2021. DOI: 10.1615/InterJEnerCleanEnv.2021036688

Kong, C., Kim, T., Han, D., and Sugiyama, Y., Investigation of Fatigue Life for a Medium Scale Composite Wind Turbine Blade, *Int. J. Fatigue*, vol. **28**, no. 10, pp. 1382-1388, 2006.

Liu, X., Wang, L., and Tang, X., Optimized Linearization of Chord and Twist Angle Profiles for Fixed-Pitch Fixed-Speed Wind Turbine Blades, *Renewable Energy*, vol. **57**, pp. 111–119, 2013.

Magomadov, R., Ezirbaev, T., Ziniev, S., Abdulkhakimov, U., and Dudaev, M., Features of the Introduction of Renewable Energy Sources in Russia, *Int. J. Energy Clean Environ*., vol. **24**, no. 1, pp. 129–140, 2023. DOI: 10.1615/InterJEnerCleanEnv.2022043764

Mandell, J.F., Samborsky, D.D., and Cairns, D.S., Fatigue of Composite Materials and Substructures for Wind Turbine Blades, Contractor Rep. SAND2002-0771, Sandia National Laboratories, Albuquerque, NM, 2002.

Mishnaevsky, L., Branner, K., Petersen, H.N., Beauson, J., McGugan, M., and Sørensen, B.F., Materials for Wind Turbine Blades: An Overview, *Materials*, vol. **10**, no. 11, Article 1285, 2017.

Pourrajabian, A., Afshar, P.A.N., Ahmadizadeh, M., and Wood, D., Aero-Structural Design and Optimization of a Small Wind Turbine Blade, *Renewable Energy*, vol. **87**, pp. 837–848, 2016.

Rajadurai, J.S., Christopher, T., Thanigaiyarasu, G., and Rao, B.N., Finite Element Analysis with an Improved Failure Criterion for Composite Wind Turbine Blades, *Forsch. Ingenieurwes*., vol. **72**, no. 4, pp. 193–207, 2008.

Rosato, M.A., *Small Wind Turbines for Electricity and Irrigation: Design and Construction*, New York: CRC Press, 2018.

Shokrieh, M.M. and Rafiee, R., Simulation of Fatigue Failure in a Full Composite Wind Turbine Blade, *Compos. Struct*., vol. **74**, no. 3, pp. 332–342, 2006.

Soden, P.D., Hinton, M.J., and Kaddour, A., *Lamina Properties, Lay-Up Configurations and Loading Conditions for a Range of Fibre Reinforced Composite Laminates*, Manchester, UK: Elsevier, 2004.

Song, F., Ni, Y., and Tan, Z., Optimization Design, Modeling and Dynamic Analysis for Composite Wind Turbine Blade, *Procedia Eng*., vol. **16**, no. 2, pp. 369–375, 2011.

Sutherland, H. and Kelley, N., Fatigue Damage Estimate Comparisons for Northern European and US Wind Farm Loading Environments, Rep. SAND-94-2550C, National Renewable Energy Laboratory, Albuquerque, NM, 1995.

Sutherland, H.J. and Mandell, J.F., Effect of Mean Stress on the Damage of Wind Turbine Blades, *J. Sol. Energy Eng*., vol. **126**, no. 4, pp. 1041–1049, 2004.

Tenguria, N., Mittal, N., and Ahmed, S., Investigation of Blade Performance of Horizontal Axis Wind Turbine Based on Blade Element Momentum Theory (BEMT) Using NACA Airfoils, *Int. J. Eng. Sci. Technol*., vol. **2**, no. 12, pp. 25–35, 2010.

Wood, D., Using the IEC Simple Load Model for Small Wind Turbines, *Wind Eng*., vol. **33**, no. 2, pp. 139–154, 2009.

Wu, W.H. and Young, W.B., Structural Analysis and Design of the Composite Wind Turbine Blade, *Appl. Compos. Mater.*, vol. **19**, nos. 3–4, pp. 247–257, 2012.
Zhang, C., Chen, H.-P., and Huang, T.-L., Fatigue Damage Assessment of Wind Turbine Composite Blades Using Corrected Blade Element Momentum Theory, *Measurement*, vol. **129**, pp. 102–111, 2018. DOI: 10.1016/j.measurement.2018.06.045

applied system innovation

MDPI

Article

Optimization of Small Horizontal Axis Wind Turbines Based on Aerodynamic, Steady-State, and Dynamic Analyses

Khalil Deghoum [1,2], Mohammed Taher Gherbi [2], Hakim S. Sultan [3], Adnan N. Jameel Al-Tamimi [4], Azher M. Abed [5], Oday Ibraheem Abdullah [6,7,8,*], Hamza Mechakra [9] and Ali Boukhari [2]

1 UDERZA Laboratory, University of El Oued, El Oued 39000, Algeria
2 Department of Mechanical Engineering, University of El Oued, El Oued 39000, Algeria
3 College of Engineering, University of Warith Al-Anbiyaa, Karbala 56001, Iraq
4 College of Technical Engineering, Al-Farahidi University, Baghdad 10001, Iraq
5 Air Conditioning and Refrigeration Techniques Engineering Department, Al-Mustaqbal University College, Babylon 51001, Iraq
6 Energy Engineering Department, College of Engineering, University of Baghdad, Baghdad 10071, Iraq
7 Mechanical Engineering Department, College of Engineering, Gulf University, Sanad 26489, Bahrain
8 Institute of Laser and Systems Technologies (iLAS), Hamburg University of Technology (TUHH), Harburger Schloßstraße 28, 21079 Hamburg, Germany
9 Dynamics of Engines and Vibroacoustic Laboratory, F.S.I., M'Hamed Bougara University of Boumerdes, Boumerdes 35000, Algeria
* Correspondence: oday.abdullah@tuhh.de

Abstract: In this article, the model of a 5 kW small wind turbine blade is developed and improved. Emphasis has been placed on improving the blade's efficiency and aerodynamics and selecting the most optimal material for the wind blade. The QBlade software was used to enhance the chord and twist. Also, a new finite element model was developed using the ANSYS software to analyze the structure and modal problems of the wind blade. The results presented the wind blade's von Mises stresses and deformations using three different materials (Carbon/epoxy, E-Glass/epoxy, and braided composite). The modal analysis results presented the natural frequencies and mode shapes for each material. It was found, based on the results, that the maximum deflections of E-glass, braided composite and carbon fiber were 46.46 mm, 33.54 mm, and 18.29 mm, respectively.

Keywords: aerodynamic; wind turbine; modal analysis; composite material; FE method; QBlade software

Citation: Deghoum, K.; Gherbi, M.T.; Sultan, H.S.; Jameel Al-Tamimi, A.N.; Abed, A.M.; Abdullah, O.I.; Mechakra, H.; Boukhari, A. Optimization of Small Horizontal Axis Wind Turbines Based on Aerodynamic, Steady-State, and Dynamic Analyses. *Appl. Syst. Innov.* **2023**, *6*, 33. https://doi.org/10.3390/asi6020033

Academic Editors: Emmanuel Karapidakis and Sergio Nardini

Received: 30 January 2023
Revised: 18 February 2023
Accepted: 21 February 2023
Published: 24 February 2023

1. Introduction

The world is moving rapidly towards using renewable energies to reduce dependency on fossil fuels to reduce emissions and pollution. One of the important renewable energy sources is wind energy, which is available for free and sufficient in many places around the world. Wind turbines are widely used worldwide to produce electricity from wind energy. This energy can be used in different applications and fields, such as agriculture and factories, as well as supplying homes with electricity [1]. According to the World Wind Energy Association (AWEA) report, the demand for wind energy is growing quickly worldwide. The installed capacity of wind turbines in all countries of the world for the year 2021 is approximately 840 GW, with increasing of 97.3 GW compared to the year 2020 [2]. The blade is one of the most important components of the wind turbine, as it is responsible for rotating the generator shaft to produce the power. Wind and gravitational loads are some of the biggest problems a blade faces during its lifetime. For this reason, many researchers investigate how to improve the blade's design and manufacturing material so that it is more resistant to external factors. Wind turbine blade design is essential for obtaining high efficiency, where improving the blade's aerodynamic characteristics is considered the main key.

Rašuo and Bengin [3] used the Genetic Algorithm method to optimize the power production of a single wind turbine by shifting its location in a wind farm to avoid the influence of vortex and free wakes between them. Norouzi and Bozorgian [4] worked on a new system for wind turbines called Wind Thermal Energy Systems (WTES). This system relies on generating thermal energy through simple and light electric brakes at the top of the tower. It depends on the wind in the rotation process, and the energy coefficient reached 62.5%. Yee Win and Thianwiboon [5] used experimental and numerical methods to study the ground effect on the Naca 4412 airfoil in order to optimize the parameters for different angles of attack. Mousavi et al. [6] used OpenFOAM to simulate the Subsonic turbulent flow over the NACA0012 airfoil at various Reynolds numbers. They focused mainly on the transitional and turbulent regions and extracted the velocity and pressure distributions for different angles of attack. Garcia-Ribeiro et al. [7] used the experimental and CFD simulation to investigate the effect of the taper ratio of winglets on the performance of a Horizontal Axis Wind Turbine (HAWT). Bai and Wang [8] investigated the aerodynamic performance of a small HAWT using experimental and numerical methods (CFD and BEM). Maizi et al. [9] applied computational fluid mechanics (CFD) to optimize the shape of Horizontal Axis Wind Turbine (HAWT) NREL with different blade tip ratios. Kaya et al. [10] designed a 0.9 m HAWT blade and optimized the aerodynamic performance using a numerical simulation CFD. Parezanovic et al. [11] applied the CFD, and Xfoil software to optimize the wind turbine blade airfoil by choosing three different types. In their study, the lift and drag coefficients were calculated and compared with the experimental results.

Creating a new wind turbine structure is complicated because of the difficulty of designing and choosing the optimal material. In modern wind turbines, composite materials are selected for their lightweight and high strength/stiffness to withstand the impact. In addition to their increased safety and reliability, as well as being recyclable and environmentally friendly [12]. Due to its extreme importance, many studies are concerned with designing and developing the wind turbine blade structure. Lipian et al. [13] used the experimental and fluid-structure interaction simulation to study a small wind turbine's deformations and stresses of 350 W. Boudounit et al. [14] simulated the offshore wind turbine blade using the finite element method (ABAQUS software) under different wind speeds. A comparison was made between the glass and carbon fiber materials to reduce the turbine weight. Also, they optimized the structure by studying the displacements, and von mises stress to determine the damaged area of the blade using each material. Abdullah et al. [15] studied the dynamic problem of the composite material of the rotating blade and the structure by applying the finite element method. Altmimi et al. [16] optimized the blade of the small wind turbines and studied the aero-structural design. Tüfekci et al. [17] investigated the core and multiple layers of composite materials of DTU-10MW-RWT wind turbine blades. The modal and structural problems were studied by applying the Finite Element Method. The composite blades' mode shapes and natural frequencies were found (edgewise bending, flapwise bending, torsional bending, and coupled the flapwise edgewise). Navadeh et al. [18] used the Finite Element Method (both ABAQUS and ANSYS packages) to analyze the vibrations of the wind turbine blade based on longleaf pine and UD composite skin material. Lagdani et al. [19] compared the results of Vibration for carbon and glass epoxy materials of the wind turbine to obtain the characteristics of the dynamic response under the effect of different ice thicknesses.

This study aims to design a new mathematical model of the small wind turbines of 5 kW, and optimize the aerodynamic characteristics of the new proposed model. This part focused on enhancing the power coefficient and power of wind turbines. The second part of the work investigated the selection process of the optimal material for wind blades to improve the strength and stiffness of the structure. The deformations of the tip and natural frequencies were considered as the criterion to optimize the wind blade. Figure 1 shows the main step developed in this work to optimize the wind turbine blade.

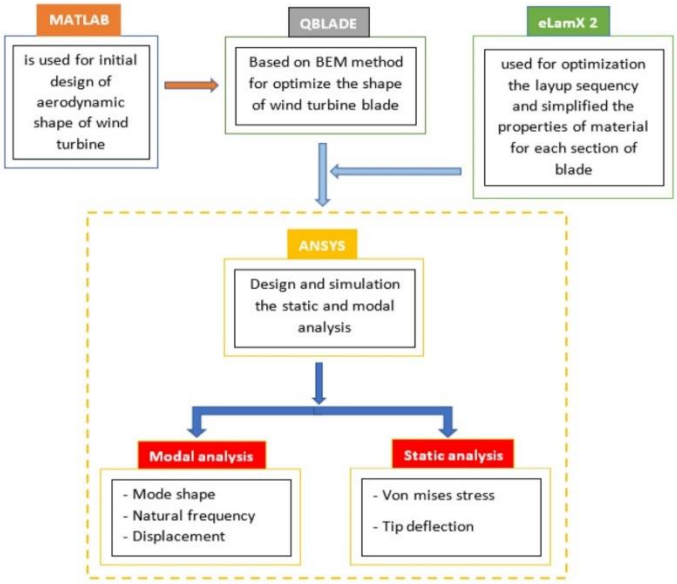

Figure 1. The main steps to optimize small wind turbines.

2. Structural Analysis and Design of the Blade

2.1. Wind Turbine Blade Design

Designing the shape of the wind turbine blade is one of the most complex and important steps in order to manufacture a wind turbine blade. Firstly, the pitch-regulated turbines were selected based on the design of a single airfoil (NACA 4412). This airfoil is well-established, tested, and used for small wind turbine blades [20]. There are many theories to predict aerodynamic performance to calculate the ideal chord length and the optimal twist angle distribution [21]. The simplest model of the ideal concept for wind turbine blade design was developed by Betz [22]. In order to obtain the optimum aerodynamic design of the blade, it was applied the blade element momentum theory (BEM) [8]. Where QBlade software is built based on the BEM theory [23]. This software is used to optimize the shape of the wind blade and determine the aerodynamic loads.

A new code was developed using MATLAB software based on the Betz concept to calculate the parameter of the blade geometry (relative angle (φ), chord length (c), twist angle (θ)). Then, all the parameters are transferred to QBlade software to estimate the load and performance of the blade based on the BEM method. Figure 2 shows the aerodynamic loads for each blade element. BEM theory splits the blade into a finite number of independent sections that are uniformly distributed along the blade's length. A two-dimensional airfoil was used to determine the aerodynamic forces that were generated in each blade section based on a certain radial position. In this work, the blade is divided into 10 sections. The first step in QBlade is to calculate the airfoil's coefficients (lift and drag), where the lift and drag are affected by the Reynolds number (Re) and the angle of attack. Reynolds number is defined as the ratio between the inertial force to the viscous force, which is given by the following equation [21]:

$$Re = \frac{\rho U_{rel} c}{\mu} \tag{1}$$

and

$$U_{rel} = \sqrt{(\Omega R)^2 + \left(U_{design}\right)^2} \tag{2}$$

where μ is the air viscosity, U_{rel} is the relative velocity [m/s], c is the chord length [m], Ω is the rotational speed of the blade [rad/s], R is the blade length [m], and U_{design} is the design wind speed [m/s]. The design parameters of the actual blade are listed in Table 1.

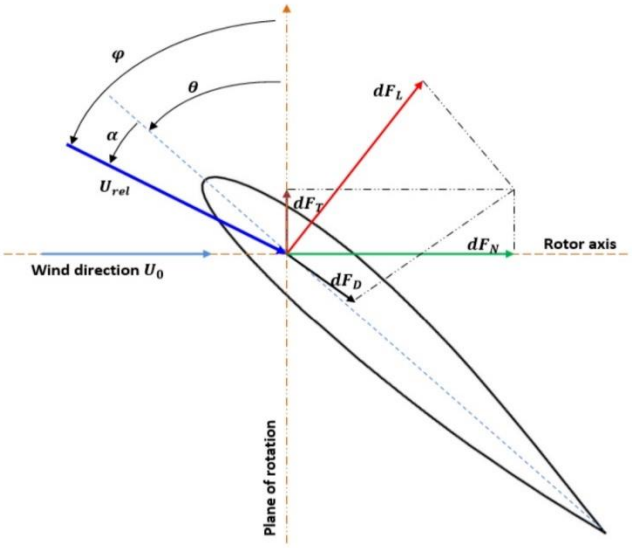

Figure 2. Airfoil section with aerodynamic loads.

Table 1. Initial design parameters of 5 kW small wind turbine.

Design Parameter	Value	Unit
Rated power	5	[kW]
Design Wind speed	10.5	m/s]
Number of blades	3	[-]
Design tip speed ratio	6	[-]
Design angle of attack	6	[°]
Rotor radius	2.5	[m]
Design rotational speed	240	[rpm]
Density of air	1.22	[kg/m^3]
Airfoil type	NACA4412	[-]

According to Equation (1), the Reynolds number changes in terms of the chord (c) and the radius (r). Therefore, it is difficult to determine the initial value to start the calculation process, so it assumed the average value of the Reynolds number to facilitate the calculation process of a 5 kW HAWT with a rotor diameter of 5 m. It was found that the value of Reynolds number is about 450,000 at the tip chord of 0.106 m of the blade. In order to calculate the lift and drag coefficients, the XFoil software was used. Where the XFoil is embedded in QBlade, and the results are shown in Figure 3. The maximum ratio Cl/Cd is 119 at the angle of attack (AOA) which is equal to 6°. This angle is called the design or optimal angle of attack. The lift coefficient at the optimal angle is $Cl_{,design}$ = 1.12. can be used to find the relative angle [21]:

$$\varphi = \left(\frac{2}{3}\right) \tan^{-1}\left(\frac{1}{\lambda_r}\right) \quad (3)$$

and

$$\lambda_r = \lambda_0(r/R) \tag{4}$$

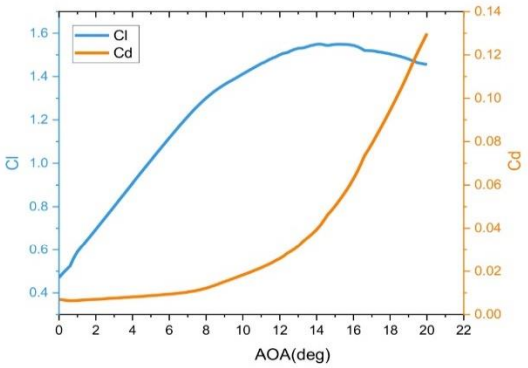

Figure 3. The variation of Lift (*Cl*) and drag (*Cd*) coefficients with the angle of attack.

The chord length in each section can be found as follows,

$$c = \frac{8\pi r}{BC_{l,design}}(1 - \cos\varphi) \tag{5}$$

and the twist angle is,

$$\theta = \varphi - \alpha_{opt} \tag{6}$$

where λ_r is the local speed ratio of the blade, r is the distance from the blade section to the rotor center [m], α_{opt} is the optimal angle of attack, and λ_0 is the design tip speed ratio, which is equal to 6. The 3D distribution of the blade element section, chord length, and twist angle are shown in Figure 4.

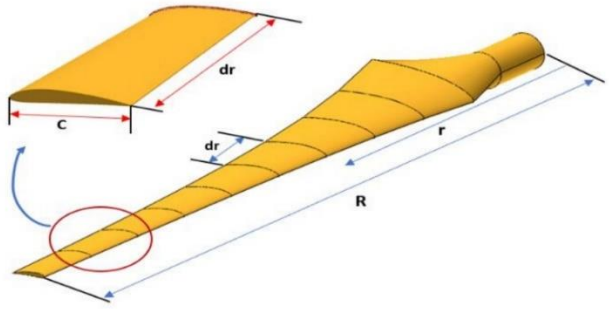

Figure 4. Schematic of blade sections.

2.2. Blade's Material and Lay-Up Sequence

The blades of a small wind turbine are manufactured from several materials; among the most common typical materials are E-glass/epoxy, S-glass/epoxy, carbon/epoxy, braided composite, aluminum, etc. Because of the diversity of materials used to manufacture the wind turbine blade, it was selected in this study the most typical materials to optimize the blade structure. Also, it will optimize the wind blade to reach high stiffness with minimum weight. It will certainly minimize the cost of the wind turbine and improve its performance. Table 2 shows the properties of the three selected materials used to optimize the wind turbine blade [24,25].

Table 2. Material properties of wind turbine blade.

Material	E-Glass/Epoxy [24]	Carbon/Epoxy [24]	Braided Composite [24,25]
E_1 (GPa)	48.7	136.7	62.8
E_2 (GPa)	16.8	8.2	62.8
G_{12} (GPa)	5.83	4.45	9.68
G_{23} (GPa)	6	2.91	7.97
v_{12}	0.28	0.29	0.33
v_{23}	0.20	0.42	0.40
X_T (MPa)	1170	1604	460
X_C (MPa)	977	1305	420.4
Y_T (MPa)	30.5	40.5	526.2
Y_C (MPa)	114	239.7	420.4
ρ(kg/m^3)	2000	1518	1800

The blade of a small wind turbine consists of four basic parts: the root, the neck, the shell, and the shear web. Each part of the blade has a different layer thickness and fiber orientation. Determining proper fiber orientation and laminate thickness is significant in decreasing the difficulties of manufacturing and increasing the structural stiffness. The lay-up sequence, orientation, and laminate thickness are optimized for the selected composite materials. Table 3 presents the layers sequence of the blade, and Figure 5 shows the 3D model of wind turbine blade materials. Where each section is marked with diffident color. These colors reflect the difference in the thickness and fiber orientation of the composite material (Table 3).

Table 3. The lay-up sequence of 2.5 m small wind turbine.

Section Name	Location (m)	Shell Layup	Thickness (m)	Shear Web Lay-Up	Thickness (m)
1	0.200–0.400	[(±45)3/08/(±45)]s	0.0064	[(±45)3/09/(±45)]s	0.0070
2	0.400–0.600	[(±45)3/07/(±45)]s	0.0058	[(±45)3/08/(±45)]s	0.0064
3	0.600–0.811	[(±45)3/06/(±45)]s	0.0052	[(±45)3/07/(±45)]s	0.0058
4	0.811–1.022	[(±45)2/06/(±45)]s	0.0048	[(±45)3/06/(±45)]s	0.0052
5	1.022–1.233	[(±45)2/05/(±45)]s	0.0042	[(±45)2/06/(±45)]s	0.0048
6	1.233–1.444	[(±45)2/04/(±45)]s	0.0036	[(±45)2/05/(±45)]s	0.0042
7	1.444–1.655	[(±45)2/03/(±45)]s	0.0030	[(±45)2/04/(±45)]s	0.0036
8	1.655–1.866	[(±45)2/02/(±45)]s	0.0024	[(±45)2/03/(±45)]s	0.0030
9	1.866–2.077	[(±45)/02/(±45)]s	0.0020	[(±45)2/02/(±45)]s	0.0024
10	2.077–2.288	[(±45)/01/(±45)]s	0.0014	[(±45)/02/(±45)]s	0.0020
11	2.288–2.500	[(±45)/01/(±45)]	0.0007	[(±45)/01/(±45)]s	0.0014

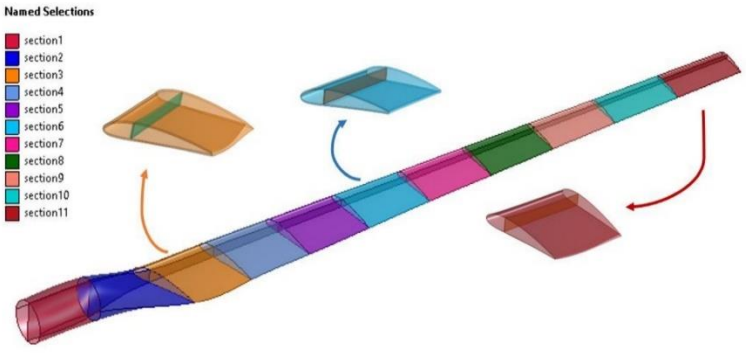

Figure 5. 3D model of the composite blade with 10 sections.

2.3. Finite Element Analysis of Steady-State Problem

The finite element model of the wind turbine blade was created using the Ansys software to study the steady-state structural problem. This simulation aims to select the most optimal material for the wind turbine blade under the aerodynamic loads. The output results of this analysis present the tip deflection, von-mises stress, and deformation. Computational fluid dynamics (CFD) was used (Ansys software) to calculate the aerodynamic loads, but this analysis requires a high-performance computer and consumes time [26]. Therefore, using the QBlade software based on BEM theory to calculate the aerodynamic loads can save time and effort. Table 4 presents the results of the applied loads on the wind turbine blade.

Table 4. The normal and tangential loads applied in the FE model.

$Z\ (m)$	$\Delta Z\ (m)$	$F_T(N/m)$	$F_N(N/m)$
0.200	0.200	−1.535	2.930
0.400	0.200	−4.415	8.825
0.600	0.200	27.610	57.455
0.811	0.211	38.052	81.014
1.022	0.211	36.047	93.246
1.233	0.211	35.260	106.279
1.444	0.211	34.701	120.023
1.655	0.211	34.492	134.815
1.866	0.211	33.881	147.971
2.077	0.211	32.781	161.331
2.288	0.211	29.654	172.156
2.500	0.212	9.8160	81.7452

2.4. Boundary Conditions

The blade of the wind turbine is fixed at the root side, so it was considered that all degrees of freedom (DOF) are null at the root, and on the tip, the blade is free to move. The blade rotates at a constant rotational speed during the analysis. The applied pressure is distributed over the shell of the blade. But the loads were calculated by the BEM theory applied at the center of the loads for each section of the blade. It was considered the force of gravity in the center of gravity of the blade mass. The loads and boundary conditions that are applied to the wind blade are shown in Figure 6.

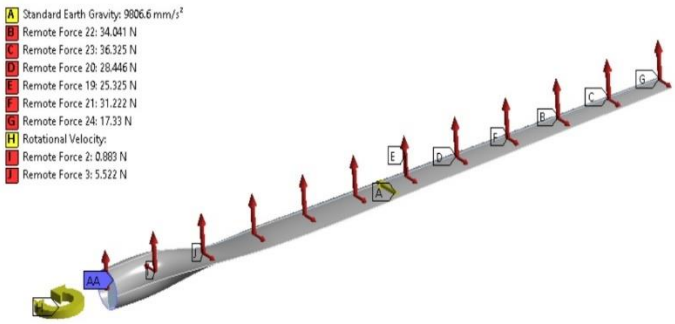

Figure 6. Boundary conditions and applied loads.

2.5. FE Modeling of Wind Blade

During the operation of the wind turbine blade, it is subjected to several loads, which leads to occur the bending and deflection of the blade. In order to simulate the wind turbine blade, the appropriate mesh should be chosen to match the geometry and material composition. In this study, it was selected the element (shell 281) to build the FE model. This element has eight nodes, and each node has six DOF. The Grid Independence Test was achieved to find the wind turbine blade's most optimal mesh, as shown in Table 5. Figure 7 shows the most optimal mesh of the wind blade.

Table 5. The mesh convergence of wind turbine blade.

Mesh Segments	No. Nodes	No. Elements	Max. Total Deflection [mm]	Difference
1	19,824	3694	18.392	-
2	26,722	7431	18.371	−0.021
3	34,624	11,385	18.365	−0.006
4	45,857	15,124	18.361	−0.004
5	74,154	24,475	18.356	−0.005
6	108,789	35,970	18.354	−0.002
7	225,602	75,053	18.358	0.004

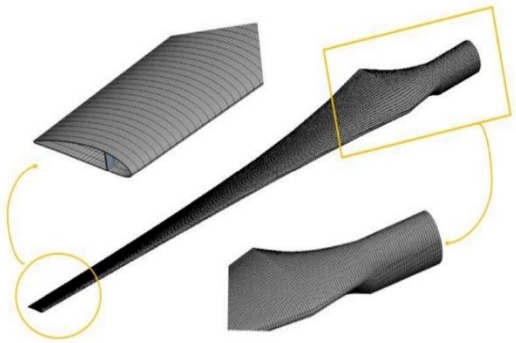

Figure 7. FE model wind turbine mesh.

2.6. The FE Formulation

The finite element can be applied to solve the modal analysis problem using the following equation to determine the steady-state response of wind turbine blades [27,28]:

$$[K]\{u\} = \{F\} \tag{7}$$

where $\{F\}$ is load vector, $\{u\}$ is displacement vectors, and $[K]$ is the stiffness matrix of the system. In Equation (7), it was assumed that the inertia forces and damping forces are equal to zero. Suppose a structure is placed in a suitable position at a zero moment in time, where the structure can be vibrated. This Vibration is known as the natural frequency, and this frequency follows certain patterns known as distortion patterns called mode shapes. The mode shapes and Vibration of the structure depend on mass and stiffness [27]. Assuming that the external force vector and the damping are zero, where the free vibration equation can be written as [28]:

$$[M]\{\ddot{u}\} + [K]\{u\} = 0 \tag{8}$$

where $[M]$ is the mass matrix, $\{\ddot{u}\}$ is the acceleration vector. Equation (8) is the equation of motion of the undamped free vibration system. In order to solve the last equation, the harmonic solution is assumed in the following form:

$$\{u\} = \{\varnothing\} \sin \omega t \tag{9}$$

where ω is the natural angular frequency of mode and $\{\varnothing\}$ is the vector of contractual amplitude for mode shapes. After deriving the displacement in Equation (9) twice with respect to time, it can be got the following:

$$\{\ddot{u}\} = -\omega^2 \{\varnothing\} \sin \omega t \tag{10}$$

Substitute Equations (9) and (10) into Equation (8) to get the following formula:

$$\left([K] - \omega^2 [M]\right) \{\varnothing\} = 0 \tag{11}$$

Equation (11) is the form of the eigenvalue problem (structural Vibration). It is a set of homogeneous algebraic equations for the eigenvector components. The eigenvalue problem can be written as follows:

$$([A] - \lambda [I])\, X = 0 \tag{12}$$

where $[A]$ is a symmetric matrix or dynamic matrix, λ is the value of eigenvalue, $[I]$ is an identity matrix, and X is an eigenvector. By substituting Equation (11) into Equation (12) by entering one of the two matrices $[K]$ or $[M]$, and then using the Cholisky method (square root method), it can be obtained the dynamic response [27].

3. Results and Discussions

The main target of the optimization process of the wind turbine blade is to find the most optimal design to obtain the maximum power. The Betz method (BEMT) was used to design the primary chord and the twist angle of the blade, but one of the disadvantages of this method it's does not adopt the linear design of the chord and the twist angle. This analysis should be optimized the wind blade according to the linearization approach. Figure 8 shows the initial and the final optimum blade design.

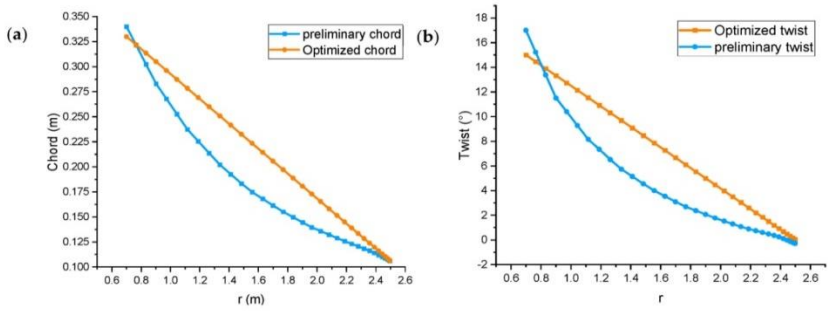

Figure 8. Blade distribution (**a**) chord Length and (**b**) twist angle.

Figure 8 shows the difference between the initial design based on the Betz theory (BEM), which is a parabolic curve, and the new design (improved). The improved design is based on the linearization design, where it is a straight line from the root to the tip for both the chord and the twist angle. Figure 9 shows the initial and optimized wind turbine design's power coefficient and power curve.

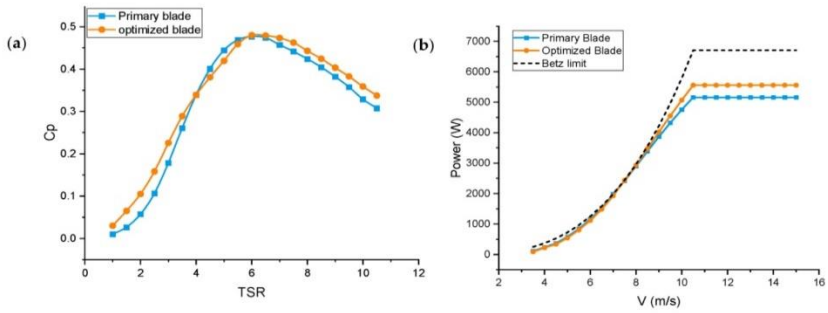

Figure 9. (**a**) power coefficient with tip speed ratio, (**b**) Power output with wind speed.

It can be noticed from Figure 9 that there is an increase in the power coefficient of the improved design. Where the power coefficient increased at the low TSR from 1 to 4 and is close to the initial design at the medium values of TSR. Later on, the power coefficient decreased for the TSR values greater than 6. This means that the improved design increased the power coefficient at low and high rotational speeds with an average increase of up to 8%. According to the obtained results in Figure 9, it can be concluded that the effect of improving the design to increase the power of the wind turbine is evident at the medium wind speed that starts from 8 m/s, and the improvement in the power at the rated wind speed is 7% compared with the initial design.

The steady-state finite element model was used to determine the variation of blade tip deflection and the Von Mises stresses of the wind blade using three different materials to find the most optimal material (with minimum tip deflection). Also, the zones of stress concentration of the blade structure can be determined, and the structure's strength can be improved to obtain an optimal wind blade. Figure 10 shows the distribution of Von-Mises stresses of the wind blade using the proposed materials. Figure 11 shows the distribution of deflection (tip deflection) of the wind turbine blade using different materials.

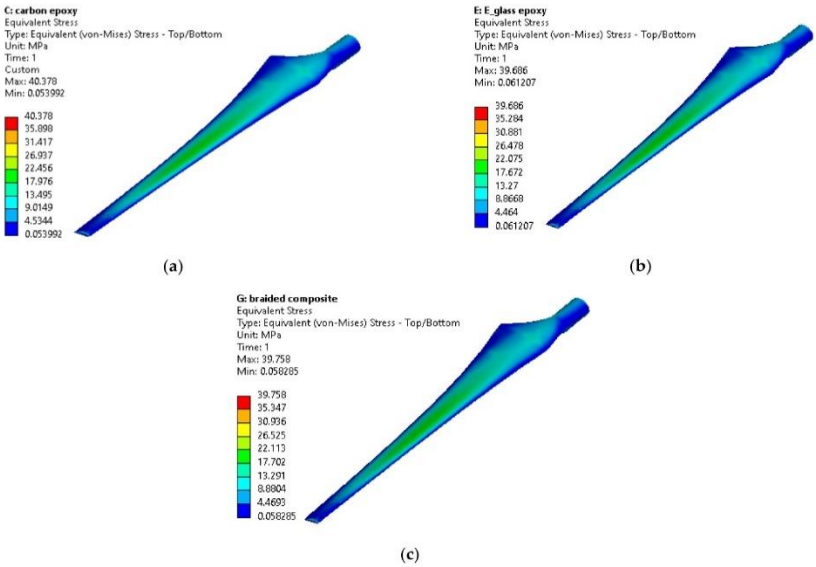

Figure 10. Distribution of Von Mises stresses of (**a**) carbon/epoxy, (**b**) E-glass/epoxy, and (**c**) Braided composite.

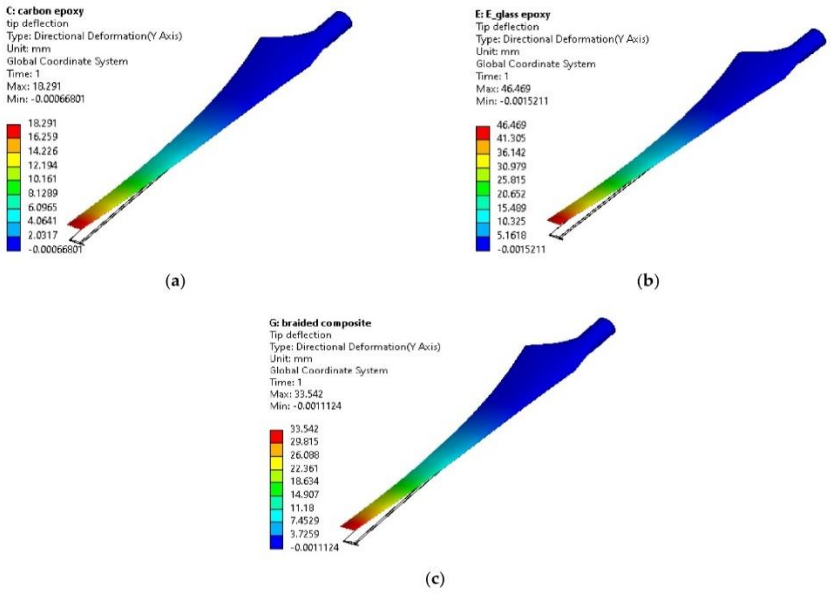

Figure 11. Tip deflections of (**a**) carbon/epoxy, (**b**) E-glass/epoxy, and (**c**) Braided composite.

In order to verify the selected approach to analyze the blade of a wind turbine, the comparations between the results of QBlade software and ANSYS software were made to determine the tip deflection and Von-Mises stresses. High agreement was found between the results of QBlade software and ANSYS software, as shown in Table 6.

Table 6. The tip deflections and von mises stress using different materials.

	E-Glass/Epoxy			Braided Composite			Carbon/Epoxy		
	QBlade	**ANSYS**	**Difference %**	**QBlade**	**ANSYS**	**Difference %**	**QBlade**	**ANSYS**	**Difference %**
Von mises stress [MPa]	38.51	39.68	2.94	39.20	39.75	1.38	39.96	40.37	1.015
Tip deflection [mm]	43.20	46.46	7.016	29.32	33.54	6.61	16.86	18.29	7.81

According to the results of Figure 11, it can be seen that the blade bends in the direction of the lift forces due to the low pressure on this side. The Von-Mises stresses for glass fibers and carbon fibers are 39.68 MPa and 40.37 MPa, respectively. Where they are greater than the Von-Mises stresses for the braided composite material (39.75 MPa). It can be noticed that the maximum stresses are concentrated in the middle of the wind turbine blade length, and this indicates that the distribution of the fibers and the thickness is suitable for the structure. Regarding the tip deflection, Figure 11 shows a noticeable difference between the three blades that used different materials. The carbon fiber deflection was 18.29 mm, the glass fiber deflection was 46.46 mm, and the Braided composite deflection was 33.54 mm. However, these results for all cases remain acceptable, where the given distance between the tower and the tip of the blade is about 400 mm, which makes the three materials usable. But the low cost of E-glass compared to the other two materials makes it the most suitable material to manufacture the wind blade. Figure 12 shows the variations of blade deflections and Von-Mises stresses along the blade length, respectively. Figure 13 illustrates the distributions of mass along the blade length and the stiffness distribution using the three different materials under the same working condition.

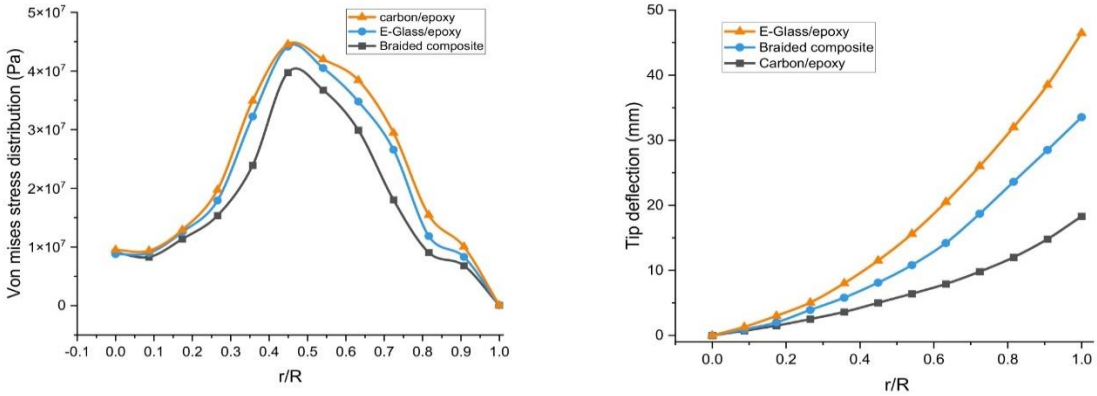

(**a**) (**b**)

Figure 12. Variations of (**a**) Von mises stress and (**b**) tip deflection along the blade.

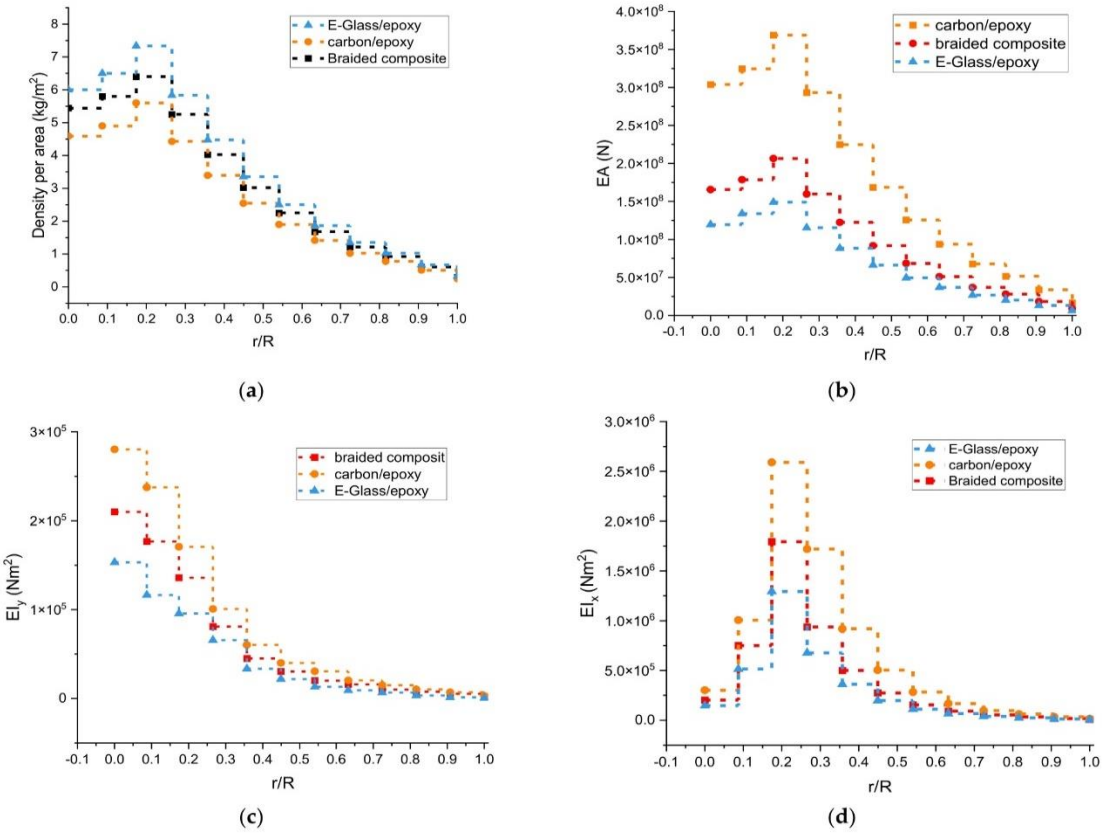

(**a**) (**b**)

(**c**) (**d**)

Figure 13. Distributions of (**a**) the density, (**b**) longitudinal stiffness, (**c**) Flapwise Stiffness, and (**d**) Edgewise Stiffness along the blade.

Based on the results of Figure 12, it can be seen that the largest value of the stresses occurred at $r/R = 0.5$, i.e., in the middle of the blade. This is accrued because the thickness distribution of the shell at the root is appropriate. This causes the stress concentration in the middle of the blade, i.e., in the area of least damage and risk. While results of Figure 12b showed that the largest deflection occurred for E-glass material, followed by braided composite material, and then carbon epoxy material. Figure 13 shows the wind turbine blade's distributions of mass and stiffness. It is clear that this distribution was linear, thicker on the root side and less thick on the tip side. This makes it a suitable distribution for the composite materials layers along the length of the blade.

The main objective of studying the dynamic problem of the wind blade is to determine the compatibility of the aerodynamic shape design with the structure of the blade or the status of mass distribution/stiffness that is appropriate along the length of the blade. The optimal mesh was selected depending on the mesh of the steady-state analysis, as shown in Figure 7. Figure 14 presents the natural frequencies and the displacements of the wind turbine blade for the first 6th mode shapes using the selected materials, respectively. Figures 15–17 show the first 6th mode shapes of the wind turbine blade using the selected materials. It A comparison was made between the results of Ansys software and QBlade to find the frequencies for different materials, as shown in Table 7.

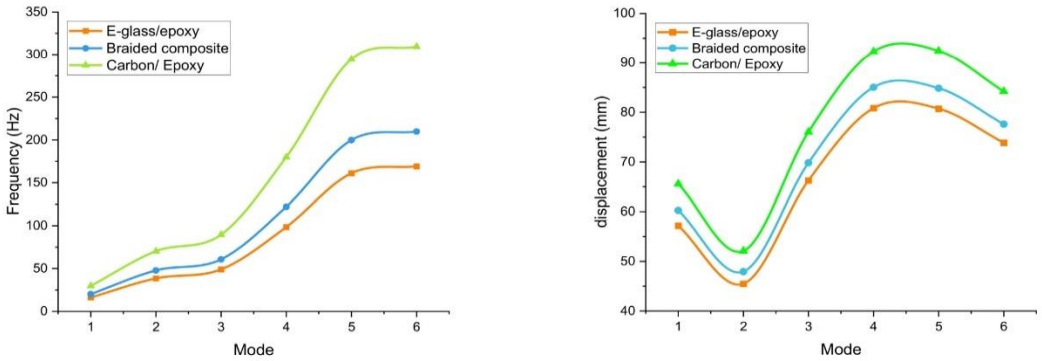

Figure 14. The variation of (**a**) natural frequency and (**b**) displacement with modes.

The wind turbine blade's structural stiffness depends on the materials' properties, especially Young's modulus (E) and the density (ρ). Therefore, the natural frequencies of the wind turbine structure depend basically on the ratio ($\sqrt{E/\rho}$). According to the results of the modal analysis of the wind turbine blade in Figure 14a, it's observed that the frequencies of the E-glass fiber material were less than those of braided composite and carbon epoxy materials, which made it less resistant to vibrations. Despite this, the braided composite and E-glass material results are not considered far away due to the convergence of their ratio ($\sqrt{E/\rho}$). While the carbon/epoxy material has the highest natural frequencies compared with the other materials because it has the highest ratio of ($\sqrt{E/\rho}$). Figure 14b shows the displacements of the blade tip at the selected modes shape of the three proposed materials. It can be seen that the carbon/epoxy material had the least displacement, due to the high stiffness of the material, followed by the braided composite material and then the E-glass/epoxy material. Also, it can be noticed that the highest value of the displacement occurred in the 4th and 5th modes, which makes them the two critical/dangerous modes for blade design.

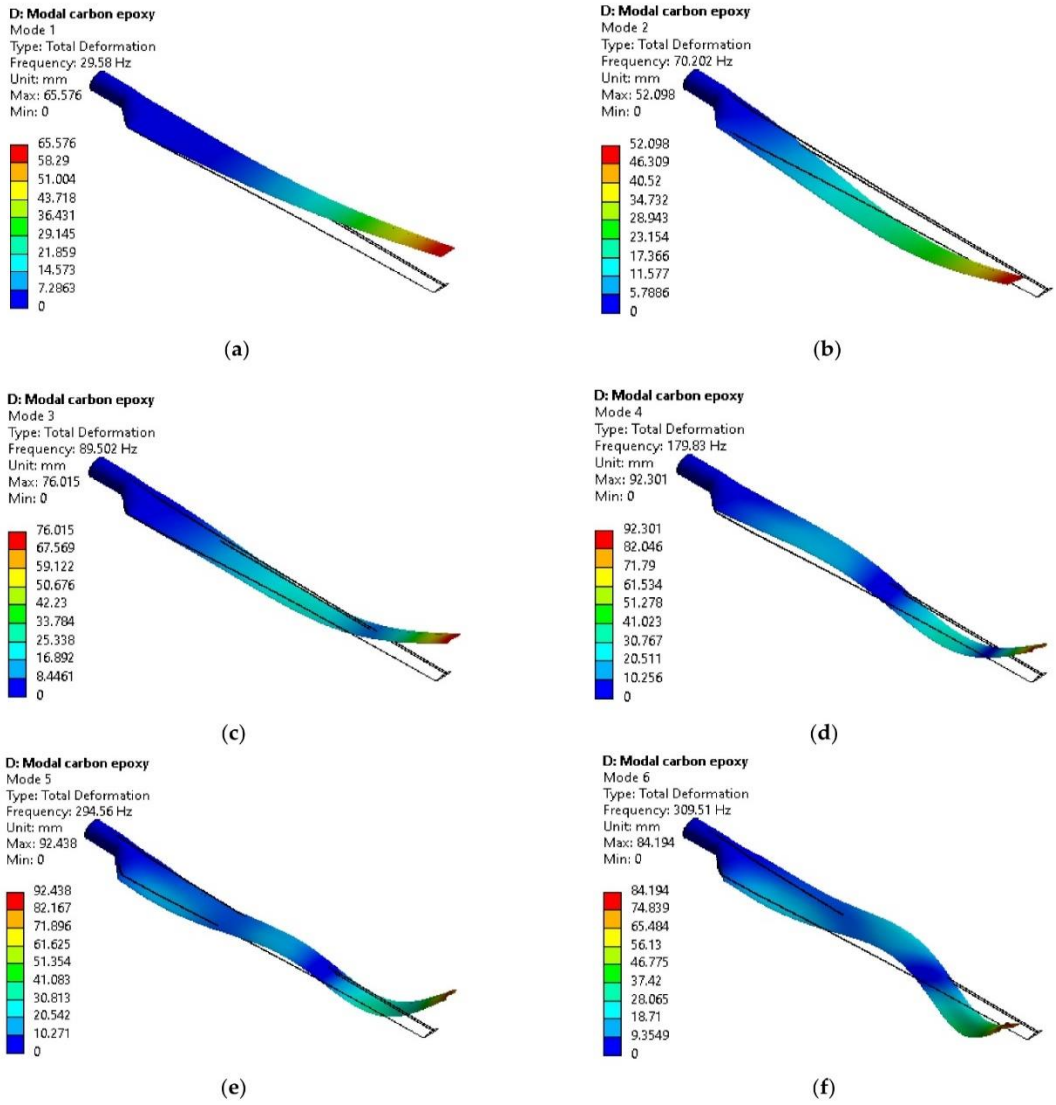

Figure 15. The first 6th mode shape of Carbon/Epoxy material. (**a**) 1st mode. (**b**) 2nd mode. (**c**) 3rd mode. (**d**) 4th mode. (**e**) 5th mode. (**f**) 6th mode.

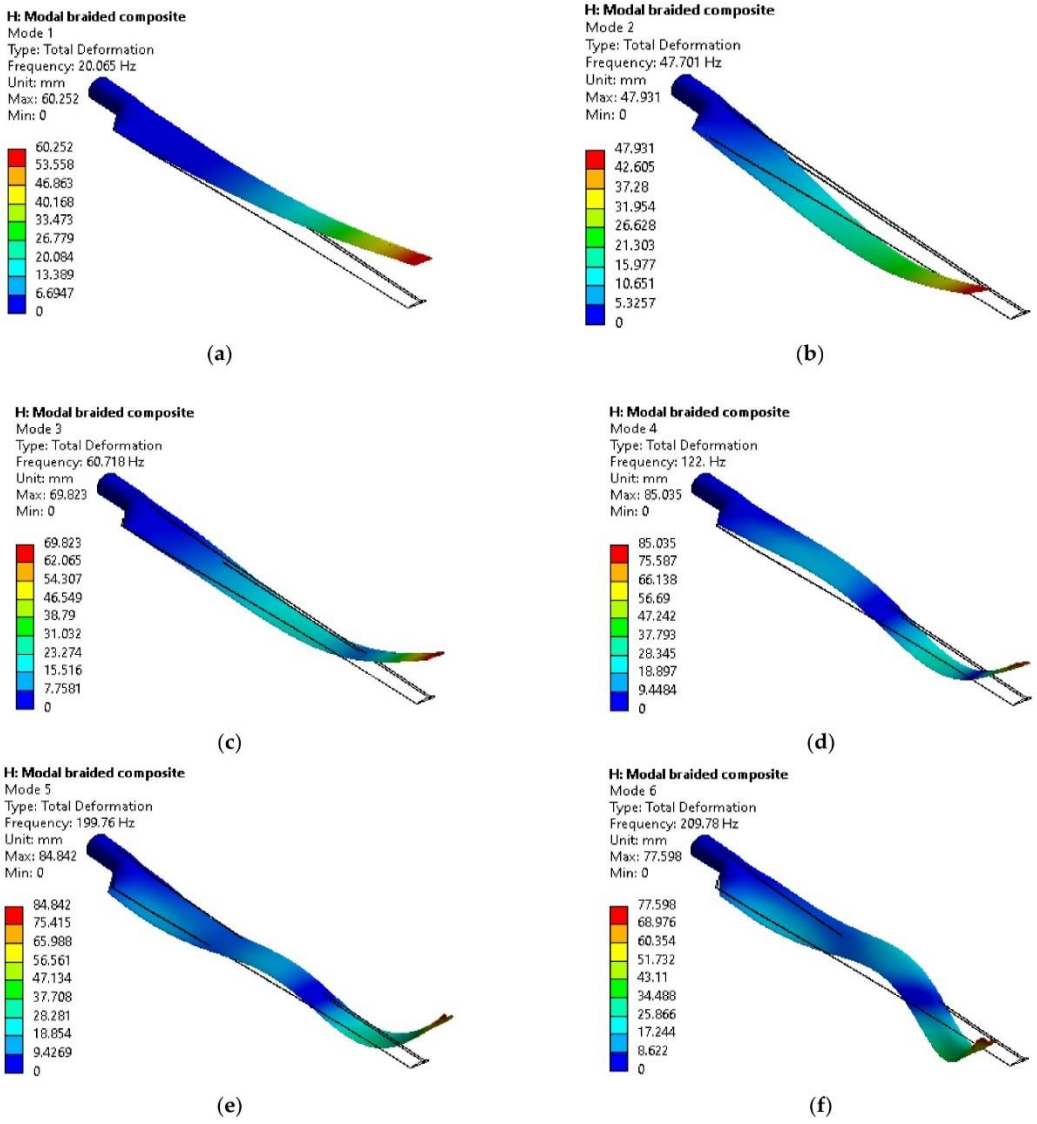

Figure 16. The first 6th mode shape of Braided composite material. (**a**) 1st mode. (**b**) 2nd mode. (**c**) 3rd mode. (**d**) 4th mode. (**e**) 5th mode. (**f**) 6th mode.

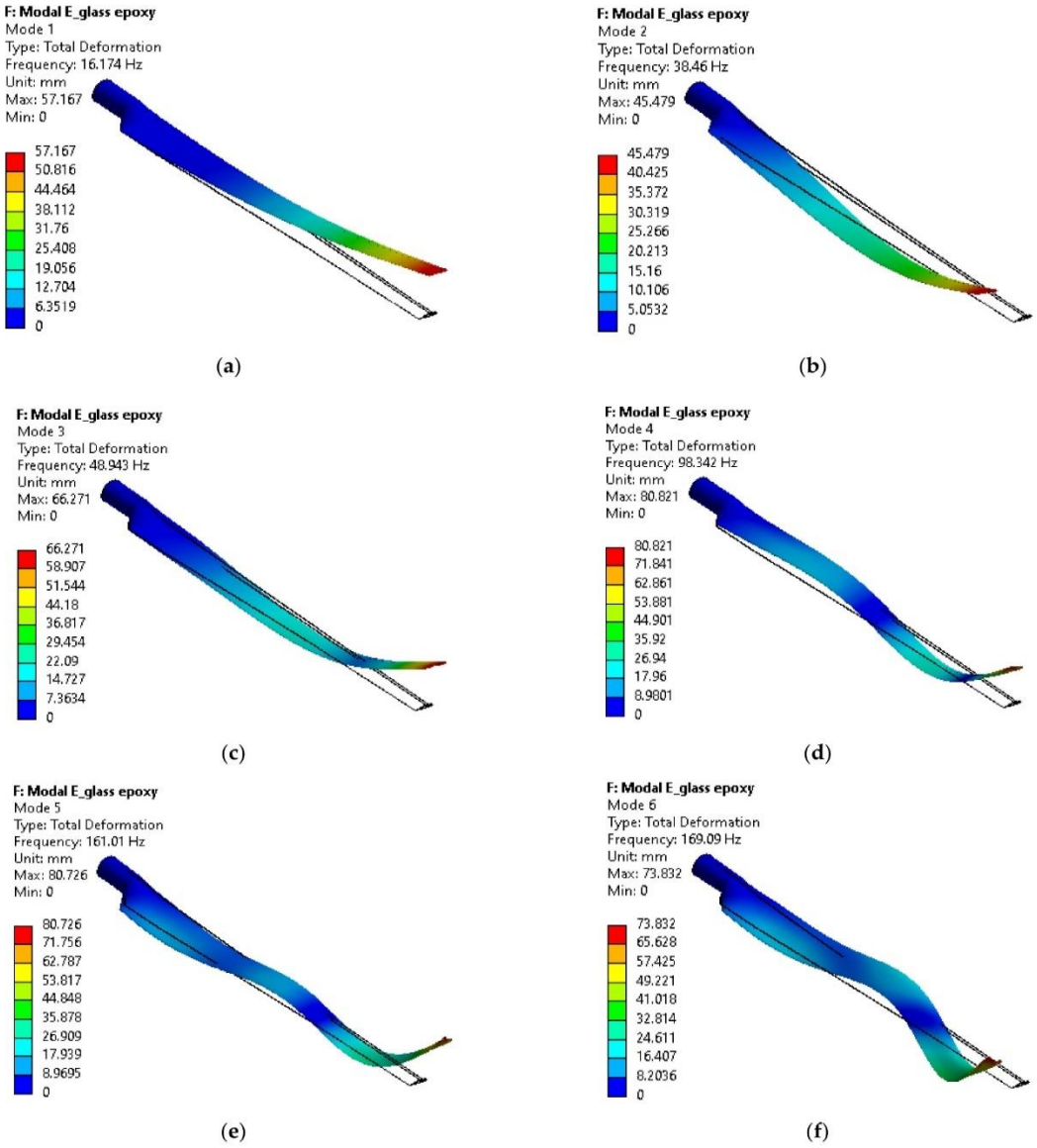

Figure 17. The first 6th mode shape of E-glass/epoxy material. (**a**) 1st mode. (**b**) 2nd mode. (**c**) 3rd mode. (**d**) 4th mode. (**e**) 5th mode. (**f**) 6th mode.

Table 7. The comparison of Frequencies using different materials.

Mode	E-glass/Epoxy			Braided Composite			Carbon/Epoxy		
	QBlade	ANSYS	Difference %	QBlade	ANSYS	Difference %	QBlade	ANSYS	Difference %
1	15.13	16.17	6.43	19.80	20.06	1.30	28.29	29.58	4.36
2	36.19	38.46	5.90	48.32	47.70	1.30	74.11	70.20	5.57
3	45.39	48.94	7.25	63.41	60.71	4.45	92.20	89.50	3.02
4	99.56	98.34	1.24	130.59	122	7.04	185.14	179.83	2.95
5	165.82	161.01	2.99	196.43	199.76	1.67	289.23	294.56	1.81
6	172.93	169.09	2.27	221.15	209.78	5.42	315.67	309.51	1.99

4. Conclusions and Future Work

In this study, a new model design of a small wind turbine (5 kW) was built from scratch. The main aim is to improve wind turbine aerodynamic characteristics and find the blade model's most optimal design parameters. It enhanced the power coefficient, reaching the value of 0.47 when TSR was equal to 6 for the optimal design. In other words, the efficiency increased by 8% compared to the initial design. At the same time, the power of the optimized wind turbine increased by 7% at rated wind speeds. A new finite element model was built for a small wind turbine blade of 5 kW based on the optimized wind turbine blade design. The steady-state and modal problems solutions were found to obtain the optimal material for the wind blade.

Further, it was found that the minimum tip deflections were 18.29 mm, 33.54 mm, and 46.46 mm, corresponding to the blade being made of carbon fiber material, Braided composite, and E-glass material, respectively. Hence, it can be concluded that the optimal material in terms of the magnitude of deflection is carbon fiber material. The modal analysis results showed that the natural frequencies of wind blade made from E-glass has the lowest natural frequencies (1st: 16.17 Hz and 2nd: 38.46 Hz). On the other hand, the wind blade made of carbon fiber has the largest natural frequencies (1st: 29.58 Hz and 2nd: 70.20 Hz).

In future works, some important problems should be investigated deeply. Fatigue is one of the main failure problems of wind turbine blades during operating periods, especially when it has a crack in the structure [29]. So, it's necessary to study the fatigue of the wind turbine using different materials under normal and extreme operating conditions. In recent research, nanotechnology has been adopted to improve composite materials [30]. This composite material can be applied to small wind turbines to enhance their efficiency. The other problem of wind turbines that should be investigated is the annoying sounds and noise during rotation in order to reduce it.

The climate of the locations of wind turbines varies from one site to another, from very hot to very cold. Thus, the study of the influence of climate on the dynamic characteristics of the wind turbine blade [31] is considered an essential issue as well.

Author Contributions: Formal analysis, investigation, writing—review and editing, K.D.; methodology, resources, M.T.G. and H.S.S.; resources, funding acquisition, writing—review and editing, A.N.J.A.-T. and A.M.A.; writing—review and editing, supervision, O.I.A.; writing—review and editing, H.M. and A.B. All authors have read and agreed to the published version of the manuscript.

Funding: This research received no external funding.

Institutional Review Board Statement: Not applicable.

Informed Consent Statement: Not applicable.

Data Availability Statement: The study did not report any data.

Acknowledgments: The authors acknowledge the "System Technologies and Engineering Design Methodology"—Hamburg University of Technology for supporting research and providing facilities.

Conflicts of Interest: The authors declare no conflict of interest.

Nomenclature

c	Chord length
C_P	Power coefficient
Re	Reynolds number
U_{rel}	Relative velocity
U_{design}	Design wind speed
r	Local radius
R	Wind turbine radius
$C_{l,design}$	Design lift coefficient
B	Number of blades
F_T	Tangential load
F_N	Normal load
$\{F\}$	Load vector
$\{u\}$	Displacement vectors
[K]	Stiffness matrix
[M]	Mass matrix
$\{\ddot{u}\}$	Acceleration
[A]	dynamic matrix
$[I]$	Identity matrix
X	eigenvector
E	Young's modulus
Greek symbols	
θ	Twist angel
$\{\varnothing\}$	Reynolds or turbulent stress
μ	viscosity
ω	angular natural frequency
ρ	Air density
α_{opt}	Optimal angel of attack
λ_r	Local speed ratio
λ_0	Design tip speed ratio
φ	Relative angle
Ω	Rotational speed
Superscripts	
WWEA	World wind energy association
GWEC	Global wind energy council
AEP	Annual energy production
FEM	Finite element method
UD	Unidirectional
BEM	blade element momentum
AoA	Angle of Attack
DOF	degrees of freedom
HAWT	Horizontal axis wind turbine
CFD	computational fluid dynamics

References

1. Rosato, M.A. *Small Wind Turbines for Electricity and Irrigation: Design and Construction*; CRC Press: New York, NY, USA, 2018.
2. WWEA. World Wind Energy Association. Available online: https://wwindea.org/information-2/statistics-news/ (accessed on 24 March 2022).
3. Rašuo, B.P.; Bengin, A.Č. Optimization of wind farm layout. *FME Trans.* **2010**, *38*, 107–114.
4. Norouzi, N.; Bozorgian, A. A Wind-Thermal System Design Based on an Energetic and Exergetic Approch. *Iran. J. Chem. Chem. Eng.* **2022**. [CrossRef]
5. Win, S.Y.; Thianwiboon, M. Parametric optimization of NACA 4412 airfoil in ground effect using full factorial design of experiment. *Eng. J.* **2021**, *25*, 9–19.
6. Mousavi, S.M.; Shafiei, N.; Dadvand, A. Numerical simulation of subsonic turbulent flow over NACA0012 airfoil: Evaluation of turbulence models. *Sigma J. Eng. Nat. Sci.* **2017**, *35*, 133–155.

7. Garcia-Ribeiro, D.; Flores-Mezarina, J.A.; Bravo-Mosquera, P.D.; Cerón-Muñoz, H.D. Parametric CFD analysis of the taper ratio effects of a winglet on the performance of a Horizontal Axis Wind Turbine. *Sustain. Energy Technol. Assess.* **2021**, *47*, 101489. [CrossRef]
8. Bai, C.-J.; Wang, W.-C. Review of computational and experimental approaches to analysis of aerodynamic performance in horizontal-axis wind turbines (HAWTs). *Renew. Sustain. Energy Rev.* **2016**, *63*, 506–519. [CrossRef]
9. Maizi, M.; Mohamed, M.; Dizene, R.; Mihoubi, M. Noise reduction of a horizontal wind turbine using different blade shapes. *Renew. Energy* **2018**, *117*, 242–256. [CrossRef]
10. Kaya, M.N.; Kose, F.; Ingham, D.; Ma, L.; Pourkashanian, M. Aerodynamic performance of a horizontal axis wind turbine with forward and backward swept blades. *J. Wind. Eng. Ind. Aerodyn.* **2018**, *176*, 166–173. [CrossRef]
11. Parezanovic, V.; Rasuo, B.; Adzic, M. Design of airfoils for wind turbine blades. In Proceedings of the French-Serbian European Summer University: Renewable Energy Sources and Environment-Multidisciplinary Aspect, Vrnjacka Banja, Serbia, 17–24 October 2006.
12. Song, F.; Ni, Y.; Tan, Z. Optimization design, modeling and dynamic analysis for composite wind turbine blade. *Procedia Eng.* **2011**, *16*, 369–375. [CrossRef]
13. Lipian, M.; Czapski, P.; Obidowski, D. Fluid–structure interaction numerical analysis of a small, urban wind turbine blade. *Energies* **2020**, *13*, 1832. [CrossRef]
14. Boudounit, H.; Tarfaoui, M.; Saifaoui, D.; Nachtane, M. Structural analysis of offshore wind turbine blades using finite element method. *Wind Eng.* **2020**, *44*, 168–180. [CrossRef]
15. Wu, W.H.; Young, W.B. Structural analysis and design of the composite wind turbine blade. *Appl. Compos. Mater.* **2012**, *19*, 247–257. [CrossRef]
16. Pourrajabian, A.; Afshar, P.A.N.; Ahmadizadeh, M.; Wood, D. Aero-structural design and optimization of a small wind turbine blade. *Renew. Energy* **2016**, *87*, 837–848. [CrossRef]
17. Tüfekci, M.; Genel, Ö.E.; Tatar, A.; Tüfekci, E. Dynamic Analysis of Composite Wind Turbine Blades as Beams: An Analytical and Numerical Study. *Vibration* **2021**, *4*, 1–15. [CrossRef]
18. Navadeh, N.; Goroshko, I.; Zhuk, Y.; Etminan Moghadam, F.; Soleiman Fallah, A. Finite Element Analysis of Wind Turbine Blade Vibrations. *Vibration* **2021**, *4*, 310–322. [CrossRef]
19. Lagdani, O.; Tarfaoui, M.; Nachtane, M.; Trihi, M.; Laaouidi, H. Modal analysis of an iced offshore composite wind turbine blade. *Wind Eng.* **2022**, *46*, 134–149. [CrossRef]
20. Puterbaugh, M.; Beyene, A. Parametric dependence of a morphing wind turbine blade on material elasticity. *Energy* **2011**, *36*, 466–474. [CrossRef]
21. Alkhabbaz, A.; Yang, H.-S.; Weerakoon, A.S.; Lee, Y.-H. A novel linearization approach of chord and twist angle distribution for 10 kW horizontal axis wind turbine. *Renew. Energy* **2021**, *178*, 1398–1420. [CrossRef]
22. Gupta, M.K.; Subbarao, P. Design and Performance Analysis of Hydrokinetic Turbine with Aerodynamic Stall Model. In *Advances in Thermofluids and Renewable Energy*; Springer: Singapore, 2021; pp. 221–231.
23. Marten, D.; Wendler, J. *QBlade Guidelines v0.6*; TU Berlin: Berlin, Germany, 2013.
24. Zhou, S.; Wu, X. Fatigue life prediction of composite laminates by fatigue master curves. *J. Mater. Res.* **2019**, *8*, 6094–6105. [CrossRef]
25. Gao, X.; Yuan, L.; Fu, Y.; Yao, X.; Yang, H. Prediction of mechanical properties on 3D braided composites with void defects. *Compos. Part B Eng.* **2020**, *197*, 108164. [CrossRef]
26. Pagano, A. Aerodynamic Analyses of Tiltrotor Morphing Blades. In *Morphing Wing Technologies*; Elsevier: Amsterdam, The Netherlands, 2018; pp. 799–839. [CrossRef]
27. Zuheir, S.; Abdullah, O.I.; Al-Maliki, M. Stress and vibration analyses of the wind turbine blade (A NREL 5MW). *J. Mech. Eng. Res. Dev.* **2019**, *42*, 14–19. [CrossRef]
28. Garinis, D.; Dinulović, M.; Rašuo, B. Dynamic analysis of modified composite helicopter blade. *FME Trans.* **2012**, *40*, 63–68.
29. Abdullah, O.I. A finite element analysis for the damaged rotating composite blade. *Al-Khwarizmi Eng. J.* **2011**, *7*, 56–75.
30. Miau, J.-J.; Li, S.-R.; Tsai, Z.-X.; Van Phung, M.; Lin, S.-Y. On the aerodynamic flow around a cyclist model at the hoods position. *J. Vis.* **2019**, *23*, 35–47. [CrossRef]
31. Abdullah, O. Vibration analysis of rotating pre-twisted cantilever plate by using the finite element method. *J. Eng.* **2009**, *15*, 3492–3505.

Int. J. Renew. Energy Dev. 2023, 12(1), 193-202

Contents list available at IJRED website

International Journal of Renewable Energy Development

Journal homepage: https://ijred.undip.ac.id

Research Article

An investigation of the Steady-State and Fatigue Problems of a Small Wind Turbine Blade Based on the Interactive Design Approach

Khalil Deghoum[1,2], Mohammed T. Gherbi[2], Muhsin J. Jweeg[3], Hakim S. Sultan[4], Azher M. Abed[5], Oday I. Abdullah[6,7,8*], Necib Djilani[2]

[1]*UDERZA Laboratory, University of El Oued, 39000 El Oued, Algeria*

[2]*Department of Mechanical Engineering, University of El Oued, 39000 El Oued, Algeria*

[3]*College of Technical Engineering, Al-Farahidi University, Baghdad 10005, Iraq*

[4]*University of Warith Al-Anbiyaa, College of Engineering Karbala, Iraq*

[5]*Air Conditioning and Refrigeration Techniques Engineering Department, Al-Mustaqbal University College, Iraq*

[6]*Department of Energy Engineering, University of Baghdad, Iraq*

[7]*Department of Mechanics Al-Farabi Kazakh National University, Kazakhstan, Baghdad, Iraq*

[8]*System Technologies and Engineering Design Methodology, Hamburg University of Technology, Hamburg, Germany*

Abstract. A wind turbine blade is an essential system of wind energy production. During the operation of the blade, it is subjected to loads resulting from the impact of the wind on the surface of the blade. This leads to appear large deflections and high fatigue stresses in the structure of blades. In this paper, a 5 kW horizontal axis wind turbine blade model is designed and optimized using a new MATLAB code based on blade element momentum (BEM) theory. The aerodynamic shape of the blade has been improved compared with the initial design, the wind turbine power has been increased by 7% and the power coefficient has been increased by 8%. The finite Element Method was used to calculate the loads applied to the blade based on Computational Fluid Dynamics (CFD) and BEM theory. High agreements were obtained between the results of both approaches (CFD and BEM). The ANSYS software was also used to simulate and optimize the structure of the blade by applying variable static loads 3.3, 6, and 8.3 kg and compared the results with the experimental results. It was reduced the maximum deflections with 37%, 42.85%, and 42.61% when using CFRP material and 4.5%, 15.45%, and 16.19% for GFRP material that corresponds to the applied forces. Based on the results, the mass of the optimized model decreased by 47.86% for GFRP and 71.24% for CFRP. IEC 61400.2 standard was used to estimate the fatigue loads, damage, blade life prediction, and verify blade safety using a Simplified Load Model (SLM) and FAST software. It was found that the blade will be safe under extreme wind loads, and the lifetime of the wind blade (GFRP) is 5.5 years and 10.25 years, according to SLM and FAST software, respectively. At the same time, the lifetime of the wind blade (CFRP) is more than 20 years, according to the two applied methods.

Keywords: damage, composite materials, fatigue life, standard IEC 61400.2, Simplified Load Model, FAST software.

Received: 29th August 2022; Revised: 12th Nov 2022; Accepted: 8th Dec 2022; Available online: 18th Dec 2022

1. Introduction

Wind turbine energy is one of the most important sources used in the renewable energy sector. It is a source available everywhere in the world, where it is clean and free accessible. Wind turbines are used to generate electricity to supply homes, farms, factories, etc. (Rosato 2018).

The blade is the most important component of a wind turbine because it is responsible for rotating the generator to obtain electrical power. The process of optimizing the blade is an essential point from two different perspectives, the first one is to improve the external shape or aerodynamic characteristics to enhance the efficiency of the wind turbine. While the second one aims to improve the strength of the blade's structure so that it is more resistant to the loads applied on the surface of the blade due to wind and gravitational forces (Song *et al.* 2011).

Many recent studies used computational fluid dynamics (CFD) (Make *et al.* 2015) and the blade element momentum theory (BEM) (Tenguria *et al.* 2010) to calculate the aerodynamic loads. Also, to improve the aerodynamic characteristics and wind turbine power. Uchida *et al.* (2020) created a new approach for studying wind turbine farms based on computational fluid dynamics and a porous disk approach, and they explained the effect of vortices on the 2 MW wind turbines at various wind speeds. Zidane *et al.* (2020) simulated wind turbines in arid regions under the influence of sandstorms and debris flow based on the CFD and BEM methods and then coupled them with the neural network to study and improve the wind turbine performance. Ajirlo *et al.* (2021) simulated a micro wind turbine using CFD and BEM and compared it with the experimental results to develop a new model and verify the effect of the yaw angle on the extracted power.

* Corresponding author
Email: oday.abdullah@tuhh.de (OI Abdullah)

https://doi.org/10.14710/ijred.2023.48616
ISSN: 2252-4940/© 2023.The Author(s). Published by CBIORE

Modern wind turbines are manufactured from composite materials; as most of the studies in this field, these studies seek to develop the structure of the wind turbine blade to withstand the applied loads. The finite element method (FEM) is one of the most widely used methods for analyzing and optimizing blade structure. Peeters *et al.* (2018) achieved the numerical analysis of a wind turbine with a length of 43 m under static loads to obtain the results of displacements and local strains and then compare between FE model based on solid and FE model based on shell. Wu *et al.* (2012) based on the finite element analysis, studies the distribution and orientation of the fiber using the composite material of wind turbines. Pourrajabian *et al.* 2016) optimized the blade of the small wind turbines by studying the aero-structural design. Kim *et al.* (2009) studied the efficiency of large wind turbines under the influence of rotational and aerodynamic loads. Kim *et al.* (2013) created a new finite element model using an anisotropic material to develop the fabrication of a wind turbine based on the aeroelastic nonlinear multibody code (HAWC2 program). They also simplified the wind turbine model to a rectangular beam to get the results with lower time due to the complex shape of the blade.

Fatigue is one of the problems that occur to the material of the wind turbine blade when working for some time under fluctuating operating loads. That is why fatigue is one of the most important problems, and because of this, most researchers focus on this problem in their studies. Du *et al.* (2020) did a comprehensive study that provided the last six modern methods of detecting damage to wind turbine blades. (Bazilevs et al. 2016) predicted the fatigue damage of the wind turbine blade Sandia CX-100 of the full size that is made by composite materials using the fluid-structure interaction (FSI), and in their results reported the number of cycles until failure and the area of the most damage. Lee *et al.* (2015) performed an experimental work to study the fatigue failure of a 3 MW and length 56 m wind turbine blade at the root. They also used a FE model to verify the obtained results and gave more explanations. Rubiella *et al.* (2018) published a state-of-the-art paper and showed a method for calculating the fatigue loads of composite materials of wind turbines. The results showed large differences in the results. Shokrieh *et al.* (2006) used the FE model to simulate and predict the fatigue failure of composite material of the entire blade model and extracted the critical zone where the crack begins. Dervilis *et al.* (2014) deduced damage to a 9 m CX-100 wind turbine blade using Artificial Neural Networks (ANNs) and vibration modes.

Fatigue load is one of the complex problems due to the difficulty of complex interaction among the different parameters such as aerodynamics parameters, material, and fluctuating wind turbine loads. Therefore, the technical team of the International Electrotechnical Commission (IEC) has been trying for several years to simplify these loads for small wind turbines; its latest report was published under the IEC 61400-2 sequence (Commission 2013). The IEC report presented three methods for studying the fatigue of small wind turbines (testing, aeroelastic, and the simplified load model (SLM)). The new in these three methods is the SLM method, which has been divided into several cases. Each case was studied a specific load applied on a small wind turbine, such as fatigue load "case A" and extreme wind loads "case H". SLM approach is characterized by ease of use. Based on this approach, the computation time was reduced, and the safety factor was high (Wood 2009).

The current study aims to optimize the structure and material of the wind turbine blade with a power of 5 kW by studying the deflections and deformations under the influence of fluctuating wind. This study also aims to analyze and simplify the fatigue loads to calculate the damage and the number of fatigue cycles to predict the life of the wind turbine blade.

2. Blade structure design and FE model

The external structure of the blade consists of four basic parts: the shell, the neck, and the root, in addition to the spar cap. The function of the shell lies in building the aerodynamic structure and distributing the wind force on the blade's surface. As for the neck, it connects the shell and the root parts, and its purpose is to withstand the torques resulting from loads and deflection. While the root is used to connect the blade with the hub using metal screws, and the spar cap function is to resist flapwise of the blade, usually is not used in micro wind turbine blades. Fig.1-a. shows the main parts of the wind turbine blade.

In this study, BEM theory was used to design the blade (Tenguria *et al.* 2010). The airfoil NACA 4412 was chosen to design the aerodynamic shape of the blade, which the National Advisory Committee for Aeronautics created (NACA). The ratio of lift coefficient (Cl) to drag coefficient (Cd) at the angle of attack α= 5.25 is 129.

The BEM theory is used to evaluate the applied load to the wind turbine blade, and it is also used to calculate the parameters of the blade geometry (twist angle (θ), chord length (c), and angle of attack (α)).

Matlab software was used to develop a new special code that solves the BEM equations using the iterative approach methods to calculate the chord and twist angle. Fig.2-a and Fig.2-b shows the results of the design parameters. Table 1. shows the details of specifications for the design parameters of a small wind turbine used in the first step to start the design process.

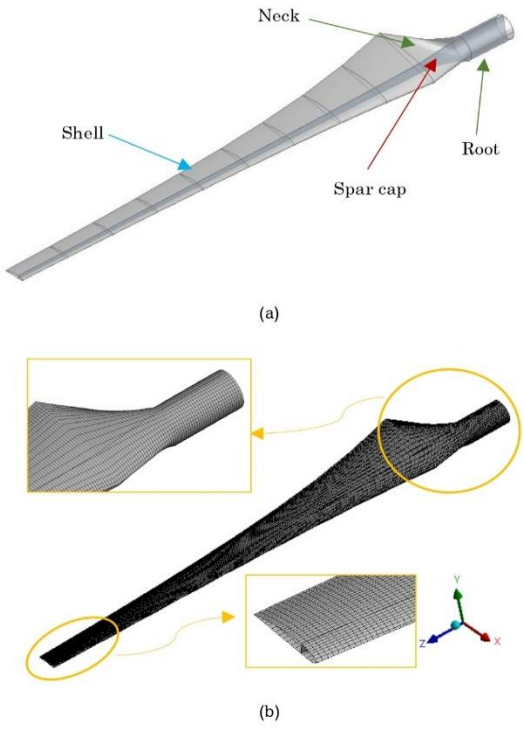

Fig.1 (a) part components of the blade and (b) FE model mesh

Table 1
The design parameters of a small wind turbine.

Design parameter	Value	Unit
Rated power	5	kW
Wind speed	10.5	m/s
Number of blades	3	-
Design tip speed ratio	6	-
Design angle of attack	5.25	°
Rotor radius	2.5	m
Design rotational speed	240	rpm
Density of air	1.22	kg/m3
Airfoil type	NACA4412	-

Table 2
Specifications design of 5 kW wind turbine blade.

Parameter	specification
root chord length	0.386 m
tip chord length	0.120 m
blade length	2.5 m
root diameter	0.080 m
hub length	0.300 m
hub to neck length	0.300 m

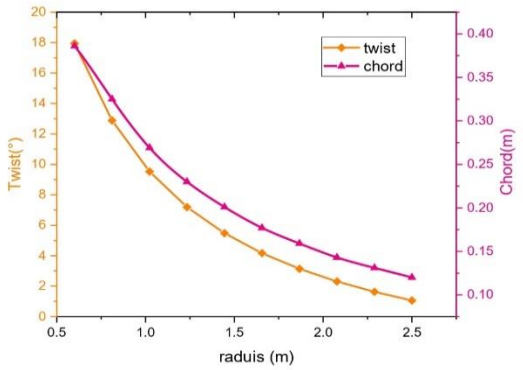

(a)

(b)

Fig.2 (a) Twist angle and Chord distribution, and (b) The twisted airfoil of 2.5 m small wind turbine blade

The commercial finite element method Ansys software was used to simulate the wind turbine blade model. For the blade mesh, the element "shell 281" was used, the element consists of eight-node Each node contains six degrees of freedom (DOF). mesh convergence is made depending on the error rate, which does not exceed 1 %. When the required convergence is reached, the number of nodes and the number of elements is determined. The last nodes of the FE model were 17820 elements and 18205 nodes. The final form of the FE mesh model is shown in Fig 1-b

Table 3
Mechanical properties of used material

Properties		GFRP	T300 CFRP
Young's modulus	E_{xx} (GPa)	44	136.7
	E_{yy} (GPa)	17	8.2
	E_{zz} (GPa)	16.7	8.2
Poisson's ratio	υ_{xy}	0.26	0.29
	υ_{zx}	0.26	0.42
	υ_{yz}	0.35	0.29
Shear modulus	G_{xy} (GPa)	3.49	4.45
	G_{zx} (GPa)	3.77	4.45
	G_{yz} (GPa)	3.46	2.91
Density	ρ (kg/m^3)	1800	1300

Source:(Korkiakoski *et al.* 2016), (Zhou *et al.* 2019)

3. Material properties of the blade

In this study, we will use composite materials to manufacture a wind turbine blade. In order to optimize the blade structure and reduce the deflection, we will choose the materials glass fiber reinforced polymer (GFRP) and carbon fiber reinforced polymer (CFRP), to create a FE model, and compare them with the experimental results to identify the most suitable material for manufacturing small wind turbine blades. the mechanical properties of the GFRP and CFRP materials are shown in Table 3.

To create the FE model of the blade made from composite materials, it needs to determine the direction of rotation of the fibers. This study selected the following sequence of the lay-up of the shell fibers: $[0/90]_3$ and $[0/90]_4$ for the CFRP and GFRP materials, respectively. At the same time, the lay-up sequence of the spar cap is $[45/-45]_3$. Each ply thickness is equal to 0.25 mm, with determines the direction of the length for the blade, i.e., the z-axis (see Fig. 1) is the 0° of the fiber lay-up sequence.

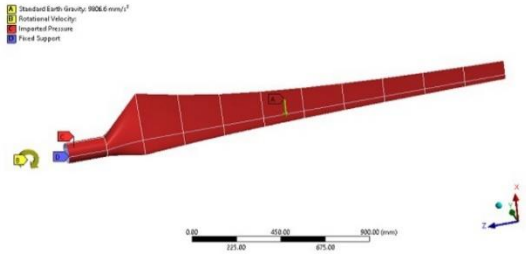

(a)

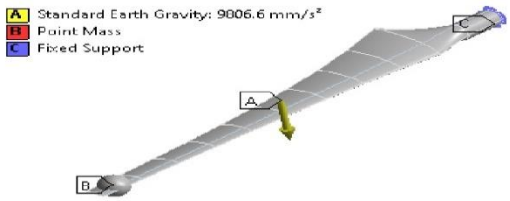

(b)

Fig.3 The boundary conditions of 2.5m wind turbine (a) load from CFD, and (b) static load

4. Blade boundary conditions

When the small wind turbine blade rotates, it will be subjected to pressure caused by wind speed in addition to the centrifugal force that results due to the rotation of the blade. The blade is fixed at the hub; therefore, all the DOF are null on the side of the root. Also, the force of gravity is affected by the blade's center of mass in a direction parallel to the tower. Fig. 3 shows the boundary conditions applied on the wind blade.

5. Study-state and aerodynamic load

To improve the structure of the wind turbine blade, it will discuss the comparison between the results of the FE model with the experimental results (Da Costa *et al.* 2020) and (Costa *et al.* 2017). In order to achieve this task, three magnitudes of static loads/ masses (3.3, 6, 8.3 kg) are fixed near the tip area to determine the maximum deflection of the blade tip.

During the operation of the wind blade, a collision occurs between the air stream that passes through the rotating wind turbine disk and the blade shell. These results appeared as aerodynamic loads (fluid-structure interaction-FSI). In order to calculate the aerodynamic loads, the computational fluid dynamics (CFD) method is adopted due to the possibility of simulating the 3D model by taking external influences such as blade tip vortices into consideration. Ansys Fluent software was used to simulate the wind turbine and compared the results with the BEM theory to verify the results. Fig.4 shows the aerodynamic loads applied to the blade surface section.

The fluent software uses the finite volume method (FVM) to solve the Navier-Stokes (N-S) equation (Bechmann et al. 2011). The main objective of solving this equation is to calculate the coefficients of normal force (Cn) and tangential force (Ct), in addition to the coefficient of drag force (Cd) and coefficient of lift force (Cl). The BEM theory and CFD simulation based on the equations 1 to 11 for obtaining the blade force and power results. It can be calculated the coefficient of lift and drag forces by Eq. 1 and Eq. 2 (Rosato 2018).

$$F_L = \frac{1}{2}\rho U_{rel}^2 c C_L \tag{1}$$

$$F_D = \frac{1}{2}\rho U_{rel}^2 c C_D \tag{2}$$

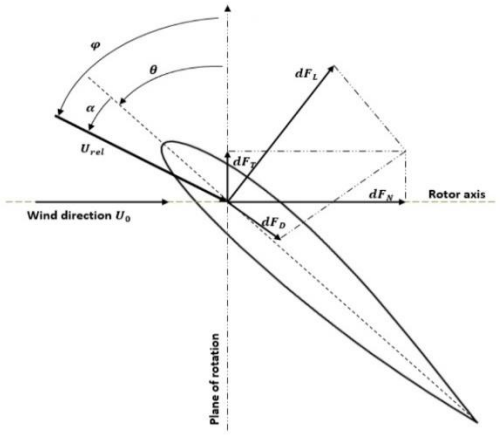

Fig 4. The airfoil section with aerodynamic loads and wind direction. α is the angle of attack and θ is the twist angle, φ is the inflow angle. FD, FL, FN, and FT are the drag force, lift force, normal force, and tangential force, respectively.

It can be calculated the normal coefficient force by using Eq.3 and Eq.4,

$$C_n = \frac{F_N}{\frac{1}{2}\rho U_{rel}^2 c} \tag{3}$$

$$C_n = C_L \cos\varphi + C_D \sin\varphi \tag{4}$$

It can be calculated the coefficient of the tangential force by Eq.5 and Eq.6

$$C_t = \frac{F_T}{\frac{1}{2}\rho U_{rel}^2 c} \tag{5}$$

$$C_t = C_L \sin\varphi - C_D \cos\varphi \tag{6}$$

It can be written the form of the relative wind velocity using Eq.7 (Liu *et al.* 2013),

$$U_{rel} = \sqrt{\left(\frac{\Omega R}{2}\right)^2 + (U_0)^2} \tag{7}$$

Where: c is the chord and $U_0$is the wind velocity.

In order to calculate the gravitational force and the centrifugal force, it can be using Eq. 8 and Eq. 9 (Rajadurai *et al.* 2008)

$$F_G = m_b g \tag{8}$$

$$F_C = m_b \omega^2 R \tag{9}$$

The rotor power is calculated from:

$$P = \mathrm{T}\omega \tag{10}$$

And the power coefficient are calculated from (Liu *et al.* 2013)

$$C_p = \frac{\mathrm{P}}{\frac{1}{2}\rho\pi R^2 U_0^2} \tag{11}$$

Where: F_G, and F_C are the gravitational and the centrifugal force, respectively. $m_b$is the blade mass, ω is the angular velocity of blade rotation, and T is the rotor torque

6. Aeroelastic simulation and SLM of IEC 61400-2

The wind turbine blade is exposed to fatigue due to the wind loads. In order to assess the impact of the loads on the blade of the wind turbine, an aeroelastic simulation should be created by developing a new model of a 5-kW wind turbine in the FAST software (version 7). This software is free and open-source software, it was developed by the National Renewable Energy Laboratory (NREL) (Jonkman *et al.* 2005). In order to start the simulation process using FAST software, the previous parameters of the blade (airfoil, blade length, rotation speed, etc.) will be used. The simplified load model (SLM) has also been adopted due to the straightforward with less complexity of model based on the primary loads with high safety factors (Wood 2009). The importance of SLM is to simplify the equations for calculating the forces acting on the root of the blade. SLM is divided into many parts that are arranged alphabetically (A to J), and each part is concerned with a specific case study.

6.1 SLM formulation (loads of case A)

Although all cases are in the SLM approach, the Normal operation is the only case that studies fatigue (Case A). The objective of SLM "case A" is to calculate the loads and predict the fatigue life of the blade and damage. The loads of case A based on SLM are applied to the root of the wind turbine blade. The flapwise moment of "case A" is applied in a range between the minimum value (50%) and the maximum value (150%). When applied the SLM equations, the generated stresses at the root are a combination of three forces: the centrifugal

force(ΔF_{zB}) in the direction of the blade tip, the flapwise moment (ΔM_{yB}) which is parallel to the blade length, and the lead-lag moment (ΔM_{xB}) in the direction of the rotation. The equations of case A are not included any unstable effects, such as the yaw error or the effect of gyroscopic loads. The following equations 12 to Eq 16 were used to calculate fatigue loads and compare the results with FAST simulation and the experimental work (Commission 2013; Evans *et al.* 2021; Evans 2017; Wood 2009):

$$\Delta F_{zB} = 2m_b r_g \omega_n^2 \quad (12)$$

$$\Delta M_{xB} = \frac{Q_{design}}{B} + 2m_b g r_g \quad (13)$$

$$\Delta M_{yB} = \frac{\lambda_{design} Q_{design}}{B} \quad (14)$$

$$Q_{design} = \frac{30 P_{design}}{\eta \pi \omega_n} \quad (15)$$

$$\eta = 0.6 + 0.005 P_{design} \quad (16)$$

Where: m_b is the mass of the blade, r_g is the radial distance from the center of the hub and the blade's center of gravity (0.880 m), and B is the number of blades. $\omega_n$is the design speed of rotation (rad/s), $P_{design}$is the design power, Q_{design} is the design torque (Nm), and η is the efficiency (limited between 0.6 and 0.7).

6.2. Equivalent stress and safety factors of the blade

In SLM approach, there is a difference in the equations for equivalent stresses σ_{eqB} according to the geometry of the root section (cylindrical or rectangular). In this study the fatigue was analyzed using the cylindrical shape of the root. In order to calculate the equivalent stresses of the case A, the following equation can be used (Wood 2009):

$$\sigma_{eqB} = \sigma_{zB} + \sigma_{MB} \quad (17)$$

Axial stress associated with centrifugal force is given by:

$$\sigma_{zB} = \frac{F_{zB}}{A_B} \quad (18)$$

Where A_B is the cross-section area of the blade root (5.024x10^{-3} m^2). The stress of bending σ_{MB} is given by:

$$\sigma_{MB} = \frac{\sqrt{M_{xB}^2 - M_{yB}^2}}{W_B} \quad (19)$$

Where: W_B is the section modulus of the blade (i.e., the second moment of inertia for the root section of the blade (m^4) divided by the distance between the root's centroid and the point of the maximum stress (m). For the current study, the blade section modulus is 5.5x10^{-5} m^3. It was found that the equivalent stresses of the fatigue load are σ_{eqB} =20.16 MPa.

SLM approach has a high safety factor and thus can be relied upon to calculate various stresses to verify the safety of the wind turbine blade. IEC standard 61400-2 has defined the partial safety factor based on the load type and the material's characterization. Where it was defined the safety factor for the loads (γ_f), as well as the safety factor for the materials (γ_m). Table 4 gives the partial safety factor values used in the IEC 61400-2. The material is assumed to be well characterized, so the partial safety factor for the minimum characterization is very high. This explains why most researchers used the full characterization (i.e., the lower safety factors). There are several conditions, including the blade properties derived from materials and configurations, representing the final structure. The fatigue tests were conducted with an acceptable load range and effects rate. Also, the material properties were calculated at a 95 % high probability and at a 95 % confidence level (Wood 2009).

The safety factors and the ultimate stress of SLM are used to determine the allowable stress σ_{all} according to the Eq. 20 (Wood 2009):

$$\sigma_{all} = \frac{\sigma_u}{\gamma_f \gamma_m} \quad (20)$$

Where: σ_u is the ultimate material strength. In other words, the final safety factor is obtained by multiplying the load safety factor γ_f and material safety factor γ_m. For the safety condition, the equivalent Von Mises stress must be less than the allowable stress:

$$\sigma_{eq} < \sigma_{all} \quad (21)$$

6.3 SLM (Loads of case H)

Small wind turbines often operate at wind speeds greater than the design wind speed. Owing this reason, the blade structure must be designed to withstand extreme wind loads. In the SLM approach, Case H is dedicated to the study of extreme wind loads applied to the blade. The objective of case H is to ascertain the rigidity of the blade structure and its resistance to extreme wind loads so that the blade is safe. In the case H equations, the design wind speed is not used to calculate the extreme wind loads, but the extreme wind speed for 50 years is used to calculate the flapwise moment and stresses. In the standard IEC 61400-2, wind turbines are categorized by average wind speed into Sections I to IV and Special Status S (Commission 2013). In this study, the design wind speed is 10.5 m/s, which means that the average wind speed is 7.5 m/s; this means that the section of the studied wind turbine is Class III according to IEC 61400-2, that is, the reference wind speed is U_{ref}= 37.5 m/s. Therefore, the extreme wind speed for 50 years can be determined by the equation $U_{e50} = 1.4\, U_{ref}$ =52.5 m/s. To calculate the equivalent stress σ_{MB} for case H it can be used the Eq. 23 (Commission 2013).

$$M_{yB} = \frac{1}{4} C_d \rho U_{e50}^2 A_{p,B} R = 1617.51 \text{Nm} \quad (22)$$

$$\sigma_{MB} = \frac{M_{yB}}{W_B} \quad (23)$$

WhereM_{yB}, is flapwise moment of the extreme wind speed and $A_{p,B}$ is the blade's projected area.

Table 4
Partial safety factors of IEC standard 61400-2 for loads and materials

Method	Partial safety factors for loads(γ_f)		Partial safety factor for the materials(γ_m)			
			Fatigue loads		Ultimate loads	
	Fatigue loads	Ultimate loads	Minimal characterization	Full characterization	Minimal characterization	Full characterization
SLM	1.0	3.0	10	1.25	3.0	1.1
aeroelastic	1.0	1.35	10	1.25	3.0	1.1

Source:(Commission 2013; Wood 2009)

6.4 Blade fatigue damage analysis

To assess the wind turbine blade damage caused by fatigue loads, it will apply the miner's law recommended by the standard IEC 61400-2. Miner's law relies on cumulative statistics to calculate the damage, and according to this law, the blade will fail if the damage exceeds a certain value. The following equation is used to calculate the damage of the blade: (Zhang *et al.* 2018)

$$D_B = \sum_i \frac{n_i}{N_f(\gamma_f \gamma_m \sigma_B)} \leq 1 \quad (24)$$

Where n_i is the number of performed cycles in bin i of the load characteristic spectrum, N_f is the number of cycles to failure, which is a variable function in terms of the stress level of fatigue cycles σ_B. The number of cycles to failure has a relationship to the associated stress level. For SLM, case A contains one 'bin' and it can be calculated the number of fatigue cycles by using Eq. 25,

$$n = \frac{B\Omega_{design} T_d}{60} = 7.59\text{x}10^9 \quad (25)$$

Where Ω_{design} is the rotational speed, T_d is the design life of the composite material of a wind turbine blade, where the lifetime is found to be about 20 years (i.e., $6.31\text{x}10^8$ s). In order to determine N_f, an S-N curve should be used; this curve will give the number of cycles to reach the failure versus maximum applied stress (stress level of fatigue cycles σ_B). At a constant stress ratio $\bar{R} = \sigma_{min}/\sigma_{max}$, the S-N curve of the composite material is a linear decreasing (i.e., the proportional relation between the stress and the $\log N_f$ is found). N_f can be calculated by applying the following Basquin's equation:(Hu et al. 2013),

$$\frac{\sigma_B}{\sigma_0} = 1 - \beta \log_{10} \mathrm{N_f} \quad (26)$$

Here σ_B is the maximum applied stress (associated stress level is 25.20MPa), $\sigma_0$is the ultimate strength of the blade material, and β is the S-N curve slope coefficient of the materials.

7. Results and discussions

7.1 Power aerodynamic load of the blade

The aerodynamic structure of the blade has been improved to increase the power of the wind turbine. From Fig. 5-a, it can be noticed for the optimized design, the power coefficient increased when the tip speed ratio (TSR) is less than 4 and when TSR is greater than 6. This means that the range of increment for the power coefficient of the new improved design occurred within low and high periods of rotational speeds with an average increase of up to 8%. Fig. 5-b shows the power of the wind turbine for the initial and improved design, it can be observed that the power of the improved design increased when the wind speed is equal to or greater than 8 m/s. While the rated power at the rated wind speed is higher than by 7% compared with the initial design.

Fig. 6 shows the distribution of tangential and normal force coefficients. The CFD simulation and BEM theory were compared in seven different sections along the blade. As shown in Fig 6-a and Fig 6-b, the results are well approximated, and the difference between them is due to the difference in the calculation method because CFD studies a 3D model that depends on the number of elements and the number of nodes. At the same time, BEM method considers the blade as an ideal 1D rotating disk. The lift and the drag forces were calculated based on BEM method that was applied to the blade, and they were found to be 380.2 N and 7.9 N, respectively. At the same time, the gravitational force and the centrifugal forces were found to be 241.32 N and 1544.88 N, respectively.

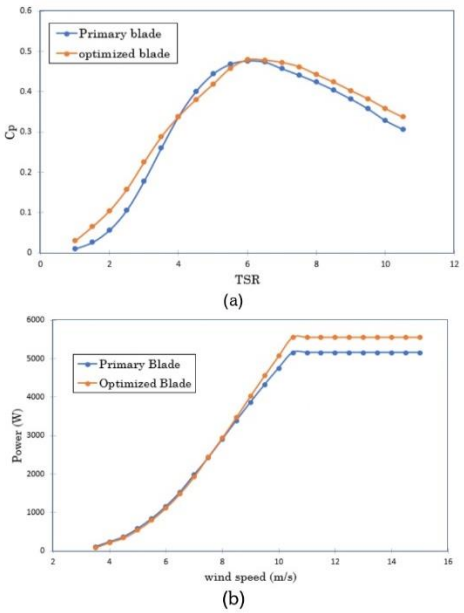

Fig. 5 (a) power coefficient, and (b) power for initial and optimized wind turbine blade rotor

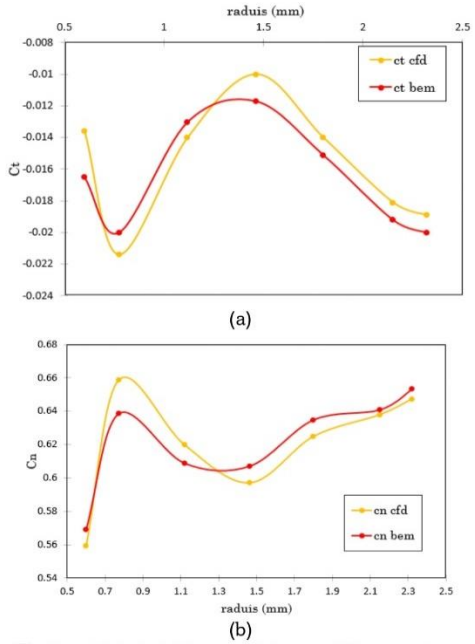

Fig.6 coefficient of **a**) tangential force and **b**) normal force

7.2 *Deflection of the blade under the static loads*

The wind turbine blade deflects due to the loads applied to the blade surface. The intensity of the loads varies with the wind speed. In the experimental study, (Costa et al. 2017; Da Costa et al. 2020) fabricated a wind turbine blade shell of GFRP and filled it with H80 foam with three loads/ masses (3.3, 6, and 8.3 kg) that were fixed near the blade tip to obtain the maximum blade deflection. In their study, the FE model was made from GFRP and CFRP to optimize the blade structure and the H80 foam change by the spar cap part to reduce the mass and study the deflection behavior of the blade.

Based on the obtained results, Fig.7 shows that the maximum deflections of the blade when applying a load of 3.3 kg for the CFRP and the GFRP materials are 23.08 mm and 35.35 mm, respectively. While the experimental deflection was 37 mm, its means that the deflections of carbon fiber and glass fiber are less by 37% and 4.5% compared to the experimental results. When applying a 6 kg load, the deflections of CFRP blade and GFRP blade are 40 mm and 59.18 mm, corresponding to 42.85% and 15.45% less than the experimental deflection (70 mm). When applying a load of 8.3 kg, the maximum deflection of the CFRP blade was 54.42 mm, which is 42.61% less than the experimental results, while the deflection of GFRP blade was 79.48 mm, which is 16.19% less than the experimental result (94.83 mm).

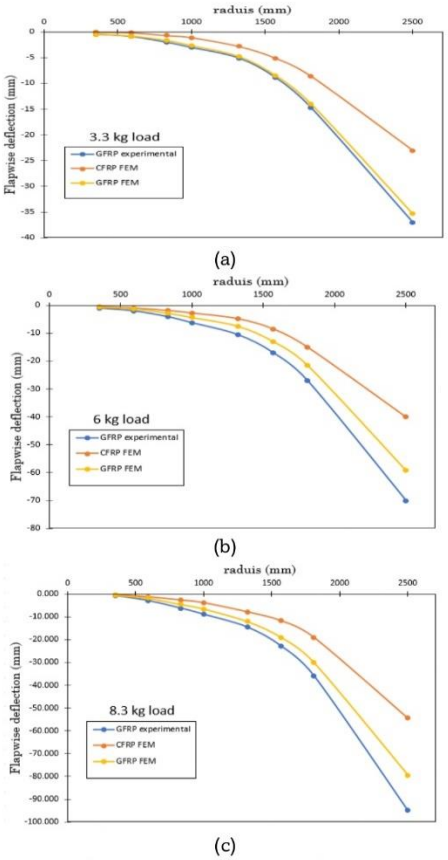

Fig.7 The blade flapwise deflection of a) 3.3 kg load and b) 6 kg load, and (c) 8.3 kg load.

When analysing the results, it can be noticed that the deflection of the blade made of CFRP material has the lowest deflection for all different loads. In contrast, the deflection of the blade of the GFRP material when carrying 3.3 kg was close to the experimental results. The difference in the deflection values increased when applying a load of 6 kg and 8.3 kg, which means that the improved structure of the blade appears due to resistance when applying significant loads. Despite the acceptable results of the enhanced structure of the blade in terms of deflection value, the enhanced value is evident in reducing the blade mass, as shown in Fig 8. Where the value of the blade mass in the experimental study is 6.3 kg, while the blade mass for the FE model of GFRP is 3.3 kg, which is reduced by 47.86%, The mass of the CFRP blade is 1.8 kg, which means the reduction is 71.24%.

7.3 Fatigue load calculation for SLM case A

Fig.9-a shows the flapwise moment of the wind turbine blade at 10.5 m/s design wind speed. Table 5 lists the fatigue loads under normal wind conditions. SLM approach considered the fatigue loads as a constant at a design speed. In fact, the blade will have a longer life due to the change in fatigue loads during periods of operation as well as periods of rest and maintenance. the SLM fatigue load changes with a constant sinusoidal field, and the maximum flapwise moment calculated by SLM is 1.5x ΔM_{yB}=952.38.

The results obtained by SLM approach were compared with the aeroelastic simulation of FAST software to validate the flapwise moment results. Fig.9-b shows the comparison between SLM and FAST approaches. It can be noticed that the flapwise moment of the SLM is constant over time. While it can be seen the fluctuation in the values when using the simulation of FAST software. The fluctuation in the values using FAST is due to the change in instantaneous wind speed and is closer to reality because the fatigue loads cannot always be constant.

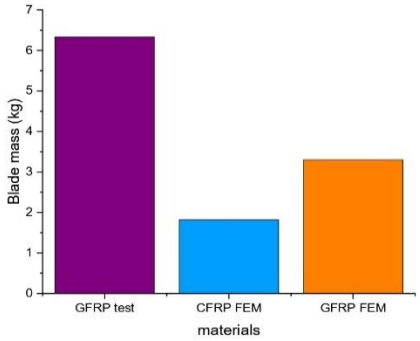

Fig.8 Mass of the wind turbine blade

Table 5
The fatigue Loads at normal wind conditions (10.5 m/s).

Loads type	SLM	FAST
Centrifugal force(kN)	27.49	23.83
Flapwise bending (Nm)	635	742
Edgewise bending (Nm)	531	1268
Design torque Q_{design}(Nm)	317	295

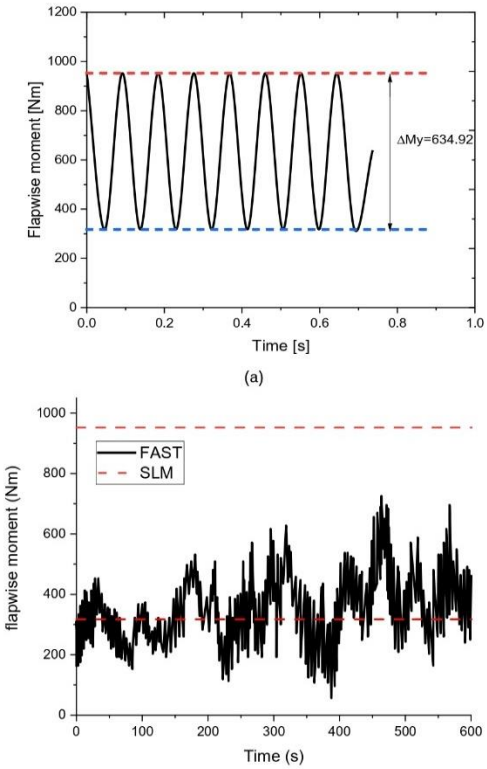

Fig.9 Flapwise moment of blade (a) the SLM sinusoidal range, and (b) comparison between SLM and fast simulation

7.4 Extreme wind load for SLM (case H)

In the case H of the SLM approach is imposed if the stress of the von Mises is less than the allowable stress limit, then the blade will be in a safe state. Table 6 shows the equivalent stress value of GFRP and CFRP blades which are 19.23 MPa and 26.84 MPa, respectively. Since the equivalent stress is less than the allowable stress limit, this means that the blade will be safe under extreme wind loads.

A simulation was performed using the ANSYS software to check the results of the SLM method. Initially, the CFD is used to study the effect of airflow at a wind speed of 52.5 m/s to calculate the pressure applied to the blade surface and then to the FE model to assess the stress at the root zone. Fig.10-a, b shows the distribution of von Mises stress on the blade for blades that are made from CFRP and GFRP materials.

From Fig. 10-a, b, it can be noticed that the average von-mises stress at the root of GFRP and CFRP blades are 20.58 MPa and 35.31 MPa, respectively, which means there is a convergence between the results of SLM and ANSYS in the distribution of von-mises stresses at the root zone. Hence, it can be concluded that the SLM "case H" results can be relied upon to verify the blade's safety when applying extreme wind loads.

Table 6
Extreme wind condition load case H of SLM

Material	Allowable Stress Limit (MPa)	Calculated equivalent Stress (MPa)	Conclusion
GFRP	151.52	19.23	SAFE
CFRP	248.48	26.84	SAFE

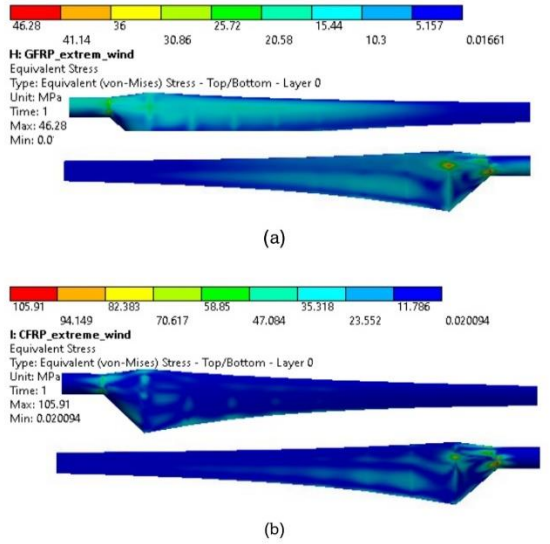

Fig.10 The von-Mises stress distribution of extreme wind conditions (a) GFRP material and (b) CFRP material

7.5 Damage analyses and blade life

In order to predict blade damage, Miner's law was applied. The GFRP material has an S-N slope parameter β of 0.106 (Mandell et al. 2002), and the CFRP material has a parameter less than 0.085 (Backe et al. 2018). Based on Eq.24, it was found that the number of cycles to reach the failure for the GFRP blade is $N_{f,GFRP} = 2.06\text{x}10^{9}$ cycles, and for the CFRP blade is $N_{f,CFRP} = 8.84 \times 10^{10}$. The damage of the GFRP blade was calculated by SLM approach and was found $D_{SLM,GFRP} = 3.68 > 1$. Since the damage is greater than 1, this means that the wind turbine blade will fail before reaching the design life. The damage of the blade (CFRP) is $D_{SLM,CFRP} = 8.59 \times 10^{-2}$, where the damage is less than one, this means that the blade will exceed the required design life. The damage was predicted by using M-Life of FAST software. The damage of the GFRP blade is found $D_{FAST,GFRP} = 2.01$, and for the CFRP blade it is found $D_{FAST,CFRP} = 4.27 \times 10^{-2}$.

According to SLM approach, a GFRP blade will withstand periodic fatigue loads for 5.5 years, while a CFRP blade will have a lifespan of more than 20 years. According to aerodynamic simulation achieved by FAST software, a GFRP blade will withstand loads for 10.25 years, while a CFRP blade will have a very long life of over 20 years. Table 7 compares the results obtained by SLM and FAST approaches with the experimental results of a wind turbine blade.

Table 7
Fatigue damage load and blade life for different methods and materials

Method	materials	SLM	FAST	Measured (Evans 2017)
Fatigue damage loads (Nm)		634	195	71
Blade fatigue life (years)	GFRP	5.5	10.25	9.18
	CFRP	over 20	over 20	-

From the previous results, it can be concluded that the SLM method is the most conservative (the safest results), followed by aeroelastic simulations, where the measured results are the least conservative. Somewhat disturbingly, all established methods predict a lifetime less than the design life of 20 years for the GFRP material, while the CFRP material has a fatigue life of more than 20 years.

8. Conclusions and future works

In this paper, the geometric parameters of the 5-kW blade are optimized using the MATLAB code developed based on the blade element momentum theory (BEMT). This paper aims to improve the blade structure and predict fatigue life.
As the first step in this study, the aerodynamic shape of the wind turbine blade was improved, and through the results, it was found that the power of the optimized shape increased by 7%, and the power coefficient increased by 8% compared to the initial design. Also, the aerodynamic loads using CFD and BEM were compared for the improved shape. Where, it was found that the results of both methods are compatible, and it can be relied upon them to find the aerodynamic loads. When applying different static mass/loads (3.3 kg, 6 kg, and 8.3 kg), the deflections of the GFRP blade were found to be 35.35 mm, 59.18 mm, and 79.48 mm, respectively.

At the same time, the deflections of the CFRP blade were found to be 23.08 mm, 40 mm, and 54.42 mm, respectively. On the other hand, the deflections of the optimized CFRP blade were reduced by (37%, 42.85%, and 42.61%) corresponding to the loads (3.3 kg, 6 kg, and 8.3 kg). While, it was found that the reductions of deflections for the optimized GFRP blade were (4.5%, 15.45%, and 16.19%) corresponding to the loads (3.3 kg, 6 kg, and 8.3 kg). The mass of the optimized blade structure was reduced by 47.86% when using GFRP and 71.24% when using CFRP, and it was also shown that the optimized blades made of CFRP and GFRP materials would be safe under extreme wind loads.

Furthermore, the blade damage was calculated using the SLM approach and FAST software. The percentage difference between the results of the two methods were 45.3% for GFRP and 50.29% for CFRP. The expected life of a wind turbine blade made of GFRP is 5.5 years, according to the SLM approach, and 10.25 years, according to the results of the FAST software. At the same time, the life of the blade made of CFRP material will be more than 20 years using both methods.

Assuming the gyroscopic loads play an essential role in the fatigue of wind turbine blades by affecting the root zone during blade yaw. Therefore, a developed approach in future research will be presented to predict the fatigue spectra of the small wind turbines caused by gyroscopic loads.

Funding: This research was funded by the University of Baghdad.

Conflicts of Interest: authors declare no conflict of interest.

References

Ajirlo, K. S., Tari, P. H., Gharali, K., & Zandi, M. (2021). Development of a wind turbine simulator to design and test micro HAWTs. *Sustainable Energy Technologies and Assessments*, 43100900; https://doi.org/10.1016/j.seta.2020.100900

Backe, S., & Balle, F. (2018). A novel short-time concept for fatigue life estimation of carbon (CFRP) and metal/carbon fiber reinforced polymer (MCFRP). *International Journal of Fatigue*, 116317-22 https://doi.org/10.1016/j.ijfatigue.2018.06.044

Bazilevs, Y., Korobenko, A., Deng, X., & Yan, J. (2016). Fluid–structure interaction modeling for fatigue-damage prediction in full-scale wind-turbine blades. *Journal of Applied Mechanics*, 83(6): https://doi.org/10.1115/1.4033080

Bechmann, A., Sørensen, N. N., & Zahle, F. (2011). CFD simulations of the MEXICO rotor. *wind energy*, 14(5): 677-89 https://doi.org/10.1002/we.450

Commission, I. E. (2013). IEC 61400-2: 2013-Wind Turbines. part 2. Small Wind Turbines. In. Australia: International Electrotechnical Commission

Costa, M. S., Evans, S. P., Bradney, D. R., & Clausen, P. D. (2017). A method to optimise the materials layout of small wind turbine blades. *Renewable Energy and Environmental Sustainability*, 219 https://doi.org/10.1051/rees/2017006

Da Costa, M., & Clausen, P. (2020). Structural Analysis of a small wind turbine blade subjected to gyroscopic load. In *Journal of Physics: Conference Series*, 042006. IOP Publishing https://doi:10.1088/1742-6596/1618/4/042006

Dervilis, N., Choi, M., Taylor, S., Barthorpe, R., Park, G., Farrar, C., & Worden, K. (2014). On damage diagnosis for a wind turbine blade using pattern recognition. *Journal of sound and vibration*, 333(6): 1833-50 https://doi.org/10.1016/j.jsv.2013.11.015

Du, Y., Zhou, S., Jing, X., Peng, Y., Wu, H., & Kwok, N. (2020). Damage detection techniques for wind turbine blades: A review. *Mechanical Systems and Signal Processing*, 141106445 https://doi.org/10.1016/j.ymssp.2019.106445

Evans, S., Dana, S., Clausen, P., & Wood, D. (2021). A simple method for modelling fatigue spectra of small wind turbine blades. *Wind Energy*, 24(6): 549-57 https://doi.org/10.1002/we.2588

Evans, S. P. (2017). Aeroelastic measurements, simulations, and fatigue predictions for small wind turbines operating in highly turbulent flow, The University of Newcastle, Australia; http://hdl.handle.net/1959.13/1349817

Hu, W., Park, D., & Choi, D. (2013). Structural optimization procedure of a composite wind turbine blade for reducing both material cost and blade weight. *Engineering Optimization*, 45(12): 1469-87 https://doi.org/10.1080/0305215X.2012.743533

Jonkman, J. M., & Buhl, M. L. (2005). *FAST user's guide* (National Renewable Energy Laboratory Golden, CO, USA).https://www.nrel.gov/wind/nwtc/fastv7.html

Kim, D.-M., Kim, D.-H., Park, K.-K., & Kim, Y.-S. (2009). Efficient Super-element Structural Vibration Analyses of a Large Wind-turbine Rotor Blade Considering Rotational and Aerodynamic Load Effects. *Transactions of the Korean Society for Noise Vibration Engineering*, 19(7): 651-58 https://doi.org/10.5050/KSNVN.2009.19.7.651

Kim, T., Hansen, A. M., & Branner, K. (2013). Development of an anisotropic beam finite element for composite wind turbine blades in multibody system. *Renewable Energy*, 59172-83, https://doi.org/10.1016/j.renene.2013.03.033

Korkiakoski, S., Brøndsted, P., Sarlin, E., & Saarela, O. (2016). Influence of specimen type and reinforcement on measured tension–tension fatigue life of unidirectional GFRP laminates. *International Journal of Fatigue*, 85114-29 https://doi.org/10.1016/j.ijfatigue.2015.12.008

Lee, H. G., Kang, M. G., & Park, J. (2015). Fatigue failure of a composite wind turbine blade at its root end. *Composite Structures*, 133878-85 https://doi.org/10.1016/j.compstruct.2015.08.010

Liu, X., Wang, L., & Tang, X. (2013). Optimized linearization of chord and twist angle profiles for fixed-pitch fixed-speed wind turbine blades. *Renewable Energy*, 57111-19 https://doi.org/10.1016/j.renene.2013.01.036

Make, M., & Vaz, G. (2015). Analyzing scaling effects on offshore wind turbines using CFD. *Renewable Energy*, 831326-40 https://doi.org/10.1016/j.renene.2015.05.048

Mandell, J. F., Samborsky, D. D., & Cairns, D. S. (2002). Fatigue of composite materials and substructures for wind turbine blades. In. Albuquerque, California: Sandia National Laboratories

Peeters, M., Santo, G., Degroote, J., & Van Paepegem, W. (2018). Comparison of shell and solid finite element models for the static certification tests of a 43 m wind turbine blade. *Energies*, 11(6): 1346 https://doi.org/10.3390/en11061346

Pourrajabian, A., Afshar, P. A. N., Ahmadizadeh, M., & Wood, D. (2016). Aero-structural design and optimization of a small wind turbine blade. *Renewable energy*, 87837-48 https://doi.org/10.1016/j.renene.2015.09.002

Rajadurai, J. S., Christopher, T., Thanigaiyarasu, G., & Rao, B. N. (2008). Finite element analysis with an improved failure criterion for composite wind turbine blades. *Forschung im Ingenieurwesen*, 72(4): 193-207 http://doi.org/10.1007/s10010-008-0078-8

Rosato, M. A. (2018). *Small Wind Turbines for Electricity and Irrigation: Design and Construction* (CRC Press: New York, USA)

Rubiella, C., Hessabi, C. A., & Fallah, A. S. (2018). State of the art in fatigue modelling of composite wind turbine blades. *International Journal of Fatigue*, 117230-45 https://doi.org/10.1016/j.ijfatigue.2018.07.031

Shokrieh, M. M., & Rafiee, R. (2006). Simulation of fatigue failure in a full composite wind turbine blade. *Composite Structures*, 74(3): 332-42 https://doi.org/10.1016/j.compstruct.2005.04.027

Song, F., Ni, Y., & Tan, Z. (2011). Optimization design, modeling and dynamic analysis for composite wind turbine blade. *Procedia Engineering*, 16369-75 https://doi.org/10.1016/j.proeng.2011.08.1097

Tenguria, N., Mittal, N., & Ahmed, S. (2010). Investigation of blade performance of horizontal axis wind turbine based on blade element momentum theory (BEMT) using NACA airfoils. *International Journal of Engineering, Science and Technology*, 2(12): 25-35 https://doi.org/10.1260/1708-5284.12.1.83

Uchida, T., Taniyama, Y., Fukatani, Y., Nakano, M., Bai, Z., Yoshida, T., & Inui, M. (2020). A new wind turbine CFD modeling method based on a porous disk approach for practical wind farm design. *Energies*, 13(12): 3197 https://doi.org/10.3390/en13123197

Wood, D. (2009). Using the IEC Simple Load Model for Small Wind Turbines. *Wind Engineering*, 33(2): 139-54 https://doi.org/10.1260/0309-524X.34.3.241

Wu, W. H., & Young, W. B. (2012). Structural analysis and design of the composite wind turbine blade. *Applied Composite Materials*, 19(3-4): 247-57 https://doi.org/10.1007/s10443-011-9193-z

Zhang, C., Chen, H.-P., & Huang, T.-L. (2018). Fatigue damage assessment of wind turbine composite blades using corrected blade element momentum theory. *Measurement*, 129102-11 https://doi.org/10.1016/j.measurement.2018.06.045

Zhou, S., & Wu, X. (2019). Fatigue life prediction of composite laminates by fatigue master curves. *Journal of Materials Research and Technology*, 8(6): 6094-105 https://doi.org/10.1016/j.jmrt.2019.10.003

Zidane, I. F., Swadener, G., Ma, X., Shehadeh, M. F., Salem, M. H., & Saqr, K. M. (2020). Performance of a wind turbine blade in sandstorms using a CFD-BEM based neural network. *Journal of Renewable and Sustainable Energy*, 12(5): 053310; https://doi.org/10.1063/5.0012272

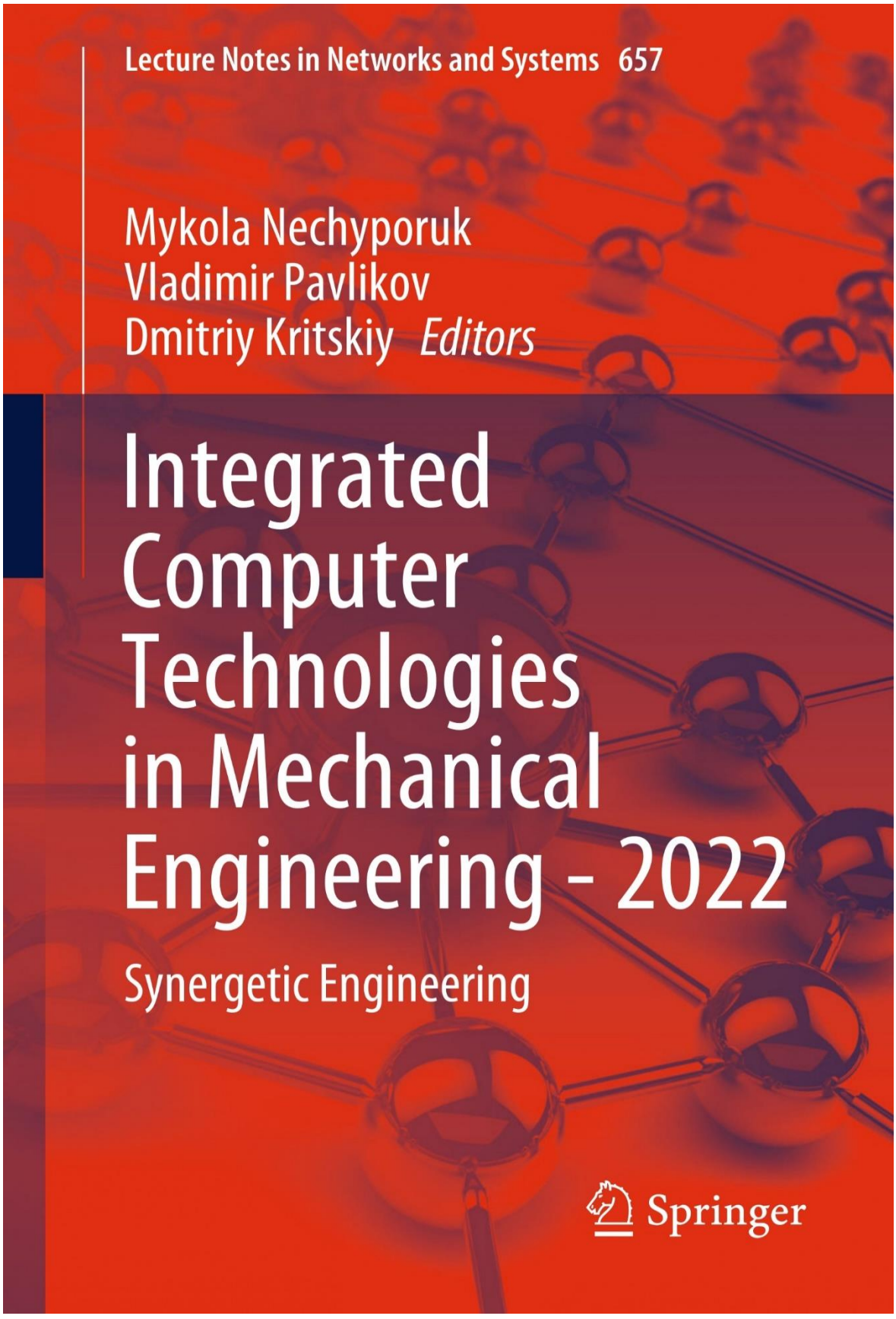
Lecture Notes in Networks and Systems 657
Mykola Nechyporuk
Vladimir Pavlikov
Dmitriy Kritskiy Editors
Integrated Computer Technologies in Mechanical Engineering - 2022
Synergetic Engineering
Springer

Lecture Notes in Networks and Systems 657

The series "Lecture Notes in Networks and Systems" publishes the latest developments in Networks and Systems—quickly, informally and with high quality. Original research reported in proceedings and post-proceedings represents the core of LNNS.

Volumes published in LNNS embrace all aspects and subfields of, as well as new challenges in, Networks and Systems.

The series contains proceedings and edited volumes in systems and networks, spanning the areas of Cyber-Physical Systems, Autonomous Systems, Sensor Networks, Control Systems, Energy Systems, Automotive Systems, Biological Systems, Vehicular Networking and Connected Vehicles, Aerospace Systems, Automation, Manufacturing, Smart Grids, Nonlinear Systems, Power Systems, Robotics, Social Systems, Economic Systems and other. Of particular value to both the contributors and the readership are the short publication timeframe and the world-wide distribution and exposure which enable both a wide and rapid dissemination of research output.

The series covers the theory, applications, and perspectives on the state of the art and future developments relevant to systems and networks, decision making, control, complex processes and related areas, as embedded in the fields of interdisciplinary and applied sciences, engineering, computer science, physics, economics, social, and life sciences, as well as the paradigms and methodologies behind them.

Indexed by SCOPUS, INSPEC, WTI Frankfurt eG, zbMATH, SCImago.

All books published in the series are submitted for consideration in Web of Science.

For proposals from Asia please contact Aninda Bose (aninda.bose@springer.com).

Mykola Nechyporuk · Vladimir Pavlikov ·
Dmitriy Kritskiy
Editors

Integrated Computer Technologies in Mechanical Engineering - 2022

Synergetic Engineering

Springer

Editors
Mykola Nechyporuk
National Aerospace University "Kharkov Aviation Institute"
Kharkov, Ukraine

Vladimir Pavlikov
National Aerospace University "Kharkov Aviation Institute"
Kharkov, Ukraine

Dmitriy Kritskiy
National Aerospace University – Kharki
Kharkov, Ukraine

ISSN 2367-3370 ISSN 2367-3389 (electronic)
Lecture Notes in Networks and Systems
ISBN 978-3-031-36200-2 ISBN 978-3-031-36201-9 (eBook)
https://doi.org/10.1007/978-3-031-36201-9

International Scientific and Technical Conference

Integrated Computer Technologies in Mechanical Engineering—Synergetic Engineering

Kharkiv, Ukraine
November 18, 2022

ICTM integrated computer technologies in mechanical engineering - synergetic engineering

Organized by:

National Aerospace University "Kharkiv Aviation Institute"

Kharkiv Regional State Administration

Patronage:

Ministry of Education and Science of Ukraine

(*continued*)

(GMT+2)	
13:20	Oleg Baranov. **Substrate thickness as a control factor in growth of copper oxide nanostructures**
13:30	Valeriy Sikulskyi, Kateryna Maiorova, Ihor Bychkov, Svitlana Myronova and Stanislav Sikulskyi. **Shape of Part Edges with the Various Surface Finish of the Adjacent Surfaces**
13:40	Gennadii Martynenko, Natalia Smetankina, Volodymyr Martynenko, Vyacheslav Merculov and Mykola Kostin. **Influence of Using Different Material Models of an Aircraft Gas Turbine Engine Fan Blade and a Bird When Simulating the Dynamics of a Collision Process in Flight**
13:50	TECHNICAL BREAK
14:10	Vitaliy Gaidachuk, Tetyana Nabokina, Igor Taranenko, Oleksandr Gaidachuk and Andrii Kondratiev. **Analysis of Gluing Assembly Defects of Ultra-Thin Composite Face Sheets with Honeycomb Core**
14:20	Sergey Filipkovskij, Valentin Chigrin, Alexander Sobolev and Evgeny Vasilevskij. **Simulation of Aircraft Engine Dynamic Effect on Aircraft Wing Caused by a Fan Blade-Off**
14:30	Kateryna Maiorova, Valeriy Sikulskyi, Iurii Vorobiov, Oleksandra Kapinus and Anton Knyr. **Study of a Geometry Accuracy of the Bracket-type Parts Using Reverse Engineering and Additive Manufacturing Technologies**
14:40	Danylo Krasii and Oleksiy Larin. **Application of Markov processes theory for computational prediction of turbine blade reliability**
14:50	Dmytro Zhyriakov, Oleksandr Grebenikov, Andrii Humennyi and Dmytro Konyshev. **Design of high fatigue life joints of fuselage structures considering fracture mechanics**
15:00	Osamah Ihsan Ali and Istvan Gabor Gyurika. **Recent Advances in Development and Characterization of CVD Multilayer Composite Coatings — A Comprehensive Review**
15:10	Julia Viazovychenko and Oleksiy Larin. **Algorithm of computational modeling the self-heating process of pneumatic tire in operation**
15:20	Volodymyr Martynenko. **Design Improvements of an Industrial Centrifugal Fan Based on the Computer Mathematical Simulation**
15:30	Khalil Deghoum, Oday Ibraheem Abdullah, Mohammed Tahar Gherbi, Hakim S. Sultan and Adnan N. Jameel Al-Tamimi. **Optimization of the Small Horizontal Axis Wind Turbine Blade Based on The Interactive Design Approach**
15:40	Dmytro Kritskiy, Oleksandr Karatanov, Andrii Pohudin, Sergii Koba. **Information Technology for Determining the Flight Performance of a Paraglider Wing**
15:50	CONCLUSIONS
15:55	CLOSING OF THE CONFERENCE : LOOKING TO THE FUTURE
11:00	SESSION 2—SOFTWARE ENGINEERING AND PROJECT MANAGEMENT https://meet.google.com/cry-xyej-pkm Dr. Dmytro Chumachenko – Chairman

(*continued*)

Information Technology in the Design and Manufacture of Engines

Nano-Modeling

Optimization of the Small Horizontal Axis Wind Turbine Blade Based on the Interactive Design Approach

Khalil Deghoum[1(✉)], Oday I. Abdullah[2,3,4], Mohammed T. Gherbi[5], Hakim S. Sultan[6], and Adnan N. Jameel Al-Tamimi[7]

[1] UDERZA Laboratory, University of El Oued, 39000 El Oued, Algeria
deghoum-khalil@univ-eloued.dz
[2] Department of Energy Engineering, College of Engineering, University of Baghdad, Baghdad, Iraq
[3] Mechanical Engineering Department, College of Engineering, Gulf University, Sanad, Kingdom of Bahrain
[4] Institute of Laser and Systems Technologies, Hamburg University of Technology, Hamburg, Germany
[5] Department of Mechanical Engineering, University of El Oued, 39000 El Oued, Algeria
[6] College of Engineering Karbala, University of Warith Al-Anbiyaa, Karbala, Iraq
[7] College of Technical Engineering, Al-Farahidi University, Baghdad, Iraq

Abstract. Wind energy is one of the most important sources in the renewable energy field. The modern small wind turbine blade is manufactured from composite materials. In this study, the finite element technique was used to simulate a 3D model of a small wind turbine blade to optimize the blade material. Four composite materials were used (carbon/epoxy, Kevlar/epoxy, E-glass/epoxy, and S-glass/epoxy) to find the most suitable material for the wind blade. Firstly, the computational Fluid Dynamics (CFD) method was used to calculate the pressure applied to the blade, and then use it as input load in the finite element model. From the obtained results, it was found that the maximum flapwise and edgewise deflections are for S-glass of 8.22 mm and 5.87 mm, respectively. While the weight of the finite element model of Kevlar material was the lightest at 1.93 kg. Based on the stress analysis, it was found that the root region is the most exposed region to the influence of loads, making it the most to crack initiation and blade failure.

Keywords: Composite materials · stress analysis · FEM · wind turbine blade · CFD

1 Introduction

The demand for energy in the world is increasing day by day due to the increase in population and industry around the world [1]. The wind turbines are considered one of the most important sources in the production of clean energy and one of the solutions to the growing demand for energy, as stated in the World Wind Energy Association (WWEA) report. The capacity installed of wind turbines in all countries of the world for the year 2021 is approximately 840 GW, an increase of 97.3 GW compared to the year 2020 [2].

M. Nechyporuk et al. (Eds.): ICTM 2022, LNNS 657, pp. 396–406, 2023.
https://doi.org/10.1007/978-3-031-36201-9_34

The blade is an important element in the wind turbine to generate power by rotating the generator after being exposed to variable wind loads that lead to rotating the shaft. Where in some cases, under extreme load conditions, the blade of the wind turbine fails before the premature. One of the important reasons to enhance the strength and lifetime of the wind turbine blade is the optimal selection of the material, as the blades are mostly made of composite materials due to their lightweight and high stiffness [3].

There is a lot of research that studied the structure and material of the wind turbine blade [4–6]. Pourrajabian et al. [7] developed a methodology to simplify the design of a small wind turbine using the genetic algorithm. He improved the blade structure and the shell of the composite material of the blade as well as calculated the stresses and the deformation of the blade. Boudounit et al. [8] used the finite element method to simulate the structure of the offshore wind turbine to predict the most sensitive area for damage to fiberglass and carbon fiber materials using the ABAQUS software in the simulation process. Haselbach and Branner [9] studied the failure of the trailing edge of a 34 m wind turbine to show the importance of nonlinear finite element analysis and verified the results with the experimental work. Finnegan et al. [10] used three different Finite Element softwares (ABAQUS, ANSYS, and CalculiX) to compare their results in calculating the flapwise deflection and leading and trailing edge deflection for a model of a 13 m full-scale wind turbine.

The main aim of this research paper is to present full details of the simulation for a small wind turbine with a power of 5 kW using the Finite Element Method (ANSYS software) to find the most optimal material for the wind turbine blade.

2 Structure and Blade Design

2.1 Design Wind Turbine

The selected model in this work is a 5-kW small wind turbine. Based on the Betz's theorem [11] and MATLAB software, the chord and the twist will be calculated for each section along the blade length. The NACA 4412 was selected as an airfoil from root to tip of the blade. The design wind speed is 10.5 m/s, and the optimal angle of attack is 6°. Table 1 shows the specifications of the selected wind turbine blade. It was build a model based on Betz theory and then coded using MATLAB software to calculate the blade geometry parameters. The blade is divided into 10 sections; in each radial position, the chord, twist angle, and angle of attack was calculated. Figure 1 shows the chord and twist angles of the blade. Figure 2 illustrates the 3D geometry of the wind turbine blade.

Table 1. Initial design parameters of 5 kW small wind turbine.

Design parameter	Value	Unit
Rated power	5	kW
Design Wind speed	10.5	m/s
Number of blades	3	-
Design tip speed ratio	6	-
Rotor radius	2.5	m
Design rotational speed	240	rpm
Airfoil type	NACA4412	-

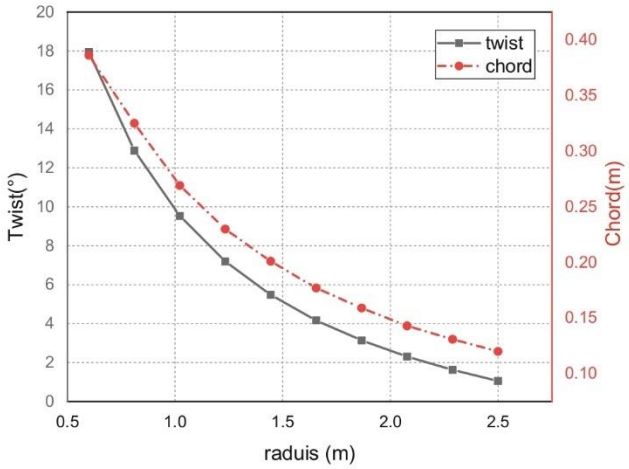

Fig. 1. Twist angle and Chord distribution of the studied blade.

2.2 Finite Element Model

The FE model was created using the Ansys software to simulate a small wind turbine under wind load, gravity, and centrifugal force. The mesh, boundary conditions, and materials lay-up will be explained in this section.

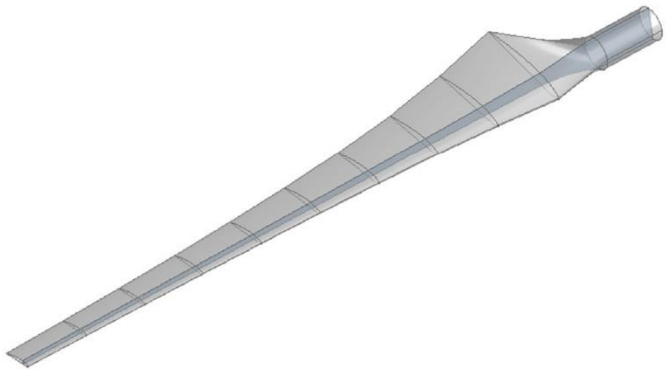

Fig. 2. 3D geometry model of 5 kW wind turbine blade

Material Properties

Four types of composite materials were selected (carbon fiber, Kevlar, E-glass, and S-glass) to build the numerical model (structure) and simulate the wind turbine blade. The lay-up sequence of fibers for a small wind turbine was described with full details. In this study, it was adopted the same lay-up ply for all selected materials $[0/90]_3$ for the shell and $[45/-45]_3$ for the spar cap of the blade, where each ply has a 0.25 mm thickness. Table 2 lists the mechanical properties of the four selected materials. Figure 3 shows the lay-up of fiber used in the developed model.

Table 2. Materials Properties of UD composite used

Material Properties	E-glass/epoxy [8]	S-glass/epoxy [12]	Carbon/epoxy [12]	Kevlar/epoxy [12]
Density (kg/m^3)	1900	2000	1600	1380
E_1 (GPa)	48.16	43	177	87
E_2 (GPa)	11.21	8.9	10.8	5.5
G_{12} (GPa)	4.42	4.5	7.6	2.2
υ_{12}	0.274	0.27	0.27	0.34
υ_{21}	0.096	0.06	0.02	0.02
X_T (MPa)	1021.3	1280	2860	1280
Y_T (MPa)	29.5	49	49	30
X_C (MPa)	978	690	1875	335
Y_C (MPa)	171.8	158	846	158

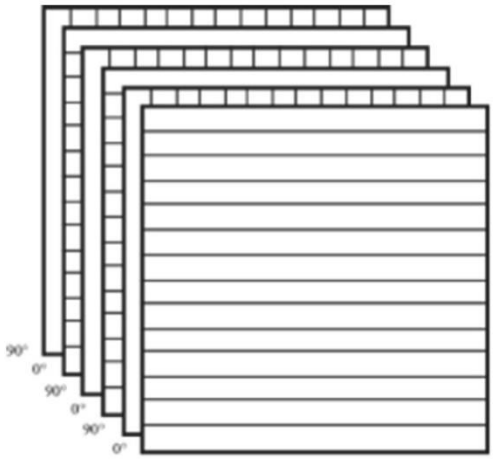

Fig. 3. The Lay-up sequence of composite materials used

Selected Optimal Mesh

After establishing the design of the blade using Ansys design Modeler (DM) software, as shown in Fig. 1. The final design was exported to the ANSYS static structure software to simulate the model using the finite element method. During the meshing process, a Tetrahedron element was selected to build the FE model of the blade. The mesh convergence analysis is needed before selecting the required mesh size. The analysis of mesh convergence has been done to determine the most optimal size of mesh for the FE model of the blade. The final results of the finite element model were accepted when the relative errors were less than 1% to ensure the accuracy of the results. The optimal mesh in the considered model consists of 122108 elements and 122393 nodes. Figures 4 (a and b) show the difference between the initial mesh and the final mesh size of the FE model.

Boundary Conditions

In structural analysis, the (DOFs), loads, and rotations were defined. The blade is fixed at the root side, so all degrees of freedom are null at this region. Loads are produced when wind speed collides with the surface of the blade. For this purpose, it was used the ANSYS/ Fluent to calculate the applied loads to the surface of the blade. In the next step, the loads were converted to the static structure model to estimate the stresses and deflections of the blade. Figure 5 shows the boundary conditions that were applied to the wind turbine blade.

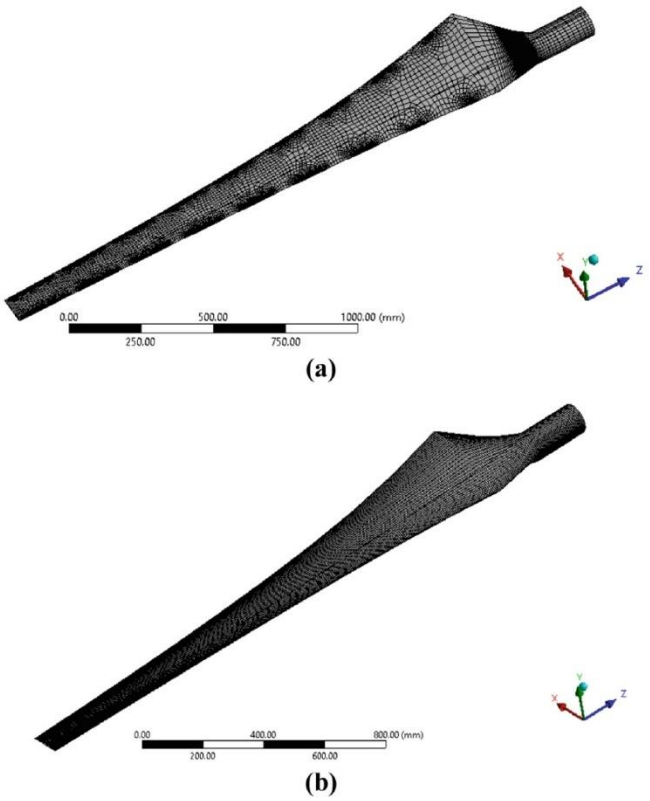

Fig. 4. FE model blade (a) the initial mesh (b) final mesh

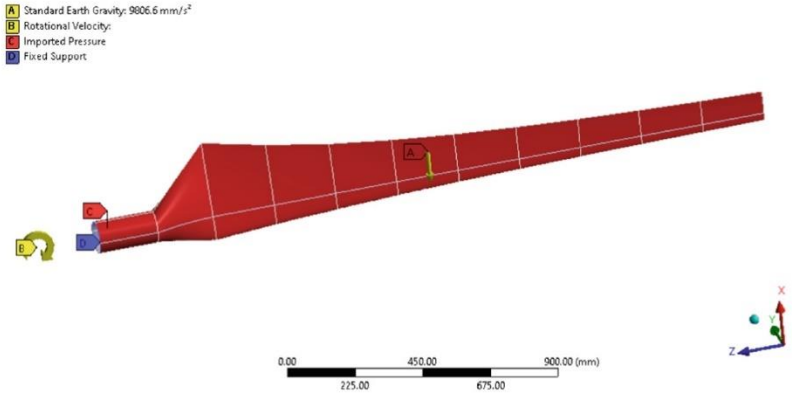

Fig. 5. Boundary conditions that applied to the FE model of blade

3 Results and Discussions

In this study, it was developed an approach that couples (called fluid-solid interaction) the computational fluid dynamics analysis to find the pressure distributions and use them as load in the structural analysis. Where the loads applied to the wind turbine blade under the influence of 10 m/s were calculated to investigate the most optimal material for the blade based on the obtained results of stresses and deflections for each model. Figure 6. Shows the pressure of wind speed of 10 m/s applied on the blade surface.

Deflection is considered one of the problems for wind turbine blades, which is caused by applied loads on the blade surfaces due to pressure, rotational speed, and gravity. Figure 7 shows the flapwise deflections of the selected materials. It can be seen from Fig. 7 (a-d), that the tip deflections of the blade that is made from the carbon fiber material is 2.01 mm, E-glass is 6.77 mm, Kevlar is 3.79 mm, and the S-glass is 8.22 mm.

In Fig. 8, it can be seen that the leading-edge deflection of the wind turbine blade. From these results, it can be noticed that the blade deflection of the carbon fiber material is 1.95 mm, E-glass is 5.87 mm, Kevlar is 4.03 mm, and s-glass is 6.98 mm. This means that the largest deflection occurred for the s-glass.

Based on the obtained results, the comparison between the four materials to choose the most suitable material for manufacturing the wind turbine blade. Furthermore, it was calculated the von mises stresses as shown in Fig. 9, where it can be noticed that the stress concentrated on the root region. This means this region is most region tends to fail. Also, it can be observed that the largest stresses that occurred when using s-glass material are 35.82 MPa, followed by carbon fiber material with 35.61 MPa, then Kevlar with 32.91 MPa, then E-glass with 32.67 MPa.

Choosing the most optimal material is not based on the most strength or least deflection, but it must also focus on the material that gives the lightest weight with high stiffness because the weight of the blade has a major issue on the life of the blade, as well as the load of gravity that has an effective role with the weight of the blade. Figure 10 illustrates the weight of the blade using the selected materials, as the weight of the carbon fiber blade is 2.24 kg, the blade of E-glass is 2.60 kg, the blade of Kevlar is 1.93 kg, and the blade of S-glass material is 2.8 kg.

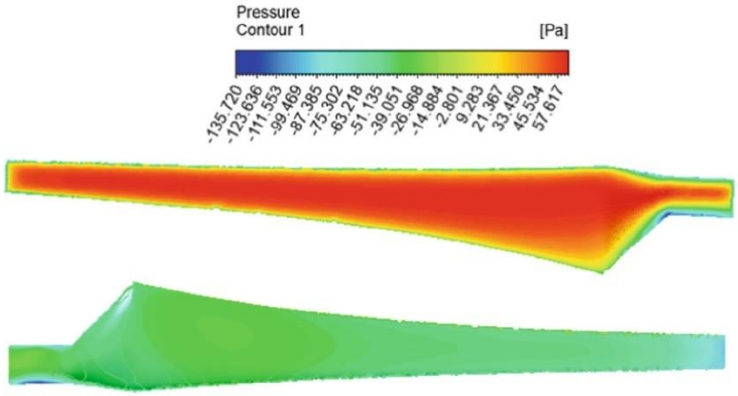

Fig. 6. The distribution of local pressure on the suction side and pressure side.

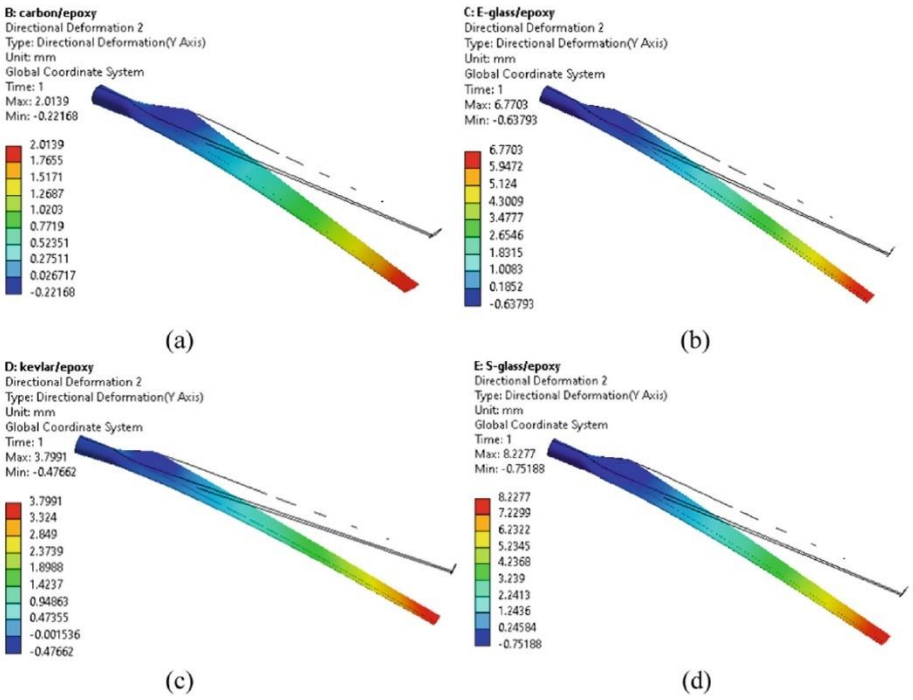

Fig. 7. Flapwise deflection of (a) carbon epoxy, (b) E-glass, (c) kevlar, and (d) S-glass

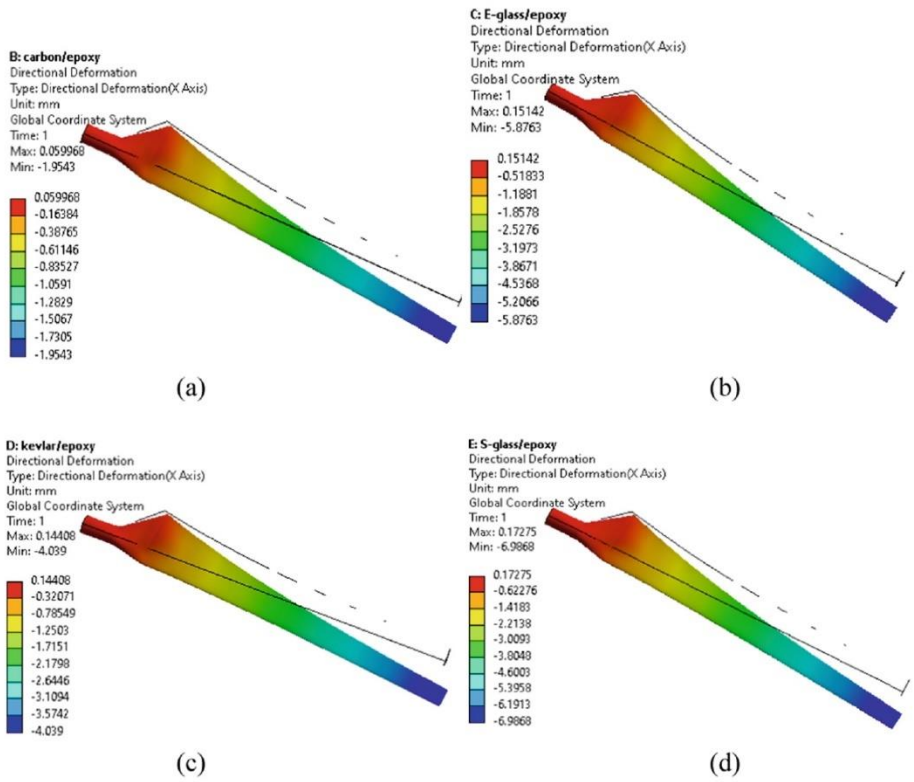

Fig. 8. Edgewise deflection of (a) carbon epoxy, (b) E-glass, (c) kevlar, and (d) S-glass

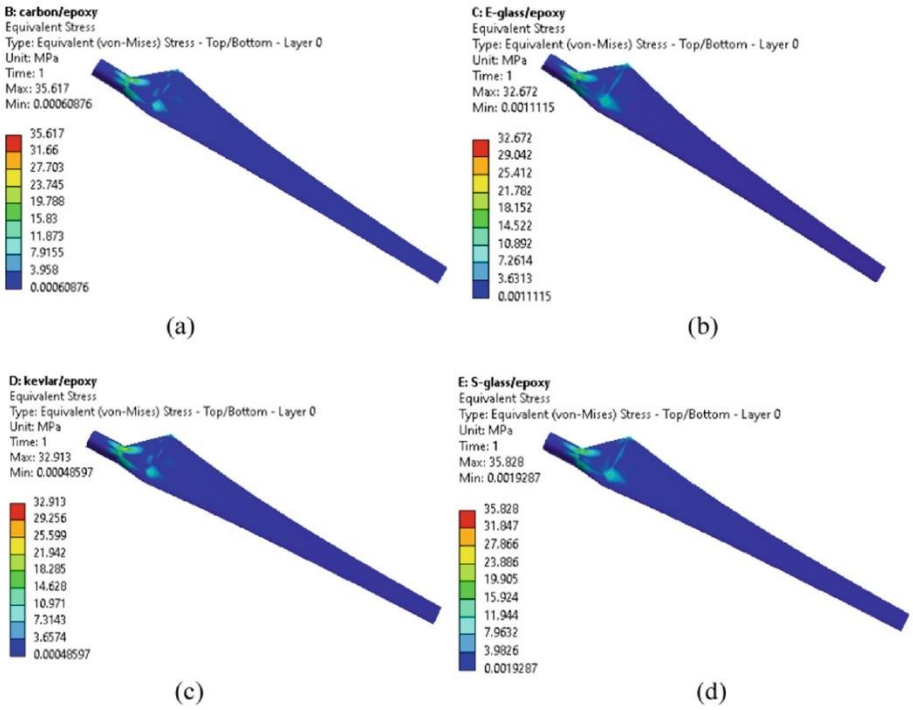

Fig. 9. Von mises stresses of (a) carbon epoxy, (b) E-glass, (c) kevlar, and (d) S-glass

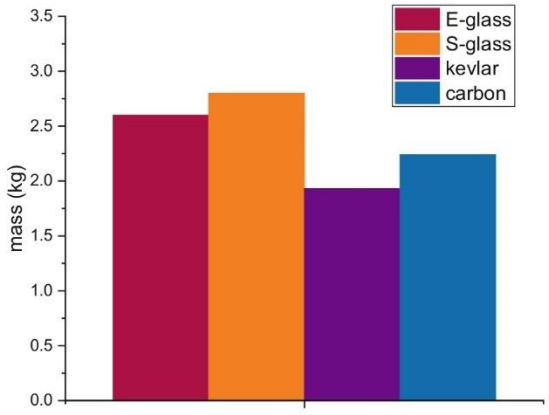

Fig. 10. The masses of blades using the selected materials

4 Conclusions and Future Works

It can be considered that selecting the optimum material to build the structure of the wind turbine blade is the most important element to obtain the optimal design of the blade to ensure get the highest efficiency with the best performance. Also, a developed

approach (fluid-solid interaction) was presented to compute the pressure distributions and, based on it, find the stresses and deflections.

Four typical composite materials, carbon fibre, Kevlar, E-glass, and S-glass were selected to find the optimal one for the blade. The comparison was based on the flapwise deflection, the edgewise deflection, and the von Mises stresses. The stresses for the blade that was exposed to the wind speed of 10 m/s. It was found that the highest flapwise deflection was for S-glass material with a value of 8.22 mm, followed by E-glass material with a value of 6.77 mm, then Kevlar with a value of 3.79 mm, and the lowest deflection was for carbon fiber material with 2.01 mm. While the largest edgewise deflection was for S-glass by 6.98 mm, then by E-glass with a deflection of 5.87 mm, then by Kevlar and carbon fiber by 4.03 mm, respectively. The stresses were calculated for the four studied materials, and after analyzing the results, it was found that the stress concentration region occurred at the root of the blade, and this makes it the most likely region for the initiation of a crack.

The wind turbine blade works under fluctuating loads for a period of time; therefore, the blade material is subjected to fatigue load. In future work, it will investigate the fatigue of the wind turbine blade under operating conditions of loads.

References

1. Tüfekci, M., Genel, Ö.E., Tatar, A., Tüfekci, E.: Dynamic analysis of composite wind turbine blades as beams: an analytical and numerical study. Vibration **4**(1), 1–15 (2020)
2. WWEA. https://wwindea.org/information-2/statistics-news/. Accessed
3. Wu, W.-H., Young, W.-B.: Structural analysis and design of the composite wind turbine blade. Appl. Compos. Mater. **19**(3), 247–257 (2012)
4. Basri, E.I., Sultan, M.T.H., Basri, A.A., Mustapha, F., Ahmad, K.A.: Consideration of lamination structural analysis in a multi-layered composite and failure analysis on wing design application. Materials **14**(13), 3705 (2021)
5. Park, H.: A study on structural design and analysis of small wind turbine blade with natural fibre (flax) composite. Adv. Compos. Mater **25**(2), 125–142 (2016)
6. Rafiee, R., Tahani, M., Moradi, M.: Simulation of aeroelastic behavior in a composite wind turbine blade. J. Wind Eng. Ind. Aerodyn. **151**, 60–69 (2016)
7. Pourrajabian, A., Afshar, P.A.N., Ahmadizadeh, M., Wood, D.: Aero-structural design and optimization of a small wind turbine blade. Renew. Energy **87** 837–848 (2016)
8. Boudounit, H., Tarfaoui, M., Saifaoui, D., Nachtane, M.: Structural analysis of offshore wind turbine blades using finite element method. Wind Eng. **44**(2), 168–180 (2020)
9. Haselbach, P.U., and Branner, K.: Initiation of trailing edge failure in full-scale wind turbine blade test. Eng. Fract. Mech. 162, 136–154 (2016)
10. Finnegan, W., Jiang, Y., Dumergue, N., Davies, P., Goggins, J.: Investigation and validation of numerical models for composite wind turbine blades. J. Mar. Sci. Eng. **9**(5), 525 (2021)
11. De Lellis, M., Reginatto, R., Saraiva, R., Trofino, A.: The Betz limit applied to airborne wind energy. Renew. Energy **127**, 32–40 (2018)
12. Mian, H.H., Wang, G., Dar, U.A., Zhang, W.: Optimization of composite material system and lay-up to achieve minimum weight pressure vessel. Appl. Compos. Mater. **20**(5), 873–889 (2013)

Author Index

M. Nechyporuk et al. (Eds.): ICTM 2022, LNNS 657, pp. 767–769, 2023.
https://doi.org/10.1007/978-3-031-36201-9

ANNEXE. 5 Certificates of Participation in International Conferences in Algeria

People's Democratic Republic of Algeria
Ministry of Higher Education and Scientific Research
Echahid Hamma Lakhdar University - El-Oued
International Pluridisciplinary PhD Meeting (IPPM'20)
1st Edition, February 23-26, 2020
Theme: Modern Technology and Fineness Life

Certificate of Participation

This Certifies that the paper entitled as

Simulation by the finite element method of the wind turbine blade material under the influence of the variable wind force

Has been presented with successfully as (Poster) presentation at the IPPM'20

By. **DEGHOUM Khalil**

Co-Authors: Mohammed Tahar Gherbi

Algeria, Sunday, March 22, 2020
IPPM'20 Chairman

We look forward to your continued and outstanding contribution for our university in the future ...

The First International Conference on Materials, Energy and Environment

El Oued 12/12/2019

NOTIFICATION OF ACCEPTANCE

N°: MP67

Dear **Khalil Deghoum**

The Scientific Committee of the First International Conference on Materials, Energy and Environment (MEE'2020) has the great pleasure to inform you that your contribution Entitled:

Simulation by finite element method of wind turbine materials

has been peer reviewed and accepted as an **poster** presentation at the MEE'2020 to be held in University of Echahid Hamma Lakhdar at El Oued (Algeria) between January 20-21, 2020.

With sincere greetings, we look forward to welcoming you to El Oued in January 2020.

Sincerely Yours,

General Chair

Mohammed El Hadi ATTIA

Echahid Hamma Lakhdar University of El Oued Faculty of Exact Sciences The First International Symposium on Materials, Energy and Environment (MEE 2020) Department of Physics

ANNEXE. 6 Certificates of Participation International Conferences in other countries

Conferences in Ukraine

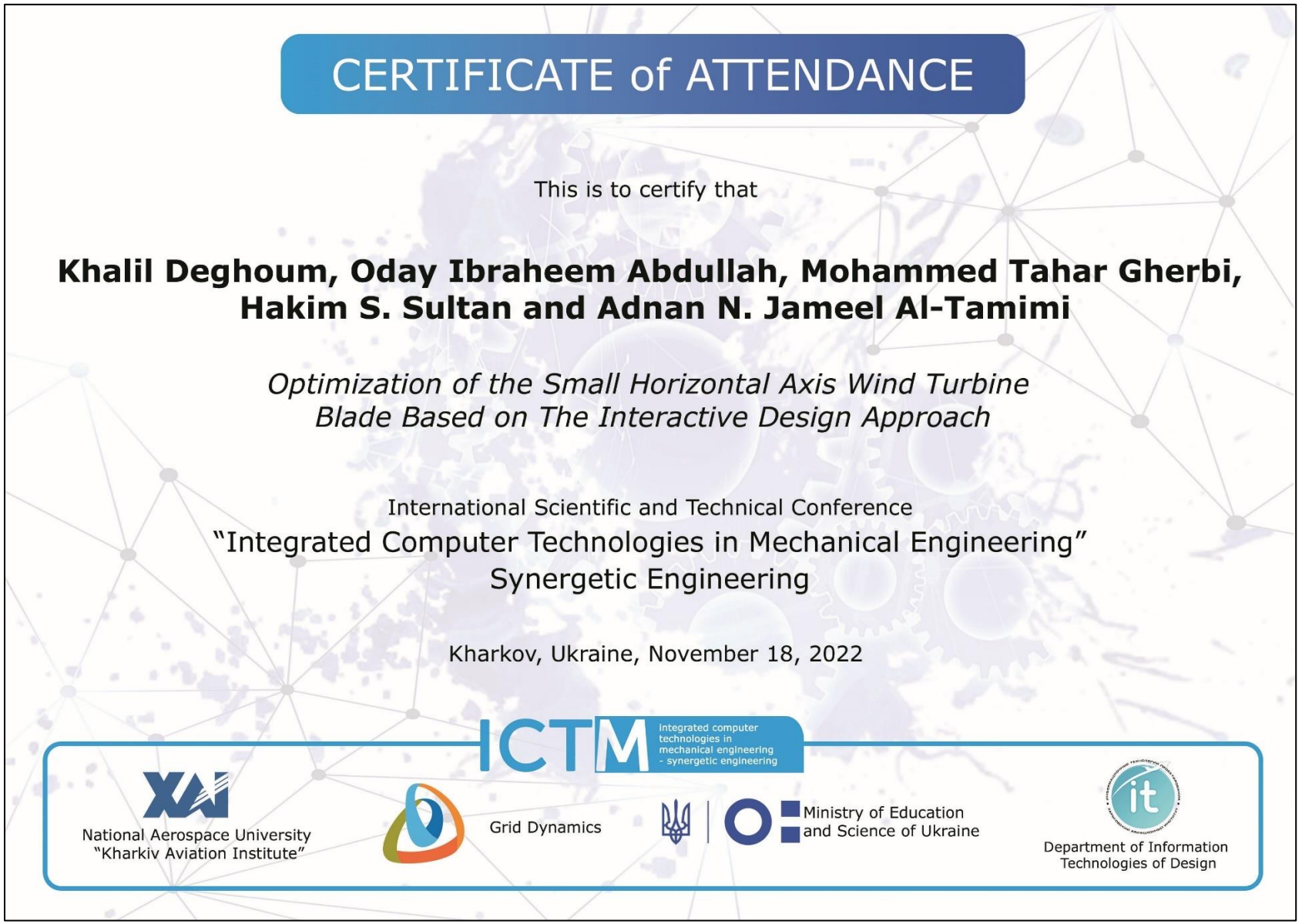

Conferences in Iraq

The 3rd International Conference on Electromechanical Engineering & its Applications

ICEMEA-2022

CERTIFICATE of PARTICIPATION

THIS IS TO CERTIFY THAT

« Khalil DEGHOUM, Adnan N. Jameel Al-TAMIMI, Mohammed T. GHERBI, Smail HAMIDATOU, and Oday I. ABDULLAH » presented the paper entitled

« A New Approach for Designing Small Horizontal Axis Wind Turbine Blades «

in the 3rd International Conference on Electromechanical Engineering and its Applications (ICEMEA-2022) which is held by Electromechanical Engineering Department University of Technology, Baghdad, Iraq, in 19th – 20th July, 2022

The Chairman of ICEMEA-2022

Professor Dr. Hosham Salim

3rd International Conference on Engineering & Science (ICES2023)
3 -4 MAY 2023
AL-SAMAWA, IRAQ

Initial Acceptance Letter

Manuscript Number: 164_Abdullah_ICES2023 **Decision ID. :** 070_IAL_ICES
Date : 15/4/2023

Dear Khalil Deghoum,

Co-Authors : Hakim S. Sultan, Mahir H. Majeed, Adnan Naji Jameel Al-Tamimi, Mohammed T. Gherbi, M. N. Mohammed, Oday I. Abdullah, and Ali Boukhari

Congratulations!

It's a great pleasure to inform you that, after the peer review process, your manuscript entitled

Study of the Crack in Wind Turbine Blade Using the XFEM Method

Has been **ACCEPTED** for participating in the **3rd International Conference on Engineering & Science,** and considered for publication in **AIP Conference Proceedings.**

* This is not a final acceptance letter, we will issue the final letter after receiving the registration fees.

Thank you for your valuable participation in the ICES2023 conference.

Dr.Ahmed Razzaq H. Al-Manea
ICES2023 Scientific Committee | AIP Conference Proceedings Editor
3 - 4 MAY 2023 | SAMAWA| IRAQ

Certificate of Paper Acceptance

Dear Khalil Deghoum, Adnan Naji J. Al-Tamimi, Mohammed T. Gherbi, Azher M. Abed, M. N. Mohammed, Oday I. Abdullah, Ali Boukhari and Smail Hamidatou,

Thank you for your submission to the IRCEAS2023 conference. We are pleased to inform you that your paper entitled "**Steady-State and Vibration Analyses of Wind Turbine Blades Based on Numerical Approach Using Different Materials"** has been **accepted as a full paper** for oral presentation at the upcoming International Research Conference on Engineering and Applied Sciences 2023 (IRCEAS2023), which will be held on 9th to 10th October 2023 at College of Engineering building, Al-Iraqia University, Saba'a Abkar Complex, Baghdad, Iraq. Knowing that all accepted papers will be published in **AIP conference proceedings (Scopus-Indexed).**

Your paper was reviewed by our expert panel of reviewers and was found to be relevant to the conference theme and of high quality. We appreciate the effort and time you have put into your research.

Once again, congratulations for the acceptance, and we look forward to your participation in the conference.

Sincerely,

Prof. Dr. Muwafaq Shyaa Alwan
Chairman of the Conference

College of Engineering, Al-Iraqia University, saba'a Abkar Complex, Baghdad, Iraq
Website: www.irceas.com
Email: conf@irceas.com

ANNEXE. 7 Participating secondary author in academic research

Conference Participation

PEOPLE'S DEMOCRATIC REPUBILC OF ALGERIA

MINISTRY OF HIGHER EDUCATION AND SCIENTIFIC RESEARCH
UNIVERSITY OF KASDI MERBAH OUARGLA
FACULTY OF MATHEMATICS AND MATTER SCIENCES

****

N° : TAM188/2021

1st International Conference on Sustainable Energy and Advanced Materials
IC-SEAM'21 April 21-22, 2021, Ouargla, ALGERIA (Virtual conference)

****

CERTIFICATE OF PARTICIPATION

The organizing committee of the first International Conference on Sustainable Energy and Advanced Materials IC-SEAM'21 April 21-22, 2021, Ouargla, ALGERIA, certifies that:

Smail HAMIDATOU

presented an Oral communication entitled:

An Investigation Simulation of the Effect of Different Nanofluids on the Thermal Performance of Geothermal Heat Exchanger Vertical Square Shape (GHEVSS) Using Two Different Types of Nanoparticles

Co-author (s): **Khalil Deghoum**

Dean of the Faculty
Pr. Djamel BECHKI

IC-Coordinator of IC-SEAM'21
Dr. Lazhar BENMEBROUK

Chairman of the IC-SEAM'21
Dr. Lazhar MOHAMMEDI

PEOPLE'S DEMOCRATIC REPUBILC OF ALGERIA

MINISTRY OF IIIGHER EDUCATION AND SCIENTIFIC RESEARCH
UNIVERSITY OF KASDI MERBAH OUARGLA
FACULTY OF MATHEMATICS AND MATTER SCIENCES

****

N° : TAM373/2021

1st International Conference on Sustainable Energy and Advanced Materials
IC-SEAM'21 April 21-22, 2021, Ouargla, ALGERIA (Virtual conference)

****

CERTIFICATE OF PARTICIPATION

The organizing committee of the first International Conference on Sustainable Energy and Advanced Materials IC-SEAM'21 April 21-22, 2021, Ouargla, ALGERIA, certifies that:

Mohammed Iliasse BOULIFA

presented an Oral communication entitled:

Evaluation of structural and mechanical properties of a metallic material destined to wind turbine industry

Co-author (s): **Ali HADJI, Khalil DEGHOUM, Assem DJABALLAH, Khalil KENIOUA and Mohamed Nadir LABIDI**

Dean of the Faculty
Pr. Djamel BECHKI

Coordinator of IC-SEAM'21
Dr. Lazhar BENMEBROUK

Chairman of the IC-SEAM'21
Dr. Lazhar MOHAMMEDI

Article participation 1

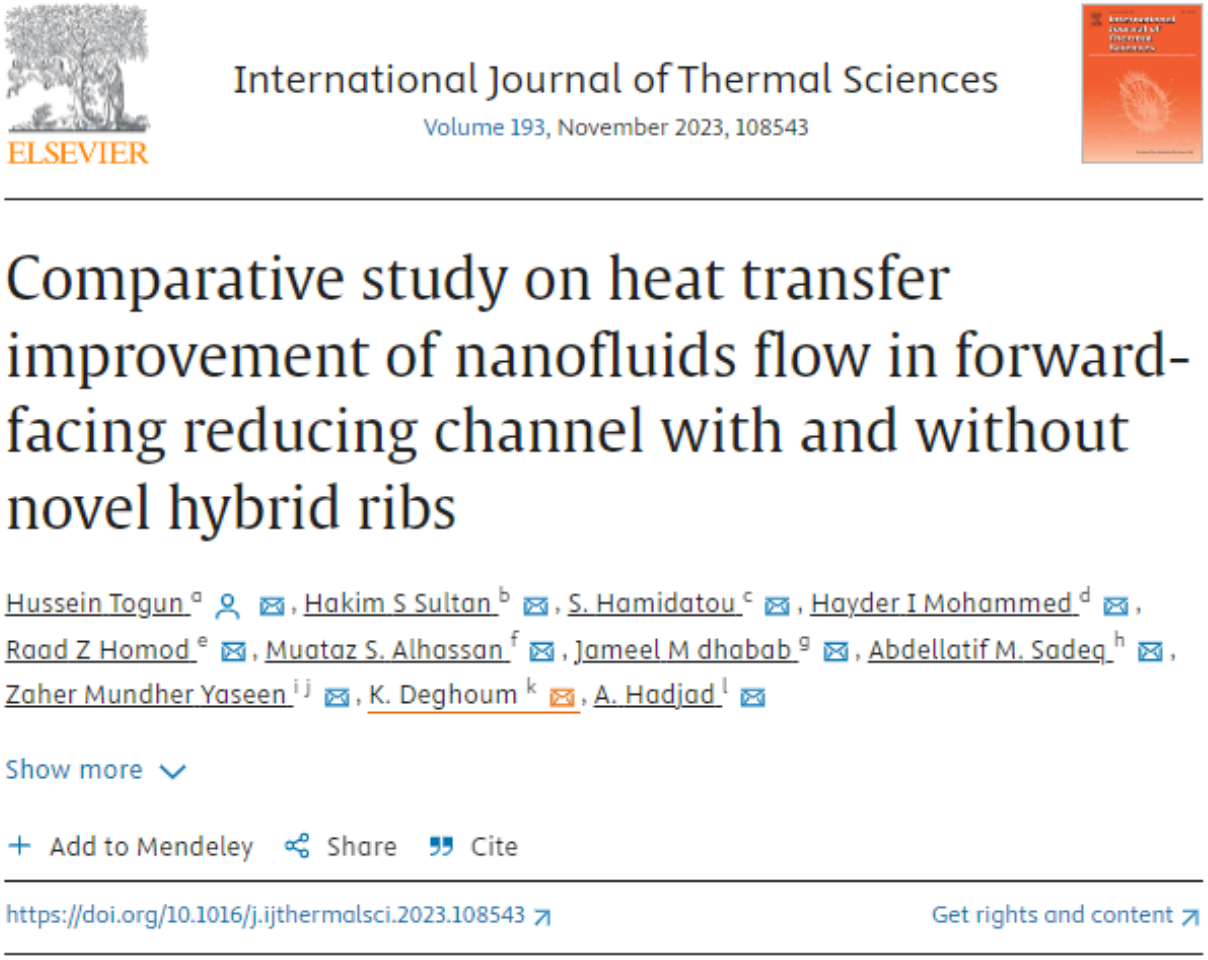

International Journal of Thermal Sciences
Volume 193, November 2023, 108543

Comparative study on heat transfer improvement of nanofluids flow in forward-facing reducing channel with and without novel hybrid ribs

Hussein Togun [a], Hakim S Sultan [b], S. Hamidatou [c], Hayder I Mohammed [d], Raad Z Homod [e], Muataz S. Alhassan [f], Jameel M dhabab [g], Abdellatif M. Sadeq [h], Zaher Mundher Yaseen [i j], K. Deghoum [k], A. Hadjad [l]

Show more

https://doi.org/10.1016/j.ijthermalsci.2023.108543

H. Togun *et al.*, "Comparative study on heat transfer improvement of nanofluids flow in forward-facing reducing channel with and without novel hybrid ribs," *International Journal of Thermal Sciences,* vol. 193, p. 108543, 2023.
https://doi.org/10.1016/j.ijthermalsci.2023.108543

Article participation 2

S. Hamidatou *et al.*, "Experimental investigation of a novel heat exchanger for optimizing heat transfer performance using Al2O3-water nanofluids," *Heat and Mass Transfer,* pp. 1-12, 2023. https://doi.org/10.1007/s00231-023-03356-w